DISSERTATION

BULK AND INTERFACE VIBRATIONAL RAMAN SPECTROSCOPY WITH COHERENCE MODULATED OPTICAL SUSCEPTIBILITIES

Submitted by

Jesse W. Wilson

Electrical and Computer Engineering Department

In partial fulfillment of the requirements

For the Degree of Doctor of Philosophy

Colorado State University

Fort Collins, Colorado

Fall 2010

COLORADO STATE UNIVERSITY

July 28, 2010

WE HEREBY RECOMMEND THAT THE DISSERTATION PREPARED UNDER OUR SUPERVISION BY JESSE W. WILSON ENTITLED BULK AND INTERFACE VIBRATIONAL RAMAN SPECTROSCOPY WITH COHERENCE MODULATED OPTICAL SUSCEPTIBILITIES BE ACCEPTED AS FULFILLING IN PART REQUIREMENTS FOR THE DEGREE OF DOCTOR OF PHILOSOPHY.

Committee on Graduate Work

Diego Krapf

Mario Marconi

Jacob Roberts

Advisor: Randy Bartels

Department Head: Anthony Maciejewsky

ABSTRACT OF DISSERTATION

BULK AND INTERFACE VIBRATIONAL RAMAN SPECTROSCOPY WITH COHERENCE MODULATED OPTICAL SUSCEPTIBILITIES

The effect on an ultrashort probe pulse of an impulsively prepared vibrational coherence is described by effective linear and nonlinear optical susceptibility perturbations. Linear susceptibility perturbations modulate both the amplitude and phase of a probe pulse. Three spectral interferometry methods are described for measuring this phase modulation, geared toward spectral resolution, noise suppression, and rapid data acquisition. Third-order nonlinear interactions perturbations may be used to acquire surface-specific Raman spectra. While second-order spectroscopy is an established surface-specific technique, odd-order methods have been passed over because the signal is generated in the bulk media. We show that through a surface Fresnel modulation, coherence-modulated third harmonic generation can be used to obtain surface-specific vibrational information. Bulk and interface contributions to the vibrational signal are separated by scanning the interface through the focus of the laser beam.

Jesse W. Wilson
Electrical and Computer Engineering Department
Colorado State University
Fort Collins, Colorado 80523
Fall 2010

ACKNOWLEDGEMENTS

I would like to thank my adviser, Randy Bartels for his patience, encouragement, and especially his enthusiasm. His notes on nuclear modulation of harmonic generation laid the foundation for our theoretical understanding of the interface scans described in this thesis. I owe many thanks to Philip Schlup for his construction of the 2DFFT set-up and time spent taking data. His experience in optical laboratory practices and software development have been indispensable throughout my career as a graduate student. Omid Masihzadeh and David Kupka have both contributed to getting the coherence modulated third harmonic experiment running, and to taking data.

I also thank Louis Scharf for his discussions on LPSVD and spectral estimation methods in general, and Roberto Merlin for his correspondence regarding surface and bulk phonons. In addition, the collaboration we have had with Nancy Levinger have led to many exciting prospects for the future of the coherence-modulated THG setup. Thanks to Ryan Trott and Kevin Dillman, the setup described in the second Part of this dissertation will live on and hopefully provide more results.

Thanks go to the developers of GNU Emacs, LaTeX, Emacs org-mode, and Zotero. I cannot imagine putting together such a large document without these indispensable software tools.

Last but certainly not least, I would like to thank my dear wife Juli for her support, especially through the home stretch of finishing this dissertation.

TABLE OF CONTENTS

LIST OF TABLES

LIST OF FIGURES

PART I

Effective linear modulation

CHAPTER I

INTRODUCTION

1.1 Interface vibrational motion and its importance

1.1.1 General interface studies

The study of interface vibrational motion plays an important role in surface chemistry, lending insight to energy conversion, adsorption, surface catalysis, interface structure and composition. This prominent role motivated significant development of spectroscopy techniques with surface specificity. A general overview of these methods is found in Brune, et al [1] and in particular methods of probing surface vibrational modes are reviewed in Esser and Richter [2].

Characterizing and probing interfaces may benefit research in dye-sensitized solar cell technology [3]. Resonance Raman scattering has already yielded information about chemical processes in these systems [4]. Efficiency of these solar cells is reduced by any possible energy transfer mechanism that does not result in a photo-excited charge being deposited at the anode. Femtosecond spectroscopy has been shown capable of measuring vibrational energy transfer at surfaces [5]. The development of a technique that can distinguish near-surface bulk and surface-specific vibrational motion in tandem with measuring charge transfer interactions could be of great importance.

1.1.2 Vibrational motion at interfaces

Low-frequency vibrational modes at interfaces are important, as they will have an appreciable population at room temperature (at room temperature, $kT/h/c = 193\text{cm}^{-1}$. We expect these modes play an important role in interface processes in ordinary devices and biological processes.

Two types of vibrational modes may be found at clean surface, categorized as either

macroscopic or microscopic surface modes [2]. Macroscopic modes are similar to bulk vibrations, but modified by the termination of bulk symmetry at the interface. The lack of restriction on the free side of the interface should lead to a shift toward lower frequency and higher amplitude [2]. An example of macroscopic modes is the Fuchs-Kliewer surface phonon-polariton modes [6], which are often picked up by electron scattering experiments. The second type, true surface modes or microscopic modes, result from the structural peculiarities to be found only at an interface, extending a distance no greater than the crystal lattice unit cell into the bulk [7] . For example, the Si-O-Si bond angle at the surface of quartz differs from the bulk angle by more than 10°, shifting the symmetric stretch mode by almost 100 cm^{-1} [8].

At an interface that has been exposed to a chemical environment, bonds of chemisorbed species may exhibit vibrational modes, revealing the particulars of how the molecule is chemisorbed. Another example from quartz is the surface silanols, Si-OH, that form on hydroxylation of the surface [8]. In addition physisorbed species may exhibit shifts in their vibrational mode frequencies and amplitudes due to the confinement from the nearby interface and possibly charge transfer interactions [9, 10]. A review of Raman scattering from adsorbed molecules is found in Ref. [11].

1.2 Measuring interfaces

The nature of an interface makes measuring its physical properties difficult. Bulk material on either side, in virtue of containing far more scattering sites, and leads to a stronger signal. Traditional interface measurements are done in vacuum with energetic beams of large particles that do not penetrate appreciably into the bulk, providing a surface specificity of 0.2 nm [1]. Optical methods penetrate materials and can reach buried interfaces, but give rise to Rayleigh scattering in the bulk, leaving the surface specificity around 0.1 μm [1] for linear methods, and second-order nonlinear processes can push surface specificity down to 10 nm [1] depending on the symmetry and composition of the interface.

1.2.1 Overview of non-optical interface probes

Many surface characterization techniques exist [1, 12]. In these, a sample is placed under ultra high vacuum conditions, bombarded with a probing particle, typically an electron or a helium atom. An electron of well-defined energy scatters off the surface, and the energy loss is measured (electron energy loss spectroscopy, or EELS) [13]. The electron energy is varied, and the resulting energy loss spectrum corresponds to resonances at the surface. High resolution and low-energy electron variants of this technique grant EELS access to the same resonant frequencies as optical spectroscopies. Alternatively, larger particles such as helium atoms may be used, which do not penetrate into dense bulk material at all [7], and give a more surface-specific measurement.

These highly successful methods do suffer from certain limitations. The ultra-high vacuum requirements preclude measurement of liquid surfaces, and make in-situ measurements of many chemically- or biologically-relevant surfaces impractical. Also, the very property of electrons and helium atoms that makes them very surface specific (they do not penetrate the bulk material) makes them unable to probe hidden interfaces, or interfaces between two materials. Finally, even the high resolution methods are limited to a few wavenumbers , which can be surpassed by optical techniques. Electron spectroscopies are limited in resolution by the uniformity of the electron momenta to $\Delta E = 0.3\text{meV}$ [14],

$$\Delta\bar{\nu}\ [\text{cm}^{-1}] = \frac{\Delta E\ [\text{eV}]}{h\ [\text{eV s}]c\ [\text{cm/s}]} = 2.4\ \text{cm}^{-1}, \tag{1.1}$$

where h is Planck's constant and c is the vacuum velocity of light. Commercial frequency-domain Raman spectrometers, such as the Perkins Elmer RamanMicro 300 can reach 1 cm^{-1}, while time-resolved phase sensitive methods, such the synthetic aperture method described later, has been demonstrated to reach 0.89 cm^{-1}, and could be extended to higher resolution by longer delay scanning.

1.2.2 Linear optical scattering

Optical probes do not share the the ultra-high vacuum restrictions of electron scattering methods [15]. This opens up a number of opportunities to probe interfaces of materials with

atmospheres, chemical environments, and buried interfaces. For example, surface infrared (IR) spectroscopy has probed surface reactions at high pressure [16] and sum frequency generation spectroscopy was demonstrated on the surface of liquid water, [17]. To probe buried interfaces that are inaccessible by electron scattering, optical wavelengths that non-resonant with the bulk media, and are not absorbed, may be used [18]. In addition, the use of ultrafast pulses enables time-resolved probing of femtosecond vibrational dynamics [19].

Linear optical surface techniques measure subtle changes in reflection due to surface phenomena [16, 1]. But material below the surface also scatters light, leading to surface-bulk ambiguity. Various methods aimed at isolating surface reflections from bulk scattering include reflection difference spectroscopy, reflection anisotropy, ellipsometry, and 45-degree reflectometry [20, 21].

The most simple optical method of probing an interface consists of illuminating the interface and collecting the light reflected at the boundary. Since the Fresnel reflection coefficient depends on the different indices of refraction across the interface, we anticipate the reflected light to be sensitive to interface properties. Indeed this method has been successfully applied to IR [16] and Raman scattering [22].

But unlike EELS and HAS these optical measurements are plagued by scattering of light from the bulk media surrounding the interface. There is frequently more light scattered from the bulk than the interface; separation of these two signals has become an important challenge in surface optics. In some cases, when optical anisotropy is different at the surface than in the bulk, surface ellipsometry maybe used to distinguish the contributions [23]. Also electronic resonances may be leveraged to obtain surface-specific vibrational spectroscopy with Raman scattering, in spite of a normally strong bulk contribution to the Raman signal [2].

1.2.3 Second order optical probes

Improved sensitivity, spatial resolution, and surface selectivity are achieved by probing coherences with nonlinear optical interactions. Under most conditions, even-order nonlinear optical interactions will not take place in media with inversion symmetry. Such symmetry is necessarily broken at an interface, giving rise to an interface-specific nonlinear signal.

Making use of this effect, surface second-harmonic generation (SHG) and sum frequency generation (SFG) [24] have probed vibrations on crystal [25] and liquid interfaces [26, 27].

Just as with linear methods, any second-order signal arising from the bulk media confuses the measurement. Complete suppression of the bulk response only occurs in centrosymmetric media when higher-order multipole terms in the bulk polarization may be neglected [28, 29]. But these bulk contributions are not always negligible [30], which has led to many studies aimed at separating bulk and interface contributions in second-order nonlinear surface measurements. Knowledge of the surface and the adjacent bulk media is required to make these separations [31]. Bulk and surface SHG may respond differently to various combinations of polarization and sample orientations [32, 33] Second-order surface spectroscopies measured in reflection mode have less of a bulk contribution than transmission mode [34, 30]. Chemically perturbing the surface suppresses surface modes, leaving bulk modes unaffected [8].

1.2.4 Third order optical measurements

Even though 3rd order processes are not interface-specific (unlike even-order nonlinear interactions), they can still be used for interface measurements. A good review of 3rd order interactions can be found in Ref. [35].

1.2.4.1 History of THG at interfaces

It was first observed by Tsang that an intense laser beam focused at an interface produced more third harmonic than when focused in a bulk material [36]. The effect was initially attributed to a surface-specific third-order susceptibility, $\chi^{(3)}_{\text{surface}}$. The sensitivity of THG to interfaces led to its successful application as microscopy technique [37]. It has been shown that the affinity of THG for interfaces is more consistent explained by bulk THG disrupted by the interface [37, 38]. It is important to note that even though THG is a bulk process, the presence of an interface still leaves an imprint on the far-field collected third harmonic.

1.2.4.2 Mechanism of interface sensitivity

THG in bulk, for phase matched conditions in a tight focus, produces no net third harmonic [39]. The harmonic generated on one side of the focus cancels the harmonic generate

on the other side, due to the Gouy phase shift. But any sort of asymmetry across the interaction region breaks this cancellation, giving rise to a net signal. The most dramatic impact on this process is from a difference in third-order susceptibility, $\Delta\chi^{(3)}$ [37]. But there will also be Fresnel reflections, as with any boundary. In the second section of this dissertation, we discuss how vibrational perturbation of these Fresnel boundary conditions modulate THG, making it possible to obtain surface-specific Raman measurements with THG.

1.3 Summary

In surface studies, usually no single method is sufficient to gather all the needed information [1]. E.J. Suonien put it [40],

> "It is, however, important always to keep in mind that surface characterization is almost always an inherently more difficult task than the corresponding bulk characterization. Hence, the use of one method only is seldom enough for a satisfactory solution." (p. 15)

This dissertation will focus on time-resolved Raman spectroscopy. The first section will develop the idea of an effective linear susceptibility perturbation caused by a vibrational coherence. This lays the groundwork for the second section, where the ideas are extended to third-order effective susceptibility modulations.

CHAPTER II

PUMP-INDUCED COHERENCE EFFECTIVE SUSCEPTIBILITY

Femtosecond impulsive Raman scattering was first demonstrated in 1985, in α-perylene crystals [41]. The set-up involved crossing a pair of pump pulses to create a transient grating, measured by time-delayed diffraction of a probe pulse. It was later found that a vibrational coherence is prepared by a single ultrashort pulse, no grating necessary, and that this excitation occurs for short enough pulses with no intensity threshold condition [19].

Initial measurements of these prepared coherences involved amplitude and detecting red-shifting of a probe pulse. The transient index perturbation also led to the possibility of transient birefringence measurements [42] A phase perturbation of the probe could be detected directly by heterodyne detection [43], and it was later shown these phase-sensitive methods provided more sensitivity than amplitude-sensitive methods [44]. Sinusoidal phase modulations also cause sideband scattering with long, narrow-band probes [45, 46]. Phase perturbations have also been measured directly with spectral interferometry [47].

This chapter lays the groundwork for theory. We describe just how a pump pulse induces a vibrational coherence (or wavepacket) in the sample. Then we describe how this coherence modulates a time-delayed probe pulse through effectively modifying the linear and nonlinear optical susceptibilities as a function of nuclear coordinate displacement. This susceptibility perturbation is shown to lead directly to both amplitude and phase modulation of the probe pulse. This susceptibility perturbation is distinct from a Raman susceptibility, though both are connected through the Raman differential polarizability $\partial\alpha/\partial q$ (See Appendix B).

2.1 Optically driving the harmonic oscillator

Following the notation in Appendix A, the real-valued electric field of the pump pulse is decomposed into an imaginary field and its complex conjugate.

$$\mathcal{E}_{\mathrm{p}} = \widetilde{\mathcal{E}}_{\mathrm{p}} + \widetilde{\mathcal{E}}_{\mathrm{p}}^{*} \tag{2.1}$$

where * denotes complex conjugate. The complex field is broken down into a slowly-varying complex envelope and a carrier with respect to propagation direction z and time:

$$\widetilde{\mathcal{E}}_{\mathrm{p}} = E_{\mathrm{p}}(x, y, z, t) e^{i(\omega_1 t - k_{0,1} z)}. \tag{2.2}$$

Where the propagation wavenumber is $k_{0,1} = n(\omega_1)\omega_1/c$. (This is written with the subscript $_{0,1}$ to avoid confusion with the the zeroth term of the Taylor expansion for the frequency-dependent $k(\omega)$; see Eq. (A.22) in Appendix A.)

In this first Part, focusing on linear modulations, we will consider only plane wave propagation in the theoretical treatment of ISRS. Focusing Gaussian beams will be treated in Section 4.5.2 on page 76. The envelope E is represented by an amplitude and a normalized envelope U_t,

$$E_{\mathrm{p}}(x, y, z, t) = E_{0,3\mathrm{o}} U_t(t - u_{\mathrm{p}}^{-1} z), \tag{2.3}$$

with the Gaussian temporal envelope advancing at the group velocity, described by

$$U_t(t - u_{\mathrm{p}}^{-1} z) = \exp\left[-2\ln 2 \left(\frac{t - u_{\mathrm{p}}^{-1} z}{\tau_{\mathrm{p}}}\right)^2\right] e^{i\phi(t - u_{\mathrm{p}}^{-1} z)} \tag{2.4}$$

where τ_{p} is the pump pulse FWHM (possibly chirped) and $\phi(t - u_{\mathrm{p}}^{-1} z)$ is the temporal phase of the pump pulse, and the group velocity is the derivative of optical frequency with respect to wavenumber [39, 48]

$$u_{\mathrm{p}} = \frac{\partial \omega}{\partial k} \tag{2.5}$$

In order to shorten notation, we will work in the group frame of the pump pulse with coordinates $t'_{\mathrm{p}} = t - u_{\mathrm{p}}^{-1} z$ and $\zeta_{\mathrm{p}} = z$.

2.1.1 Semi-classical intuitive picture

2.1.1.1 Classical harmonic oscillator model

Here we examine the classical model of molecular vibrations under the influence of an external electric field in order to describe the action of the intense pump pulse. In this section, we will discuss the nuclear motion in terms of the displacement coordinate R instead of the reduced mass coordinate,

$$Q = \frac{R}{\sqrt{MN}}, \tag{2.6}$$

(where M is the reduced mass and N is the number density of oscillators) in order to elucidate the physics of a harmonic oscillator being driven by a force due to the optical electric field. In what is usually referred to as the Placzek model, we model the molecular vibrations as a classical harmonic oscillator,

$$\frac{\partial^2 R}{\partial t^2} + \gamma \frac{\partial R}{\partial t} + \Omega_v^2 R = F(t), \tag{2.7}$$

where R is the displacement coordinate, γ is the dampening term, Ω_v is the resonant frequency, and $F(t)$ is the driving term, composed of the applied force $\bar{F}(t)$ and the reduced mass of the oscillator M depends on the electric field of the driving optical pulse and the Raman differential polarizability:

$$F(t) = \frac{\bar{F}(t)}{M} = \frac{1}{M}\left(\frac{\partial \alpha}{\partial R}\right)_0 \mathcal{E}_{\mathrm{p}}^2. \tag{2.8}$$

As a consequence of the square dependence in the driving term, impulsive excitation will depend only on the square of the temporal envelope of an ultrafast pulse. To show this, we use the previous definition of a pump pulse, Eq. (4.32), but neglect the spatial dependence and examine interaction only at the plane $z = 0$:

$$\mathcal{E}_{\mathrm{p}}(t) = \tfrac{1}{2} E_{\mathrm{p}}(t) e^{i\omega_1 t} + \tfrac{1}{2} E_{\mathrm{p}}(t)^* e^{-i\omega_1 t}. \tag{2.9}$$

The square of the field is

$$\mathcal{E}_{\mathrm{p}}(t)\ \mathcal{E}_{\mathrm{p}}(t) = \tfrac{1}{2}|E_{\mathrm{p}}(t)|^2 + \tfrac{1}{4}|E_{\mathrm{p}}(t)|^2 e^{+i\ 2\omega_1 t} + \tfrac{1}{4}|E_{\mathrm{p}}(t)|^2 e^{-i\ 2\omega_1 t}. \tag{2.10}$$

The square of the pump field thus contains a slowly varying contribution and a component at the optical second harmonic. Since the second harmonic frequency is much greater than

the resonant frequency of the oscillator, $2\omega_1 \gg \Omega_v$, we neglect these, which results in the vibrational motion being driven only by the slowly varying envelope of the pulse,

$$F(t) = \frac{1}{2M}\left(\frac{\partial\alpha}{\partial R}\right)_0 E^2_{0,3o}|U_t(t)|^2. \tag{2.11}$$

This is similar to the equation coupling an optical field pump pulse to vibrational motion in Ref. [19]:

$$\frac{\partial^2 Q}{\partial t^2} + 2\gamma\frac{\partial Q}{\partial t} + \omega_0^2 Q = \tfrac{1}{2}N\left(\frac{\partial\alpha}{\partial Q}\right)_0 : EE, \tag{2.12}$$

where Q is the displacement of the vibrational coordinate, E is the pump pulse field, α is the optical polarizability of the molecules, N is the number density of molecules, ω_0 is the vibrational frequency, and γ is the vibrational damping constant. This result was built upon the more general theory of stimulated Raman scattering developed in 1965 by Shen and Bloembergen [49]. This equation describes damped oscillatory motion with a driving term on the right hand side proportional to the square of the optical field EE and the Raman differential polarizability $(\partial\alpha/\partial Q)_0$. Any vibrational mode that causes a change in optical polarizability α with respect to a change in the mode's displacement coordinate Q is said to be Raman active. It follows that larger changes in polarizability lead to a stronger Raman cross-section.

2.1.1.2 Frequency response of a harmonic oscillator

In order to determine the oscillator's exact response to a particular pump envelope, we move to the frequency domain by decomposing the nuclear displacement coordinate $R(t)$ and the driving force $F(t)$ as Fourier series

$$R(t) = \sum_{\Omega=-\infty}^{\infty} R(\Omega)e^{i\Omega t} \tag{2.13}$$

$$F(t) = \sum_{\Omega=-\infty}^{\infty} F(\Omega)e^{i\Omega t} \tag{2.14}$$

where $R(\Omega)$ and $F(\Omega)$ are the amplitudes of each oscillatory component. We insert these definitions into the equation for a classical harmonic oscillator, Eq. (2.7) , evaluate the

partial derivatives, and divide by the $\sum e^{i\Omega t}$ term common to both sides, resulting in

$$R(\Omega)\left[-\Omega^2 + i\gamma\Omega + \Omega_v^2\right] = F(\Omega) \tag{2.15}$$

We treat this as a linear shift invariant system, phrasing $R(\Omega)$ in terms of a frequency response $H(\Omega)$, which is the Fourier transform of the impulse response.

$$R(\Omega) = H(\Omega)\ F(\Omega) \tag{2.16}$$

where the frequency response

$$H(\Omega) = \frac{1}{\Omega_v^2 + i\gamma\Omega - \Omega^2} \tag{2.17}$$

In the time domain, the oscillator's motion $R(t)$ is found by the convolution of the driving force with the impulse response

$$R(t) = \int_{-\infty}^{+\infty} F(\tau)h(t-\tau)d\tau. \tag{2.18}$$

In order to find $R(t)$ for a particular driving pulse, we will need to know the impulse response $h(t)$. We begin by factoring the denominator of $H(\Omega)$ as follows:

$$H(\Omega) = \frac{1}{(\Omega - \Omega_1)(\Omega - \Omega_2)} \tag{2.19}$$

where the complex roots are

$$\Omega_{1,2} = i\frac{\gamma}{2} \pm \sqrt{\Omega_v^2 - \frac{\gamma^4}{4}}. \tag{2.20}$$

The inverse Fourier transform is now written and evaluated by the residue theorem.

$$\begin{aligned} h(t) &= \frac{1}{2\pi}\int_{-\infty}^{+\infty} \frac{e^{i\Omega t}}{(\Omega - \Omega_1)(\Omega - \Omega_2)} d\Omega \\ &= \frac{2\pi i}{2\pi}\left\{\lim_{\Omega\to\Omega_1}(\Omega - \Omega_1)\left[\frac{e^{i\Omega t}}{(\Omega - \Omega_1)(\Omega - \Omega_2)}\right] + \lim_{\Omega\to\Omega_2}(\Omega - \Omega_2)\left[\frac{e^{i\Omega t}}{(\Omega - \Omega_1)(\Omega - \Omega_2)}\right]\right\} \end{aligned} \tag{2.21}$$

Evaluating the limits results in

$$h(t) = \frac{2\pi i}{2\pi}\left[\frac{e^{i\Omega_1 t}}{\Omega_1 - \Omega_2} - \frac{e^{i\Omega_2 t}}{\Omega_1 - \Omega_2}\right]. \tag{2.22}$$

We can coax this solution to the form of a damped oscillator by rewriting the exponential term

$$e^{i\Omega_1 t} = e^{i\Omega_1 t/2} e^{i\Omega_1 t/2} e^{-i\Omega_2 t/2} e^{i\Omega_2 t/2}, \tag{2.23}$$

and vice-versa for $e^{i\Omega_2 t}$, while moving the i to the denominator:

$$h(t) = -\frac{4\pi}{2\pi \cdot 2i}\left[\frac{e^{i\Omega_1 t/2} e^{i\Omega_1 t/2} e^{-i\Omega_2 t/2} e^{i\Omega_2 t/2}}{\Omega_1 - \Omega_2} - \frac{e^{i\Omega_2 t/2} e^{i\Omega_2 t/2} e^{-i\Omega_1 t/2} e^{i\Omega_1 t/2}}{\Omega_1 - \Omega_2}\right]. \tag{2.24}$$

Factoring out the common $e^{i(\Omega_1+\Omega_2)t/2}/(\Omega_1 - \Omega_2)$ leaves us with the following:

$$h(t) = -\frac{4\pi}{2\pi} \cdot \left[\frac{e^{i(\Omega_1+\Omega_2)t/2}}{\Omega_1 - \Omega_2}\right] \cdot \left[\frac{e^{i(\Omega_1-\Omega_2)t/2} - e^{-i(\Omega_1-\Omega_2)t/2}}{2i}\right]. \tag{2.25}$$

The expression in the right-hand brackets looks suspiciously like a sine function, but first we need to examine the sum and difference of the roots. Recalling Eq. (2.20),

$$\Omega_1 + \Omega_2 = i\gamma \tag{2.26}$$

and

$$\Omega_1 - \Omega_2 = 2\sqrt{\Omega_v^2 - \frac{\gamma^2}{4}} \approx 2\Omega_v, \tag{2.27}$$

since for gases, the oscillation rate is far greater than the damping rate. Inserting these into Eq. (2.25) yields the final expression for the impulse response of the oscillator:

$$h(t) = -\frac{e^{-\gamma t/2}}{\Omega_v} \sin(\Omega_v t), \text{ for } t > 0. \tag{2.28}$$

Note that since this is a causal system, $h(t) = 0$ for $t \leq 0$.

2.1.2 Impulsive Excitation

Before examining the system's response to an infinitely short pulse of light, let's rewrite the driving term $F(t)$ in a more convenient form. The definition of irradiance (commonly called intensity) is

$$I_{\mathrm{p}}(t) = \tfrac{1}{2}\epsilon_0 cn E_{0,3\mathrm{o}}^2 |U_t(t)|^2 = \tfrac{1}{2}\epsilon_0 cn I_{0,3\mathrm{o}} |U_t(t)|^2, \tag{2.29}$$

where ϵ_0 is the vacuum permittivity, c is the speed of light in a vacuum, n is the refractive index of the medium in question, $U_t(t)$ is the previously defined pulse envelope, and $I_{0,3\mathrm{o}} = E_{0,3\mathrm{o}}^2$ is the peak intensity. We then rewrite the driving term,

$$F(t) = \kappa \cdot I_0 U(t), \tag{2.30}$$

where

$$\kappa = \frac{1}{M\ n\ c\ \epsilon_0} \left(\frac{\partial \alpha}{\partial R}\right)_0 \tag{2.31}$$

Let us also define in the frequency domain,

$$D(\Omega) = I_0 \int_{-\infty}^{+\infty} U(t) e^{-i\Omega t} dt. \tag{2.32}$$

Note that the pulse fluence is given by the zero-frequency component of D:

$$D(\Omega)\Big|_{\Omega=0} = I_0 \int_{-\infty}^{+\infty} U(t) dt = \int_{-\infty}^{+\infty} I(t) dt = \Phi_p \tag{2.33}$$

Returning to Eq. (2.16), the frequency response becomes

$$R(\Omega) = \kappa \cdot H(\Omega) \cdot D(\Omega) \tag{2.34}$$

For impulsive excitation,

$$U(t) = \delta(t), \tag{2.35}$$

so that

$$D(\Omega) = I_0 \int_{-\infty}^{+\infty} \delta(t) e^{-i\Omega t} dt = \Phi_p. \tag{2.36}$$

Since D is a constant in frequency space, the time-domain convolution to obtain $R(t)$ is simple,

$$R(t) = \kappa I_0 h(t) = R_0 e^{-\gamma t/2} \sin(\Omega_v t). \tag{2.37}$$

This describes damped oscillations with an initial displacement

$$R_0 = \frac{I_0}{M\ n\ c\ \epsilon_0\ \Omega_v} \left(\frac{\partial \alpha}{\partial R}\right)_0. \tag{2.38}$$

In terms of the more commonly found reduced mass coordinate Eq. (2.6) and the Raman differential polarizability, the initial displacement of the oscillator after impulsive pumping is

$$Q_0 = \frac{I_0}{M^2\ N\ n\ c\ \epsilon_0\ \Omega_v} \left(\frac{\partial \alpha}{\partial Q}\right)_0, \tag{2.39}$$

where we have made use of the chain rule to relate the differential polarizabilities,

$$\frac{\partial \alpha}{\partial R} = \left(\frac{\partial \alpha}{\partial Q}\right)\left(\frac{\partial Q}{\partial R}\right) = \frac{1}{\sqrt{MN}} \left(\frac{\partial \alpha}{\partial Q}\right). \tag{2.40}$$

2.1.2.1 Gaussian pulse excitation, neglecting group velocity

To consider pumping by a short Gaussian pulse is slightly more complex. Here we assume a Gaussian pulse envelope as in Eq. (4.34), and disregard group velocity and assume a transform-limited pulse ($\phi = 0$) to simplify the discussion:

$$U(t) = e^{-2at^2}, \tag{2.41}$$

where the full width at half maximum (FWHM) duration τ_p of the pulse is related to a by

$$a = \frac{2\ln 2}{\tau_\mathrm{p}^2}. \tag{2.42}$$

As with the impulsive picture, we proceed to find the frequency domain expression for the driving term,

$$D(\Omega) = I_0 \int_{-\infty}^{+\infty} e^{-2at^2} e^{-i\Omega t} dt = I_0 \sqrt{\frac{\pi}{2a}} e^{-\Omega^2/8a} = I_0 \tau_\mathrm{p} \sqrt{\frac{\pi}{4\ln 2}} e^{-(\Omega\tau_\mathrm{p})^2/(16\ln 2)} \tag{2.43}$$

Recalling that the $\Omega = 0$ component is the pulse fluence, and introducing a new constant $\Gamma^{-1} = 16\ln 2$, we have a slightly more compact expression:

$$D(\Omega) = \Phi_p \cdot e^{-\Gamma(\Omega\tau_\mathrm{p})^2}. \tag{2.44}$$

This time we find the driving term, in frequency space, to be a Gaussian with an amplitude determined by the pulse fluence and a bandwidth inversely proportional to the pulse duration in time.

Now we continue to find a time-domain expression for the behavior of the oscillator. The frequency-domain equation, is

$$R(\Omega) = \kappa\Phi_p H(\Omega) e^{-\Gamma(\Omega\tau_\mathrm{p})^2}. \tag{2.45}$$

Evaluating the inverse Fourier transform will reveal what we're after:

$$R(t) = \frac{\kappa\Phi_p}{2\pi} \int_{-\infty}^{+\infty} \frac{e^{-\Gamma(\Omega\tau_\mathrm{p})^2} e^{i\Omega t}}{(\Omega - \Omega_1)(\Omega - \Omega_2)} d\Omega, \tag{2.46}$$

where $\Omega_{1,2}$ are the same as defined in Eq. (2.20). Using the same technique to find the impulse response $h(t)$, the integral is evaluated using the residue theorem.

$$R(t) = \frac{\kappa\Phi_p \cdot 2\pi i}{2\pi} \left[\frac{e^{-\Omega_1 t} e^{-\Gamma(\Omega_1\tau_\mathrm{p})^2}}{\Omega_1 - \Omega_2} - \frac{e^{-\Omega_2 t} e^{-\Gamma(\Omega_2\tau_\mathrm{p})^2}}{\Omega_1 - \Omega_2} \right] \tag{2.47}$$

In the impulse response analysis, the next step was to manipulate the exponentials in order to factor out some common terms and draw out a sine term. We shall do the same thing here, beginning with the exponentials related to the pump pulse. First, we will make the following approximation, valid for the gas phase where $\Omega_v^2 \gg \gamma^2$,

$$\Omega_{1,2} = i\frac{\gamma}{2} \pm \sqrt{\Omega_v^2 - \frac{\gamma^2}{4}} \approx i\frac{\gamma}{2} \pm \Omega_v. \tag{2.48}$$

The exponential terms expand as follows,

$$\begin{aligned} e^{-\Gamma(\Omega_{1,2}\tau_\mathrm{p})^2} &\approx e^{-\Gamma(i\gamma\tau_\mathrm{p}/2 \pm \Omega_v\tau_\mathrm{p})^2} \\ &= e^{-\Gamma\left[-(\gamma\tau_\mathrm{p}/2)^2 + (\Omega_v\tau_\mathrm{p})^2 \pm i\gamma\Omega_v\tau_\mathrm{p}^2\right]} \\ &= e^{-\Gamma\tau_\mathrm{p}^2(\Omega_v^2 - \gamma^2/4)} e^{\mp i\Gamma\gamma\Omega_v\tau_\mathrm{p}^2} \\ &= e^{-\Gamma\tau_\mathrm{p}^2\Omega_v^2} e^{\mp i\Gamma\gamma\Omega_v\tau_\mathrm{p}^2}, \end{aligned} \tag{2.49}$$

Where in the last step, we re-apply the approximation. Combining this with the results in equations 2.22-2.25 yields another damped sine

$$\begin{aligned} R(t) &= -\kappa\Phi_p \cdot e^{-\Gamma\tau_\mathrm{p}^2\Omega_v^2} \cdot \left[\frac{e^{-\gamma t/2}}{\Omega_v}\right] \cdot \left[\frac{e^{i\left(\Omega_v t - \Gamma\gamma\Omega_v\tau_\mathrm{p}^2\right)} - e^{-i\left(\Omega_v t - \Gamma\gamma\Omega_v\tau_\mathrm{p}^2\right)}}{2i}\right] \\ &= -\kappa\Phi_p \cdot e^{-\Gamma\tau_\mathrm{p}^2\Omega_v^2} \cdot \left[\frac{e^{-\gamma t/2}}{\Omega_v}\right] \sin\left(\Omega_v t - \Gamma\gamma\Omega_v\tau_\mathrm{p}^2\right) \\ &= R_0' e^{-\gamma t/2} \sin\left(\Omega_v t - \phi_0'\right) \end{aligned} \tag{2.50}$$

Here the effects of a finite-bandwidth excitation pulse manifest themselves in a reduced initial amplitude of the oscillations,

$$R_0' = \frac{\Phi_p}{M\ n\ c\ \epsilon_0\ \Omega_v}\left(\frac{\partial\alpha}{\partial R}\right)_0 e^{-(\Omega_v\tau_\mathrm{p})^2/16\ln 2} = R_0 e^{-(\Omega_v\tau_\mathrm{p})^2/16\ln 2}, \tag{2.51}$$

and an initial phase, which is approximately zero if the pump duration is much shorter than the vibrational period $\tau_\mathrm{p} << 1/\Omega_v$

$$\phi_0' = \frac{\gamma\Omega_v\tau_\mathrm{p}^2}{16\ln 2} \approx 0. \tag{2.52}$$

As we would expect, as the duration of the pulse approaches zero, these results approach those we computed for impulsive excitation:

$$\begin{aligned} \lim_{\tau_\mathrm{p}\to 0} R_0' &= R_0, \\ \lim_{\tau_\mathrm{p}\to 0} \phi_0' &= 0. \end{aligned} \tag{2.53}$$

2.1.2.2 Impulse pump-induced effective susceptibility perturbation

We will consider Raman excitation of a nuclear coherence and consider the effect of the transient effective susceptibility that results.

The optical susceptibility χ relates an induced polarization density $\mathcal{P}$ to an incident optical field $\mathcal{E}$. Considering a single frequency ω_1,

$$Pe^{i\omega_1 t} = \epsilon_0 \chi^{(1)} E e^{i\omega_1 t} \tag{2.54}$$

For a single molecule, the dipole moment μ induced by a field is related by the polarizability α,

$$\mu = \epsilon_0 \alpha E \tag{2.55}$$

This is related to the polarization density by the number density of molecules N:

$$P = \epsilon_0 \chi^{(1)} E = \epsilon_0 N \alpha E, \tag{2.56}$$

and we make the relationship

$$\chi^{(1)} = N\alpha, \tag{2.57}$$

so that vibrational perturbations of the polarizability, $\partial\alpha/\partial Q$ are directly proportional to the susceptibility perturbations $\partial\chi/\partial Q = N(\partial\alpha/\partial Q$, so that the perturbation to the linear optical susceptibility is

$$\begin{aligned} \delta\chi^{(1)} &= \left(\frac{\partial\chi^{(1)}}{\partial Q}\right)_0 Q \\ &= N\left(\frac{\partial\alpha}{\partial Q}\right)_0 Q_0 \sin\left(\Omega_v \tau_{\mathrm{pp}}\right) \\ &= \frac{I_0}{M^2\ n\ c\ \epsilon_0\ \Omega_v}\left(\frac{\partial\alpha}{\partial Q}\right)_0^2 \sin\left(\Omega_v \tau_{\mathrm{pp}}\right). \end{aligned} \tag{2.58}$$

2.1.2.3 Illustration

As an illustration of the excitation mechanism just described, we use MATLAB to model the response of the molecular harmonic oscillator to several pump fields. The model operates in the frequency domain to determine $R(\Omega) = D(\Omega)H(\Omega)$, finding $r(t)$ by the `ifft()` inverse Fourier transform function. Our first trial pulses are, of course, the recently studied impulse

function and a Gaussian pulse. We also investigate the effects of stretching that pulse with a linear chirp, and also pulse trains of resonant and off-resonant periodicity.

The response of the impulse function $I(t) = I_0\delta(t)$ is simply $r(t) = h(t)$, by definition.

We construct a transform-limited Gaussian pulse of FWHM duration τ_{p},

$$E(t) = \sqrt{I_0}e^{-\frac{2\ln 2}{\tau_{\mathrm{p}}^2}t^2}, \tag{2.59}$$

which has a Fourier transform $E(\omega) = \frac{F}{E(t)}$. The chirped Gaussian pulse with chirp parameter b is constructed by

$$E(\omega)_{\mathrm{chirp}} = E(\omega)e^{ib\omega^2}. \tag{2.60}$$

Fig. 2.1 shows the vibrational frequency response overlapped with the transform-limited and chirped Gaussian pulses. Note that the transform limited pulse has greater spectral energy where it overlaps with the vibrational frequency response. The horizontal line shows the overlap for an impulsive $\delta(t)$ function excitation. From a practical standpoint, several things can be done with a Gaussian pulse to improve pumping. By ensuring the pulse has as short a temporal duration as possible, its spectral width is enhanced, and will lead to greater overlap with the vibrational frequency response. Also note that if we choose a molecule with a small Ω_v (that is, a longer vibrational period) then the pump pulse will not need to have as broad a bandwidth. In addition, we observe that a pulse with a broad bandwidth will not effectively pump the molecules unless it is compressed to its transform-limited duration.

2.1.3 Quantum coherence

The transient phase perturbation probed by the probe pulses originates from a quantum coherence prepared between vibrational levels on the electronic ground state through ISRS excitation by a short pump pulse [50]. The quantum coherence manifests as a macroscopic, real-valued polarization density $P^{(3)}$, which arises via a temporal response function $\mathcal{S}^{(3)}(t_3, t_2, t_1)$ and the third power of the field. With standard time-domain quantum mechanical perturbation theory, this is written as [51]

$$P^{(3)}(\mathbf{r}, t) = \epsilon_0 \int_0^\infty \mathrm{d}t_3 \int_0^\infty \mathrm{d}t_2 \int_0^\infty \mathrm{d}t_1 \mathcal{S}^{(3)}(t_3, t_2, t_1) \times \mathcal{E}_3(\mathbf{r}, t - t_3)\mathcal{E}_2(\mathbf{r}, t - t_3 - t_2)\mathcal{E}_1(\mathbf{r}, t - t_3 - t_2 - t_1) \tag{2.61}$$

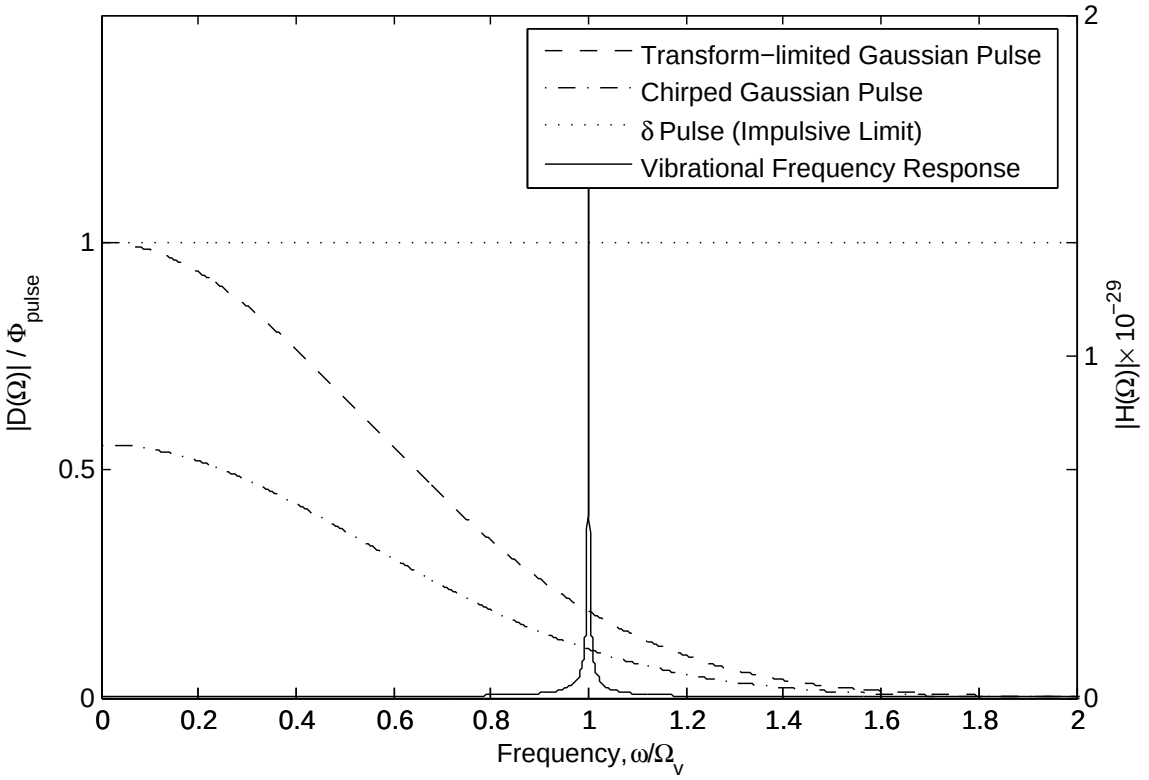

Figure 2.1: Frequency response of molecular vibrations in response to impulse, transform-limited Gaussian, and chirped Gaussian pump pulses.

where $\mathcal{E}_j(\mathbf{r},t)$ are the interacting fields—all of which are real quantities. There are three interacting fields under the integral, plus one field emitted by the induced polarization, so this is a four wave mixing (4WM) experiment, where two waves are associated with the pump pulse, and the other two are associated with the probe pulse. Our experiments are arranged in a pump–probe configuration, with the pump preceding the probe by delay τ_{pp}. We will insert into this expression pump and probe fields, similar to the definition for the pump field above in Eq. (2.1). Here we will neglect the spatial dependence U_s, assuming plane waves. We write the complex pump and probe electric field as

$$E_j(\mathbf{r},t) = E_{0,j}U_{t,j}(t)\, e^{i(\mathbf{k}_j\cdot\mathbf{r}-\omega_j t)} \tag{2.62}$$

decomposed into a complex valued temporal envelope $U_{t,j}(t)$ and a plane-wave propagation term. Here, $j = \{\mathrm{p},\mathrm{pr}\}$ denote the pump and probe pulses, respectively.

The pump and probe fields are non-resonant since they are composed of optical frequencies well below the electronic absorption frequencies; with non-resonant ISRS spectral measurements, only ground electronic state dynamics are considered. We can make use of the Born–Oppenheimer approximation (BOA) where the electrons are assumed to adiabatically follow perturbations to nuclear coordinates and instantaneously follow the electric fields. The latter is equivalent to neglecting dispersion of the electronic response, so that the response is instantaneous with respect to time variables t_1 and t_3 and they may be eliminated from Eq. (2.61) [52]. Application of time-dependent perturbation theory in the BOA yields an expression for the nonlinear polarization density given by [35]

$$P^{(3)}(\mathbf{r},t) = \frac{\epsilon_0}{2}E_{\mathrm{o}}(\mathbf{r},t)\int_0^\infty \mathrm{d}t_2 \mathcal{S}_{\mathrm{ISRS}}(t_2)\times I_{0,3\mathrm{o}}\,|U_{t,3\mathrm{o}}(t+\tau_{\mathrm{pp}}-t_2)|^2 + \mathrm{c.c.} \tag{2.63}$$

Since this third-order polarization density is proportional to the probe field E_{o}, we can define an effective transient *linear* susceptibility perturbation

$$\delta\chi(t) \equiv \int_0^\infty dt_2\, \mathcal{S}_{\mathrm{ISRS}}(t) I_{0,3\mathrm{o}} |U_{t,3\mathrm{o}}(t+\tau_{\mathrm{pp}}-t_2)|^2 \tag{2.64}$$

such that the real perturbation to the polarization density is

$$P^{(3)}(\mathbf{r},t) = \frac{\epsilon_0}{2}\delta\chi(t)E_{\mathrm{o}}(\mathbf{r},t) + \mathrm{c.c.} \tag{2.65}$$

The quantum vibrational coherence excited by the pump pulse through ISRS thus creates a time-varying perturbation to the index of refraction. For a weak excitation, we may write $n(t) = n_1 + \delta n(t)$, where $\delta n(t) = \delta\chi(t)/2n_1$ and $n_1^2 - 1 = \chi_0^{(1)}$.

Following Mukamel's treatment [52], the time domain response for ISRS simplifies to

$$\mathcal{S}_{\mathrm{ISRS}}(t) \equiv -\frac{i}{\hbar}\left\langle [\alpha(t), \alpha(0)]\, \rho_o \right\rangle . \tag{2.66}$$

Here ρ_o is the equilibrium density operator,

$$\alpha(t) = e^{+iH_g t/\hbar} \alpha e^{-iH_g t/\hbar} \tag{2.67}$$

is the interaction-picture polarizability operator, and H_g is the ground-state Hamiltonian. For weak vibrational excitation, we may expand the polarizability operator in the set of normal vibrational coordinates

$$\alpha = \alpha_0 + \sum_v \alpha'_v q_v \tag{2.68}$$

where q_v is the normal mode displacement and $\alpha'_v \equiv (\partial\alpha/\partial q_v)_0$. Here, we have truncated the expansion to first order in the vibrational modes, thereby neglecting hyper-Raman effects and vibrational modal coupling. Substitution of Eq. (2.68) into (2.66) under the assumption that the normal vibrational modes are uncorrelated [52] yields

$$\mathcal{S}_{\mathrm{ISRS}}(t) = -\frac{i}{\hbar}\sum_v \left(\alpha'_v\right)^2 \langle [q_v(t), q_v(0)]\rho_o\rangle, \tag{2.69}$$

where $q_v(t) = e^{+iH_g t/\hbar} q_v e^{-iH_g t/\hbar}$. For each vibrational mode v, we expand the trace operator in the basis of vibrational states $|U_v\rangle$ of the unperturbed ground state Hamiltonian [35]

$$\left\langle [q_v(t), q_v(0)]\, \rho_o \right\rangle = \sum_{a,b} w_{va} \langle va|q_v|vb\rangle\langle vb|q_v|va\rangle e^{i\Omega_{v,ba}t} - \text{c.c.} \tag{2.70}$$

where w_a is the statistical weight, and the vibrational beat frequency is defined by the difference in eigenenergies U_v for states a and b such that $\hbar\Omega_{v,ba} = U_{v,b} - U_{v,a}$. We will restrict our attention to quantum coherences prepared between the two lowest levels of the vibrational mode and write $\Omega_v \equiv \Omega_{v,21}$ for the v^{th} vibrational mode. With this restriction, Eq. (2.70) becomes

$$\left\langle [q_v(t), q_v(0)]\, \rho_o \right\rangle = -2iQ_v \sin\Omega_v t \tag{2.71}$$

with $Q_v = (w_{v2} - w_{v1})|\langle v2|q_v|v1\rangle|^2$. Combining Eqs. (2.64), (2.66) and (2.71) gives an expression for the time-varying perturbation to the effective linear susceptibility

$$\delta\chi(t) = \frac{2}{\hbar}\sum_v (\alpha'_v)^2 Q_v I_{0,3\mathrm{o}} \int_0^\infty \mathrm{d}t_2 \sin[\Omega_v t_2] \times |U_{t,3\mathrm{o}}(t + \tau_{\mathrm{pp}} - t_2)|^2 . \tag{2.72}$$

For ISRS excitation, the pump pulse intensity temporal profile $|A_{\mathrm{p}}(t)|^2$ contains temporal structure that is of the order or shorter than the vibrational period $2\pi/\Omega_v$. In this regime, after the pump pulse, a time-varying sinusoidal susceptibility perturbation persists, which is determined by the product of the Fourier transform of the pump pulse intensity and the spectral profile of the vibrational resonance which is evident by considering a Fourier transform of Eq. (2.72). After ISRS excitation by an impulsive pump pulse, the transient index of refraction perturbation can be then expressed as a superposition of sinusoidal oscillations,

$$\delta n(t) = \sum_v \delta n_v \sin \Omega_v t, \tag{2.73}$$

where

$$\delta n_v = \frac{(\alpha'_v)^2 Q_v I_{0,3\mathrm{o}}}{\hbar n_1} \int_0^\infty \mathrm{d}t_2 \, |U_{t,3\mathrm{o}}(t + \tau_{\mathrm{pp}} - t_2)|^2 \sin[\Omega_v t_2]. \tag{2.74}$$

The end result is similar in form to the classical picture. The initial amplitude of the vibrational coherence is proportional to the convolution of the pump pulse with the sinusoidal form of the vibrations.

2.1.3.1 Gaussian pump-induced effective susceptibility perturbation

Now we consider that the pump pulse travel at a group velocity u_{p}, and so the vibrational coherence will inherit this group velocity from the pump. Let's insert Eq. (4.34) into the integral in the effective susceptibilities, Eq. (2.72)

$$\int_{-\infty}^{\infty} \sin[\Omega_v t'] \exp\left[-4\ln 2 \left(\frac{t + \tau_{\mathrm{pp}} - u_{\mathrm{p}}^{-1} z - t'}{\tau_{\mathrm{pu}}}\right)^2\right] \mathrm{d}t' \tag{2.75}$$

Let $\eta = t + \tau_{\mathrm{pp}} - u_{\mathrm{p}}^{-1} z - t'$ and $\mathrm{d}t' = \mathrm{d}\eta$, then the integral becomes

$$\int_{-\infty}^{\infty} \sin[\Omega_v(\xi - \eta)] \exp\left[-4\ln 2 \left(\frac{\eta}{\tau_{\mathrm{p}}}\right)^2\right] \mathrm{d}\eta \tag{2.76}$$

with $\xi = t + \tau_{\rm pp} - u_{\rm p}^{-1} z$. Let $A = -4\ln 2/\tau_{\rm p}^2$, then

$$\frac{1}{2i}\int_{-\infty}^{\infty}\left(e^{i\Omega_v\xi}e^{-i\Omega_v\eta} - e^{-i\Omega_v\xi}e^{i\Omega_v\eta}\right)e^{A\eta^2}\mathrm{d}\eta \tag{2.77}$$

or

$$\frac{1}{2i}\left(e^{i\Omega_v\xi}\int_{-\infty}^{\infty}e^{-i\Omega_v\eta}e^{A\eta^2}\mathrm{d}\eta - e^{-i\Omega_v\xi}\int_{-\infty}^{\infty}e^{i\Omega_v\eta}e^{A\eta^2}\mathrm{d}\eta\right) \tag{2.78}$$

Making use of the identity

$$\int e^{-Ax^2-2Bx}dx = \sqrt{\frac{\pi}{A}}e^{B^2/A}, \tag{2.79}$$

we obtain

$$\frac{\tau_{\rm p}}{2\sqrt{\ln 2}}\exp\left[-\frac{\Omega_v^2\tau_{\rm p}^2}{16\ln 2}\right]\sin[\Omega_v(t+\tau_{\rm pp}-u_{\rm pu}^{-1}z)] \tag{2.80}$$

Thus, the effective susceptibility perturbation can be written as

$$\delta\chi^{(n)}(\mathbf{r},t) = |E_0|^2|U_s(x,y,z)|^2\frac{\sigma_n\tau_{\rm p}}{2\sqrt{\ln 2}}\exp\left[-\frac{1}{\ln 2}\left(\frac{\Omega_v\tau_{\rm p}}{4}\right)^2\right]\sin[\Omega_v(t+\tau_{\rm pp}-u_{\rm p}^{-1}z)] \tag{2.81}$$

We define the time-independent amplitude of the perturbation as

$$\delta\chi_0^{(n)} = |E_0|^2\frac{\sigma_n\tau_{\rm p}}{2\sqrt{\ln 2}}\exp\left[-\frac{1}{\ln 2}\left(\frac{\Omega_v\tau_{\rm p}}{4}\right)^2\right] \tag{2.82}$$

so that we can write

$$\delta\chi^{(n)}(\mathbf{r},t) = \delta\chi_0^{(n)}|U_s(x,y,z)|^2\sin[\Omega_v(t+\tau_{\rm pp}-u_{\rm p}^{-1}z)]. \tag{2.83}$$

Note that $\delta\chi_0^{(n)}$ is a quantity that depends pump characteristics and σ_n, which may depend on the frequency of the probe.

The other observation is that the sine form indicates that the initial displacement of the vibrational coordinate is *zero*. As the pump wavelength is tuned to an electronic resonance, this term becomes a cosine, and the vibrational oscillations are kicked not only with an initial momentum, but also an initial displacement away from equilibrium [53].

2.2 Solve for wavenumber perturbations

We will now compute the effective source terms for a probe pulse given by

$$\mathcal{E}_{\rm o}(\mathbf{r},t) = E_{\rm o}(\mathbf{r},t-u_{\rm o}^{-1}z)e^{i(\omega_1 t - k_1 z)} \tag{2.84}$$

with

$$E_{\mathrm{o}}(x,y,z,t) = E_{0,\mathrm{o}} U_{s,\mathrm{o}}(x,y,z) U_{t,\mathrm{o}}(t - u_{\mathrm{o}}^{-1} z) \tag{2.85}$$

with the spatial profile given by

$$U_{s,\mathrm{o}}(x,y,z) = \frac{1}{\left[1 + \frac{i2z}{w_1^2 k_1}\right]} \exp\left\{ -\frac{(x^2+y^2)}{w_1^2 \left[1 + \frac{i2z}{w_1^2 k_1}\right]} \right\} \tag{2.86}$$

The probe pulse has an amplitude $E_{0,\mathrm{pr}}$ and group velocity u_{pr}. It is centered at $t = 0$ and follows the pump by delay τ_{pp}. It will be shown that the perturbation results in a modified wavenumber, k.

2.2.1 Effective linear susceptibility source term

We start with the results from Appendix A. Equation (A.36) describes probe pulse envelope propagation in the presence of an additional polarization source term,

$$\left\{ \frac{i}{2k_{0,1}} \nabla_{\perp}^2 + \frac{\partial}{\partial z} + \frac{1}{u} \frac{\partial}{\partial t} \right\} E(\mathbf{r},t) = -i \frac{\omega_1}{2cn_1\epsilon_0} \left(1 - \frac{i}{\omega_1} \frac{\partial}{\partial t} \right) p^A(\mathbf{r},t), \tag{2.87}$$

The source term in the spatial domain is given by

$$\mu_0 \frac{\partial^2}{\partial t^2} \mathcal{P}^A(\mathbf{r},t) = \mu_0 \epsilon_0 \frac{\partial^2}{\partial t^2} \delta\chi^{(1)}(\mathbf{r},t) \mathcal{E}_{\mathrm{o}}(\mathbf{r},t) \tag{2.88}$$

The relevant "additional" polarization oscillating at ω_1 that goes in our wave equation for the envelope of the probe is proportional to the susceptibility perturbation and the probe field,

$$p^A(\mathbf{r},t) = \epsilon_0 \delta\chi^{(1)}(\mathbf{r},t) E_{\mathrm{o}}(\mathbf{r},t) \tag{2.89}$$

2.2.2 Influence of source term on propagation

In this section, we insert the vibrational coherence-induced polarization, Eq. (2.89), into the pulse propagation equation, Eq. (2.87)

This goes into the wave equation

$$\left\{ \frac{i}{2k_1} \nabla_{\perp}^2 + \frac{\partial}{\partial z} + \frac{1}{u_{\mathrm{o}}} \frac{\partial}{\partial t} \right\} E_{\mathrm{o}}(\mathbf{r},t) = -i \frac{\omega_1}{2cn_1} \left(1 - \frac{i}{\omega_1} \frac{\partial}{\partial t} \right) \delta\chi^{(1)}(\mathbf{r},t) E_{\mathrm{o}}(\mathbf{r},t) \tag{2.90}$$

where we have neglected dispersion and we are in the lab frame. Note the change of notation $\omega_1 \to \omega_1$, $n_1 \to n_1$, $k_{0,1} \to k_1$, and $v_g \to u_{\mathrm{o}}$.

Recall that the susceptibility perturbation is

$$\delta\chi^{(n)}(\mathbf{r},t) = \delta\chi_0^{(n)}|U_s(x,y,z)|^2 \sin[\Omega_v(t+\tau_{\rm pp}-u_{\rm p}^{-1}z)] \tag{2.91}$$

so the time derivative is

$$\frac{\partial\delta\chi^{(n)}(\mathbf{r},t)}{\partial t} = \Omega_v\delta\chi_0^{(n)}|U_s(x,y,z)|^2 \cos[\Omega_v(t+\tau_{\rm pp}-u_{\rm p}^{-1}z)] \tag{2.92}$$

We can rewrite the wave equation. We evaluate the temporal derivative of the right hand side of Eq. (2.90),

$$\begin{aligned}\frac{\partial}{\partial t}\delta\chi^{(1)}E_{\rm o} &= \delta\chi^{(1)}\left(\frac{\partial}{\partial t}E_{\rm o}\right) + \left(\frac{\partial}{\partial t}\delta\chi^{(1)}\right)E_{\rm o} \\ &= \delta\chi^{(1)}\frac{\partial}{\partial t}E_{\rm o} + \Omega_v\delta\chi_0^{(n)}|U_s(x,y,z)|^2\cos[\Omega_v(t+\tau_{\rm pp}-u_{\rm p}^{-1}z)]E_{\rm o}.\end{aligned} \tag{2.93}$$

Inserting this into the right hand side of Eq. (2.90) yields

$$\begin{aligned}&-i\frac{\omega_1}{2cn_1}\left(1-\frac{i}{\omega_1}\frac{\partial}{\partial t}\right)\delta\chi^{(1)}(\mathbf{r},t)E_{\rm o}(\mathbf{r},t) \\ &\qquad = -i\frac{\omega_1}{2cn_1}\left\{\delta\chi^{(1)}(\mathbf{r},t)E_{\rm o}(\mathbf{r},t) - \frac{i}{\omega_1}\delta\chi^{(1)}\frac{\partial}{\partial t}E_{\rm o}\right. \\ &\qquad\qquad \left. -\frac{i}{\omega_1}\Omega_v\delta\chi_0^{(n)}|U_s(x,y,z)|^2\cos[\Omega_v(t+\tau_{\rm pp}-u_{\rm p}^{-1}z)]E_{\rm o}\right\}.\end{aligned} \tag{2.94}$$

Cleaning this up results in

$$\begin{aligned}&= \frac{1}{2cn_1}\left\{-i\omega_1\delta\chi^{(1)}(\mathbf{r},t)E_{\rm o}(\mathbf{r},t) + \delta\chi^{(1)}\frac{\partial}{\partial t}E_{\rm o}\right. \\ &\qquad\qquad \left. +\Omega_v\delta\chi_0^{(n)}|U_s(x,y,z)|^2\cos[\Omega_v(t+\tau_{\rm pp}-u_{\rm p}^{-1}z)]E_{\rm o}\right\}.\end{aligned} \tag{2.95}$$

Now we gather the terms proportional to $E_{\rm o}$:

$$\begin{aligned}&= \frac{1}{2cn_1}\delta\chi^{(1)}\frac{\partial}{\partial t}E_{\rm o} - i\frac{\omega_1}{2cn_1} \\ &\qquad\qquad \times\left\{\delta\chi^{(1)}E_{\rm o} - i\frac{\Omega_v}{\omega_1}\delta\chi_0^{(n)}|U_s(x,y,z)|^2\cos[\Omega_v(t+\tau_{\rm pp}-u_{\rm p}^{-1}z)]E_{\rm o}.\right\}\end{aligned} \tag{2.96}$$

2.2.3 Complex wavenumber perturbations

Introducing a complex perturbation to the wavenumber k given by

$$\begin{aligned}\delta k_1(\mathbf{r},t) \equiv{}& \frac{\omega_1}{2cn_1}\delta\chi_0^{(1)}|U_s(x,y,z)|^2 \\ &\times\left(\sin\left[\Omega_v\left(t+\tau_{\rm pp}-u_{\rm p}^{-1}z\right)\right] - i\frac{\Omega_v}{\omega_1}\cos\left[\Omega_v\left(t+\tau_{\rm pp}-u_{\rm p}^{-1}z\right)\right]\right),\end{aligned} \tag{2.97}$$

the right hand side takes on a more compact form:

$$= \frac{1}{2cn_1}\delta\chi^{(1)}\frac{\partial}{\partial t}E_{\rm o} - i\delta k_1 E_{\rm o} \tag{2.98}$$

The final result after applying differentiation of the right hand side in Eq. (2.90) and moving the remaining temporal derivative of the probe envelope to the l.h.s is

$$\left\{\frac{i}{2k_1}\nabla_\perp^2 + \frac{\partial}{\partial z} + \left(\frac{1}{u_{\rm o}} + \frac{\delta\chi^{(1)}(\mathbf{r},t)}{2cn_1}\right)\frac{\partial}{\partial t}\right\}E_{\rm o}(\mathbf{r},t) = -i\delta k_1(\mathbf{r},t)E_{\rm o}(\mathbf{r},t). \tag{2.99}$$

We proceed to neglect group velocity distortions described by

$$\frac{\delta\chi^{(1)}(\mathbf{r},t)}{2cn_1}\frac{\partial}{\partial t}E_{\rm o}(\mathbf{r},t), \tag{2.100}$$

resulting in

$$\left\{\frac{i}{2k_1}\nabla_\perp^2 + \frac{\partial}{\partial z} + \frac{1}{u_{\rm o}}\frac{\partial}{\partial t}\right\}E_{\rm o}(\mathbf{r},t) = -i\delta k_1(\mathbf{r},t)E_{\rm o}(\mathbf{r},t). \tag{2.101}$$

Moving to the frame traveling with the probe pulse with $t_{\rm o} = t - u_{\rm o}^{-1}z$ and $\zeta = z$ and making the substitutions, we obtain

$$\left\{\frac{i}{2k_1}\nabla_\perp^2 + \frac{\partial}{\partial\zeta}\right\}E_{\rm o}(x,y,\zeta,t_{\rm pr}) = -i\frac{\omega_1}{2cn_1}\delta\chi^{(1)}(\mathbf{r},t_{\rm pr})E_{\rm o}(x,y,\zeta,t_{\rm o}) \tag{2.102}$$

We shall define wavenumber k perturbations as

$$\delta k_1 = \frac{\omega_1}{2cn_1}\left(\delta\chi^{(1)} - \frac{i}{\omega_1}\frac{\partial\delta\chi^{(1)}}{\partial t}\right) \equiv \delta k_1' + i\delta k_1'' \tag{2.103}$$

with real and imaginary parts of the wavenumber k perturbations,

$$\delta k_1' = \Re\{\delta k_1\} = \frac{\omega_1}{2cn_1}\delta\chi_0^{(1)}|U_s(x,y,z)|^2\sin[\Omega_v(t_{\rm o}+\tau_{\rm pp})] \tag{2.104}$$

and

$$\delta k_1'' = \Im\{\delta k_1\} = -\frac{\Omega_v}{2cn_1}\delta\chi_0^{(1)}|U_s(x,y,z)|^2\cos[\Omega_v(t_{\rm o}+\tau_{\rm pp})] \tag{2.105}$$

here the subscript 1 denotes the fundamental probe frequency.

Finally we write the wave equation describing effective linear modulation of a probe pulse propagating through a coherence.

$$\left\{\frac{i}{2k_1}\nabla_\perp^2 + \frac{\partial}{\partial\zeta}\right\}E_{\rm o}(x,y,\zeta,t_{\rm pr}) = -i\delta k_1(\mathbf{r},t_{\rm o})E_{\rm o}(x,y,\zeta,t_{\rm pr}) \tag{2.106}$$

To demonstrate this is a modification to the propagation wavenumber, we will consider the plane wave case where $\nabla_\perp^2 = 0$. The solution to Eq. (2.102) is

$$E_{\rm o} = E_{0,{\rm o}}e^{-i\delta k_1\zeta} = E_{0,{\rm o}}e^{-\delta k_1''\zeta}e^{-i\delta k_1'\zeta} \tag{2.107}$$

2.3 Summary of linear propagation perturbation

We began with the wave equation, inserted an additional driving term, the additional polarization density p^A that is related to the susceptibility perturbations $\delta\chi^{(1)}$ that were set up in response to a pump pulse. Upon taking the time derivative of p^A we found the wave equation could be coaxed into the form of Eq. (2.102), written in the traveling frame of the probe pulse, where the susceptibility perturbation $\delta\chi^{(1)}$ has been shown to manifest itself in terms of a modified propagation wavenumber δk_1 in Eq. (2.106)

It can be seen clearly from Eq. (2.107) that the real part of the wavenumber perturbation, $\delta k'$, contributes to a phase shift, whereas the imaginary part, $\delta k''$, contributes to absorption. If one records either the phase shift or the amplitude modulation of the probe with respect to τ_{pp}, the vibrational modulation will be visible as a sinusoid. The magnitude of the phase effect is proportional to the central frequency of the probe, while the magnitude of the amplitude effect is proportional to the vibrational frequency itself. For instance, we predict the phase shift to be more sensitive for a blue probe than a red probe. Furthermore if one records both the phase shift and amplitude modulation of the probe with respect to τ_{pp} and compares the two signals, they will exhibit sinusoidal oscillations at the same frequency Ω_v, but with a relative phase shift of $\pi/2$.

2.3.1 Amplitude modulation from an energy density perspective

This picture is in accordance with an early account that considered the probe amplitude modulations from the perspective of energy exchange with the nuclear motion [19]. In sum, the vibrational energy density after pumping is

$$U_0 = \tfrac{1}{2}\Omega_v^2 Q_0^2, \tag{2.108}$$

where Ω_v is the vibrational frequency and Q_0 is the initial displacement of the reduced-mass coordinate. The probe pulse acts as a pump for further excitation with initial amplitude Q_1. The square of the sum vibrational coherence after probe interaction, neglecting damping,

$$Q_\Sigma^2 = Q_0^2 + Q_1^2 + 2Q_0Q_1\cos\Omega_v\tau_{\mathrm{pp}}, \tag{2.109}$$

where τ_{pp} is the delay between the pump and probe pulses. By substituting Q_Σ for Q_0 in Eq. (2.108) we find the vibrational energy stored in the medium after probe pulse interaction,

$$U_1 = \tfrac{1}{2}\Omega_v^2 \left[Q_0^2 + Q_1^2 + 2Q_0 Q_1 \cos(\Omega_v \tau_{\mathrm{pp}})\right]. \tag{2.110}$$

The change in energy density, found by subtracting Eq. (2.108) from Eq (2.110) and assuming the probe to be significantly weaker than the pump ($Q_1 \ll Q_0$) is

$$\Delta U = U_1 - U_0 \approx \Omega_v^2 Q_0 Q_1 \cos(\Omega_v \tau_{\mathrm{pp}}). \tag{2.111}$$

By conservation of energy, ΔU must be subtracted from the probe pulse. This result is in agreement with the amplitude modulations predicted by the imaginary part of the k wavenumber perturbations, $\delta k''$.

2.3.2 Conclusion

Now that we have arrived at a mathematical understanding of the coherence modulation of an ultrashort probe pulse, and established that phase measurements will be more sensitive than amplitude measurements we will present a three experiments to measure the phase shift $\delta k'$ in the next chapter.

CHAPTER III

LINEAR RAMAN MEASUREMENTS

3.1 Introduction

It was shown in the previous chapter that the perturbation to the linear susceptibility results in a perturbation of the complex wavenumber, δk, that results in amplitude and phase modulation of a probe pulse that is delayed from the pump pulse by τ_{pp}. The phase modulation samples the vibrational displacement coordinate

$$\delta k_1' = \Re\{\delta k_1\} = \frac{\omega_1}{2cn_1}\delta\chi_0^{(1)}|U_s(x,y,z)|^2\sin[\Omega_v(t_{\mathrm{o}}+\tau_{\mathrm{pp}})] \tag{3.1}$$

while the amplitude modulation samples the momentum, or time derivative of the displacement

$$\delta k_1'' = \Im\{\delta k_1\} = -\frac{\Omega_v}{2cn_1}\delta\chi_0^{(1)}|U_s(x,y,z)|^2\cos[\Omega_v(t_{\mathrm{o}}+\tau_{\mathrm{pp}})] \tag{3.2}$$

It is clear from the above that the amplitude modulation is weaker than the phase modulation by a factor of ω/Ω_v. For a typical optical wavelength of 800 nm and a vibrational frequency of 500 cm^{-1}, this ratio is $\omega/\Omega_v = 25$. Measurement of the phase is achieved by mixing the probe pulse with a reference pulse in a detector, and has been shown experimentally to be more sensitive than amplitude measurements [44]. The experiments described here differ in that we take spectrally resolved measurements of the probe–reference interference.

3.2 Spectral interferometry and phase retrieval

3.2.1 Experimental set-up

An interferometer provides a means of measuring the relative phase difference between a reference and a probe pulse. So we design an experiment to deliver the pulses in such a way that the probe is modulated by the pump-induced coherence, and the reference remains unmodulated, and is combined to interfere with the probe at the detection end.

An optical pulse is split into three pulses: pump, probe, and reference. The pulses are split, and only the pump and probe pulses are sent to interact with the sample. The pump is rejected, either chromatically or by polarization, and the probe is recombined with the reference in a spectrometer. These pulses are assumed to be transform-limited, or at least shorter than a vibrational period, so that the pulse samples the vibration, or takes a snapshot of the molecular motion, hence the need for a prism compressor at the front of the set-up. The probe pulse is written in the frequency domain as a spectral amplitude and phase,

$$E_{\mathrm{o}}(\omega) = A_{\mathrm{o}}(\omega)e^{i\phi_{\mathrm{o}}(\omega)}, \tag{3.3}$$

and the time-delayed reference pulse,

$$E_{\mathrm{r}}(\omega) = A_{\mathrm{r}}(\omega)e^{i\phi_{\mathrm{r}}(\omega)}e^{i\tau_{\mathrm{pr}}\omega}, \tag{3.4}$$

where τ_{pr} is the delay between the probe and the reference. These two pulses incident on a square-law detector, such as the CCD of a spectrometer, interfere in the frequency domain,

$$S(\omega) = |E_{\mathrm{r}}(\omega) + E_{\mathrm{o}}(\omega)|^2 \tag{3.5}$$

Expanding the measured power spectrum:

$$\begin{aligned} S(\omega) &= (E_{\mathrm{r}} + E_{\mathrm{o}}) \times (E_{\mathrm{r}}^* + E_{\mathrm{o}}^*) \\ &= |E_{\mathrm{r}}|^2 + |E_{\mathrm{o}}|^2 + E_{\mathrm{r}}^* E_{\mathrm{o}} + E_{\mathrm{r}} E_{\mathrm{o}}^* \\ &= A_{\mathrm{r}}^2 + A_{\mathrm{o}}^2 + A_{\mathrm{r}}A_{\mathrm{o}}e^{i(\phi_{\mathrm{o}}-\phi_{\mathrm{r}}-\tau_{\mathrm{pr}}\omega)} + A_{\mathrm{r}}A_{\mathrm{o}}e^{i(-\phi_{\mathrm{o}}+\phi_{\mathrm{r}}+\tau_{\mathrm{pr}}\omega)} \\ &= A_{\mathrm{r}}^2 + A_{\mathrm{o}}^2 + 2A_{\mathrm{r}}A_{\mathrm{o}}\cos\left(\tau_{\mathrm{pr}}\omega + \phi_{\mathrm{r}} - \phi_{\mathrm{o}}\right) \end{aligned} \tag{3.6}$$

3.2.2 Phase retrieval algorithm

To retrieve phase information from the recorded interferograms, we employ the technique described by Takeda *et al.* [54], which originally described numerical analysis of off-axis holography. Following the notation in [54], we let $a(\omega) = A_{\mathrm{r}}^2 + A_{\mathrm{o}}^2$, $b(\omega) = 2A_{\mathrm{r}}A_{\mathrm{o}}$, and $\phi(\omega) = \phi_{\mathrm{r}} - \phi_{\mathrm{o}}$. For a particular spectral interferogram, fringes are observed with a modulation frequency related to the time delay between the two pulses,

$$g(\omega) = a(\omega) + b(\omega)\cos\left[\tau_{\mathrm{pr}}\omega + \phi(\omega)\right], \tag{3.7}$$

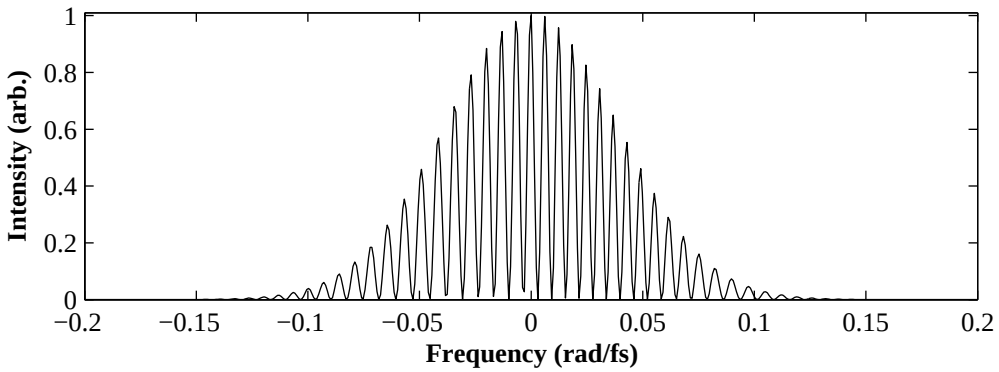

Figure 3.1: Sample spectral interferogram showing fringes.

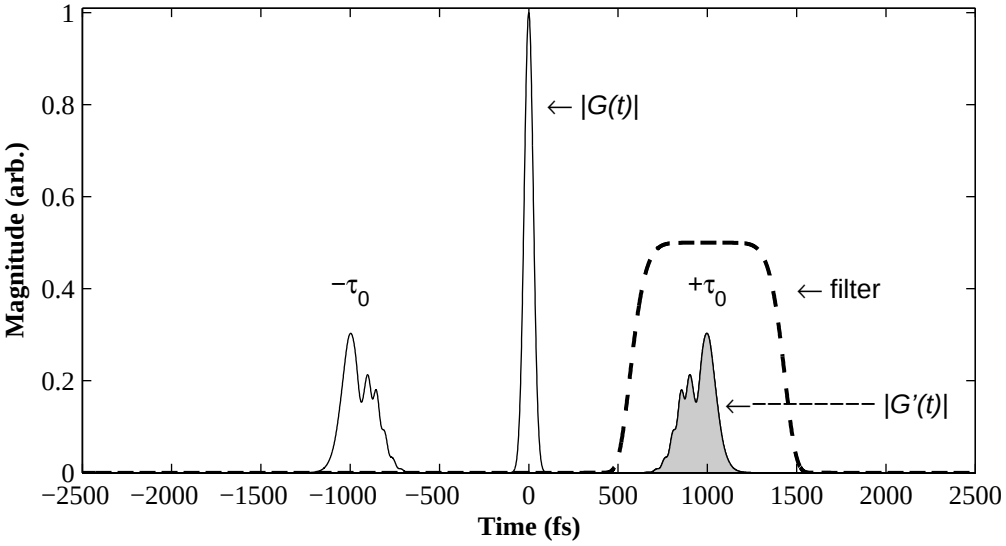

Figure 3.2: Typical Fourier transform of spectral interferogram.

where $\tau_{\rm pr}$ is the temporal delay between the two interferometer arms, $a(\omega)$ and $b(\omega)$ are due to spectral intensity variations, and $\phi(\omega)$ is the phase difference between the two arms. The above can be rewritten

$$g(\omega) = a(\omega) + c(\omega)e^{i\tau_{\rm pr}\omega} + c^*(\omega)e^{i\tau_{\rm pr}\omega}, \tag{3.8}$$

where

$$c(\omega) = \frac{1}{2}b(\omega)e^{i\phi(\omega)}, \tag{3.9}$$

and $c^*(\omega)$ is its complex conjugate. A typical interferogram is shown in Fig. 3.1. Taking

the Fourier transform of Eq. (3.8),

$$G(t) = A(t) + C(t - \tau_{\mathrm{pr}}) + C^*(t + \tau_{\mathrm{pr}}). \tag{3.10}$$

Examining the Fourier transform of the signal, we see two peaks at $\pm\tau_{\mathrm{pr}}$ and a DC component caused by $A(t)$, as shown in Fig. 3.2. Since we are only after the phase information contained in $C(t - \tau_{\mathrm{pr}})$, we multiply $G(t)$ by a super-Gaussian filter,

$$G'(t) = G(t) \times \exp\left[\frac{-(t - \tau_{\mathrm{pr}})^4}{2\sigma^4}\right]. \tag{3.11}$$

to obtain, with an appropriate choice of σ,

$$G'(t) \approx C(t - \tau_{\mathrm{pr}}). \tag{3.12}$$

An inverse Fourier transform of $C(t - \tau_{\mathrm{pr}})$ yields $c(\omega)$ as defined in Eq. (3.9), the phase of which is the phase difference between the shaped and reference pulses. In practice, this transform is obtained by circularly shifting this sideband to DC, for example by using the MATLAB `circshift()` function. The difference in this result between a zero mask and a particular phase mask yields the spectral phase imparted by a particular SLM phase mask.

3.2.3 Remarks

Also it is important that the spectrometer data is first interpolated from the spectrometer's evenly-spaced wavelength axis to an evenly-spaced frequency axis. Otherwise the Fourier transform in Fig. 3.2 will not have a linear time axis, and step of shifting the isolated sideband to DC will introduce distortions in the retrieved phase. Usually we subtract a reference phase from the result described here. This reference phase is acquired either by blocking the pump or setting the pump timing such that the pump interacts with the sample after the probe and reference pair pass through. This second method is preferable because pump-related heating of the sample will be consistent between the reference phase measurement and the actual vibrational phase measurement.

3.2.4 Interferometric probe–reference stability

A source of phase noise, limiting measurement sensitivity, is interferometric stability between the probe and reference pulses. By routing these pulses through different paths, they

accumulate different random phase from air turbulence and mechanical vibrations in the optics. Stability may be improved by sending the reference through the sample along with the probe.

Better yet, a birefringent delay crystal is used to split the probe and the reference [55], as shown in Fig. 6.3 on page 119. The birefringent pulse splitter is described in more detail in Chapter 6, but a brief description follows. The group delay for the eigenaxes of a birefringent crystal differs, depending on the angle of the optic axis with respect to the propagation direction. An incident pulse, polarized at 45 degrees with respect to the ordinary and extraordinary axes, will be split into a pulse pair with a group delay difference.

3.2.5 Conclusion

The drawback to the spectral interferometry method is that the reference must precede the pump, so as not to be modulated by the vibrations. This means that in order to perform longer delay scans, the final probe–reference separation must be greater than the maximum pump–probe separation. Since the probe–reference separation τ_{pr} determines the fringe spacing in the spectral interferogram, longer separations require higher spectrometer resolution. For example, our OceanOptics USB2000 will at most be able to measure a delay of 4 ps. This limits the vibrational spectral resolution to $d\nu = 1/(c\tau) \approx 8.5$ cm^{-1}. The next section describes a synthetic temporal aperture approach to achieve better spectral resolution.

3.3 Improved spectral resolution with a synthetic temporal aperture

For pump–probe delays in excess of the probe–reference delay ($\tau_{\mathrm{pp}} > \tau_{\mathrm{pr}}$), both the probe and reference pulses arrive at the sample after the pump pulse so that the sampling window can be arbitrarily long. The phase measured by spectral interferometry in this case is the difference of the perturbation induced by the vibrations,

$$\Delta\phi(\tau_{\mathrm{pr}}) = \phi_{\mathrm{o}} - \phi_{\mathrm{r}} = \phi(\tau_{\mathrm{pp}}) - \phi(\tau_{\mathrm{pp}} + \tau_{\mathrm{pr}}) \tag{3.13}$$

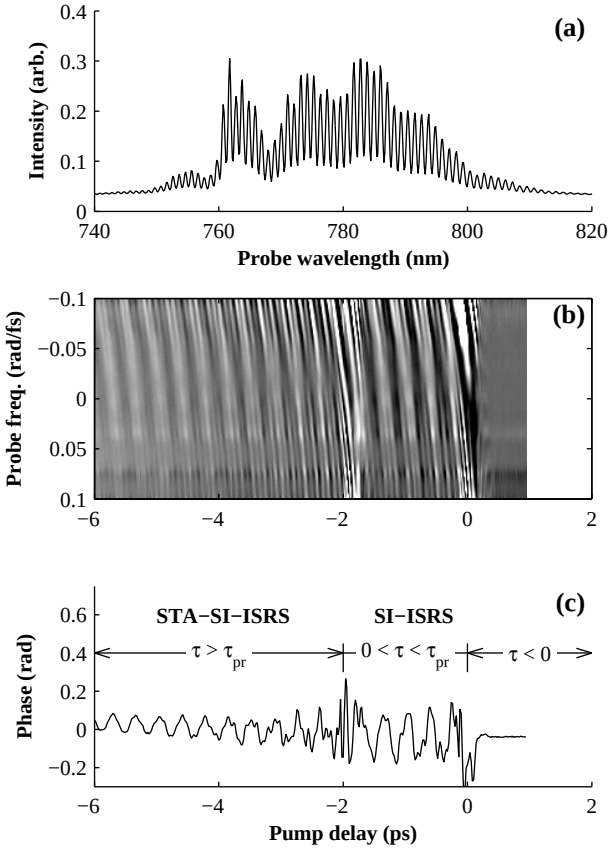

Figure 3.3: Spectral interferometry measurement of transient phase for various pump timing regimes. (a) Probe–reference interference spectrum recorded by the spectrometer. (b) Phase map retrieved by sideband filtering algorithm. (c) Line-out of the retrieved phase at the center probe wavelength indicating three pulse timing conditions. From right to left: $\tau_{\rm pp} < 0$, no interaction since pump follows both probe and reference; spectral interferometry where $0 < \tau_{\rm pp} < \tau_{\rm pr}$ and the reference phase is zero; synthetic temporal aperture where $\tau_{\rm pp} > \tau_{\rm pr}$.

(for brevity, we omit the dependence on the probe optical frequency ω). Let us define the (complex) Raman spectrum as the Fourier transform of the measured transient phase $\Phi(\Omega) = \int \phi(\tau_{\rm pp}) e^{-i\Omega\tau_{\rm pp}} {\rm d}\tau_{\rm pp}$. The Fourier transform of the STA probe–reference phase difference map data gives a spectrum of

$$\begin{aligned} \Phi'(\Omega) &= \int_{-\infty}^{\infty} \left[\phi(\tau_{\rm pp}) - \phi(\tau_{\rm pp} + \tau_{\rm pr})\right] e^{-i\Omega\tau_{\rm pp}} {\rm d}\tau_{\rm pp} \\ &= 2i\Phi(\Omega) e^{i\Omega\tau_{\rm pr}/2} \sin\left(\Omega\tau_{\rm pr}/2\right). \end{aligned} \tag{3.14}$$

3.3.1 Spectral attenuation

The modulation of the reference pulse causes an irrecoverable loss of phase information at the harmonics of the probe–reference separation and the desired Raman spectrum is modulated as shown by the sine term in Eq. (3.14). This can be understood intuitively by considering a sinusoidal temporal phase modulation sampled by a pair of pulse separated by τ_{pr}. Oscillation frequencies that are integer multiples m of the probe–reference pulse separation, $\tau_{\mathrm{pr}} = m2\pi/\Omega$ will lead to zero phase difference between the probe–reference pair since both probe and reference pulses are always at the same phase of the vibrational motion. For example, we expect a delay of $\tau_{\mathrm{pr}} = 4$ ps to produce nodes at every ~ 8 cm^{-1}.

Even though the STA-SI-ISRS measurement imposes periodic attenuation, the effect is not entirely detrimental. Consider that the Raman spectrum of each vibrational mode consists of a band of frequencies, since these modes exhibit damping and dephasing. For a vibrational mode frequency Ω_v damped at a rate Γ, we can find an explicit relationship of Eq. (3.14) of the form

$$\left|\Phi'(\Omega)\right|^2 = \left|\frac{A}{-\Omega^2 + \Omega_v^2 + i\Gamma\Omega}\right|^2 \sin^2\left(\frac{\Omega\tau_{\mathrm{pr}}}{2}\right) \tag{3.15}$$

where A depends on the excitation strength of the ISRS by the pump pulse. Due to the finite bandwidth of frequencies associated with a specific mode, the STA sinusoidal distortion will not eliminate every frequency in the band. For small values of Γ (such as in gas-phase molecules), the decay time becomes large and the narrow range of frequencies becomes more susceptible to spectral distortion with STA. However, in liquids, typical dephasing times are of the order of ~ 3 ps, so that the probe pulse samples a severely attenuated phase modulation strength compared to the reference pulse. Thus, we expect that if $\tau_{\mathrm{pr}} > \Gamma^{-1}$, the impact will be negligible. A sample numerical simulation is shown in Fig. 3.4 for a variation of the probe–reference delay, τ_{pr}, with a fixed vibrational frequency for an undamped vibrational mode indicated by the solid line for $\Gamma^{-1} = \infty$ ($\Gamma\tau_{\mathrm{pr}} \ll 1$). By contrast, a more typical decay time of $\Gamma^{-1} = 2$ ps ($\Gamma\tau_{\mathrm{pr}} > 1$) is shown by the dashed line in Fig. 3.4.

The simulations indicate no spectral lineshape distortions of Raman lines for reasonable

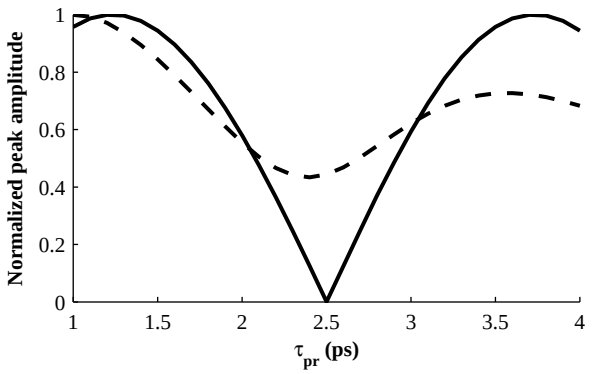

Figure 3.4: Simulation of information loss in synthetic aperture measurements of a $\bar{\nu} = 13\ \mathrm{cm}^{-1}$ mode, varying the probe–reference delay τ_{pr}. For a long-lived vibration with $\Gamma^{-1} = \infty$ ps (solid line), the periodic condition $\tau_{\mathrm{pr}} = 1/m\nu$ causes a loss of spectral information. For decay times typical of liquids, $\Gamma^{-1} = 2$ ps, the loss is not complete (dashed line).

experimental parameters. More importantly, for typical dephasing times of $\Gamma^{-1} \sim 1--15$ ps and for probe–reference delays of $\sim 3-4$ ps, STA-SI-ISRS measurements do not completely attenuate spectral lines. As indicated by Fig. 3.4, the attenuation is likely to be less than 0.5. It should be emphasized that an *undistorted* high-resolution spectrum of a particular mode can always be recorded with a suitable choice of τ_{pr}. In the experimental data that follows, no significant STA spectral distortions are evident.

3.3.2 Experimental set-up

The experimental setup is sketched in Fig. 3.5. Pulses are generated by a multipass Ti:sapphire amplifier (KMLabs Dragon) producing ~ 1 mJ, ~ 30 fs laser pulses centered at 780 nm at a repetition rate of 1 kHz. In the liquid and solid samples, we use an additional prism compressor to compensate for material dispersion in the experiment. For gas species, the amplifier grating compressor was sufficient to yield transform-limited pump pulses in the sample. Approximately 10% of the energy is split into the probe arm, which is then split into probe and reference pulses with a delay of τ_{pr} by either a Michelson interferometer, Fig. 3.5(i), or a birefringent delay crystal for exceptional fringe stability [55], Fig. 3.5(ii). A computer-controlled optical delay arm adjusts the pump–probe delay, τ_{pp}, before the pulses are focused into the samples in either collinear or non-collinear arrangements, as shown in Figs. 3.5(i,ii). After the sample, the pump light is rejected (either spatially, chromatically,

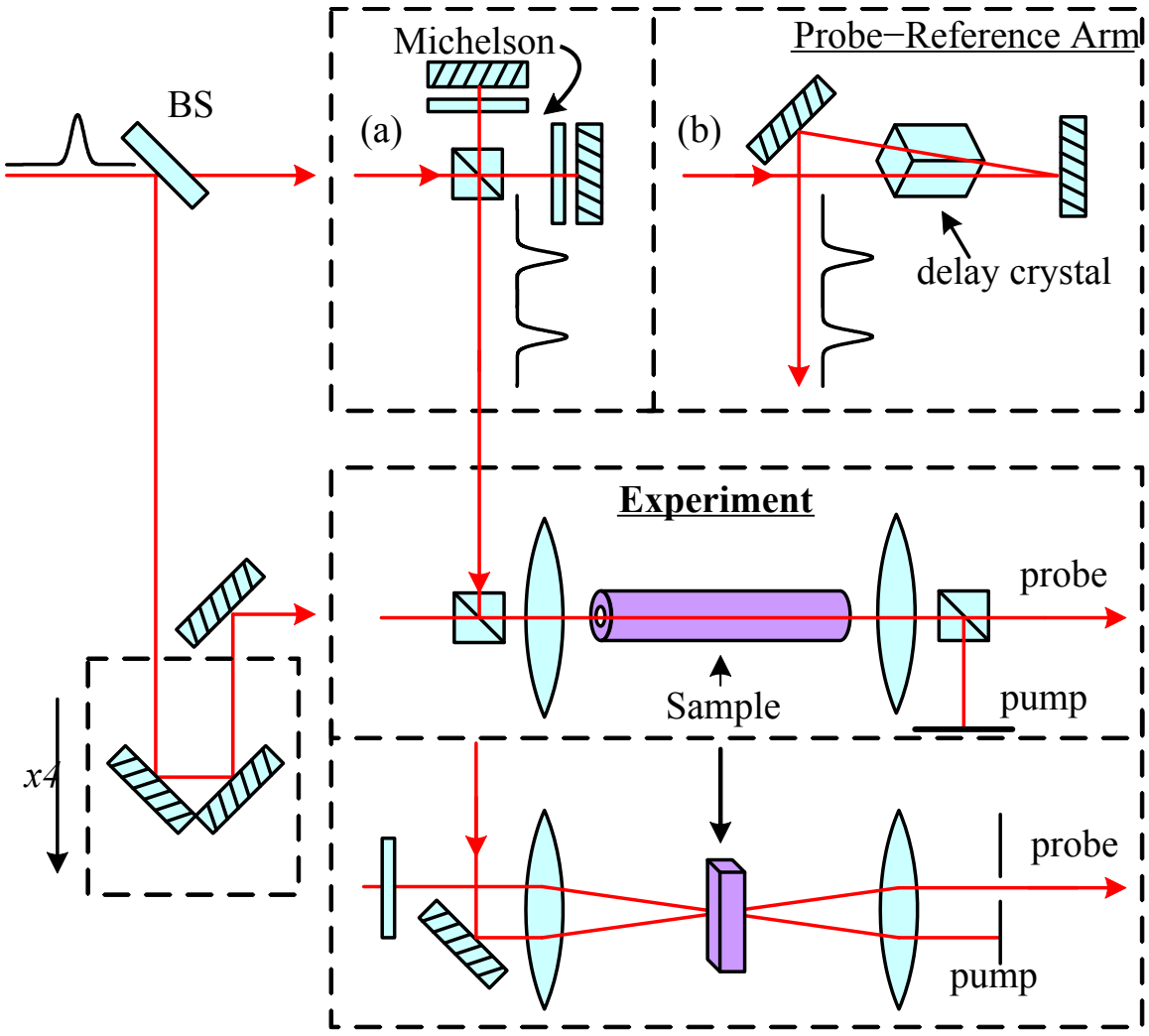

Figure 3.5: Synthetic temporal aperture experimental configurations. To measure gas-phase molecules (i), the probe–reference pair was created with a Michelson interferometer, and the pulses were coupled in to a hollow-core fiber, filled with the sample. The liquid- and solid-phase experiments (ii) utilized a thick birefringent crystal to generate the probe–reference pair, and a non-collinear sample configuration is employed.

Sample	τ_{pr}, ps	T, ps	dt, fs	$d\bar{\nu}$, cm^{-1}	config.
(a) SF_6	3.8	17.2	10	1.9	(i)
(b) $C_4H_{10}O$	3.6	2.8	5.0	12.0	(ii)
(c) $CHCl_3$	3.6	2.7	2.0	12.3	(ii)
(d) CCl_4	3.6	2.7	2.0	12.3	(ii)
(e) BGO12	1.9	37.6	20	0.89	(ii)
(f) $LaAlO_3$	3.5	9.6	50	3.5	(ii)

Table 1: Symthetic temporal aperture experimental parameters. T is the temporal window, dt is the sampling rate in time, $d\nu$ is the spectral resolution achieved in the scan. Last column shows experimental configuration (see Fig. 3.5).

or by polarization).

The flexibility of STA-SI-ISRS allows us to choose a geometry and pump-probe separation method to suit the sample under investigation. For measuring dilute gas samples and depolarized Raman modes, we use orthogonally polarized pump and probe pulses in a collinear geometry, rejecting the pump light after the sample with a polarizer (Fig. 3.5i). The collinear geometry allows for long interaction lengths, enhancing the accumulated probe phase. For liquid- and solid-phase samples with depolarized Raman modes we switch to a non-collinear geometry, allowing for arbitrary pump–probe polarizations, rejecting the pump with an aperture (Fig. 3.5ii). However, in this spatial separation method, scattered pump light can still contaminate the probe interferogram. A third method, using pump and probe pulses of different center wavelengths and dichroic optics, could provide excellent pump–probe separation for a clean probe–reference interferogram in a collinear geometry. While potential group velocity walkoff problems preclude long interaction lengths, this arrangement is ideal for microscopy applications with tight focusing.

After the pump light is rejected, the probe–reference pair is projected to be co-polarized before the spectrum is recorded by a spectrometer (OceanOptics USB2000).

We collect interferograms while sweeping the delay τ_{pp}, with typical step sizes of $dt =$ 20 fs and duration of $T = 10$ to 20 ps. Specific measurement conditions for each case are listed in Table 1.

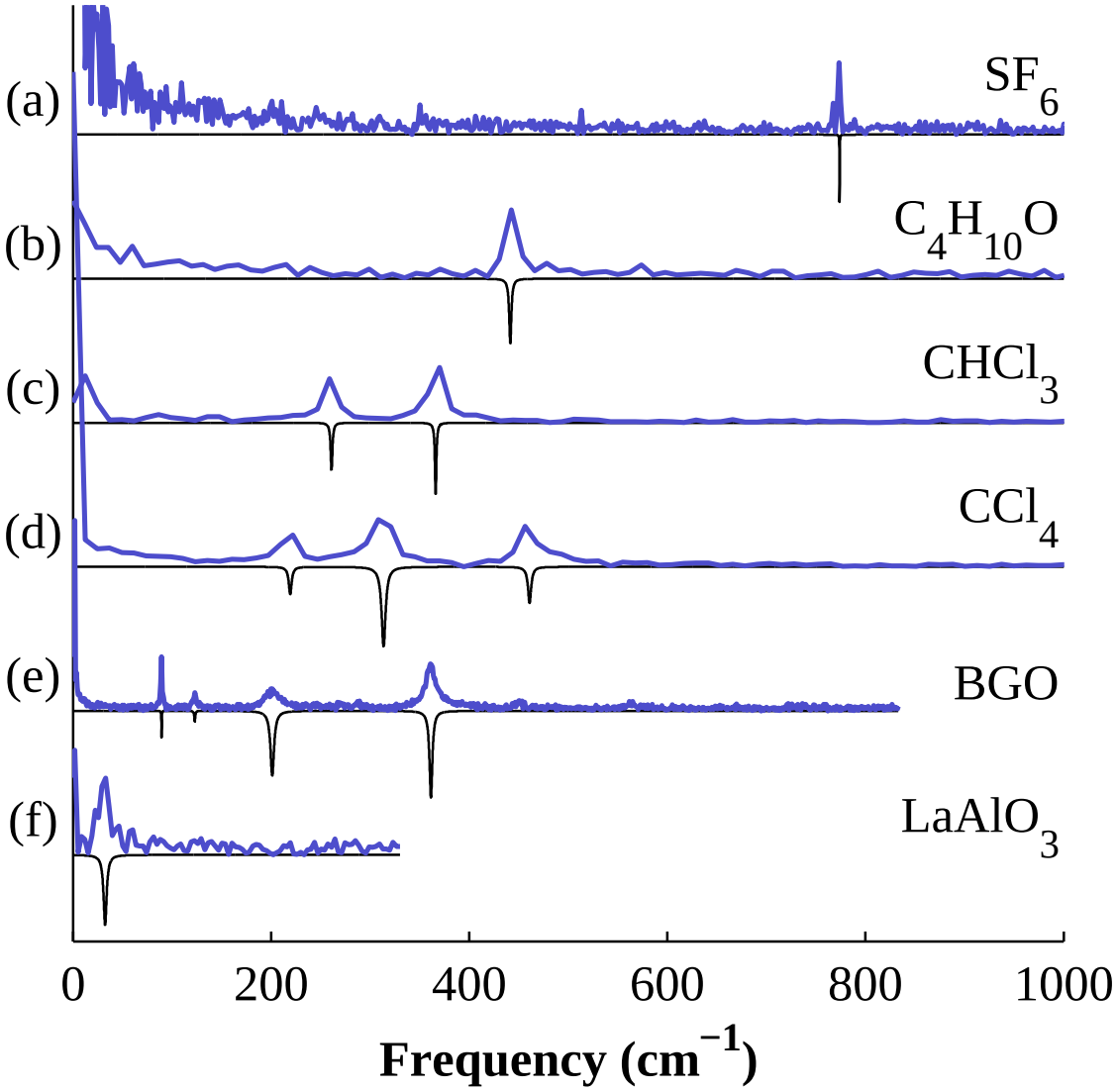

Figure 3.6: Synthetic temporal aperture Raman spectra acquired for (a) gas, (b)–(d) liquid, and (e)–(f) solid phase samples. The blue lines (upward) show spectra obtained with the Fourier transform of the retrieved probe–reference phase difference. Black lines (downward) are results obtained with the LP-SVD.

3.3.3 Results

3.3.3.1 Gas phase SF_6

In the gas phase, we examine sulfur hexafluoride (SF_6) at 660 Torr held in a 21cm long glass capillary with an inner diameter of 250μm, as depicted in Fig. 3.5(i). Here, the probe–reference separation is set to 3.8 ps. The orthogonally-polarized pump and probe pulses enable rejection of the pump by a crossed polarizer after the sample. Due to incomplete extinction on the analyzing polarizer, measurements are taken long after time overlap ($\tau_{\mathrm{pp}} \gg \tau_{\mathrm{pr}}$) to avoid spectral interference terms arising from the leaked pump. This approach is viable in the gas phase since a dilute gas typically has a vibrational mode dephasing times in excess of 100 ps. A delay scan with 10 fs steps over a range of 17.2 ps gives a Raman spectral resolution of 1.9 cm^{-1}. The Raman spectra obtained by Fourier transform and LP-SVD methods are shown in Fig. 3.6(a), with the ν_1 Raman active frequency of 773 cm^{-1}, agreeing favorably with the expected 774.58 ± 0.03 cm^{-1}[56], clearly visible. Since collinear propagation of the pump, probe, and reference pulses is permitted, long glass capillaries may be used to enhance depth of phase modulation of the probe and thus improve spectroscopic sensitivity.

3.3.3.2 Liquid phase

Liquid phase samples are shown in Figs. 3.6(b)–(d). The spectra were measured in the non-collinear arrangement shown in Fig. 3.5(ii). This allowed spatial separation of the pump and probe–reference pair, thereby avoiding the issues associated the pump contamination in the spectral interferogram. A cuvette with a 5 mm interaction length was placed at the focus of a $f = 150$ mm singlet lens, yielding an estimated spot size of 150 μm. The pulses were recollimated after the sample by a $f = 125$ mm lens. To avoid filamentation and boiling of the liquid, the incident pulse energy was severely attenuated to $\sim$ 300 nJ in the pump pulse, and $\sim$ 150 nJ in the probe–reference pulse pair. As mentioned above, STA-SI-ISRS measurement does not restrict the interaction angle since we are recording the phase perturbation imposed on the probe–reference pair and not scattering to a new spatial frequency. As a result, the crossing angle is kept small for a greater interaction length in

the sample, leading to greater depth of modulation on the probe. In practice, about 0.5° is just large enough to spatially separate the beams to block the pump from the spectrometer with an iris. Experiments using dichroic pump separation, with different pump and probe wavelengths, were frustrated by group velocity walk-off in the long liquid interaction lengths and precluded the measurement of vibrational oscillations.

In each of the liquid measurements, the probe–reference separation was set to 3.6 ps. The coherent Raman spectrum of ether ($C_4H_{10}O$) recorded with STA-SI-ISRS is shown in Fig. 3.6(b). A 2.8 ps scan with 5.0 fs steps yield a Raman spectral resolution of 12.0 cm^{-1}. Measurements of neat chloroform ($CHCl_3$) shown in Fig. 3.6(c) were measured with a 2.0 fs step over a 2.7 ps range. The Raman spectrum of neat carbon tetrachloride (CCl_4) is shown in Fig. 3.6(d), with the same step size, probe–reference separation and scan range. Both the CCl_4 and $CHCl_3$ spectra have a spectral resolution of 12.3 cm^{-1}. The spectra agree well with published results measured using spontaneous Raman scattering [57]. Longer delay scans would not narrow the liquid vibrational peaks since their width is determined by the short vibrational dephasing times in the liquid state.

3.3.3.3 Solid phase optical phonons

Finally, we demonstrated STA-SI-ISRS of optical phonons in solid-phase samples. These data were gathered with the same focusing conditions and pulse energies as were used in the liquid-phase measurements. The first data shown in Fig. 3.6(e) is for 0.5 mm thick $Bi_4Ge_3O_{12}$ (BGO12). For BGO12, we performed a scan with a probe–reference separation of 1.9 ps, a step size of 20 fs over a duration of 37.6 ps. The Fourier-limited Raman spectral resolution is 0.89 cm^{-1}. To demonstrate our ability to characterize heavily damped low-frequency modes, we measure the 1 THz mode in lanthanum aluminate ($LaAlO_3$) with a 50 fs step size over a 9.6 ps temporal window, with a 3.5 ps probe-reference separation. The coherent Raman spectrum shown in Fig. 3.6(f) demonstrates that SI-ISRS readily measures this low-frequency, ~ 30 cm^{-1} mode.

3.3.4 Conclusion

We have demonstrated a sensitive technique for time-domain coherent Raman vibrational measurements. This technique employs spectral interferometry for direct sensitive phase measurements of the transient index of refraction perturbations induced through ISRS by a pump pulse. This technique has been demonstrated to be suitable for solids, liquids, and gases and can be constructed with either a collinear or non-collinear geometry. Our ability to measure both polarized and depolarized modes could be extended by carefully selecting pump and probe polarization states to characterize the tensorial nature of the Raman differential polarizability [58]. Extension of the pump–probe delay enables a regime of synthetic temporal aperture and permits spectral resolution to be extended beyond the spectral resolution limits imposed by the spectrometer.

Moreover, since we are recording the phase difference with a probe-reference pair, and no additional spectral components are generated, phase matching considerations are relaxed and are dominated by group-velocity mismatch, which may be important when the probe–reference pair is at a different central wavelength than the pump pulse. When combined with selective ISRS pumping through temporal pulse shaping [59, 60, 61, 62], this technique could yield highly selective coherent femtosecond Raman spectroscopy. The relaxed phase matching conditions will make STA-SI-ISRS technique readily adaptable to coherent Raman microscopy.

3.4 Rapid acquisition with chirped spectral holography

3.4.1 Introduction

Scanning an optical delay line can be time-consuming. If we desired to obtain spatially-resolved Raman spectra in a scanning microscope, the drop in frame rate from having to scan a pump–probe delay at *every pixel* would be unacceptable. This chapter describes a set-up that can perform time-resolved phase-sensitive Raman spectroscopy in a single measurement. (We are careful to avoid the term 'single shot', as the method here does average more than a single shot from the laser. With a 1 kHz pulse train from the amplifier and a minimum 3 ms spectrometer integration, we record a minimum of 3 pulses per measurement.)

Techniques for high spectral resolution coherent Raman spectroscopy have recently been developed for short pump – long probe [63, 64] and for single-pulse geometries with pulse shaping [65, 66, 67]. Adaptation of coherent Raman techniques to microscopy [68] offer simultaneous measurement of a range of vibrational resonances [69]. Unfortunately, low-frequency modes (< 200 cm^{-1}) are challenging with these techniques. Time-domain spectroscopy [50, 70, 71] where a probe pulse is scanned over a long pump-probe delay window easily resolves low-frequency modes, but this technique is time consuming and not favorable for scanning imaging applications.

Here, we demonstrate a method of rapid acquisition of low-frequency vibrational modes in a non-scanning, chirped spectral holography (CSH) technique.

3.4.2 Other non-scanning methods

Multiplex CARS methods [66, 67] have been developed to rapidly acquire spectra, but are poorly suited to measuring low-frequency modes due to their reliance on measuring a frequency-shifted anti-Stokes field.

3.4.3 Spectral holography for phase encoding

In CSH a three-pulse sequence, consisting of an intense ultrafast pump pulse and two weak, chirped probe/reference pulses, interacts with a sample in the following order. First the reference passes through the sample unperturbed. Then the pump pulse produces quantum beating between vibrational levels through impulsive stimulated Raman scattering (ISRS) [50] which gives rise to a time-varying perturbation in the index of refraction $\delta n(t)$ [72].

Finally the probe experiences a phase modulation proportional to the vibrational motion. The probe–reference pair is separated in time by τ_{pr} and straddles the pump pulse such that the reference pulse arrives before the pump while the probe pulse arrives at a time τ after the pump pulse.

If the spectral phase of the probe and reference pulses is known, the phase perturbation $\delta\phi(t) = k_{0,1} L \delta n(t)$ acquired by the probe pulse with propagation through the sample length L may be extracted by use of a spectral holography algorithm [73], which is an exact analogy to the spatial off-axis holography of Leith [74]. Here, $k_{0,1} = \omega_1/c$ and ω_1 is the probe central

frequency. The restriction is that the reference pulse spectrum must not be narrower than that of the probe pulse. This implies a temporal resolution set by the inverse bandwidth of the reference spectrum, and a temporal window set by the pulse chirp. It is also possible to retrieve the phase by mapping the spectral phase to time [70, 75, 76, 77], but with lower temporal resolution.

3.4.4 Implementation with chirped pulses

CSH makes use of probe and reference pulses that are identically chirped from a transform-limited temporal duration τ_0 to a duration with $\tau_c \gg \tau_0$. We write the chirped pulses as $\tilde{\mathcal{E}}_c(t) = E_c(t)e^{i\omega_1 t}$, where $E_c(t) = A_c(t)e^{i\phi_c(t)}$ is the complex pulse envelope. In the experiments, the material dispersion in the probe arm is primarily quadratic, so the large chirp yields an instantaneous frequency sweep $\Omega_{inst}(t) = \mathrm{d}\phi_c(t)/\mathrm{d}t$ that is a nearly linear function of time t during the pulse envelope. The probe and reference pulses are separated by a delay $\tau_{pr} > \tau_c$ to prevent aliasing (i.e. temporal overlap of high and low frequencies). We may write the complex envelope of the modulated probe pulse as $E_o(t) = E_c(t)e^{i\delta\phi(t)}$. The cycle-averaged signal of probe and reference as recorded by a spectrometer causes interference fringes in the spectral domain, in a process referred to as spectral interferometry (SI).

3.4.5 Holographic phase retrieval algorithm

If the acquired phase modulation is small, $\delta\phi \ll 2\pi$ (as we expect for sensitive detection applications), there are no significant changes in the probe spectrum [78] and we can apply the CSH algorithm to the spectral interferogram $\hat{S}_{CSH}(\Omega) = |\hat{E}_c(\Omega)e^{i\Omega\tau_{pr}} + \hat{E}_{prb}(\Omega)|^2$, where $\Omega = \omega - \omega_1$. Expanding the interferogram yields

$$S_{CSH}(\Omega) = S_c(\Omega) + S_{prb}(\Omega) + K(\Omega) + K^*(\Omega), \tag{3.16}$$

where $S_c(\Omega) = |\hat{E}_c(\Omega)|^2$, $S_{prb}(\Omega) = |\hat{E}_o(\Omega)|^2$, and

$$K(\Omega) = \hat{E}_c^*(\Omega)\hat{E}_{prb}(\Omega)e^{i\Omega\tau_{pr}} \tag{3.17}$$

are the spectra of the chirped reference pulse, the probe pulse, and the CSH sideband, respectively.

An inverse Fourier transform of Eq. (3.16) will produce three time-domain terms. The inverse transforms $\mathfrak{F}^{-1}\{S_{\mathrm{c}}(\Omega)\}$ and $\mathfrak{F}^{-1}\{S_{\mathrm{prb}}(\Omega)\}$ appear centered at zero time, whereas the holographic sideband terms $\mathfrak{F}^{-1}\{K(\Omega)\}$ are centered at $\pm\tau_{\mathrm{pr}}$, so that $K(\Omega)$ may be isolated. Characterization of the chirped pulse spectral phase $\varphi(\Omega) = \angle\hat{E}_{\mathrm{c}}(\Omega)$ then allows us to extract the complex temporal envelope of the probe field by taking the inverse Fourier transform of the ratio $E_{\mathrm{o}}(t-\tau_{\mathrm{pr}}) = \mathfrak{F}^{-1}\{K(\Omega)/\hat{E}^{*}_{\mathrm{c}}(\Omega)\}$. Finally, the phase response response to the ISRS excitation by the pump pulse is given by

$$\delta\phi(t) = \angle E_{\mathrm{o}}(t) - \phi_{\mathrm{c}}(t). \tag{3.18}$$

The temporal evolution $\delta\phi(t)$ is thus encoded in a single spectral interferogram of Eq. (3.16), and can be retrieved for small phase modulations provided that the reference pulse chirp and (complex) envelope are well-characterized.

3.4.6 Experimental results

We demonstrate the technique experimentally by measuring Raman spectra in $Bi_4Ge_3O_{12}$ (BGO12). The experimental arrangement is related to that previously described for our synthetic temporal aperture SI-ISRS experiment [47]. A Ti:sapphire amplifier (KMLabs Dragon) generating 30 fs transform limited pulses at 1 kHz serves as the pump source. A surface reflection from a glass wedge splits off part of the beam, which is further split into probe and reference pulses by propagation in a thick birefringent medium (12˜mm KDP crystal) to yield a probe–reference separation $\tau_{\mathrm{pr}} \approx 3$ ps with high relative stability [55]. The probe and reference pulses are chirped to $\tau_{\mathrm{c}} \approx 2.1$ ps by propagation through 240 mm of BK7 glass and other material dispersion in the probe arm. The probe and reference pulses are overlapped with the pump pulse and focused by a $f = 35$ mm lens in the 0.5 mm thick BGO12 crystal with a non-collinear angle of about 0.5°, chosen to maximize interaction length while allowing spatial discrimination of the pump before the probe and reference pulses are focused into a spectrometer (OceanOptics USB2000).

Although a single interferogram is sufficient to extract the phase modulation $\delta\phi(t)$, we show in Fig. 3.7(a) multiple redundant spectra $S_{\mathrm{CSH}}(\Omega)$ acquired as a function of pump–probe delay τ_{pp} in order to illustrate a few features at various time delays. It will be shown

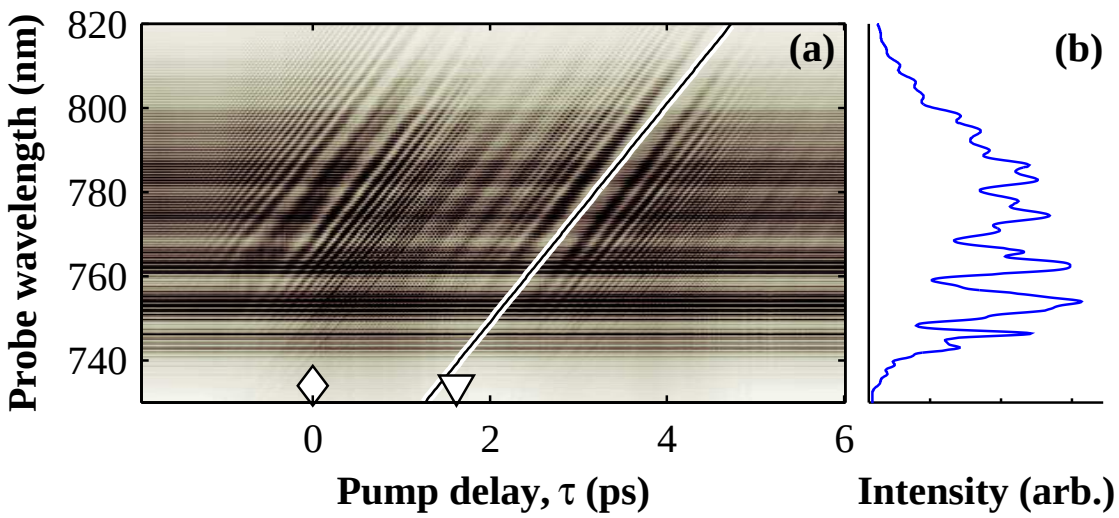

Figure 3.7: (a) Recorded interferograms for a pump delay scan. Black line shows the slope of the phase features used to estimate probe ϕ_c. (b) DC-filtered reference spectrum, equivalent to $|E_c(\omega)|^2$. Delays used for pump XPM (Fig. 3.8) and Raman measurements (Fig. 3.9) are marked with a diamond and triangle, respectively. τ is referenced at 780 nm.

in the next section how this redundancy may be leveraged to improve the SNR of phase-sensitive Raman measurements. The strong modulations due to pump-induced cross-phase modulation (XPM) are clearly visible, and for delays $|\tau_{pp}| > 3$ ps, both probe and reference trail the pump pulse and the modulated reference invalidates the CSH approach. In between, where $0 < \tau_{pp} < \tau_{pr}$, the vibrational signature is present which we can extract by CSH. We observed weaker phase modulations at shorter wavelengths, possibly due to a spatial chirp on the probe pulse causing the pump–probe overlap area to be a function of wavelength.

The slope of the XPM features in Fig. 3.7(a) confirms the probe–reference pair GDD is primarily quadratic, gives an independent measure of the quadratic spectral chirp of the probe and reference pulses, which we estimate from the data to be $\varphi_2 = 13000$ fs^2/rad. We extract the reference pulse spectrum $|\hat{E}_c(\Omega)|$ by applying a low-pass filter to the SI fringes, obviating the need for a separate spectral measurement, as shown in Fig. 3.7(b). The reference field $\hat{E}_c(\Omega)$ can thus be obtained from measured data directly. Processing the spectrogram at delay $\tau_{pp} = 0$ retrieves the phase shift induced due to cross-phase modulation (XPM), proportional to the pump pulse intensity profile. This is shown in Fig. 3.8, along with a comparison to the phase retrieved by standard sideband processing that uses a linear

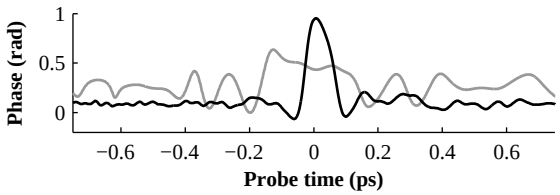

Figure 3.8: Comparison of naïve phase retrieval (gray line) with holographic phase retrieval (black line) of the cross phase modulation features at pump time delay $\tau = 0$.

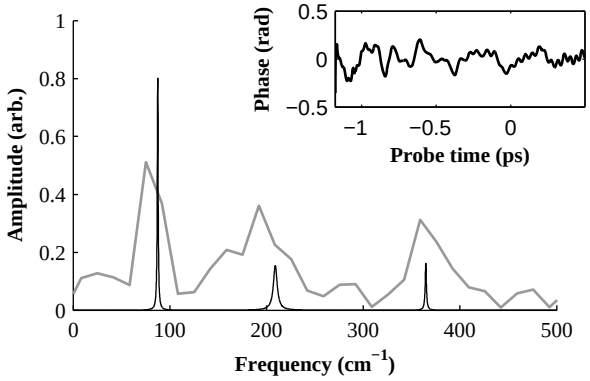

Figure 3.9: Raman spectra obtained from the holographically-retrieved phase measured at delay $\tau = 1.62$ ps by Fourier transformation (gray line) and LP-SVD (black).

frequency-to-time mapping[70].

Based on Fig. 3.7(a), we choose a delay $\tau_{\rm pp} = 1.62$ ps to extract the single-measurement Raman spectrum. The resulting phase $\delta\phi(t)$ in the time domain is shown in the inset to Fig. 3.9. We obtain the Raman vibrational spectrum shown in Fig. 3.9 (gray line) by a Fourier transformation, $I_v(\Omega_v) = \mathfrak{F}\{\delta\phi(t)\}$. The resolution of the vibrational peaks is limited by the chirp and the optical bandwidth of the probe pulses, which in this case limit the temporal window to around 2 ps. We obtained a higher resolution Raman spectrum using a linear prediction singular value decomposition (LP-SVD) [79, 80] (See Appendix C), since we know *ab initio* the exponentially-decaying sinusoidal functional form of the phase modulation for each Raman mode. The LP-SVD results are shown by the black line in Fig. 3.9. The LP-SVD allows a relatively narrow time window ($\tau_{\rm c}$) to extract low-frequency vibrations. The Raman vibrational peaks measured with the CSH are in excellent agreement with those we have measured by other techniques on the same crystal [47, 81].

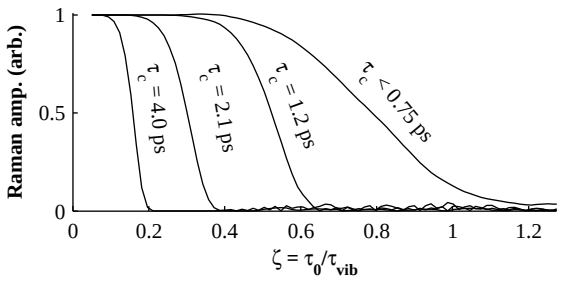

Figure 3.10: Numerical simulation of chirped spectral holography response under various pulse duration conditions. We simulate the response of a fixed vibrational mode Ω_v and vary the transform-limited probe pulse duration τ_0. Each curve shows results for a chirped probe duration τ_c.

3.4.7 Raman frequency sampling limitations

While the lowest resolvable Raman frequency is determined by the temporal duration τ_c of the chirped probe and reference pulses, the high frequency limit depends on the transform-limited duration τ_0. This can be understood intuitively by considering the temporal window must sample at least a full oscillation of low-frequency modes, while the transform-limited probe duration should be shorter than half an oscillation of the high-frequency modes.

Figure 3.10 shows the normalized sensitivity to a Raman mode with periodicity $\tau_{\mathrm{vib}} = 1/\Omega_v$ for various probe chirped durations τ_c and various transform-limited durations. The measurement response was observed to be independent of the probe–reference separation τ_{pr} provided the pulses were adequately separated in time. Each curve shows, for a fixed chirped duration τ_c, how sensitive the measurement is to a particular vibrational mode as the transform-limited duration is varied from 0 to 1.2× the vibrational period. With all four values of τ_c, the best response is given for the shortest transform-limited duration, and the response drops to zero as the τ_0 becomes comparable to τ_{vib}. It is also evident that to acquire longer delay scans with more heavily chirped pulse durations, we require more bandwidth, corresponding to shorter τ_0. From the figure, we expect an upper frequency limit of ~ 440 cm^{-1} for the measurement conditions described here.

3.4.8 Conclusion

In conclusion, we have demonstrated time-domain measurements of coherent Raman vibrational oscillations with chirped spectral holography. CSH recovers the temporal phase due to vibrational quantum beating excited with ISRS and accumulated by a probe pule from a single spectral interferogram when interfered with a reference pulse. Since the temporal evolution of the index perturbation of the sample is recovered, CSH is well suited for measurement of low frequency vibrational modes as in optical Kerr effect (OKE) spectroscopy [43], although OKE is time-consuming since a delay scan is required. Furthermore, a transient birefringence is not required since CSH makes use of spectral holography and directly measures temporal phase acquired by the probe pulse. Since the ISRS excitation occurs with a single pulse, the only phase matching consideration is the relative group velocity of the pump and probe pulses, affording the use of both collinear non-collinear geometries with negligible experimental restrictions. Although the temporal window over which CSH captures temporal phase is limited by the probe-reference pulse chirp, application of a truncated LP-SVD modal spectral analysis retrieves high spectral resolution Raman spectra. CSH is a non-scanning method and allows for rapid acquisition of Raman spectra suitable for femtosecond Raman microscopy [68] and coherent control experiments [82, 83].

3.5 Noise suppression with a chirped-probe Fourier transform method

3.5.1 Introduction

Here, we extend this approach to a highly sensitive interferometric Raman spectroscopy using broad bandwidth probe pulses. The technique attains high Raman spectral sensitivity by isolating Raman spectral lines from the majority of the measurement noise. In the experiment, a broad bandwidth pump pulse with a fast temporal structure excites coherent vibrations, inducing a time-varying perturbation of the optical index of refraction $\delta n_v(t)$ of the sample. Recording the spectrum of a pair of probe and reference pulses separated by a relative time delay τ_{pr} results in interference fringes in the (optical) frequency domain [84], referred to as spectral interferometry (SI). The SI fringes shift by an amount proportional to

the index perturbation for a pair of transform-limited pulses. In STA-SI-ISRS, the transient phase is retrieved from the SI fringes via a standard holography algorithm [54], and a Fourier transform along the pump–probe delay axis $\tau_{\rm pp}$ yields the Raman spectrum [47]. In the complementary approach that we present below, a two-dimensional Fourier transformation of the SI fringes over $\tau_{\rm pp}$ yields peaks corresponding to Raman modes separated from the principal noise components. The vibrational spectrum measured is inherently one-dimensional, but the multiple redundant measurements offer an approach for improved sensitivity. We stress that our technique is not a multi-dimensional spectroscopy; see [85, 86, 87, 88] and references therein.

3.5.2 Theory

A pulse with central frequency ω_1 acquires phase $\phi = \omega_1 nL/c$ on propagating through a medium of length L, where c is the speed of light. The refractive index perturbation of Eq. (2.72) leads to a phase modulation of the probe pulse according to

$$\delta\phi(t) = \sum_v \phi_v \sin \Omega_v t \tag{3.19}$$

with $\phi_v = (\omega_1 L/c)\delta n_v$.

A short, transform-limited probe pulse with a duration $\tau_0 \ll 2\pi/\Omega_v$ can be used to probe the phase modulation at a specific pump–probe delay $\tau_{\rm pp}$. In the experiment, we measure the phase modulation of the probe pulse $E_{\rm o}$ by beating it, in the spectral domain, with an unmodulated reference pulse $E_{\rm r}$ using a technique known as spectral interferometry (SI). The probe pulse $E_{\rm o}(t)$ acquires an additional temporal phase $\varphi(t) = \delta\phi(t + \tau_{\rm pp}) \approx \delta\phi(\tau_{\rm pp})$ due to the induced vibrational motion, which for short probe pulses will be approximately constant across the duration of the pulse. The probe is delayed with respect to the otherwise identical reference, so that we write the probe field as $E_{\rm o}(t) = E_{\rm r}(t + \tau_{\rm pr})e^{-i\delta\phi(\tau_{\rm pp})}$. The (fixed) probe–reference delay $\tau_{\rm pr}$, which is chosen independently of $\tau_{\rm pp}$, causes spectral fringes with periodicity $2\pi/\tau_{\rm pr}$ that are recorded with a spectrometer The spectral domain fields $\hat{E}_j(\omega) = \mathfrak{F}\{E_j(t)\}$ are related to the time domain fields by the Fourier transform denoted by $\mathfrak{F}$. The complex spectrum at delay $\tau_{\rm pp}$ takes the form

$$\hat{E}_{\rm SI}(\omega)_{\tau_{\rm pp}} = \mathfrak{F}\left\{E_{\rm o}(t) + E_{\rm r}(t)\right\} = \hat{E}_{\rm r}(\omega)\left[1 + e^{i\omega\tau_{\rm pr} + \delta\phi(\tau_{\rm pp})}\right]. \tag{3.20}$$

The spectral domain fields $\hat{E}_j(\omega) = \mathfrak{F}\{E_j(t)\}$ are related to the time domain fields by the Fourier transform denoted by $\mathfrak{F}$. By acquiring a multitude of spectra while the pump–probe delay is scanned, the spectrometer measures the set of spectra

$$I_{\mathrm{SI}}(\omega, \tau_{\mathrm{pp}}) = 2I_{\mathrm{r}}(\omega)\left\{1 + \cos\left[\omega\tau_{\mathrm{pr}} + \delta\phi(\tau_{\mathrm{pp}})\right]\right\} \tag{3.21}$$

so that the spectral fringes move as a function of pump–probe delay. Here, $I_{\mathrm{r}} \propto |\hat{E}_{\mathrm{r}}(\omega)|^2$ is the spectrum of the probe pulse. Since the Raman phase $\delta\phi(\tau_{\mathrm{pp}})$ appears in Eq. (3.21) independently of the optical frequency ω, the two-variable distribution $I_{\mathrm{SI}}(\omega, \tau_{\mathrm{pp}})$ contains multiple redundant measurements of $\delta\phi(\tau_{\mathrm{pp}})$, and a pump–probe delay scan at a single, fixed ω is in principle sufficient to measure the Raman spectrum $I_v(\Omega) = |\mathfrak{F}\{\delta\phi(\tau_{\mathrm{pp}})\}|^2$[47].

A two-dimensional Fourier transform over the variables $\omega, \tau_{\mathrm{pp}}$, transforming to conjugate delay t' and vibrational frequency Ω, respectively, will produce Raman *vibrational* sidebands at frequencies $\Omega = \pm\Omega_v$ that appear on top of the SI *delay* sidebands, due to the spectral fringes, at delay time $t' = \pm\tau_{\mathrm{pr}}$ in the 2D spectrum,

$$I_v(t', \Omega) = \int_{-\infty}^{\infty} \mathrm{d}\omega \int_0^T \mathrm{d}\tau_{\mathrm{pp}}\, e^{-i\omega t'} e^{-i\Omega\tau_{\mathrm{pp}}} I_{\mathrm{SI}}(\omega, \tau_{\mathrm{pp}}). \tag{3.22}$$

Under these conditions, the Raman information is difficult to isolate from the noise present in the SI sideband.

The Raman spectral sidebands can be separated from the SI delay sideband by chirping the probe–reference pulse pair. A spectral chirp $\varphi(\omega) = \frac{1}{2}\varphi_2(\omega - \omega_1)^2$ causes a sweep of the instantaneous frequency of the pulse pair. For a large chirp the reference pulse becomes $E_{\mathrm{r}}(t) = A_c(t)e^{i\phi_c(t)}$, where $A_c(t)$ is the temporal magnitude and $\phi_c(t)$ is the temporal phase of the chirped reference and unperturbed probe pulses. The instantaneous frequency difference is $\omega_{\mathrm{inst}}(t) - \omega_1 = \mathrm{d}\phi_c(t)/\mathrm{d}t \approx t/\varphi_2$, which results in a linear sweep of the temporal phase across the probe spectrum [89]. Over a pump–probe delay scan the same phase modulation appears at spectral component ω' at delay $\tau_{\mathrm{pp}} + (\omega' - \omega_1)\varphi_2$. The 2D set of measured spectra $I_{\mathrm{SI}}(\omega, \tau_{\mathrm{pp}})$ includes a cross term of the form $\mathfrak{F}\left\{A_c(t)\exp\left[i(\phi_c(t) + \phi_v \sin\Omega_v[t - \tau_{\mathrm{pp}}])\right]\right\} e^{i\omega\tau_{\mathrm{pr}}}$. Expanding the sinusoidal phase for small ϕ_v as a sum of Bessel functions results in a number of terms of the form

$$I'(t', \Omega) = 2TJ_0(\phi_v)J_1(\phi_v)e^{i\frac{1}{2}\varphi_2\Omega_v^2} e^{-\frac{i}{2}(\Omega \pm \Omega_v)T} \mathrm{sinc}\left[\tfrac{1}{2}\left(\Omega \pm \Omega_v\right)T\right] R\left(t' \mp \varphi_2\Omega_v\right), \tag{3.23}$$

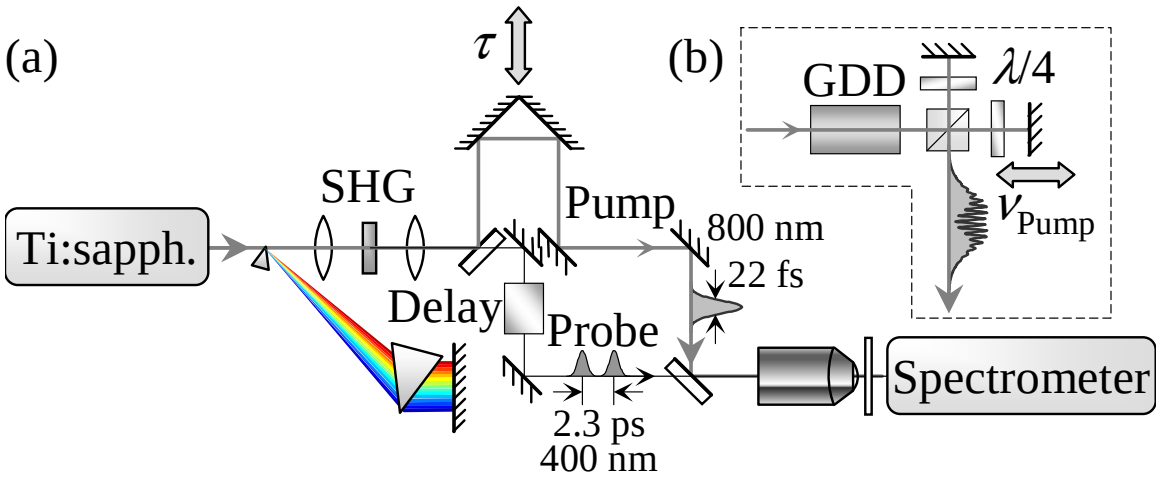

Figure 3.11: Experimental configuration for 2DFFT measurements: (a) ISRS excitation with transform-limited pump pulses and (b) selective excitation via temporal beating in the pump pulse.

where $R(t) = \mathfrak{F}^{-1}\{|U_0(\omega)U_0(\omega - \Omega_v)|\}$ is a time-domain convolution of the original and Raman-shifted probe spectrum, $U_0(\omega) = \mathfrak{F}\{E_r(t)\}$ and T is the total scan length of pump–probe delay τ_{pp}. For a damped sinusoidal vibration with decay rate Γ_v, this calculation could be repeated for each frequency component of the temporal phase oscillation, which will broaden the sideband given above. When $T \gg \Gamma_v^{-1}$, the sinc function negligibly perturbs the true spectral lineshape of the Raman vibrational resonance, and the true Raman lineshape can be measured. For each vibrational mode of the transient phase $\delta\phi(\tau_{pp})$, these terms appear as sidebands at slope φ_2, determined by the chirp of the probe pulses, in a (relatively) background-free area of the 2D spectrum $I_v(t', \Omega)$. An example of the full 2D spectrum is shown in the inset in Fig. 3.12. The vibrational spectrum is obtained by integrating with respect to t', selecting a diagonal boundary over a small range about $t' = \Omega\varphi_2$.

3.5.3 Experiment

We measured 2D Fourier transform femtosecond Raman spectra in a number of molecular solvents and in a $Bi_4Ge_3O_{12}$ (BGO12) crystal. The measurements were performed in the pump –probe configuration sketched in Fig. 3.11(a), employing $\sim$ 22 fs pump pulses from a Ti:sapphire oscillator, centered at 800 nm. A portion of the 3 nJ oscillator pulse

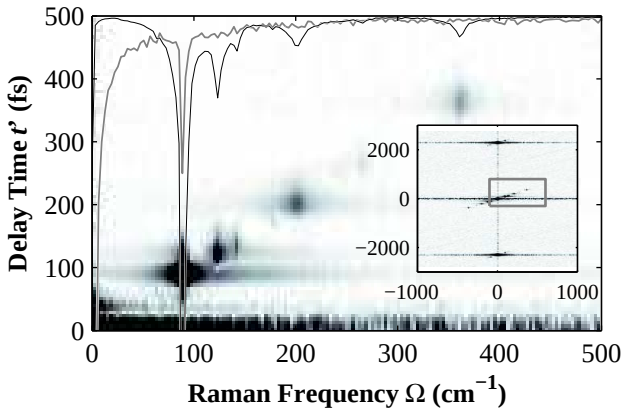

Figure 3.12: 2D-FFT vibrational spectrum measured for BGO12. The chirped probe measurement (black line) measures vibrational obscured in a 1D transform (gray). The inset shows the 2D-FFT of the entire data set with the enlarged area marked.

energy was frequency-doubled in a 100 μm KDP crystal by second-harmonic generation (SHG). Propagating the SHG pulse through a thick birefringent medium generated a pair of orthogonally-polarized, time-delayed probe and reference pulses with exceptional phase stability [55], which resulted in interference fringes on a spectrometer after an analyzing polarizer. The unconverted energy at the fundamental wavelength was separated by a dichroic optic and sent through a delay line to adjust τ_{pp} before recombining with the probe and reference pulses. A prism compressor pre-compensated for the dispersion of a Zeiss Epiplan 50$\times$ 0.50 NA long working distance objective, (GDD measured to be $\sim$ 800 fs^2/rad) and the other optics in the setup. samples were placed at the focal plane of the objective. The probe and reference pulses were recollimated with a 35 mm focal length spherical lens, passed through a BG-39 color glass filter to reject the pump light, and made co-polarized by a polarizer at 45° before being focused into the spectrometer. Near time-zero where the pump pulse overlaps with the probe or reference pulses, cross-phase modulation (XPM) gives rise to spurious phase signatures that must be omitted from the analysis. The SI data were acquired in a synthetic aperture regime [47] where both probe and reference pulses follow the pump. Measuring a 10 ps range in 10 fs steps resulted in a spectral resolution of the Raman spectra of $\sim$ 2 cm^{-1}.

Transformed data for ISRS excitation of phonon oscillations in BGO12 are shown in Fig. 3.12, where the inset shows the full transform including the SI sidebands arising from

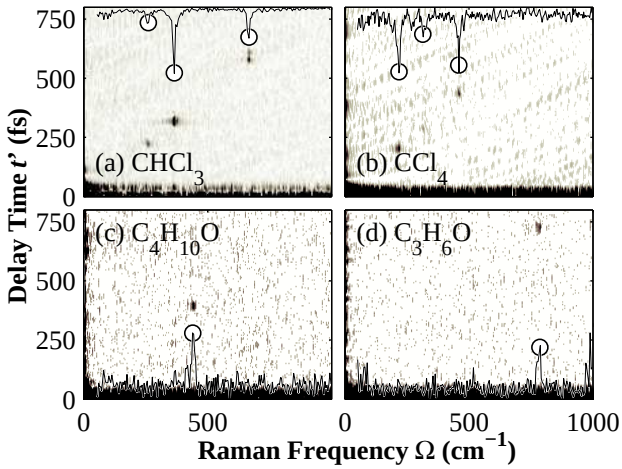

Figure 3.13: 2D-FFT vibrational spectra of liquid phase (a) chloroform, (b) carbon tetrachloride, (c) diethyl ether, and (d) acetone. Circles denote published Raman frequencies [57].

the $\tau_{\mathrm{pr}} = 2.3$ ps probe–reference delay. The enlarged section is indicated by the frame. From the slope of the peaks in (t', Ω)-space, we estimate a probe pulse chirp of $\varphi_2 = -5300$ fs^2/rad. Unlike the chirped spectral holography experiment, the probe–reference chirp arises because the compressor is adjusted to pre-compensate the pump path dispersion for transform-limited pump pulses at the sample, and the disparate dispersions accumulated by the pump and probe pulses.

Summing the transform over a 100 fs wide diagonal band reveals the vibrational spectrum $I_v(\Omega)$ as indicated by the black line. For comparison, the gray line indicates the Raman spectrum obtained by directly transforming the interferogram delay scan along only the τ_{pp} (conjugate Ω) dimension. Only the line near 90 cm^{-1} appears since the remaining lines are weaker than the noise of the temporal sideband, illustrating the improvement in sensitivity afforded by isolating the sideband from the 2D transform noise. The increased sensitivity allowed us to measure the Raman modes of a number of liquid phase samples, as shown in Fig. 3.13. Vibrational frequencies as high as 790 cm^{-1}, limited principally by the optical bandwidth of the pump pulse, were measured in acetone, carbon tetrachloride, chloroform, and diethyl ether. In each solvent, we found excellent agreement between the measured and previously published mode frequencies [57].

3.5.4 Selective ISRS pumping with pulse trains

A pulse train with a regular, periodic spacing may be used to selectively excite vibrational modes via ISRS. Two methods of producing such pulse trains are discussed here. The first, application of sinusoidal spectral phase, is shown only in the theoretical discussion to demonstrate how a pulse train can selectively excite vibrations. The second, by mixing two time-delayed chirped pulses, is shown in experiment to selectively excite modes in BGO12.

As a theoretical example, a pulse train is readily producible by use of a pulse shaper to apply a sinusoidal spectral phase mask. The phase modulation is applied to produce the following pump field in the frequency domain as such:

$$E(\omega)_{\sin} = E(\omega)E^{iA\sin(\frac{2\pi}{\tau<}\omega)}, \tag{3.24}$$

where A is the amplitude of the phase modulation and τ is period. This modulation produces a pulse train in the time domain, where the peaks are spaced by τ. If the pulse duration τ_{p} is not short enough, the peaks will be poorly resolved, so it may be convenient to use even multiples of the resonant frequency of the vibrations to produce clean pulse trains for excitation. Fig. 3.14 shows the spectral overlap of these pulse trains with the vibrational frequency response. Here we show two cases, one where τ is an even multiple of the Ω_v (on-resonance), another where τ is a fractional multiple of Ω_v (off-resonance), and we also include the transform-limited pulse (flat phase) for comparison. Note that for the on-resonance case, $|D(\Omega)|$ is nearly as large as the transform-limited pulse in proximity to Ω_v. On the other hand, the off-resonance $|D(\Omega)|$, while having large amplitudes at other frequencies, is rather small near Ω_v, effectively suppressing the excitation of vibrations. The effect is better illustrated in the time domain. Fig. 3.15 demonstrates the molecular displacement that results from a pulse train spaced at twice the resonant period. Each pulse in the train is timed just right to reinforce the movement of the vibrations. Compare this with Fig. 3.16, where the overall effect is vibrational suppression: the individual pulses are timed to work against the vibrations.

Another method of producing resonant pulse trains for selective ISRS excitation, which does not involve a pulse shaper, is described below. In either case , the selective nature of

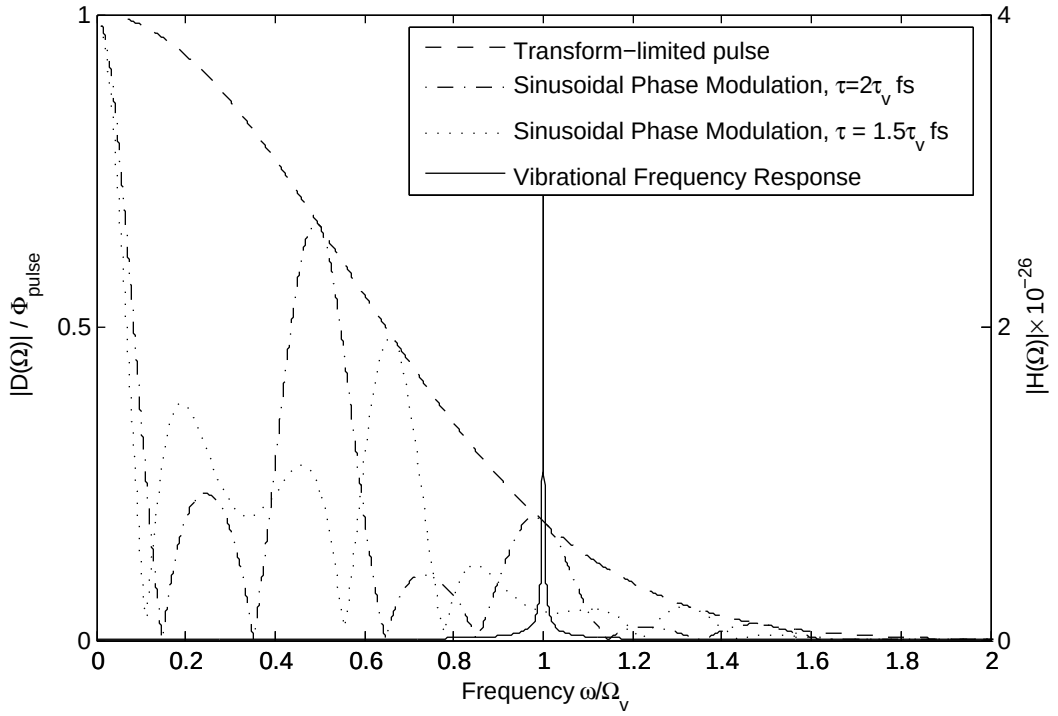

Figure 3.14: Frequency response of molecular vibrations overlapped with spectral intensity of pump pulses that have sinusoidal spectral phase, both on- and off-resonance with the vibrations.

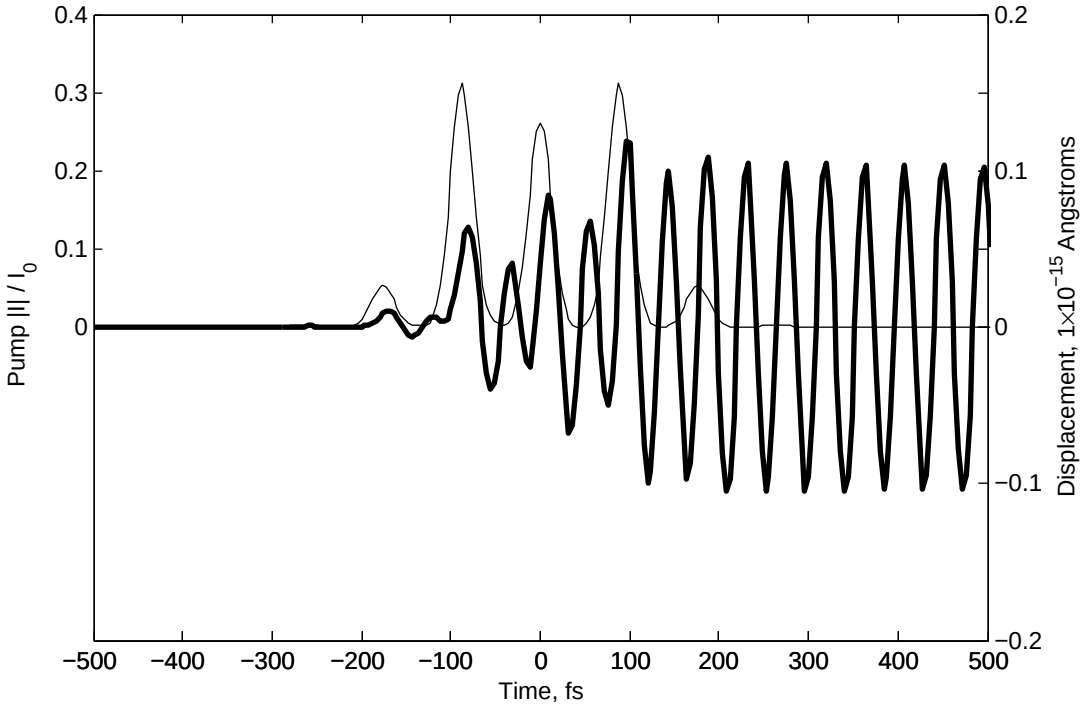

Figure 3.15: Time-domain illustration of on-resonance pulse train pumping.

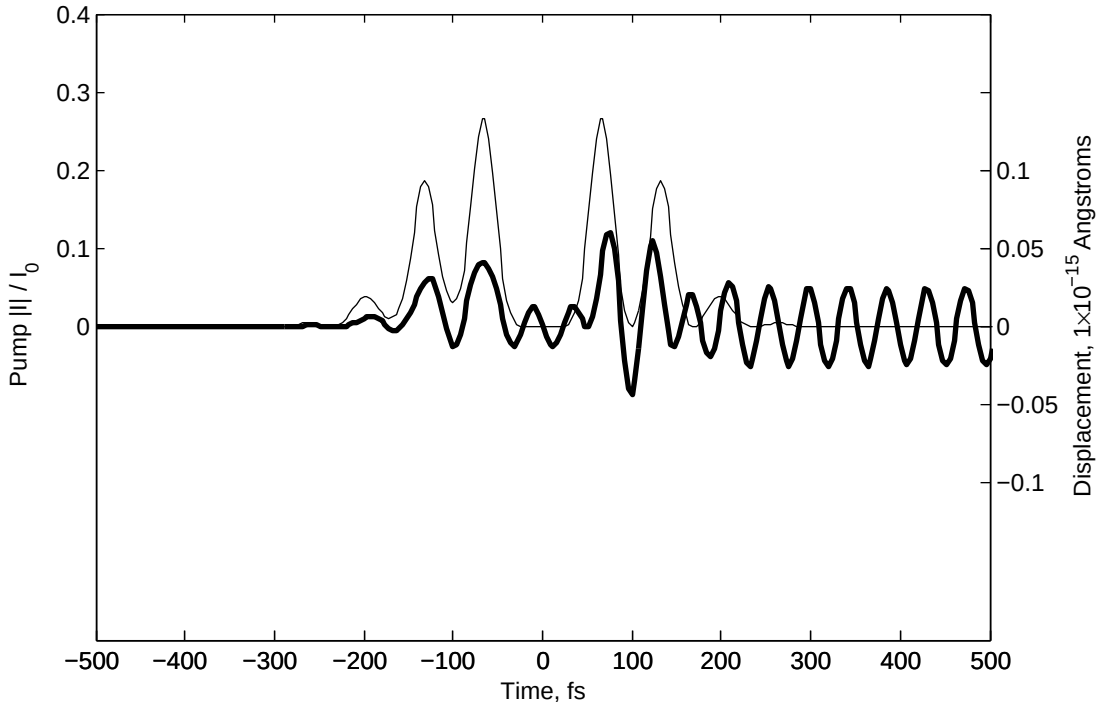

Figure 3.16: Time-domain illustration of off-resonance pulse train pumping. Vibrations are still excited, but with significantly less amplitude than the resonant case.

the excitation from a resonant pulse train still applies.

3.5.5 Selective ISRS experiment

To verify that the sidebands appearing in the 2D Fourier transform of the interferograms are due to ISRS, we selectively excite each of the observed Raman modes in BGO12 by making use of temporal beating from two strongly-chirped pump pulses [61] with the experimental setup of Fig. 3.11(b). The combination of two pump pulses with large chirp φ_p separated by τ_p gives rise to a beat frequency $\Omega_{\text{beat}} = \tau_p/\varphi_p$. Since ISRS is effectively driven by the intensity profile of the driving pulse [61, 60], the chirped pump pulse pair serves as an effective ISRS source term with a Raman excitation spectral resolution that is inversely proportional to the chirped pulse duration [61]. For selective excitation, we replaced the prism compressor in the pump arm by a double-passed a BK7 rod. A Michelson interferometer, comprising a polarizing beam splitter cube, two quarter-wave plates, and an output polarizer, resulted in a co-polarized chirped pump pulse pair with an adjustable relative delay.

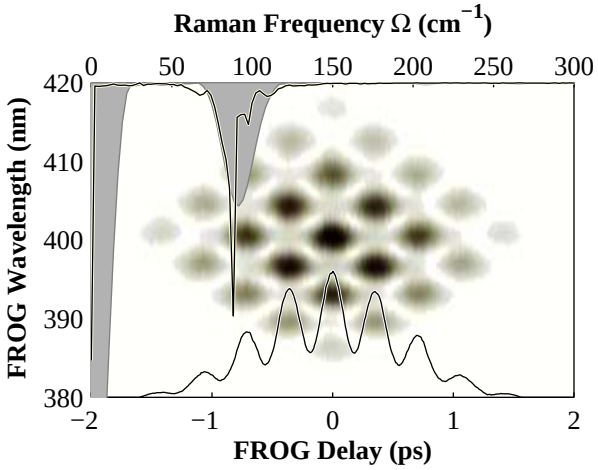

Figure 3.17: Pump characterization for resonant pulse train selective excitation of the 90 cm^{-1} mode in BGO12. The autocorrelation (bottom) is the temporal residue of the FROG trace (image), while the Fourier transform of the autocorrelation (shaded) and excited Raman mode (solid line) are shown on the upper axis.

SHG FROG measurements [90] of the pump pulses showed that the $\sim$ 22fs transform limited pulses were stretched to about 1 ps. Due to the large time–bandwidth product arising from a spectral phase that is anticipated to be primarily quadratic, we fitted a fourth-order polynomial spectral phase to the measured FROG traces in lieu of a standard FROG reconstruction [91]. From this technique, we estimate the pump pulse GDD to be approximately 8000 fs^2/rad. The temporal residue of the FROG trace, which corresponds to the pulse autocorrelation [90], exhibited periodic intensity modulations with the same periodicity as the pump pulse beating $2\pi/\Omega_{\text{beat}}$, so that the ISRS pump excitation frequency Ω_{beat} could be determined by a Fourier transformation of the temporal residue. A pump pulse measurement exciting the 90 cm^{-1} mode is shown in Fig. 3.17. The tuning rate of the pump resonance beat frequency with Michelson arm displacement was measured to be $\kappa_p = 4.5$ cm$^{-1}/\mu$m, from which we can estimate a pump pulse chirp of $\varphi_p = 1/\pi c\kappa_p = 7800$ fs^2/rad, in good agreement with the FROG trace fit.

The reduced pump pulse peak intensity required tighter focusing, which was achieved with a Zeiss Achroplan 63 $\times$ 0.80 NA objective. Delay scans with a probe–reference separation of $\tau_{\text{pr}} = 1.1$ ps were recorded for a 14 ps pump–probe delay range in 7 fs steps. Results for Raman spectra obtained with a 2D transform of the scanned SI data for 25

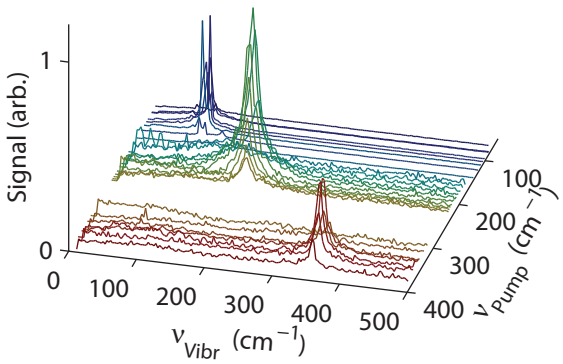

Figure 3.18: Selectively excited Raman signals measured for varying pump beating frequency in BGO12. Measurements for frequencies > 150 cm^{-1} have been scaled $10\times$.

scans with a pump excitation frequency ranging from over $\Omega_{\text{beat}}/2\pi = 30 - -400$ cm^{-1} are shown in Fig. 3.18. The traces for $\Omega_{\text{beat}}/2\pi > 150$ cm^{-1} have been magnified $10\times$ to better show the weaker modes. From the data, the selective excitation is clearly evident, as modes with frequencies $\Omega_v/2\pi \approx 90, 210$, and 360 cm^{-1}, equivalent to the ISRS spectrum shown in Fig. 3.12, are sequentially excited. In processing the data, care is taken to exclude XPM due to pump–probe temporal overlap from the 2D FFT. Since the XPM signature has the same frequency as a vibrational mode, it could falsely contribute to the vibrational measurement; tuning the pump beat frequency off vibrational resonances and observing the signal going to zero confirms that the data in Fig. 3.18 are purely due to ISRS-excited vibrational modes.

3.5.6 Summary

In summary, we have demonstrated an easy-to-implement, sensitive interferometric Raman spectroscopy by performing a two-dimensional Fourier transform of interference fringes measured in a pump–probe geometry. By stretching the probe and reference pulses with quadratic spectral phase, we isolate the vibrational signature from noise. We have demonstrated its utility in BGO12, measuring modes at 90, 210, and 360 cm^{-1}, and in several molecular liquids. Selective excitation of these modes was achieved by beating two stretched, time-delayed pump pulses in resonance with the selected mode. The improved sensitivity over analogous measurements with transform-limited pulses allows for unamplified oscillator pulses to be used, paving the way for vibrational specificity in microspectroscopy.

3.6 Fresnel modulation at a boundary

The index modulation at a material interface will modulate Fresnel transmission and reflection coefficients. We describe theory and refer to other work in this section. We will show in the second part of this dissertation how Fresnel modulation affects THG, making this chapter a segue-way to Part II. We will also briefly discuss here interface-specificity of Fresnel.

It has been shown that coherent phonon oscillations at the surface modulate the Fresnel transmission of a probe pulse in a manner distinguishable from bulk modulations by observing a phase shift in time-resolved signal [92]. In spite of the abundant techniques examining modulations of reflections, little has been done to examine the complementary effect of modulation of transmission at a boundary.

3.6.1 Fresnel coefficients of reflection and transmission

The perturbation to the optical susceptibility perturbs the Fresnel reflection and transmission coefficients. Noting that the optical (linear) susceptibility is given by

$$\chi^{(1)} = \chi_0^{(1)} + \delta\chi_0^{(1)}|U_s(x,y,z)|^2 \sin[\Omega_v(t+\tau-u_{\mathrm{p}}^{-1}z)] \equiv \chi_0^{(1)} + \delta\chi \tag{3.25}$$

The Fresnel reflection and transmission coefficients are derived for plane wave and come about from matching boundary conditions (and thus no temporal derivatives appear as is the case for source term). Note that $n^2 = \epsilon = \epsilon_0\left[1+\chi^{(1)}\right]$, and recalling the Fresnel coefficient for s

$$r_s = \frac{n_i\cos\theta_i - n_t\cos\theta_t}{n_i\cos\theta_i + n_t\cos\theta_t} = \frac{n_i\cos\theta_i - \sqrt{n_t^2 - n_i^2\sin^2\theta_i}}{n_i\cos\theta_i + \sqrt{n_t^2 - n_i^2\sin^2\theta_i}} \tag{3.26}$$

$$t_s = \frac{2n_t\cos\theta_i}{n_i\cos\theta_i + n_t\cos\theta_t} = \frac{2n_i\cos\theta_i}{n_i\cos\theta_i + \sqrt{n_t^2 - n_i^2\sin^2\theta_i}} \tag{3.27}$$

and p polarizations

$$r_p = \frac{-n_t\cos\theta_i + n_i\cos\theta_t}{n_t\cos\theta_i + n_i\cos\theta_t} = \frac{-n_t\cos\theta_i + n_i\sqrt{1-\frac{n_i^2}{n_t^2}\sin^2\theta_i}}{n_t\cos\theta_i + n_i\sqrt{1-\frac{n_i^2}{n_t^2}\sin^2\theta_i}} \tag{3.28}$$

$$t_p = \frac{2n_t \cos\theta_i}{n_t \cos\theta_i + n_i \cos\theta_t} = \frac{2n_i \cos\theta_i}{n_t \cos\theta_i + n_i \sqrt{1 - \frac{n_i^2}{n_t^2} \sin^2\theta_i}} \tag{3.29}$$

respectively and where θ_i is the incident angle and θ_t is the transmitted angle.

3.6.2 At the entrance face of a sample

The change in the the reflection or transmission coefficient is given approximately by

$$\delta R \approx \frac{\partial R}{\partial n} \delta n$$

Let's compute the derivatives of the Fresnel coefficient for s

$$\frac{\partial R_s}{\partial n_t} = -\frac{n_t(1 + R_s)}{n_t^2 - n_i^2 \sin^2\theta_i + n_i \cos\theta_i \sqrt{n_t^2 - n_i^2 \sin^2\theta_i}} \tag{3.30}$$

So that the perturbed reflection coefficient, as a function of the index perturbation, becomes

$$R_s(\delta n_t) = R_s - \left(\frac{n_t(1 + R_s)}{n_t^2 - n_i^2 \sin^2\theta_i + n_i \cos\theta_i \sqrt{n_t^2 - n_i^2 \sin^2\theta_i}} \right) \delta n_t \tag{3.31}$$

and for transmission,

$$\frac{\partial T_s}{\partial n_t} = -\frac{n_t T_s}{n_t^2 - n_i^2 \sin^2\theta_i + n_i \cos\theta_i \sqrt{n_t^2 - n_i^2 \sin^2\theta_i}} \tag{3.32}$$

So that the perturbed transmission coefficient becomes

$$T_s(\delta n_t) = T_s - \left(\frac{n_t T_s}{n_t^2 - n_i^2 \sin^2\theta_i + n_i \cos\theta_i \sqrt{n_t^2 - n_i^2 \sin^2\theta_i}} \right) \delta n_t \tag{3.33}$$

and p polarizations

$$\frac{\partial R_p}{\partial n_t} = \frac{n_i^3 \sin^2\theta_i - n_t^2 \cos\theta_i \sqrt{n_t^2 - n_i^2 \sin^2\theta_i}}{n_i n_t^3 - n_i^3 n_t \sin^2\theta_i + n_t^3 \cos\theta_i \sqrt{n_t^2 - n_i^2 \sin^2\theta_i}} \times \left(\left[\frac{n_i^3 \sin^2\theta_i + n_t^2 \cos\theta_i \sqrt{n_t^2 - n_i^2 \sin^2\theta_i}}{n_i^3 \sin^2\theta_i - n_t^2 \cos\theta_i \sqrt{n_t^2 - n_i^2 \sin^2\theta_i}} \right] - R_p \right) \tag{3.34}$$

$$\frac{\partial T_p}{\partial n_t} = -\frac{n_i^3 \sin^2\theta_i + n_t^2 \cos\theta_i \sqrt{n_t^2 - n_i^2 \sin^2\theta_i}}{n_i n_t^3 - n_i^3 n_t \sin^2\theta_i + n_t^3 \cos\theta_i \sqrt{n_t^2 - n_i^2 \sin^2\theta_i}} T_p \tag{3.35}$$

respectively.

3.6.3 Normal incidence

The Fresnel equations are greatly simplified by assuming normal incidence. At normal incidence, the unperturbed reflection coefficient is

$$R_0 = \frac{n_i - n_t}{n_i + n_t}, \tag{3.36}$$

and the unperturbed transmission coefficient is

$$T_0 = \frac{2n_t}{n_i + n_t}, \tag{3.37}$$

where the incident refractive index is n_i and the index on the transmitted side of the boundary is n_t.

3.6.3.1 Entrance face

At the entrance face of an air/crystal interface, We express the perturbation to the normal incidence as a first-order Taylor series expansion. For reflection, $R(t) = R_0 + (\mathrm{d}R/\mathrm{dn_t})\delta n(t)$. The variation of the reflection with a perturbation is

$$\frac{\partial R}{\partial n_c} = -\frac{1}{n_a + n_c}\left(1 + \frac{n_a - n_c}{n_a + n_c}\right) = -\frac{2n_a}{(n_a + n_c)^2} \tag{3.38}$$

At the entrance face, we take the crystal index as $n_t = n_c$ and the surrounding medium (air) as $n_i = n_a$, and the index perturbation is

$$\delta n = \frac{\delta\chi_0^{(1)}}{2n_c}|U_s(x,y,z)|^2 \sin[\Omega_v(t + \tau - u_{\mathrm{p}}^{-1}z)] \tag{3.39}$$

so we write the full expression

$$R(t) = R_0 + \delta R(t), \tag{3.40}$$

where

$$\begin{aligned}\delta R(t) &= \frac{\partial R}{\partial n_t}\delta n(t) \\ &= -\left(\frac{n_a}{n_c(n_a + n_c)^2}\right)\delta\chi_0^{(1)}\,|U_s(x,y,z)|^2 \sin\left[\Omega_v\left(t + \tau - u_{\mathrm{pu}}^{-1}z\right)\right]\end{aligned} \tag{3.41}$$

Similarly, the variation of the transmission coefficient with the perturbation is

$$\frac{\partial T}{\partial n_c} = \frac{2}{n_a + n_c} - \frac{2n_c}{(n_a + n_c)^2} = \frac{2n_a}{(n_a + n_c)^2} = -\frac{\partial R}{\partial n_c}, \tag{3.42}$$

which is expected, since

$$(T + \delta T) = 1 - (R + \delta R) \Rightarrow \delta T = -\delta R \tag{3.43}$$

Therefore the transmission coefficient is

$$T(t) = T_0 + \delta T(t) \tag{3.44}$$

where

$$\begin{aligned} \delta T(t) &= \frac{\partial T}{\partial n_t} \delta n(t) = -\delta R(t) \\ &= \left(\frac{n_a}{n_c (n_a + n_c)^2} \right) \delta \chi_0^{(1)} \left| U_s(x, y, z) \right|^2 \sin \left[\Omega_v \left(t + \tau - u_{\text{pu}}^{-1} z \right) \right] \\ &= \delta T \ \widetilde{\delta \chi}^{(1)}, \end{aligned} \tag{3.45}$$

where

$$\delta T = \frac{n_a}{n_c (n_a + n_c)^2}. \tag{3.46}$$

The resulting perturbation the transmission coefficient through the entrance face is simply the first-order susceptibility perturbation multiplied by a coefficient that depends on the refractive indices at either side of the interface.

3.6.3.2 Exit face

At the exit face of a crystal, we study light propagating from the crystal interior to air. The method is similar to the entrance face, taking derivatives wrt n_c except this time $n_i = n_c$ and $n_t = n_a$.

The variation of reflection with the perturbation is

$$\frac{\partial R}{\partial n_c} = \frac{2 n_a}{(n_a + n_c)^2} \tag{3.47}$$

and the time-dependent perturbation of the reflection coefficient is

$$\delta R(t) = \left(\frac{n_a}{n_c (n_a + n_c)^2} \right) \delta \chi_0^{(1)} \left| U_s(x, y, z) \right|^2 \sin \left[\Omega_v \left(t + \tau - u_{\text{pu}}^{-1} z \right) \right]. \tag{3.48}$$

The variation of transmission with the perturbation is

$$\frac{\partial T}{\partial n_c} = -\frac{2 n_a}{(n_a + n_c)^2} \tag{3.49}$$

and the time-dependent perturbation of the transmission coefficient is

$$\begin{aligned}\widetilde{\delta T} &= -\left(\frac{n_a}{n_c(n_a+n_c)^2}\right)\delta\chi_0^{(1)}\left|U_s(x,y,z)\right|^2\sin\left[\Omega_v\left(t+\tau-u_{\mathrm{pu}}^{-1}z\right)\right] \\ &= -\delta T\ \widetilde{\delta\chi}^{(1)}.\end{aligned} \tag{3.50}$$

The result for exit face transmission is the same as for the entrance face except for a minus sign. The sign flip manifests itself as a π phase delay shift between bulk modulation and exit-face interface modulation [92].

3.6.4 Perturbations at the exit face

Upon exiting a crystal it, the incident index is perturbed analogously to the transmitted above so that $n_i = n_{i0} + \Delta n$. Let's compute the derivatives of the Fresnel coefficient for s

$$\begin{aligned}\frac{\partial R_s}{\partial n_i} = &\frac{n_i\sin^2\theta_i - \cos\theta_i\sqrt{n_t^2 - n_i^2\sin^2\theta_i}}{n_t^2 - n_i^2\sin^2\theta_i + n_i\cos\theta_i\sqrt{n_t^2 - n_i^2\sin^2\theta_i}} \\ &\times\left(\left[\frac{-n_i\sin^2\theta_i - \cos\theta_i\sqrt{n_t^2 - n_i^2\sin^2\theta_i}}{n_i\sin^2\theta_i - \cos\theta_i\sqrt{n_t^2 - n_i^2\sin^2\theta_i}}\right] - R_s\right)\end{aligned} \tag{3.51}$$

and

$$\frac{\partial T_s}{\partial n_i} = \frac{2\cos\theta_i}{n_i\cos\theta_i + \sqrt{n_t^2 - n_i^2\sin^2\theta_i}}\left(1 - \left[\frac{1}{2} - \frac{n_i\sin^2\theta_i}{2\cos\theta_i\sqrt{n_t^2 - n_i^2\sin^2\theta_i}}\right]T_s\right) \tag{3.52}$$

and p polarizations

$$\frac{\partial R_p}{\partial n_i} = \frac{n_t^2 - 2n_i^2\sin^2\theta_i}{n_i n_t^2 - n_i^3\sin^2\theta_i + n_t^2\cos\theta_i\sqrt{n_t^2 - n_i^2\sin^2\theta_i}}\left(1 - R_p\right) \tag{3.53}$$

$$\frac{\partial T_p}{\partial n_i} = \frac{2n_t\cos\theta_i}{n_t^2\cos\theta_i + n_i\sqrt{n_t^2 - n_i^2\sin^2\theta_i}}\left(1 - \left[\frac{n_t^2 - 2n_i^2\sin^2\theta_i}{2n_t\cos\theta_i\sqrt{n_t^2 - n_i^2\sin^2\theta_i}}\right]T_p\right) \tag{3.54}$$

respectively.

3.6.5 Discussion

Linear optical surface techniques measure subtle changes in reflection due to surface phenomena [16, 1]. But material below the surface also scatters light, leading to surface-bulk

ambiguity. Various methods aimed at isolating surface reflections from bulk scattering include reflection difference spectroscopy, reflection anisotropy, ellipsometry, and 45-degree reflectometry [20, 21]. It has been shown that coherent phonon oscillations at the surface modulate the Fresnel transmission of a probe pulse in a manner distinguishable from bulk modulations by observing a phase shift in time-resolved signal [92]. In spite of the abundant techniques examining modulations of reflections, little has been done to examine the complementary effect of modulation of transmission at a boundary.

Fresnel transmission modulation at the exit face of a sample shows a distinct phase shift from bulk modulation. We will show how this contributes to modulation of third harmonic in the next part of this dissertation.

PART II

Effective third-order modulation

CHAPTER IV

COHERENCE-MODULATED THG FOR VIBRATIONAL RAMAN SPECTROSCOPY

4.1 Introduction

We probe vibrational coherences (VC), prepared via non-resonant impulsive stimulated Raman scattering (ISRS) [19], both at and near a crystal–air interface. We introduce a method called coherence-modulated third harmonic generation (CM-THG) where the influence of vibrations on probe pulse propagation and TH generation are observed. The measurements are performed with noncentrosymmetric crystals with a nonzero even-order nonlinear response in bulk, making surface-specific even-order measurements difficult to obtain.

Three distinct 6-wave mixing pathways contribute to the CM-THG signal: coherent second hyper-Raman scattering (CSHRS), cascaded amplitude modulations in the bulk, and Fresnel boundary modulations at the interface.

It is shown here that heterodyning with the unmodulated TH signal enables measurement of this weak phenomenon. This method provides complementary information to that obtained by second-order spectroscopies.

Unlike even-order surface spectroscopies, surface specificity in this work is made possible by the Fresnel modulated term, and occurs regardless of bulk symmetry. In addition, we can simultaneously acquire both surface and bulk information and separate the two. CM-THG may be applicable to circumstances where second-order processes may not be appropriate, such as when selection rules prevent measurement by a second-order processes, or when examining anisotropic media, where a strong second-order bulk signal would overwhelm the surface signal.

In contrast to even-order interactions, odd-order nonlinear interactions occur regardless

of media symmetry. For a tightly focused laser beam in a uniform medium, the third harmonic (TH) generated on opposite sides of the focal plane interfere destructively and cancel due to the Gouy phase shift. At an interface, the discontinuity in the third-order susceptibility $\chi^{(3)}$ breaks the symmetry about the focal plane, partially preventing the destructive interference and giving rise to an interface-sensitive TH signal [36]. Though the harmonic is generated in the bulk, the overall signal can be interface-sensitive [38].

The CM-THG experiment is depicted in Fig. 4.1. An ultrafast pulse is split into time-delayed pump and probe pair. The pump sets up a vibrational coherence in the sample, and the probe generates third harmonic, which is modulated by the coherence. Interface scans, sometimes referred to as z-scans [38] are central to the ability to separate bulk and interface contributions. This method involves translating the interface across the focal plane, and recording a pump–probe delay scan at each point. This is not to be confused with the z-scan method of measuring nonlinear optical coefficients [93].

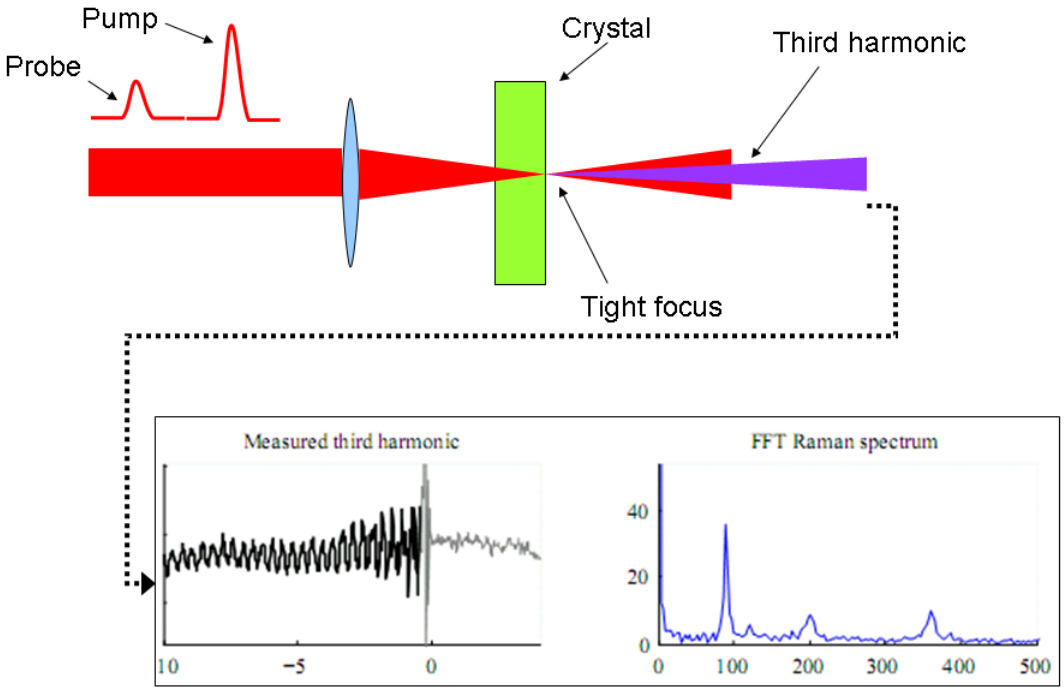

Figure 4.1: Basic coherence-modulated third harmonic generation experiment.

The remainder of this chapter will describe a theoretical model, while the following chapter will present experimental results. The model will be constructed in such a way as to show the distinct interface scan behavior of each of the signal contributions, CSHRS, cascade, and Fresnel modulations.

4.2 THG at an interface

We begin by looking at phase-matched THG of a focused CW Gaussian beam across an interface, without a vibrational coherence. This section will show the interface scan produces a maximum THG intensity when the interface is coincident with the focal plane of the beam. The interface scan profile has a Lorentzian shape with a FWHM equal to the confocal parameter, $b = 2z_R$.

4.2.1 Third harmonic generation and propagation equations

We consider a fundamental beam incident on the nonlinear medium beginning at z_0, with a waist located at z_w, written in the spatial frequency domain

$$\hat{E}_{\mathrm{o}}(k_x, k_y, z, t_{\mathrm{o}}) = E_{0,\mathrm{o}}(t_{\mathrm{o}}) \frac{w_{10}^2}{4\pi} \left\{ -(k_x^2 + k_y^2) \left[\frac{w_{10}^2}{4} - i \frac{z_w}{2k_1} \right] \right\}, \tag{4.1}$$

where $E_{0,\mathrm{o}}$ is the slowly varying temporal envelope of the probe field, presumed to be a transform-limited Gaussian here:

$$E_{0,\mathrm{o}}(t_{\mathrm{o}}) = E_{0,\mathrm{o}} e^{-a t_{\mathrm{o}}^2}. \tag{4.2}$$

We start with the equation for propagation of an ultrafast pulse in the spatial frequency domain, Eq. (A.37), and substitute the third harmonic driving term for the additional polarization $p^A \rightarrow p^{\mathrm{THG}}$ The third harmonic polarization behind ordinary third harmonic generation is given by

$$p^{\mathrm{THG}}(\mathbf{r}, t) = \frac{1}{4} \epsilon_0 \chi_0^{(3)} E_1^3(\mathbf{r}, t) e^{-i\Delta k z}, \tag{4.3}$$

where the phase mismatch between the fundamental and third harmonic is represented by $\Delta k = 3k_1 - k_3$. Neglecting group velocity mismatch between the fundamental and third harmonic, we write the equation describing evolution of the third harmonic, in the traveling

frame of the third harmonic pulse, as

$$\frac{\partial}{\partial\zeta}\hat{E}_{3\mathrm{o}}(\zeta,k_x,k_y,t_{3\mathrm{o}}) = i\frac{\omega_3 w_{10}^2}{24cn_3}\chi^{(3)}\frac{E_{0,\mathrm{o}}^3(t_{3\mathrm{o}})}{(4\pi)^3A_1^2(\zeta)}\exp\left\{-(k_x^2+k_y^2)\frac{w_{10}^2A_1(\zeta)}{12}\right\}e^{-i\Delta k\zeta} - i\frac{k_x^2+k_y^2}{2k_3}\hat{E}_{3\mathrm{o}}, \quad (4.4)$$

where we have defined

$$A_1(\zeta) = 1 + i\frac{2(\zeta - z_w)}{w_{10}^2k_1} \quad (4.5)$$

We introduce a trial solution for $\hat{E}_{3\mathrm{o}}$ in the form of a Gaussian beam with a propagation-dependent amplitude and phase $E_{0,\mathrm{o},3}(\zeta,t)$

$$\hat{E}_{3\mathrm{o}} = E_{0,3\mathrm{p}}(\zeta)\frac{w_{30}^2}{4\pi}\exp\left\{-(k_x^2+k_y^2)\frac{w_{30}^2A_3(\zeta)}{4}\right\}, \quad (4.6)$$

where $A_3(\zeta)$ is similarly defined to $A_1(\zeta)$ as in Eq. (4.136). We compute the derivative of Eq. (4.137), insert it into Eq. (4.135), and combine terms to arrive at an expression for the third harmonic amplitude and phase evolution, $E_{0,\mathrm{o},3}$, as a function of propagation

$$\frac{\partial}{\partial\zeta}E_{0,3\mathrm{p}}(\zeta,t_{3\mathrm{o}}) = i\frac{\pi\omega_3 w_{10}^2}{6cn_3w_{30}^2}\chi_0^{(3)}\frac{E_{0,\mathrm{o}}^3(t_{3\mathrm{o}})}{(4\pi)^3A_1^2(\zeta)}e^{-i\Delta k\zeta}. \quad (4.7)$$

This result should be roughly equivalent to Eq.(2.10.10) in Ref.[39]. Here we have assumed that the fundamental and TH spot sizes are fixed, $w_{10}^2 = 3w_{30}^2$, the beams are confocal (z_w is the same for both fundamental an TH), and we may neglect spatially non-Gaussian features [94]

$$\frac{1}{3k_1} - \frac{1}{k_3} = \frac{k_3 - 3k_1}{3k_1k_3} \approx 0. \quad (4.8)$$

To find the TH generated, we must integrate Eq. (4.138)

$$E_{0,3\mathrm{p}}(\zeta,t_{3\mathrm{o}}) = i\frac{\pi\omega_3 w_{10}^2}{6cn_3w_{30}^2(4\pi)^3}\chi_0^{(3)}\int\frac{E_{0,\mathrm{o}}^3(t_{3\mathrm{o}})}{A_1^2(\zeta')}e^{-i\Delta k\zeta'}\mathrm{d}\zeta'. \quad (4.9)$$

Here we have neglected group velocity mismatch, and will deal with it only briefly at the end of this chapter.

Eq. (4.140) is also expressed in terms of a J-integral,

$$E_{0,3\mathrm{p}}(\zeta,t_{3\mathrm{o}}) = i\frac{K}{n}\chi_0^{(3)}E_{0,\mathrm{o}}^3(t_{3\mathrm{o}}), \quad (4.10)$$

where the constant coefficients have been grouped into K/n and

$$J_3(\Delta k, z_0, z) = \int \frac{e^{-i\Delta k\zeta'}}{A_1^2(\zeta')}\mathrm{d}\zeta' = \int_{z_0}^{z} \frac{e^{i\Delta k z'}\mathrm{d}z'}{(1+2iz'/b)^2}, \tag{4.11}$$

expressed in terms of the confocal parameter $b = 2z_R$.

4.3 Solution for Phase-matched interface scan

For the phase-matched CW case, the J-integral reduces to:

$$J(\Delta k, z_0, z) = \int_{z_0}^{z} \frac{1}{(1+2iz'/b)^2}\mathrm{d}z. \tag{4.12}$$

For perfect phase matching in a homogeneous medium, that is $\Delta k = 0$, the result is $J_3 = 0$, and no net third harmonic is generated for the bounds $\int_{-\infty}^{\infty}$.

When an interface is placed at z_i, with material A on the left and B on the right, the integral must be performed separately for each material. Neglecting Fresnel reflection losses at the interface, the total far-field third harmonic is the sum of that which is generated on either side of the interface:

$$E_3(z=\infty) = \frac{K}{n_A}\chi_{\mathrm{A}}^{(3)}E_1^3 J_3(0,-\infty,z_i) + \frac{K}{n_B}\chi_{\mathrm{B}}^{(3)}E_1^3 J_3(0,z_i,+\infty)$$

For completeness we should consider Fresnel losses at the interface. But we'll include that later in the treatment of coherence-modulated THG.

This may be solved analytically for $\Delta k = 0$:

$$J(0,-\infty,z) = i\frac{b^2}{4iz+2b}$$

and

$$J(0,z,\infty) = -i\frac{b^2}{4iz+2b}$$

The z-scan field profile is

$$E_3 = \frac{i2\pi q\omega}{c}E_1^3\left(\frac{\chi_{\mathrm{A}}^{(3)}}{n_A} - \frac{\chi_{\mathrm{B}}^{(3)}}{n_B}\right)\frac{ib^2}{2(2iz+b)}$$

And the intensity is

$$|E_3|^2 = K^2\left(\frac{\chi_{\mathrm{A}}^{(3)}}{n_A} - \frac{\chi_{\mathrm{B}}^{(3)}}{n_B}\right)^2\frac{b^4}{4(4z^2+b^2)}$$

which is a Lorentizan with a peak value at $z = 0$ of

$$I_3(z=0) = (\chi_1^{(3)} - \chi_2^{(3)})^2 \frac{b^2}{4},$$

and a full width at half-maximum equal to the confocal parameter $b = 2z_R$. For a plot of this profile on the sapphire/air interface, see Fig. 4.13.

4.4 Effective susceptibility perturbations for THG

For third harmonic generation, we need to have an equation that describes THG, coupled to the probe propagation — all perturbed by the pump pulse. We assume that the pump pulse is a focusing Gaussian as before. Also, we will neglect depletion of the probe (fundamental) beam. First, let us calculate the transient perturbation to the THG relevant susceptibility.

4.4.1 Wave equation for THG

Starting with the wave equation, modified to include a source term for the third harmonic generation,

$$\left\{ \frac{i}{2k_3}\nabla_\perp^2 + \frac{\partial}{\partial z} + \frac{1}{v_{g3}}\frac{\partial}{\partial t} \right\} E_{\mathrm{TH}}(\mathbf{r},t) = -i\frac{\omega_3}{2cn_3\epsilon_0}\left(1 - \frac{i}{\omega_3}\frac{\partial}{\partial t}\right)\left[p^{\mathrm{THG}}(\mathbf{r},t) + p^A(\mathbf{r},t)\right], \quad (4.13)$$

we recognize that the additional polarization driving the electric field will be combination of two factors: the third harmonic of the fundamental and possible additional polarization accounting for modulation by a coherence.

4.4.2 Effective THG source term

We begin with the wave equation for a pulse generated by THG, as derived in Appendix. A:

$$\left\{ \frac{i}{2k_3}\nabla_\perp^2 + \frac{\partial}{\partial z} + \frac{1}{u_{\mathrm{th}}}\frac{\partial}{\partial t} \right\} E_{\mathrm{th}}(\mathbf{r},t) = -i\frac{\omega_3}{2cn_3\epsilon_0}\left(1 - \frac{i}{\omega_3}\frac{\partial}{\partial t}\right)\left[p^{\mathrm{th}}(\mathbf{r},t) + p^A(\mathbf{r},t)\right], \quad (4.14)$$

The source term in the spatial domain is given by for THG in an isotropic system with linear polarization

$$\frac{1}{4}\mu_0\epsilon_0\frac{\partial^2}{\partial t^2}\delta\chi^{(3)}(\mathbf{r},t)\mathcal{E}_{\mathrm{o}}^3(\mathbf{r},t) \quad (4.15)$$

with

$$\delta\chi^{(3)}(\mathbf{r},t) = \delta\chi_0^{(3)}|U_s(x,y,z)|^2 \sin[\Omega_v(t+\tau-u_{\rm p}^{-1}z)] \tag{4.16}$$

Thus the additional polarizations we insert into the wave equation for the envelope of the probe third harmonic are

$$p^{\rm th}(\mathbf{r},t) = \frac{1}{4}\epsilon_0\left[\chi_0^{(3)} + \delta\chi^{(3)}(\mathbf{r},t)\right]E_{\rm o}^3(\mathbf{r},t)e^{-i\Delta kz} \tag{4.17}$$

and

$$p^A(\mathbf{r},t) = \epsilon_0\delta\chi^{(1)}(\mathbf{r},t)E_{\rm th}(\mathbf{r},t). \tag{4.18}$$

Thus there are two sources of modulation imposed on the third harmonic field: modulation of the third-order susceptibility governing THG and modulation of the first-order susceptibility which modulates the already-generated third harmonic. Inserting these into the wave equation results in

$$\begin{aligned}&\left\{\frac{i}{2k_3}\nabla_\perp^2 + \frac{\partial}{\partial z} + \frac{1}{u_{th}}\frac{\partial}{\partial t}\right\}E_{\rm th}(\mathbf{r},t)\\ &\quad = -i\frac{\omega_3}{2cn_3}\left(1-\frac{i}{\omega_3}\frac{\partial}{\partial t}\right)\left\{\frac{1}{4}\left[\chi_0^{(3)} + \delta\chi^{(3)}(\mathbf{r},t)\right]E_{\rm o}^3(\mathbf{r},t)e^{-i\Delta kz} + \delta\chi^{(1)}(\mathbf{r},t)E_{\rm th}(\mathbf{r},t)\right\}.\end{aligned} \tag{4.19}$$

4.4.3 Working out the source term time derivative

At this point, we make a simplification typical of third harmonic generation discussions. We know that $\chi_0^{(3)} \ll \chi_0^{(1)}$, and certainly the perturbations $\delta\chi^{(3)} < \chi_0^{(3)}$, so that any $\chi^{(3)}$ term divided by the optical frequency of the third harmonic ω_3 is exceedingly small, and may be neglected:

$$\frac{1}{\omega_3}\frac{\partial}{\partial t}\left[\chi_0^{(3)} + \delta\chi^{(3)}(\mathbf{r},t)\right] \approx 0. \tag{4.20}$$

With this approximation, the right hand side becomes

$$\begin{aligned}-i\frac{\omega_3}{2cn_3}\Bigg\{&\frac{1}{4}\left[\chi_0^{(3)} + \delta\chi^{(3)}(\mathbf{r},t)\right]E_{\rm o}^3(\mathbf{r},t)e^{-i\Delta kz} + \delta\chi^{(1)}(\mathbf{r},t)E_{\rm th}(\mathbf{r},t)\\ &-\frac{i}{\omega_3}\frac{\partial}{\partial t}\left[\delta\chi^{(1)}(\mathbf{r},t)E_{\rm th}(\mathbf{r},t)\right]\Bigg\}.\end{aligned} \tag{4.21}$$

As in the previous section, we apply temporal differentiation to the right hand side using the equation

$$\frac{\partial}{\partial t}\delta\chi^{(n)}(\mathbf{r},t) = \Omega_v \delta\chi_0^{(n)} |U_s(x,y,z)|^2 \cos[\Omega_v(t+\tau-u_{\mathrm{p}}^{-1}z)], \tag{4.22}$$

We expand the derivative involving the effective linear perturbation of the third harmonic via the chain rule,

$$-\frac{i}{\omega_3}\frac{\partial}{\partial t}\left[\delta\chi^{(1)}(\mathbf{r},t)E_{\mathrm{th}}(\mathbf{r},t)\right] = -\frac{i}{\omega_3}\left[\left(\frac{\partial}{\partial t}\delta\chi^{(1)}\right)E_{\mathrm{th}} + \delta\chi^{(1)}\left(\frac{\partial}{\partial t}E_{\mathrm{th}}\right)\right], \tag{4.23}$$

and plug in the result to the right hand side, gathering the terms proportional to E_{th},

$$-i\frac{\omega_3}{2cn_3}\left\{\frac{1}{4}\left[\chi_0^{(3)}+\delta\chi^{(3)}(\mathbf{r},t)\right]E_{\mathrm{o}}^3(\mathbf{r},t)e^{-i\Delta kz} + \left[\delta\chi^{(1)} - \frac{i}{\omega_3}\left(\frac{\partial}{\partial t}\delta\chi^{(1)}\right)\right]E_{\mathrm{th}} - \frac{i}{\omega_3}\delta\chi^{(1)}\left(\frac{\partial}{\partial t}E_{\mathrm{th}}\right)\right\}. \tag{4.24}$$

Let us make the following definitions (and note how they differ from the previous section by using ω_3 instead of ω_1)

$$\begin{aligned}\delta k_3 &= \frac{\omega_3}{2nc_3}\left(\delta\chi^{(1)} - \frac{i}{\omega_3}\frac{\partial}{\partial t}\delta\chi^{(1)}\right)\\ &= \delta\chi_0^{(1)}|U_s(x,y,z)|^2\left\{\sin[\Omega_v(t+\tau-u_{\mathrm{p}}^{-1}z)] - i\frac{\Omega_v}{\omega_3}\cos[\Omega_v(t+\tau-u_{\mathrm{p}}^{-1}z)]\right\}\end{aligned} \tag{4.25}$$

so that the right hand side becomes

$$-i\frac{\omega_3}{2cn_3}\left\{\frac{1}{4}\left[\chi_0^{(3)}+\delta\chi^{(3)}\right]E_{\mathrm{o}}^3 e^{-i\Delta kz} - \frac{i}{\omega_3}\delta\chi^{(1)}\frac{\partial}{\partial t}E_{\mathrm{th}}\right\} - i\delta k_3 E_{\mathrm{th}}. \tag{4.26}$$

Now it comes time to insert this back into Eq. (4.19):

$$\left\{\frac{i}{2k_3}\nabla_\perp^2 + \frac{\partial}{\partial z} + \left(\frac{1}{u_{\mathrm{th}}} + \frac{\delta\chi^{(1)}(\mathbf{r},t)}{2cn_3}\right)\frac{\partial}{\partial t}\right\}E_{\mathrm{th}}(\mathbf{r},t) = -i\frac{\omega_3}{8cn_3}\left[\chi_0^{(3)}+\delta\chi^{(3)}(\mathbf{r},t)\right]E_{\mathrm{o}}^3(\mathbf{r},t)e^{-i\Delta kz} - i\delta k_3 E_{\mathrm{th}}(\mathbf{r},t). \tag{4.27}$$

Again we neglect group velocity distortions to arrive at

$$\left\{\frac{i}{2k_3}\nabla_\perp^2 + \frac{\partial}{\partial z} + \frac{1}{u_{\mathrm{th}}}\frac{\partial}{\partial t}\right\}E_{\mathrm{th}}(\mathbf{r},t) = -i\frac{\omega_3}{8cn_3}\left[\chi_0^{(3)}+\delta\chi^{(3)}(\mathbf{r},t)\right]E_{\mathrm{o}}^3(\mathbf{r},t)e^{-i\Delta kz} - i\delta k_3(\mathbf{r},t)E_{\mathrm{th}}(\mathbf{r},t). \tag{4.28}$$

4.4.4 Summary

The resulting equation for THG is similar to that for the fundamental, but with an extra driving term. The Eq. 4.28 is repeated here, but is not written in the rest frame of the pulse, as was the case for the fundamental:

$$\left\{\frac{i}{2k_3}\nabla_\perp^2+\frac{\partial}{\partial z}+\frac{1}{u_{\rm th}}\frac{\partial}{\partial t}\right\}E_{\rm th}(\mathbf{r},t) \\ =-i\frac{\omega_3}{8cn_3}\left[\chi_0^{(3)}+\delta\chi^{(3)}(\mathbf{r},t)\right]E_{\rm o}^3(\mathbf{r},t)e^{-i\Delta kz}-i\delta k_3(\mathbf{r},t)E_{\rm th}(\mathbf{r},t).$$

The wave number perturbation δk_3 are defined similarly to the fundamental δk_1, as they are both manifestations of the effective linear susceptibility perturbations $\delta\chi^{(1)}$. The effective third-order susceptibility perturbation $\delta\chi^{(3)}$ does not result in modification of the wave number, but does modify the conversion rate of the fundamental to third harmonic.

Three effective pathways may lead to vibrational modulation of the harmonic generated by a probe pulse. The probe itself may be modulated by the perturbation to the nonlinear optical susceptibility, $\delta\chi^{(n)}$. The term $\delta\chi^{(2)}$ term describes hyper-Raman scattering [25], while $\delta\chi^{(3)}$ describes second hyper-Raman scattering [95], and so on. Also, once generated, the harmonic will propagate along with the probe fundamental in through the vibrational coherence, albeit at a different group velocity. In this case, the propagating harmonic experiences modulation by the effective linear susceptibility perturbation $\delta\chi^{(1)}$. This effect is combined with the fundamental modulations via $\delta\chi^{(1)}$, to form the cascaded modulation term, which manifests itself as a time-varying phase mismatch.

4.5 Considering pump longitudinal intensity variation

Here we add in the spatial dependence of the pump to show that the z-dependent nature of the vibrational modulation plays a critical role in the behavior of THG as the interface is translated through the focus. As a first approximation, we had attempted to neglect all spatial variation of the pump (See Appendix D). But neglecting these variations did not match the interface scan behavior we observe in the experiment.

This is the outline of the approach. We start by examining the effects of the pump z-dependence on the probe fundamental, and discover a new behavior in the amplitude and

phase modulation. This leads to a new form for the probe as it propagates in the medium. Then we revisit the differential equation governing third harmonic generation, and use the new solution for the fundamental probe as a trial solution for the third harmonic field. Carrying through this trial solution yields the result we're after. Then we break apart the integral across the material boundary, as in the previous chapter, and observe the three effects: CsHRS, cascaded amplitude modulation, and Fresnel boundary modulation. We finish by plotting the magnitude of these effects with respect to the focal spot displacement form the material–air interface.

4.5.1 Spatial variation of the vibrational coherence

The vibrational coherence prepared by ISRS is directly proportional to the pump pulse intensity:

$$|U_s(x,y,z)|^2 = \frac{1}{1+\left(\frac{z-z_w}{z_R}\right)^2} e^{-\frac{2(x^2+y^2)}{w_0^2\left[1+\left(\frac{z-z_w}{z_R}\right)^2\right]}} = \Phi(x,y,z) \tag{4.29}$$

We transform this to the spatial frequency domain,

$$\begin{aligned}\hat{\Phi}(k_x,k_y;z) &= \frac{1}{4\pi^2}\int_{-\infty}^{\infty}\mathrm{d}x\int_{-\infty}^{\infty}\mathrm{d}y\Phi(x,y,z)e^{-i(k_x x+k_y y)} \\ &= \frac{w_0^2}{8\pi}e^{-(k_x^2+k_y^2)\frac{w_0^2}{8}\left[1+\left(\frac{z-z_w}{z_R}\right)\right]}.\end{aligned} \tag{4.30}$$

Since we will be hard-pressed to find analytic solutions accounting for transverse variations, that is k_x and k_y, we make the approximation

$$\Phi(x,y,z) \approx \Phi(z) = \frac{1}{1+\left(\frac{z-z_w}{z_R}\right)^2}. \tag{4.31}$$

4.5.2 Probe fundamental propagation

We consider Gaussian probe pulses. We can break apart the envelope into time- and space-dependent envelopes U_t and U_s

$$E_{\mathrm{p}}(x,y,z,t) = E_{0,3\mathrm{o}}U_s(x,y,z)U_t(t-u_{\mathrm{p}}^{-1}z) \tag{4.32}$$

where the Gaussian spatial profile is described by

$$U_s(x,y,z) = \frac{1}{\left[1+\frac{i2z}{w_0^2k_{0,1}}\right]}\exp\left\{-\frac{(x^2+y^2)}{w_0^2\left[1+\frac{i2z}{w_0^2k_{0,1}}\right]}\right\} \tag{4.33}$$

and the Gaussian temporal envelope is described by

$$U_t(t-u_{\rm p}^{-1}z)=\exp\left[-2\ln 2\left(\frac{t-u_{\rm p}^{-1}z}{\tau_{\rm p}}\right)^2\right]e^{i\phi(t-u_{\rm p}^{-1}z)} \tag{4.34}$$

where $\tau_{\rm p}$ is the pump pulse FWHM (possibly chirped) and $\phi(t-u_{\rm p}^{-1}z)$ is the temporal phase of the pump pulse.

Now we observe how the spatial dependence of the coherence, $\Phi(z)$, modifies the probe fundamental as it propagates through the medium. We have the equation for propagation,

$$\left\{-\frac{1}{2ik_1}\nabla_\perp^2+\frac{\partial}{\partial\zeta}\right\}E_{\rm o}(x,y,\zeta,t_{\rm o})=-i\delta k_1(\mathbf{r},t_{\rm pr})E_{\rm pr}(x,y,\zeta,t_{\rm pr}) \tag{4.35}$$

The wavenumber k modulation term, in the spatial frequency domain is approximated

$$\delta k_1(\mathbf{r},t_{\rm pr})=-i\frac{w_0^2}{8\pi}\delta k_1(t_{\rm pr})\Phi(\zeta)=-i\frac{w_0^2}{8\pi}\frac{\delta k_1(t_{\rm pr})}{\left[1+\left(\frac{\zeta-z_w}{z_R}\right)^2\right]} \tag{4.36}$$

We transform the equation to the spatial frequency domain by use of the following relationships:

$$E_{\rm pr}(x,y,\zeta,t_{\rm pr})\Leftrightarrow\hat{E}_{\rm pr}(k_x,k_y,\zeta,t_{\rm pr}), \tag{4.37}$$

and

$$-\frac{1}{2ik_1}\nabla_\perp^2E_{\rm pr}(x,y,\zeta,t_{\rm pr})\Leftrightarrow\frac{k_x^2+k_y^2}{2ik_1}\hat{E}_{\rm pr}(k_x,k_y,\zeta,t_{\rm pr}). \tag{4.38}$$

so that the differential equation in the spatial frequency domain governing propagation of the probe pulse is given by

$$\frac{\partial}{\partial\zeta}\hat{E}_{\rm pr}(k_x,k_y,\zeta,t_{\rm pr})=\left\{-i\frac{\delta k_1(t_{\rm pr})}{\left[1+\left(\frac{\zeta-z_w}{z_R}\right)^2\right]}+\frac{k_x^2+k_y^2}{2ik_1}\right\}\hat{E}_{\rm pr}(k_x,k_y,\zeta,t_{\rm pr}) \tag{4.39}$$

The solution for the probe field is then

$$\hat{E}_{\rm pr}(\zeta)=\hat{E}_{\rm pr}(\zeta_0)\exp\left\{\int_{\zeta_0}^{\zeta}\left[-i\frac{\delta k_1(t_{\rm pr})}{\left[1+\left(\frac{\zeta'-z_w}{z_R}\right)^2\right]}+\frac{k_x^2+k_y^2}{2ik_1}\right]{\rm d}\zeta'\right\} \tag{4.40}$$

or, performing the straightforward part of the integral and pulling $\delta k_1(t_pr)$, since it does not depend on the integration variable ζ'

$$\hat{E}_{\rm pr}(\zeta)=\hat{E}_{\rm pr}(\zeta_0)\exp\left[-i\delta k_{10}(t_{\rm pr})\int_{\zeta_0}^{\zeta}\frac{{\rm d}\zeta'}{1+\left(\frac{\zeta'-z_w)}{z_R}\right)^2}\right]e^{-i\frac{k_x^2+k_y^2}{2k_1}(\zeta-\zeta_0)}. \tag{4.41}$$

The remaining integral we shall define as

$$\Gamma(\zeta,\zeta_0) \equiv \int_{\zeta_0}^{\zeta} \Phi(\zeta')\mathrm{d}\zeta' = \int_{\zeta_0}^{\zeta} \frac{\mathrm{d}\zeta'}{1+\left(\frac{\zeta'-z_w}{z_R}\right)^2} = z_R\left[\tan^{-1}\left(\frac{\zeta-z_w}{z_R}\right)-\tan^{-1}\left(\frac{\zeta_0-z_w}{z_R}\right)\right]. \quad (4.42)$$

This integral depends on the pump, $\Phi(z)$, characteristics, not the probe. The solution for the probe fundamental can be written

$$\hat{E}_{\mathrm{pr}}(\zeta) = \hat{E}_{\mathrm{pr}}(\zeta_0)e^{-i\delta k_1(t_{\mathrm{pr}})\Gamma(\zeta,\zeta_0)}e^{-i\frac{k_x^2+k_y^2}{2k_1}(\zeta-\zeta_0)}. \quad (4.43)$$

This equation still depends on the input beam $\hat{E}_{\mathrm{pr}}(\zeta_0)$. So we assume a Gaussian input beam focusing to a waist at z_w,

$$\hat{E}_{\mathrm{pr}}(\zeta_0) = E_{10}\frac{w_{10}^2}{4\pi}e^{-(k_x^2+k_y^2)\left[\frac{w_{10}^2}{4}+i\frac{(\zeta_0-z_w)}{2k_1}\right]}, \quad (4.44)$$

and insert this form of the initial probe into the solution, Eq. (4.43) to obtain

$$\hat{E}_{\mathrm{pr}}(\zeta) = E_{10}\frac{w_{10}^2}{4\pi}e^{-(k_x^2+k_y^2)\frac{w_{10}^2}{4}A_1(\zeta)}e^{-i\delta k_1(t_{\mathrm{pr}})\Gamma(\zeta,\zeta_0)}, \quad (4.45)$$

where to shorten the notation we have defined

$$A_1(\zeta) = 1+i\frac{2(\zeta-z_w)}{w_{10}^2k_1} = 1+i\frac{\zeta-z_w}{z_R}. \quad (4.46)$$

We transform back to the spatial domain via

$$E_{\mathrm{pr}}(x,y,\zeta,t_{\mathrm{pr}}) = \iint_{-\infty}^{\infty}\hat{E}_{\mathrm{pr}}(k_x,k_y,\zeta,t_{\mathrm{pr}})e^{i(k_xx+k_yy)}\mathrm{d}k_x\mathrm{d}k_y \quad (4.47)$$

so the solution for the probe is finally

$$E_{\mathrm{pr}}(x,y,\zeta,t_{\mathrm{pr}}) = \frac{E_{10}}{A_1(\zeta)}\exp\left\{-\frac{(x^2+y^2)}{w_{10}^2A_1(\zeta)}\right\}e^{-i\delta k_1(t_{\mathrm{pr}})\Gamma(\zeta,\zeta_0)} \quad (4.48)$$

Expanding the Γ integral,

$$E_{\mathrm{o}}(x,y,\zeta,t_{\mathrm{o}}) = \frac{E_{10}}{A_1(\zeta)}\exp\left\{-\frac{(x^2+y^2)}{w_{10}^2A_1(\zeta)}\right\} \times\exp\left\{-i\delta k_1(t_{\mathrm{o}})z_R\left[\tan^{-1}\left(\frac{\zeta-z_w}{z_R}\right)-\tan^{-1}\left(\frac{\zeta_0-z_w}{z_R}\right)\right]\right\} \quad (4.49)$$

4.5.2.1 Explanation and example

The solution we arrived at in Eq. (4.49) describes a Gaussian probe pulse envelope multiplied by a modulation term,

$$\exp\left\{-i\delta k_1(t_{\rm pr})z_R\left[\tan^{-1}\left(\frac{\zeta-z_w}{z_R}\right)-\tan^{-1}\left(\frac{\zeta_0-z_w}{z_R}\right)\right]\right\}. \tag{4.50}$$

The probe acquires, through δk_1 both amplitude and phase modulation as it propagates through the coherence. If it were in a plane-pumped coherence with no spatial variations, the modulation depth would simply be proportional to propagation distance $\zeta-\zeta_0$. But in this case, the modulation depth at each point of propagation follows the longitudinal intensity profile of the pump, Φ. Hence the *accumulated* modulation depth follows the integral $\Gamma=\int_{\zeta_0}^{\zeta}\Phi{\rm d}\zeta'$.

To illustrate let us consider the case $z_w=0$ and $z_R=1$, in a tight focus so that we may approach the limit $\zeta_0\to-\infty$ [39]. The modulation term reduces to

$$\exp\left\{-i\delta k_1(t_{\rm pr})\left[\tan^{-1}\left(\frac{\zeta-z_w}{z_R}\right)+\frac{\pi}{2}\right]\right\}. \tag{4.51}$$

A plot is shown in Fig. 4.2 to illustrate both the pump longitudinal intensity Φ and the depth of modulation the probe pulse accumulates with propagation.

Practically, the majority of the modulation accumulates within about 10 z_R. Considering the typical Rayleigh range of a focused beam using an 50x 0.5 NA objective is about 3μm, we are justified in using the tight focus limit of $\zeta_0\to-\infty$ for samples of thickness greater than 30μm. Most of our samples will be at in the range of 0.1 to 0.5 mm.

4.5.3 THG differential equation

4.5.3.1 Spatial domain

The differential equation governing third harmonic generation and propagation, in the group frame of the third harmonic pulse, is

$$\left\{-i\frac{1}{2ik_3}\nabla_\perp^2+\frac{\partial}{\partial\zeta}\right\}E_{\rm th}(\mathbf{r},t)=-i\frac{\omega_3}{8cn_3}\left[\chi_0^{(3)}+\delta\chi^{(3)}(\zeta,t)\right]E_{\rm pr}^3(\mathbf{r},t)e^{-i\Delta k\zeta}$$
$$-i\delta k_3(\zeta,t)E_{\rm th}(\mathbf{r},t) \tag{4.52}$$

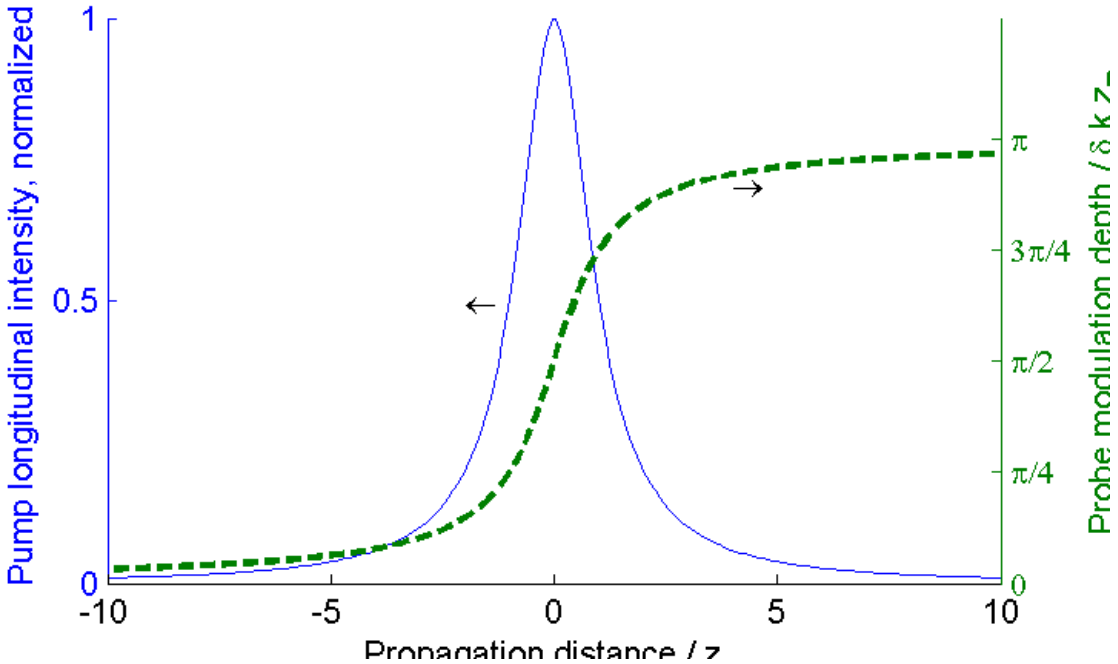

Figure 4.2: Pump longitudinal intensity dependence and probe modulation accumulation.

where the modulation of the third harmonic generation is proportional to the vibrational coherence,

$$\delta\chi^{(3)}(\zeta,t) \approx \delta\chi_0^{(3)}\Phi(\zeta)\sin[\Omega_v(t+\tau)], \tag{4.53}$$

the phase mismatch is

$$\Delta k = 3k_1 - k_3. \tag{4.54}$$

The coherence also modulates the propagating third harmonic similarly to the fundamental,

$$\delta k_3(\zeta,t_{\rm pr}) = \frac{\omega_3}{2cn_3}\delta\chi_3^{(1)}(\zeta,t_{\rm pr}) = \delta k_3'(\zeta,t_{\rm pr}) + i\delta k_3''(\zeta,t_{\rm pr}), \tag{4.55}$$

where the real and imaginary parts are

$$\delta k_3'(\zeta,t_{\rm pr}) = \frac{\omega_3}{2cn_3}\delta\chi_{30}^{(1)}\Phi(\zeta)\sin[\Omega_v(t_{\rm pr}+\tau)] \tag{4.56}$$

and

$$\delta k_3''(\zeta,t_{\rm pr}) = -\frac{\Omega_v}{\omega_3}\frac{\omega_3}{2cn_3}\delta\chi_{30}^{(1)}\Phi(\zeta)\cos[\Omega_v(t_{\rm pr}+\tau)]. \tag{4.57}$$

The undepleted fundamental which drives the third harmonic generation is given by

$$E_{\rm pr}^3(x,y,\zeta,t_{\rm pr}) = \frac{E_{10}^3}{A_1^3(\zeta)}\exp\left\{-3\frac{(x^2+y^2)}{w_{10}^2A_1(\zeta)}\right\}e^{-i3\delta k_1(t_{\rm pr})\Gamma(\zeta)} \tag{4.58}$$

4.5.3.2 Spatial frequency domain

We begin by transforming the differential equation into the spatial frequency domain. The probe fundamental transforms according to

$$E^3_{\rm pr}(x,y,\zeta,t_{\rm pr}) \Leftrightarrow \frac{w_{10}^2}{12\pi}\frac{E_{10}^3}{A_1^2(\zeta)}e^{-(k_x^2+k_y^2)w_{10}^2A_1(\zeta)/12} \tag{4.59}$$

so that the driving term in the spatial frequency domain is

$$i\frac{\omega_3 w_{10}^2}{96\pi c n_3}\left[\chi_0^{(3)}+\delta\chi^{(3)}(t)\Phi(\zeta)\right]\frac{E_{10}^3}{A_1^2(\zeta)}e^{-i3\delta k_1(t_{\rm pr})\Gamma(\zeta)}e^{-(k_x^2+k_y^2)w_{10}^2A_1(\zeta)/12} \tag{4.60}$$

So the full differential equation in the spatial frequency domain is

$$\begin{aligned}\frac{\partial}{\partial\zeta}\hat{E}_{\rm th} = &\left\{-\frac{(k_x^2+k_y^2)}{2ik_3}-i\delta k_3(t)\Phi(\zeta)\right\}\hat{E}_{\rm th}\\ &-i\frac{\omega_3 w_{10}^2}{96\pi c n_3}\left[\chi_0^{(3)}+\delta\chi_0^{(3)}\sin[\Omega_v(t+\tau)]\Phi(\zeta)\right]\\ &\times\frac{E_{10}^3}{A_1^2(\zeta)}e^{-i3\delta k_1(t_{\rm pr})\Gamma(\zeta)}e^{-(k_x^2+k_y^2)w_{10}^2A_1(\zeta)/12}e^{-i\Delta k\zeta}\end{aligned} \tag{4.61}$$

The first term describes propagation of the third harmonic, and is composed of a Gaussian propagation term plus a complex wavenumber k perturbation, which modulates the third harmonic in the same way the probe fundamental is modulated. This linear modulation of the third harmonic will be grouped with the linear modulation of the fundamental to form the cascaded modulation portion of the CM-THG signal.

The second term in Eq. 4.61 describes third harmonic generation driven by the modulated fundamental. It consists of a nonlinear susceptibility plus a vibrational perturbation multiplied by the modulated fundamental. Since the perturbations are weak, the product will be decomposed into an unmodulated third harmonic, one modulated by $\delta\chi^{(3)}$, and one modulated by the probe fundamental modulations $\delta\chi^{(1)}$.

4.5.3.3 Solutions for THG of Gaussian form

We assume the probe-generated harmonic to be Gaussian [94], and so we seek a form of the solution similar to the result arrived at for the probe fundamental. Our trial solution is

$$\hat{E}_{\rm th}(k_x,k_y;\zeta) = E_{30}(\zeta)\frac{w_{30}^2}{4\pi}e^{-(k_x^2+k_y^2)w_{30}^2A_3(\zeta)/4}e^{-i\delta k_3(t_{\rm pr})\Gamma_3(\zeta)}, \tag{4.62}$$

with a propagation-dependent envelope $\mathrm{E}_{30}(\zeta)$ which we will solve for, and

$$A_3(\zeta) = 1 + 2i\frac{\zeta - z_{w3}}{w_{30}^2 k_3} = 1 + i\frac{\zeta - z_{w3}}{z_{R,3}} \tag{4.63}$$

Assuming no input third harmonic field, we have the boundary condition at the input plane ζ_{in}:

$$E_{30}(\zeta_{\mathrm{in}}) = 0. \tag{4.64}$$

We will insert this trial solution into the differential equation for TH generation and propagation in the presence of a coherence, Eq. 4.61. First, we take the partial derivative of our trial solution with respect to ζ. Keep in mind $\Gamma = \int \Phi$, so the differentiation undoes this integral:

$$\frac{\partial \hat{E}_{\mathrm{th}}}{\partial \zeta} = -i\left\{\delta k_3(t_{\mathrm{pr}})\Phi_3(\zeta) + \frac{k_x^2 + k_y^2}{2k_3}\right\}\hat{E}_{\mathrm{th}} + \frac{w_{30}^2}{4\pi}e^{-(k_x^2+k_y^2)w_{30}^2 A_3(\zeta)/4}e^{-i\delta k_3(t_{\mathrm{pr}})\Gamma(\zeta)}\frac{\partial E_{30}(\zeta)}{\partial \zeta}. \tag{4.65}$$

We insert this directly into Eq. 4.61 Cancelling the terms common to both sides, gathering exponentials and constants on the right side to isolate the partial derivative

$$\frac{\partial E_{30}(\zeta)}{\partial \zeta} = -i\left(\frac{w_{10}}{w_{30}}\right)^2 \frac{\omega_3}{24cn_3}\frac{E_{10}^3}{A_1^2(\zeta)}\left[\chi_0^{(3)} + \delta\chi_0^{(3)}(t_{\mathrm{pr}})\Phi(\zeta)\right]e^{-i[3\delta k_1(t_{\mathrm{pr}}) - \delta k_3(t_{\mathrm{pr}})]\Gamma(\zeta)}$$
$$e^{-(k_x^2+k_y^2)\left[w_{10}^2 A_1(\zeta)/12 - w_{30}^2 A_3(\zeta)/4\right]}e^{-i\Delta k\zeta} \tag{4.66}$$

This describes the propagation-dependent evolution of the third harmonic amplitude and phase, $E_{30}(\zeta)$, in the presence of a vibrational coherence. This is inserted into the trial solution Eq. 4.62 to describe the third harmonic in the spatial frequency domain. But when we do so, the presence of the extra spatial frequency components in $E_{30}(\zeta)$,

$$e^{-(k_x^2+k_y^2)\left\{\frac{w_{10}^2 A_1(\zeta)}{12} - \frac{w_{30}^2 A_3(\zeta)}{4}\right\}} = e^{-(k_x^2+k_y^2)\left\{\left[\frac{w_{10}^2}{12} + i\frac{(\zeta - z_{w1})}{6k_1}\right] - \left[\frac{w_{30}^2}{4} + i\frac{(\zeta - z_{w1})}{2k_3}\right]\right\}}, \tag{4.67}$$

will cause the full solution in Eq. 4.62 to deviate from a Gaussian beam. These deviations are small, and can be neglected to simplify our analysis [94].

Recalling the definitions of $A_1(\zeta)$ and $A_3(\zeta)$,

$$\frac{w_{10}^2 A_1(\zeta)}{12} - \frac{w_{30}^2 A_3(\zeta)}{4} = \left[\frac{w_{10}^2}{12} + i\frac{(\zeta - z_{w1})}{6k_1}\right] - \left[\frac{w_{30}^2}{4} + i\frac{(\zeta - z_{w1})}{2k_3}\right] \tag{4.68}$$

the exponent that depends on spatial frequency is

$$e^{-(k_x^2+k_y^2)\left\{\left[\frac{w_{10}^2}{12}+i\frac{(\zeta-z_{w1})}{6k_1}\right]-\left[\frac{w_{30}^2}{4}+i\frac{(\zeta-z_{w1})}{2k_3}\right]\right\}}. \tag{4.69}$$

If we can eliminate the spatial frequency dependence, we will describe the propagation of a Gaussian beam. We do this if the following condition is met:

$$\left[\frac{w_{10}^2}{12}+i\frac{(\zeta-z_{w1})}{6k_1}\right]=\left[\frac{w_{30}^2}{4}+i\frac{(\zeta-z_{w1})}{2k_3}\right] \tag{4.70}$$

or, equivalently

$$w_{10}^2=3w_{30}^2 \tag{4.71}$$

and

$$\frac{1}{3k_1}-\frac{1}{k_3}=\frac{k_3-3k_1}{3k_1k_3}\approx 0 \tag{4.72}$$

reducing the differential equation to

$$\frac{\partial E_{30}(\zeta)}{\partial\zeta}=-i\left(\frac{w_{10}}{w_{30}}\right)^2\frac{\omega_3}{24cn_3}\frac{E_{10}^3}{A_1^2(\zeta)}\left[\chi_0^{(3)}+\delta\chi_0^{(3)}(t_{\rm pr})\Phi(\zeta)\right] \times e^{-i[3\delta k_1(t_{\rm pr})-\delta k_3(t_{\rm pr})]\Gamma(\zeta)}e^{-i\Delta k\zeta} \tag{4.73}$$

We will also collapse the following terms into a perturbation to the phase mismatch,

$$\Delta\delta k(t_{\rm pr})=3\delta k_1(t_{\rm pr})-\delta k_3(t_{\rm pr})=\Delta\delta k'(t_{\rm pr})+i\Delta\delta k''(t_{\rm pr}) \tag{4.74}$$

and define the constant

$$\mathcal{C}=i\left(\frac{w_{10}}{w_{30}}\right)^2\frac{\omega_3}{24cn_3}E_{10}^3 \tag{4.75}$$

and gather the terms in $[\cdots]$

$$\chi_0^{(3)}+\delta\chi^{(3)}(t_{\rm pr})=\chi_0^{(3)}\left(1+\frac{\delta\chi^{(3)}(t_{\rm pr})}{\chi_0^{(3)}}\right) \tag{4.76}$$

so that the differential equation is finally

$$\frac{\partial E_{30}(\zeta)}{\partial\zeta}=-i\left(\frac{w_{10}}{w_{30}}\right)^2\frac{\omega_3}{24cn_3}\frac{E_{10}^3}{A_1^2(\zeta)}\chi_0^{(3)}\left[1+\frac{\delta\chi_0^{(3)}(t_{\rm pr})\Phi(\zeta)}{\chi_0^{(3)}}\right] \times e^{\Delta\delta k''(t_{\rm pr})\Gamma(\zeta)}e^{-i[\Delta k\zeta+\Delta\delta k'(t_{\rm pr})\Gamma(\zeta)]} \tag{4.77}$$

4.5.4 Integration with Fresnel boundary modulation

4.5.4.1 Break up integral across the boundary

We consider that the probe fundamental, upon crossing the interface, will be multiplied according to a Fresnel transmission coefficient. This Fresnel transmission coefficient is sensitive to the index of refraction on both sides of the interface. As we derived earlier, there is an effective first-order susceptibility $\delta\chi^{(1)}(t)$ which modulates the index of refraction in the presence of a vibrational coherence. Thus we expect the Fresnel transmission coefficient to be modulated.

The transmission coefficient T is the initial coefficient plus a small perturbation, so its cube is approximated

$$T_1^3(\delta n) = [T_{0,1} + \delta T_1(t_{pr})]^3 \approx T_{0,1}^3 + 3T_{0,1}^2 \delta T_1(t_{\mathrm{o}}) \tag{4.78}$$

Also the third harmonic transmission perturbation multiplied by small terms is neglected,

$$T_3(\delta n) = T_{0,3} + \delta T_3(t_{\mathrm{o}}) \tag{4.79}$$

so that

$$T_3(\delta n)\delta\chi^{(3)} \approx T_{0,3}\delta\chi^{(3)} \tag{4.80}$$

and

$$T_3(\delta n)(3\delta k_1'' - \delta k_3'') \approx T_{0,3}(3\delta k_1'' - \delta k_3'') \tag{4.81}$$

We are interested in the far-field TH light generated by focusing on a material interface. So we integrate, breaking up the integral across this boundary

$$E_{30}(z) = T_3 \int_{-\infty}^{z_L} \left[\frac{\partial E_{30}(z)}{\partial z}\right] \mathrm{d}z + \int_{z_L}^{\infty} \left[\frac{\partial E_{30}(z)}{\partial z}\right] \mathrm{d}z. \tag{4.82}$$

We consider that the probe fundamental, upon crossing the interface, will be multiplied according to a Fresnel transmission coefficient. This Fresnel transmission coefficient is sensitive to the index of refraction on both sides of the interface. As we derived earlier, there is an effective first-order susceptibility $\delta\chi^{(1)}(t)$ which modulates the index of refraction in the presence of a vibrational coherence. Thus we expect the Fresnel transmission coefficient to be modulated.

The field transmission coefficient T is the initial coefficient plus a small perturbation, so its cube is approximated

$$T_1^3(\Delta n) = [T_{0,1} + \Delta t_1(t_{pr})]^3 \approx T_{0,1}^3 + 3T_{0,1}^2 \Delta T_1(t_o) \tag{4.83}$$

Also the third harmonic transmission perturbation multiplied by small terms is neglected, So we rewrite the integral solution. All terms generated in the crystal are multiplied by the transmission of the third harmonic, while terms generated outside will have the source E_1 multiplied by the fundamental transmission coefficient. Note E_1 is inside an integral, and the z-dependent coherence causes ΔT_3 to depend on z. Defining the new coordinates $u = \zeta/z_R$ and $u_w = z_w/z_R$ for convenience, we rewrite the integral solution,

$$\begin{aligned} E_{30} = T_{0,3}\mathcal{C} z_R \delta\chi^{(3)}(t) \int_{-\infty}^{z_L} \frac{\Phi(u)}{A_1^2(u)} e^{i\Delta k z_R u} \mathrm{d}u \\ + \left[T_{0,3} + \Delta T_3\right] \mathcal{C} z_R \chi_{\mathrm{cr}}^{(3)} \int_{-\infty}^{z_L} \frac{e^{-\Delta\delta k'' \Gamma(u)} e^{i[\Delta k z_R u + \Delta\delta k' \Gamma(u)]}}{A_1^2(u)} \mathrm{d}u \\ + \mathcal{C} z_R \chi_{\mathrm{air}}^{(3)} \int_{z_L}^{\infty} \frac{e^{i\Delta k z_R u}}{A_1^2(u)} \left[T_{0,1}^3 + 3T_{0,1}^2 \Delta t_1(t)\right] \mathrm{d}u \end{aligned} \tag{4.84}$$

The first integral captures the modified third harmonic generation (CSHRS), the second captures modulation of the third harmonic and the fundamental by the coherence (cascaded modulation), and the third captures THG in air after the interaface. This final term will later be shown to capture vibrational modulations of the Fresnel boundary conditions at the interface.

All terms generated in the crystal are multiplied by the transmission of the third harmonic, while terms generated outside will have the source E_1 multiplied by the fundamental transmission coefficient. Note E_1 is inside an integral, and the z-dependent coherence causes δT_3 to depend on z. We rewrite the integral solution, re-inserting the air susceptibility $\chi_{\mathrm{air}}^{(3)}$, recalling that $\Delta\chi^{(3)} = \chi_{\mathrm{cr}}^{(3)} - \chi_{\mathrm{air}}^{(3)}$

$$\begin{aligned} E_{30} = T_{0,3}\mathcal{C} z_R \delta\chi^{(3)}(t) \int_{-\infty}^{z_L} \frac{\Phi(u)}{A_1^2(u)} e^{-i\Delta k z_R u} \mathrm{d}u \\ + \left[T_{0,3} + \delta T_3(t)\right] \mathcal{C} z_R \chi_{\mathrm{cr}}^{(3)} \int_{-\infty}^{z_L} \frac{e^{\Delta\delta k'' \Gamma(u)} e^{-i[\Delta k z_R u + \Delta\delta k' \Gamma(u)]}}{A_1^2(u)} \mathrm{d}u \\ + \mathcal{C} z_R \chi_{\mathrm{air}}^{(3)} \int_{z_L}^{\infty} \frac{e^{-i\Delta k z_R u}}{A_1^2(u)} \left[T_{0,1}^3 + 3T_{0,1}^2 \delta T_1(t)\right] \mathrm{d}u \end{aligned} \tag{4.85}$$

the first integral captures the modified third harmonic generation (CSHRS), the second captures modulation of the third harmonic and the fundamental by the coherence (cascaded modulation), and the third captures THG in air after the interaface. This final term captures vibrational modulations of the Fresnel boundary conditions at the interface.

4.5.4.2 Manipulations and Simplifications

Turning our attention to the last integral in Eq. (4.85), we find the transmission coefficient modulation is dependent on the interface position relative to the focus

$$\delta T_1(t, z_L) = \Phi(z_L)\delta T_1(t) = \frac{1}{1 + \left(\frac{z_L - z_w}{z_R}\right)^2}\delta T_1(t) \tag{4.86}$$

The same should hold for δT_3. So we expand the last integral of Eq. (4.85),

$$\begin{aligned}
&\mathcal{C} z_R \chi^{(3)}_{\text{air}} \int_{z_L}^{\infty} \frac{e^{-i\Delta k z_R u}}{A_1^2(u)} \left[T_{0,1}^3 + 3T_{0,1}^2 \delta T_1(t)\Phi(u)\right] \mathrm{d}u \\
&= \mathcal{C} z_R \chi^{(3)}_{\text{air}} T_{0,1}^3 \int_{z_L}^{\infty} \frac{e^{-i\Delta k z_R u}}{A_1^2(u)} \mathrm{d}u + 3\mathcal{C} z_R \chi^{(3)}_{\text{air}} T_{0,1}^2 \delta T_1(t)\Phi(z_L) \int_{z_L}^{\infty} \frac{1}{A_1^2(u)} e^{-i\Delta k z_R u} \mathrm{d}u
\end{aligned} \tag{4.87}$$

The middle integral of Eq. (4.85) describes cascaded modulations, and can be approximated in a tight focusing condition. Since $\Delta k z_R \ll 1$ and $\Delta\delta k' \ll 1$, their presence in the exponential argument leads to a slowly oscillating term that hardly changes in the integral across the short confocal parameter, and they may be neglected:

$$\int_{-\infty}^{z_L} \frac{e^{\Delta\delta k''\Gamma(u)} e^{-i[\Delta k z_R u + \Delta\delta k'\Gamma(u)]}}{A_1^2(u)} \mathrm{d}u \approx \int_{-\infty}^{z_L} \frac{e^{\Delta\delta k''\Gamma(u)}}{A_1^2(u)} \mathrm{d}u \tag{4.88}$$

The argument in the numerator is small, so the integral describing cascaded modulations breaks apart into

$$\left(T_{0,3} + \delta T_3\right) \mathcal{C} z_R \chi^{(3)}_{\text{cr}} \left\{ \int_{-\infty}^{z_L} \frac{1}{A_1^2(u)} \mathrm{d}u + \Delta\delta k'' \int_{-\infty}^{z_L} \frac{\Gamma(u)}{A_1^2(u)} \mathrm{d}u \right\} \tag{4.89}$$

The product of the $\delta T_3 \Delta\delta k''$ is exceedingly small, so we are left with

$$\left(T_{0,3} + \delta T_3\right) \mathcal{C} z_R \chi^{(3)}_{\text{cr}} \int_{-\infty}^{z_L} \frac{1}{A_1^2(u)} \mathrm{d}u + T_{0,3} \mathcal{C} z_R \chi^{(3)}_{\text{cr}} \Delta\delta k''(t) \int_{-\infty}^{z_L} \frac{\Gamma(u)}{A_1^2(u)} \mathrm{d}u \tag{4.90}$$

and the total E_3, from Eq. (4.85) is, with a few rearrangements and applying the approximation $\Delta k z_R \ll 1$

$$\begin{aligned} E_{30} = T_{0,3}\mathcal{C}z_R\delta\chi^{(3)}(t)\int_{-\infty}^{z_L}\frac{\Phi(u)}{A_1^2(u)}\mathrm{d}u \\ + T_{0,3}\mathcal{C}z_R\chi_{\mathrm{cr}}^{(3)}\Delta\delta k''(t)\int_{-\infty}^{z_L}\frac{\Gamma(u)}{A_1^2(u)}\mathrm{d}u \\ + 3T_{0,1}^2\delta T_1(t)\mathcal{C}z_R\chi_{\mathrm{air}}^{(3)}\Phi(z_L)\int_{z_L}^{\infty}\frac{1}{A_1^2(u)}\mathrm{d}u \\ + \left[T_{0,3}+\delta T_3(t)\Phi(z_L)\right]\mathcal{C}z_R\chi_{\mathrm{cr}}^{(3)}\int_{-\infty}^{z_L}\frac{1}{A_1^2(u)}\mathrm{d}u \\ + T_{0,1}^3\mathcal{C}z_R\chi_{\mathrm{air}}^{(3)}\int_{z_L}^{\infty}\frac{1}{A_1^2(u)}\mathrm{d}u \end{aligned} \tag{4.91}$$

It will now be shown that the three terms containing integrals of $1/A_1^2(u)$ may be condensed together in two steps, leveraging the fact that this integral over the range $[-\infty,\infty]$ is zero. There are two Fresnel modulation terms which are coherence-dependent:

$$3T_{0,1}^2\delta T_1(t)\mathcal{C}z_R\chi_{\mathrm{air}}^{(3)}\Phi(z_L)\int_{z_L}^{\infty}\frac{1}{A_1^2(u)}\mathrm{d}u + \delta T_3(t)\mathcal{C}z_R\chi_{\mathrm{cr}}^{(3)}\Phi(z_L)\int_{-\infty}^{z_L}\frac{1}{A_1^2(u)}\mathrm{d}u \tag{4.92}$$

Defining $\overline{\Delta\chi}_B^{(3)}$ such that

$$\delta T_3(t)\chi_{\mathrm{cr}}^{(3)}\Phi(z_L) = \overline{\Delta\chi}_B^{(3)}(t,z_L) + 3T_{0,1}^2\delta T_1(t)\chi_{\mathrm{air}}^{(3)}\Phi(z_L) \tag{4.93}$$

or explicitly

$$\overline{\Delta\chi}_B^{(3)}(t,z_L) = \left[\delta T_3(t)\chi_{\mathrm{cr}}^{(3)} - 3T_{0,1}^2\delta T_1(t)\chi_{\mathrm{air}}^{(3)}\right]\Phi(z_L) \tag{4.94}$$

we write those two terms instead as

$$\begin{aligned} 3T_{0,1}^2\delta T_1(t)\mathcal{C}z_R\chi_{\mathrm{air}}^{(3)}\Phi(z_L)\int_{-\infty}^{\infty}\frac{1}{A_1^2(u)}\mathrm{d}u + \overline{\Delta\chi}_B^{(3)}(t,z_L)\mathcal{C}z_R\int_{-\infty}^{z_L}\frac{1}{A_1^2(u)}\mathrm{d}u \\ = \overline{\Delta\chi}_B^{(3)}(t,z_L)\mathcal{C}z_R\int_{-\infty}^{z_L}\frac{1}{A_1^2(u)}\mathrm{d}u \end{aligned} \tag{4.95}$$

reducing the expression for the total third harmonic field to

$$E_{30} = T_{0,3}\mathcal{C}z_R\delta\chi^{(3)}(t)\int_{-\infty}^{z_L}\frac{\Phi(u)}{A_1^2(u)}\mathrm{d}u + T_{0,3}\mathcal{C}z_R\chi_{\mathrm{cr}}^{(3)}\Delta\delta k''(t)\int_{-\infty}^{z_L}\frac{\Gamma(u)}{A_1^2(u)}\mathrm{d}u + \mathcal{C}z_R\overline{\Delta\chi}_B^{(3)}(t,z_L)\int_{-\infty}^{z_L}\frac{1}{A_1^2(u)}\mathrm{d}u + T_{0,3}\mathcal{C}z_R\chi_{\mathrm{cr}}^{(3)}\int_{-\infty}^{z_L}\frac{1}{A_1^2(u)}\mathrm{d}u + T_{0,1}^3\mathcal{C}z_R\chi_{\mathrm{air}}^{(3)}\int_{z_L}^{\infty}\frac{1}{A_1^2(u)}\mathrm{d}u \quad (4.96)$$

In the second step, we will define $\overline{\Delta\chi}_A^{(3)}$, which does not vary with the coherence, such that

$$T_{0,3}\chi_{\mathrm{cr}}^{(3)} = \overline{\Delta\chi}_A^{(3)} + T_{0,1}^3\chi_{\mathrm{air}}^{(3)} \quad (4.97)$$

and the last two integrals combine

$$\left(\overline{\Delta\chi}_A^{(3)} + T_{0,1}^3\chi_{\mathrm{air}}^{(3)}\right)\mathcal{C}z_R\chi_{\mathrm{cr}}^{(3)}\int_{-\infty}^{z_L}\frac{1}{A_1^2(u)}\mathrm{d}u + T_{0,1}^3\mathcal{C}z_R\chi_{\mathrm{air}}^{(3)}\int_{z_L}^{\infty}\frac{1}{A_1^2(u)}\mathrm{d}u = \overline{\Delta\chi}_A^{(3)}\mathcal{C}z_R\int_{-\infty}^{z_L}\frac{1}{A_1^2(u)}\mathrm{d}u \quad (4.98)$$

and so the total third harmonic field is

$$E_{30} = T_{0,3}\mathcal{C}z_R\delta\chi^{(3)}(t)\int_{-\infty}^{z_L}\frac{\Phi(u)}{A_1^2(u)}\mathrm{d}u + T_{0,3}\mathcal{C}z_R\chi_{\mathrm{cr}}^{(3)}\Delta\delta k''(t)\int_{-\infty}^{z_L}\frac{\Gamma(u)}{A_1^2(u)}\mathrm{d}u + \mathcal{C}z_R\overline{\Delta\chi}_B^{(3)}(t,z_L)\int_{-\infty}^{z_L}\frac{1}{A_1^2(u)}\mathrm{d}u + \overline{\Delta\chi}_A^{(3)}\mathcal{C}z_R\int_{-\infty}^{z_L}\frac{1}{A_1^2(u)}\mathrm{d}u \quad (4.99)$$

We shall number these integrals as functions of the interface position z_L

$$\mathcal{I}_1 = \int_{-\infty}^{z_L}\frac{\Phi(u)}{A_1^2(u)}e^{-i\Delta k z_R u}\mathrm{d}u, \quad (4.100)$$

$$\mathcal{I}_2 = \int_{-\infty}^{z_L}\frac{\left[\Delta\delta k'' - i\Delta\delta k'\right]\Gamma(u)}{A_1^2(u)}e^{-i\Delta k z_R u}\mathrm{d}u, \quad (4.101)$$

and

$$\mathcal{I}_3 = \int_{z_L}^{\infty}\frac{1}{A_1^2(u)}e^{-i\Delta k z_R u}\mathrm{d}u \quad (4.102)$$

As a consequence of combining integrals, we now have

$$\int_{-\infty}^{z_L} \frac{1}{A_1^2(u)} = -\mathcal{I}_3 \tag{4.103}$$

Now we write the integral solution in a more compact form, using these earlier definitions, noting the sign flip on the $\mathcal{I}_3$ terms,

$$E_{30} = \mathcal{C} z_R \left\{ T_{0,3} \delta\chi^{(3)}(t) \mathcal{I}_1(z_L) + T_{0,3} \chi_{\mathrm{cr}}^{(3)} \Delta\delta k''(t) \mathcal{I}_2(z_L) - \overline{\Delta\chi}_B^{(3)}(t, z_L) \mathcal{I}_3 - \overline{\Delta\chi}_A^{(3)} \mathcal{I}_3 \right\} \tag{4.104}$$

In this equation, the first term reflects coherent second hyper-Raman modulation. The second term reflects cascaded amplitude modulation. The third term captures the Fresnel boundary modulation. The last term does not depend on the coherence, and expresses unperturbed THG across the interface, modified to account for Fresnel transmission at the interface.

4.5.4.3 Detected Signals, Including Fresnel

Now the detected square magnitude, neglecting products of small perturbation terms is

$$\begin{aligned} S_3 = |\mathcal{C} z_R|^2 \overline{\Delta\chi}_A^{(3)} \Big\{ & 2\overline{\Delta\chi}_A^{(3)} |\mathcal{I}_3|^2 - 2T_{0,3} \delta\chi^{(3)}(t) \Re\left[\mathcal{I}_1 \mathcal{I}_3^*\right] \\ & - 2T_{0,3} \chi_{\mathrm{cr}}^{(3)} \Delta\delta k''(t) \Re\left[\mathcal{I}_2 \mathcal{I}_3^*\right] + 2\overline{\Delta\chi}_B^{(3)}(t, z_L) \Re\left[\mathcal{I}_3 \mathcal{I}_3^*\right] \Big\}. \end{aligned} \tag{4.105}$$

As before, the first term will be filtered out by lock-in detection, so we have

$$\begin{aligned} S_3 = |\mathcal{C} z_R|^2 \overline{\Delta\chi}_A^{(3)} \Big\{ & -2T_{0,3} \delta\chi^{(3)}(t) \Re\left[\mathcal{I}_1 \mathcal{I}_3^*\right] \\ & - 2T_{0,3} \chi_{\mathrm{cr}}^{(3)} \Delta\delta k''(t) \Re\left[\mathcal{I}_2 \mathcal{I}_3^*\right] + 2\overline{\Delta\chi}_B^{(3)}(t, z_L) \Re\left[\mathcal{I}_3 \mathcal{I}_3^*\right] \Big\} \\ & = S_{\mathrm{cshrs}} + S_{\mathrm{casc}} + S_{\mathrm{frnl}}. \end{aligned} \tag{4.106}$$

4.5.4.4 Coherent second hyper-Raman term

The CSHRS term differs has a factor $T_{0,3}$ to account for TH transmission at the exit face of the CSHRS signal generated in the bulk, and a a Fresnel-modified susceptibility difference $\overline{\Delta\chi}_A^{(3)}$,

$$S_{\mathrm{cshrs}} = -2T_{0,3} \left(\frac{w_{10}}{w_{30}} \right)^4 \left(\frac{\omega_3}{24cn_3} \right)^2 E_{10}^6 z_R^2 \overline{\Delta\chi}_A^{(3)} \delta\chi^{(3)}(t) \Re\left|\mathcal{I}_1 \mathcal{I}_3^*\right|. \tag{4.107}$$

Considering that $\delta\chi^{(3)} = \delta\chi_0^{(3)}\sin(\Omega_v\tau)$, and using a computer algebra system (MAXIMA) to solve the integrals, the full expression for the CSHRS signal is

$$S_{\text{cshrs}} = 2T_{0,3}\left(\frac{w_{10}}{w_{30}}\right)^4\left(\frac{\omega_3}{24cn_3}\right)^2 E_{10}^6 z_R^2\overline{\Delta\chi_A}^{(3)}\delta\chi_0^{(3)} \times \frac{\left(2x_L^3+2x_L\right)\tan^{-1}(x_L)+\pi x_L^3+2x_L^2+\pi x_L+4}{8x_L^4+16x_L^2+8}\sin(\Omega_v\tau) \quad (4.108)$$

The second hyper-Raman term is a sine proportional to

$$S_{\text{cshrs}}(t_{\text{pr}};x_L) = 2T_{0,3}\delta\chi^{(3)}(t_{\text{pr}})\frac{\left(2x_L^3+2x_L\right)\tan^{-1}(x_L)+\pi x_L^3+2x_L^2+\pi x_L+4}{8x_L^4+16x_L^2+8} \quad (4.109)$$

a potentially more aesthetically pleasing form:

$$S_{\text{cshrs}}(t_{\text{pr}};x_L) = 2T_{0,3}\delta\chi^{(3)}(t_{\text{pr}})\left\{\frac{x_L\tan^{-1}(x_L)}{4\left(x_L^2+1\right)}+\frac{x_L^2+2}{4\left(x_L^2+1\right)^2}+\frac{\pi x_L}{8\left(x_L^2+1\right)}\right\} \quad (4.110)$$

the function with respect to interface position x_L is shown in Fig. 4.3. It is asymmetric about the focus, showing a stronger contribution when the interface is placed beyond the focus, $x_L > 0$. To clarify, that is when the focus is *inside* the crystal.

4.5.4.5 Cascade term

The cascaded modulation term undergoes similar modification from Eq. (4.111), (and we have also dropped the imaginary part of the phase mismatch perturbation),

$$S_{\text{casc}} = -2T_{0,3}\left(\frac{w_{10}}{w_{30}}\right)^4\left(\frac{\omega_3}{24cn_3}\right)^2 E_{10}^6 z_R^2\overline{\Delta\chi_A}^{(3)}\chi_{\text{cr}}^{(3)}\Delta\delta k''(t)\Re\left|\mathcal{I}_2\mathcal{I}_3^*\right| \quad (4.111)$$

We expand the time-dependent perturbation according to its definition from Eq. (4.74), and the wavenumber k perturbation definitions for the fundamental and third harmonic found in Eq. (4.57)

$$\begin{aligned}\Delta\delta k''(t) &= \Im\left\{3\delta k_3(t)-\delta k_1(t)\right\} = 3\delta k_3''(t)-\delta k_1''(t)\\ &= \left\{-3\frac{\Omega_v}{\omega_3}\frac{\omega_3}{2cn_3}\delta\chi_{30}^{(1)}+\frac{\Omega_v}{\omega_1}\frac{\omega_1}{2cn_1}\delta\chi_{10}^{(1)}\right\}\cos[\Omega_v(t_{\text{pr}}+\tau)].\\ &= -\frac{\Omega_v}{c}\left\{3\frac{\delta\chi_{30}^{(1)}}{n_3}-\frac{\delta\chi_{10}^{(1)}}{n_1}\right\}\cos(\Omega_V t) \quad (4.112)\end{aligned}$$

Using this result and recalling the real part of the cascade integrals, and the following. From a quantum definition, the strength of the first-order perturbation is

$$\delta\chi_0^{(1)} = \frac{2}{\hbar}\left(\alpha' Q\right)^2 U. \quad (4.113)$$

where

$$Q_v = (w_{v2} - w_{v1}) \left| \langle v2 | q_v | v1 \rangle \right|^2 \tag{4.114}$$

describes the transition moment strength and statistical weights of the two lower levels. We do not expect the differential polarizability to vary with wavelength, so we have

$$S_{\text{casc}} = -2T_{0,3} \left(\frac{w_{10}}{w_{30}} \right)^4 \left(\frac{\omega_3}{24cn_3} \right)^2 E_{10}^6 z_R^2 \overline{\Delta\chi}_A^{(3)} \chi_{\text{cr}}^{(3)} \frac{\Omega_v}{c} \left\{ \frac{3}{n_3} - \frac{1}{n_1} \right\} \delta\chi_0^{(1)} \times z_R \frac{2\tan^{-1}(x_L) + \pi}{2x_L^2 + 2} \cos(\Omega_V t) \tag{4.115}$$

The cascaded amplitude modulation term is a cosine,

$$S_{\text{casc}} = -2T_{0,3} \chi_{\text{cr}}^{(3)} \Delta\delta k''(t_{\text{pr}}) \frac{2\tan^{-1}(x_L) + \pi}{2\left(x_L^2 + 2\right)} \tag{4.116}$$

and is shown in Fig. 4.3. The arctangent in the numerator gives this contribution a slight asymmetry, and its contribution is strongest when the focus is just inside the crystal, closer to the interface than the peak of the CSHRS term.

4.5.4.6 Fresnel term

We now examine the new term, which describes the effect of the Fresnel modulations

$$S_{\text{frnl}} = 2 \left(\frac{w_{10}}{w_{30}} \right)^4 \left(\frac{\omega_3}{24cn_3} \right)^2 E_{10}^6 z_R^2 \overline{\Delta\chi}_A^{(3)} \times \left[\delta T_3(t) \chi_{\text{cr}}^{(3)} - 3T_{0,1}^2 \delta T_1(t) \chi_{\text{air}}^{(3)} \right] \Phi(z_L) \Re\left\{ \mathcal{I}_3 \mathcal{I}_3^* \right\} \tag{4.117}$$

Noting that typically the crystal's nonlinear response is several orders of magnitude greater than air,

$$\chi_{\text{cr}}^{(3)} \sim 10^2 \times \chi_{\text{air}}^{(3)},$$

this reduces to

$$S_{\text{frnl}} = 2 \left(\frac{w_{10}}{w_{30}} \right)^4 \left(\frac{\omega_3}{24cn_3} \right)^2 E_{10}^6 z_R^2 \overline{\Delta\chi}_A^{(3)} \delta T_3(t) \chi_{\text{cr}}^{(3)} \Phi(z_L) \Re\left\{ \mathcal{I}_3 \mathcal{I}_3^* \right\} \tag{4.118}$$

Inserting the definition of the Fresnel perturbation from Eq. 3.50,

$$S_{\text{frnl}} = -2 \left(\frac{w_{10}}{w_{30}} \right)^4 \left(\frac{\omega_3}{24cn_3} \right)^2 E_{10}^6 z_R^2 \overline{\Delta\chi}_A^{(3)} \left(\frac{n_a}{n_c(n_a + n_c)^2} \right) \times \delta\chi_0^{(1)} \left| U_s(x,y,z) \right|^2 \sin\left[\Omega_v \left(t + \tau - u_{\text{pu}}^{-1} z \right) \right] \chi_{\text{cr}}^{(3)} \Phi(z_L) \Re\left\{ \mathcal{I}_3 \mathcal{I}_3^* \right\}. \tag{4.119}$$

The overall signal is proportional to $S_{\text{frnl}} \propto -\sin(\Omega_v t)$, and has opposite sign of the CSHRS term.

The interface-dependent functional form, in the transformed coordinates x,

$$\Phi(x_L)\Re\left\{\mathcal{I}_3\mathcal{I}_3^*\right\} \tag{4.120}$$

The product is

$$\frac{1}{1+x_L^2}\left(\int_{x_L}^{\infty}\frac{1}{(1+ix)^2}\mathrm{d}x\right)\left(\int_{x_L}^{\infty}\frac{1}{(1+ix)^2}\mathrm{d}x\right)^* \tag{4.121}$$

and the real part is

$$\Phi(x_L)\Re\left\{\mathcal{I}_3\mathcal{I}_3^*\right\} = \frac{1}{x_L^4+2x_L^2+1} \tag{4.122}$$

This function is symmetric about the focus.

Fresnel modulation is

$$S_{\text{frnl}} = \left[\delta T_3\chi_{\text{cr}}^{(3)} - 3T_{0,1}^2\delta T_1\chi_{\text{air}}^{(3)}\Phi(z_L)\right]\frac{1}{x_L^4+2x_L^2+1} \tag{4.123}$$

It can be argued that the overall sign of this expression is negative, since $\delta T_3 \approx \delta T_1$

$$3T_{0,1}^2\chi_{\text{air}}^{(3)} > \chi_{\text{cr}}^{(3)} \tag{4.124}$$

Note this appears inverse from the CSHRS term. It has opposite sign and has a peak when the focal plane is coincident with the interface.

4.5.5 Sum of detected terms

All the individual terms, normalized, are shown in Fig. 4.3 for comparison of their interface scan shape and peak position. The Fresnel term has been inverted to aid visual comparison with the other terms.

For now we ignore the imaginary part of the cascaded modulations. When we add up these terms with their sine and cosine parts, we can observe the amplitude and phase of the resulting sum of sinusoids. The signal is

$$S = S_{\text{cshrs}}\sin(\Omega t) + S_{\text{casc}}\cos(\Omega t) + S_{\text{frnl}}\cos(\Omega t) = g_{\text{sin}}\sin(\Omega t) + g_{\text{cos}}\cos(\Omega t) \tag{4.125}$$

where $g_{\text{sin}} = S_{\text{cshrs}} + S_{\text{frnl}}$ and $g_{\text{cos}} = S_{\text{casc}}$. The sum of sinusoids can be expressed as a single sinusoid $A\sin(\Omega t + \phi)$ with amplitude

$$A = g_{\text{sin}}^2 + g_{\text{cos}}^2 \tag{4.126}$$

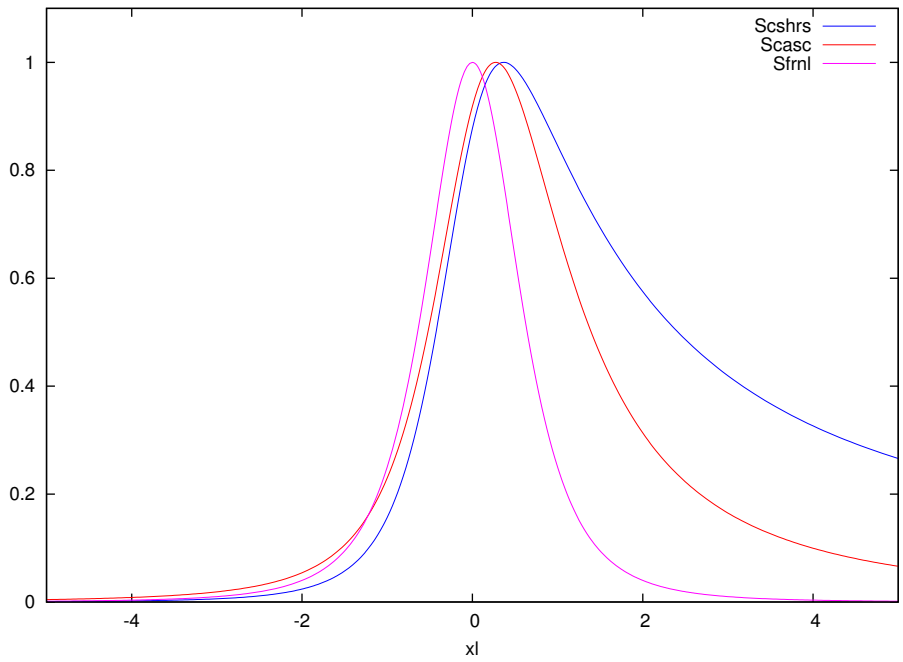

Figure 4.3: Interface translation dependence of the three CM-THG terms, coherent second hyper-Raman, cascaded amplitude modulation, and Fresnel boundary modulation. Curves normalized for visual comparison.

and phase

$$\phi = \tan^{-1}\left(\frac{g_{\sin}}{g_{\cos}}\right) \tag{4.127}$$

We don't have simple analytic expressions, so a plot will have to do. The combined amplitude is shown in Fig. 4.4. The dip in the middle reflects the fact that the strongest contributors are sine terms with opposite signs, and cancel each other out near the middle. The asymmetry is caused by the asymmetry in the cascaded amplitude modulation cosine term. The phase is shown in Fig. 4.5. It has an arctangent-like behavior, the π phase shift reflecting the shift between two sines of opposite sign. The transition in the middle is smoothed over by the presence of the cascaded amplitude modulation cosine term.

4.5.6 Relative strength of various terms

Here we investigate how changing relative strength of the various terms affects the appearance of a z-scan.

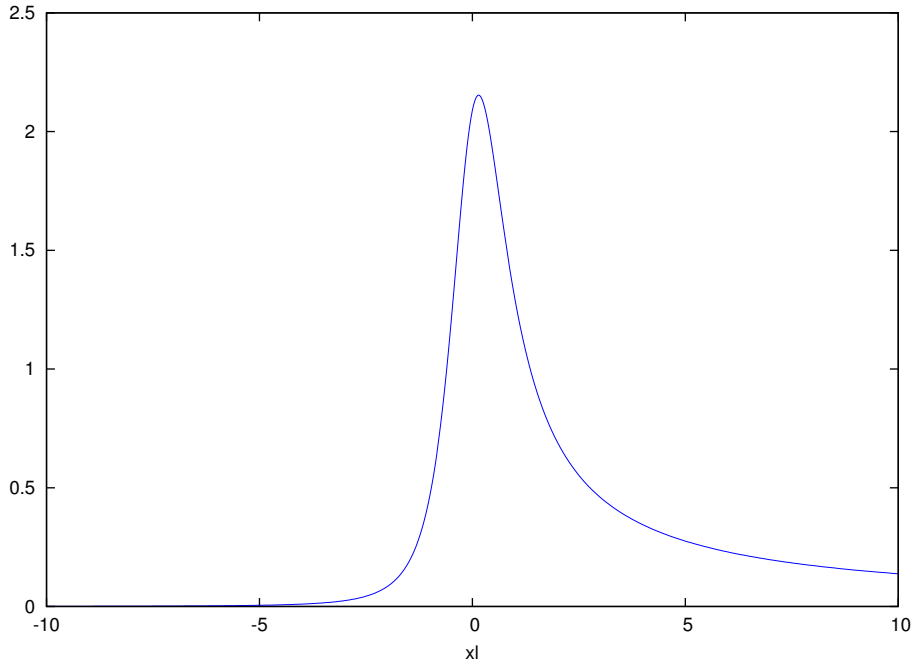

Figure 4.4: Combined amplitude of the detected CM-THG signal. Note the dip in the middle and asymmetry.

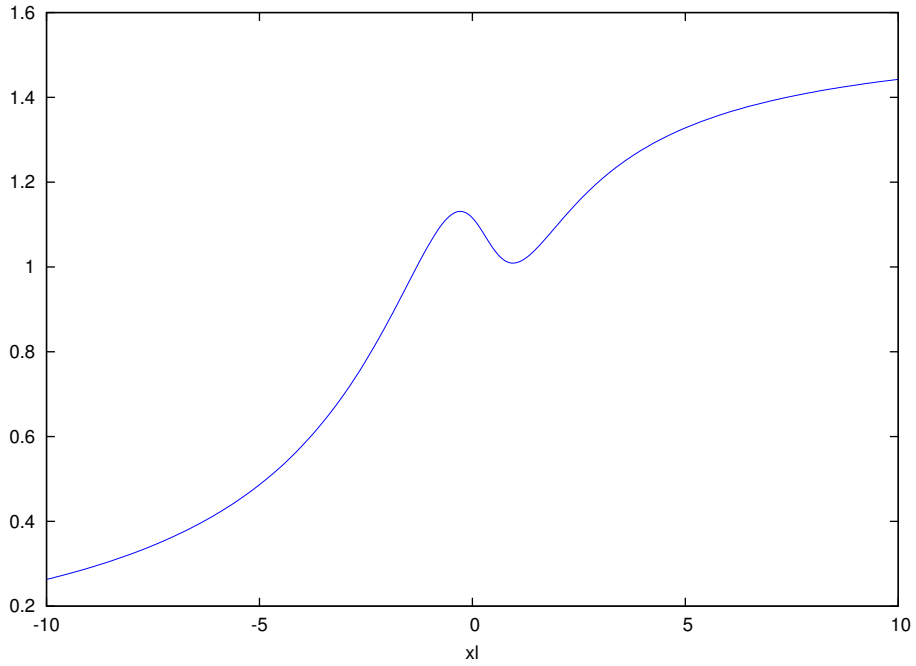

Figure 4.5: Combined phase of the detected CM-THG signal.

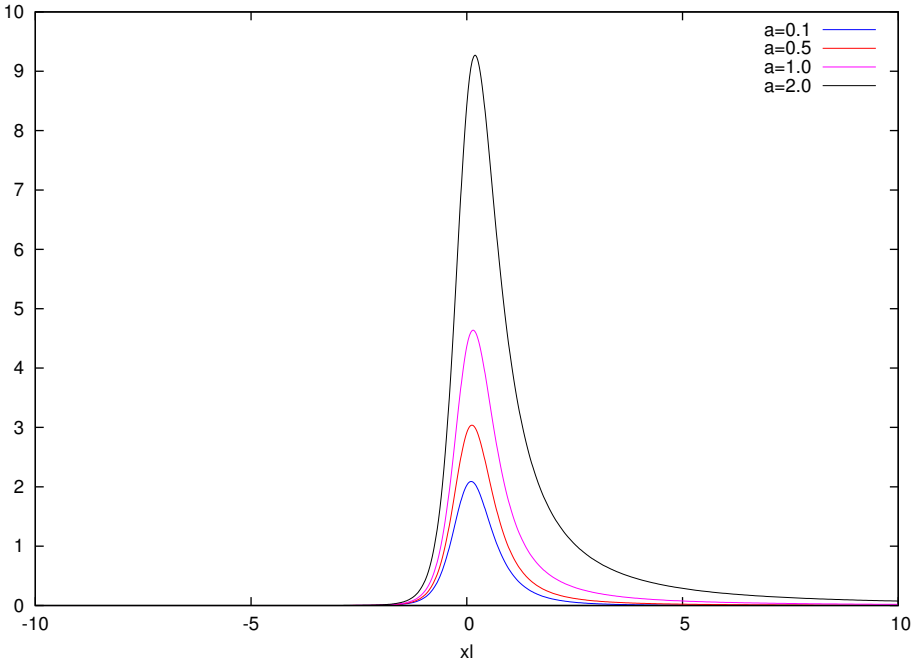

Figure 4.6: Amplitude for varying CSHRS contribution.

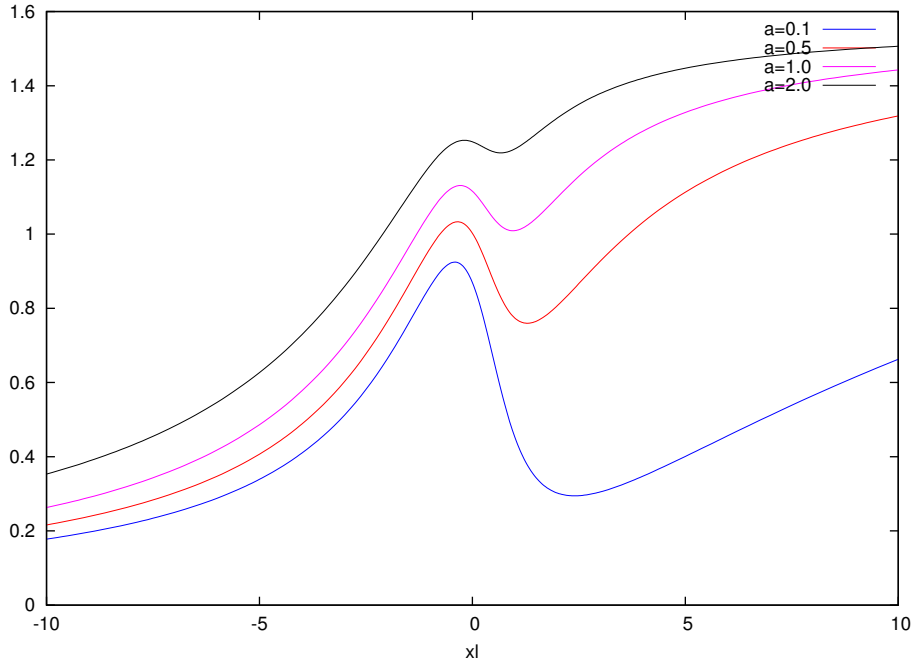

Figure 4.7: Phase for varying CSHRS contribution.

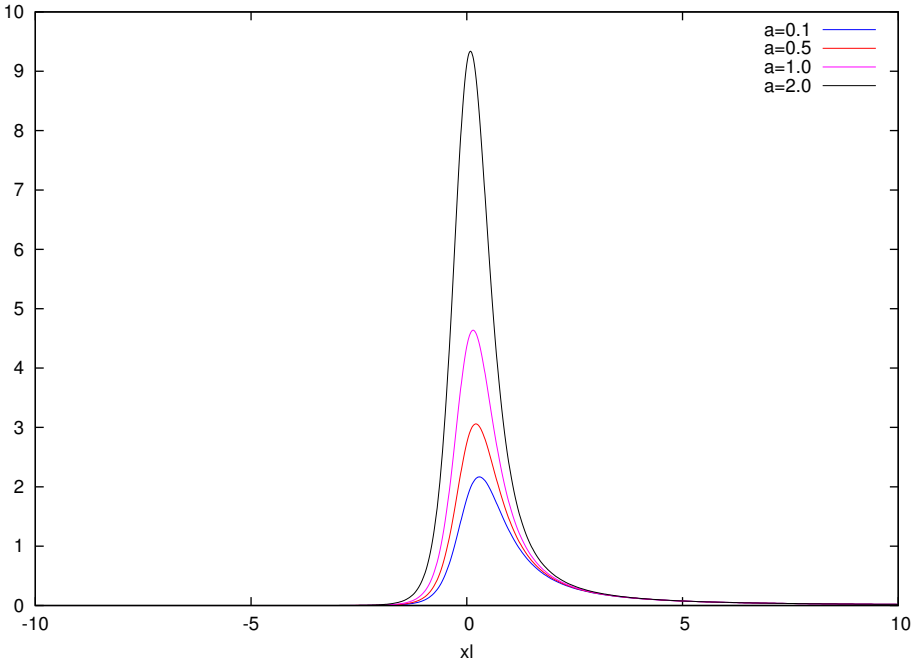

Figure 4.8: Amplitude for varying Fresnel modulation contribution.

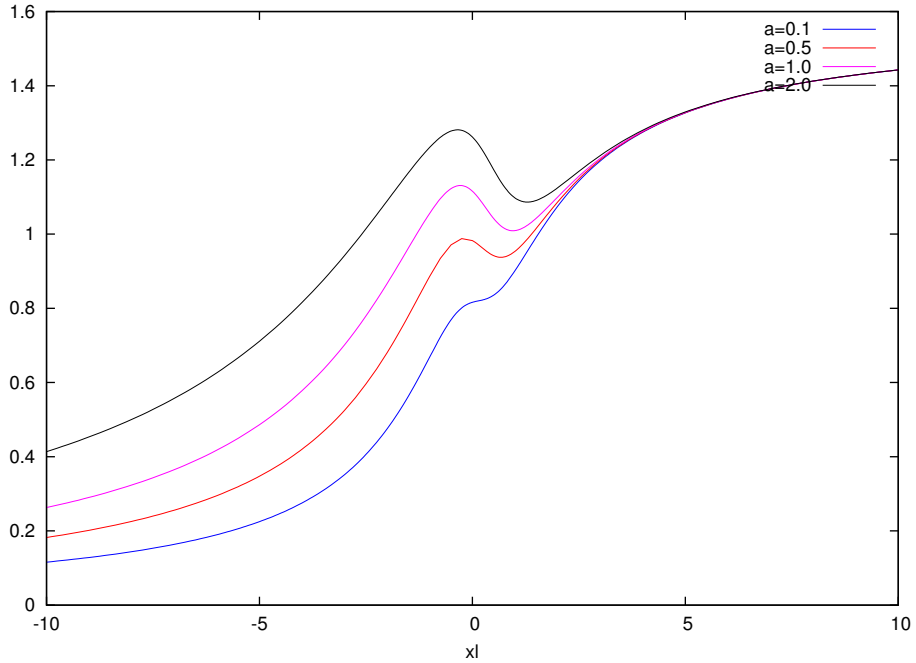

Figure 4.9: Phase for varying Fresnel modulation contribution.

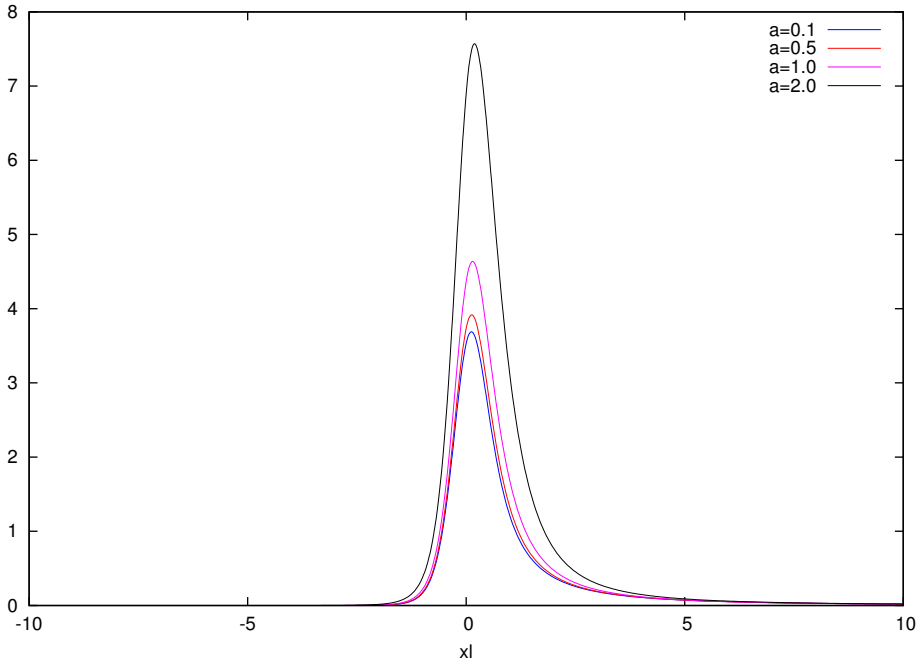

Figure 4.10: Amplitude for varying cascade contribution.

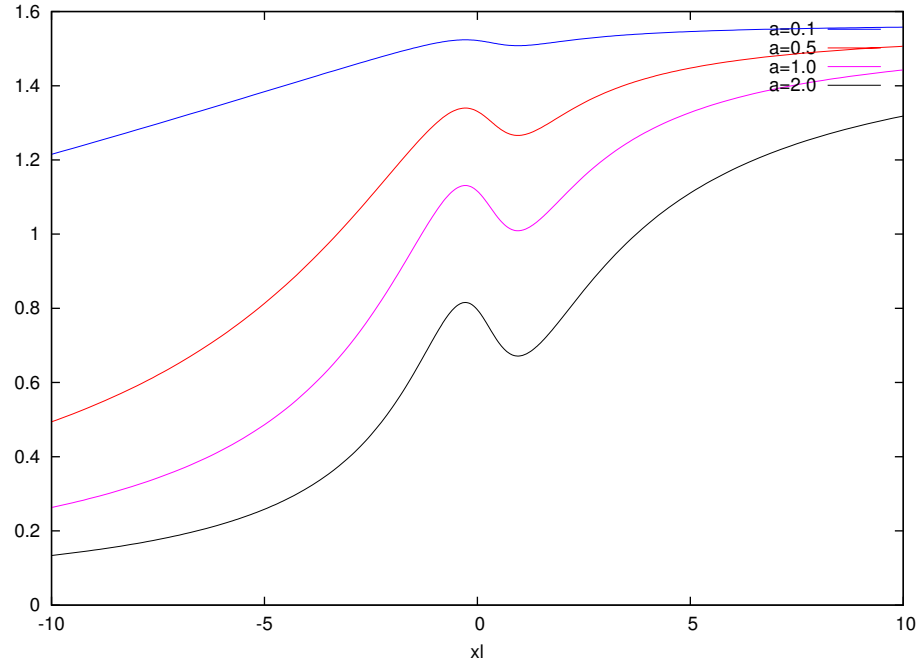

Figure 4.11: Phase for varying cascade contribution.

4.6 Note on group velocity mismatch

Recent investigations have shown group velocity mismatch (GVM) to be an important effect in third harmonic generation by tightly focused ultrafast pulses [94, 38]. Much work remains to be done in order to understand the effect that GVM has on CM-THG measurements. For now, a simplified analysis will show that GVM will cause an apparent narrowing of the interface scan profile, with no appreciable deviation from the Lorentzian lineshape. From this we anticipate the interface scan profiles of the CSHRS, cascade, and Fresnel modulation contributions will be preserved, and the general behavior of an interface scan will be preserved.

The group velocities for each of our samples are tabulated here, and may make a difference in terms of signal to noise ratio. BGO12 Sellmeier was reported in Ref [96].

Table 2: Phase and group velocity mismatch values for THG in selected materials. Fundamental wavelength is 800 nm.

Sample	n_{fnd}	n_{th}	$n_{g,\mathrm{fnd}}$	$n_{g,\mathrm{th}}$	Δk, $1/\mu$m	Δu, nm/ps
Quartz (o)	1.5383	1.5916	1.5543	1.722	-1.2466	0.55558
Fused silica	1.4533	1.4997	1.4671	1.6147	-1.0857	0.48864
BGO12	2.0712	2.6071	2.1565	4.5126	-12.5167	7.769
Sapphire (o)	1.7601	1.833	1.7816	2.0137	-1.7073	0.76875
BaF_2	1.4705	1.511	1.4802	1.6097	-0.94864	0.42925

4.6.1 Group velocity mismatch and vibrational sampling

The vibrational coherence will travel in the sample with the group velocity of the pump pulse [19]. In experiments that involve probing the coherence with a different color of light than was used to pump the coherence, this can lead to smearing of the sampled vibrations, or an attenuation of the sampled vibrational signal [45]. As the probe propagates in the coherence, it samples a different time delay at the front end of the sample, $\sin(\Omega_v \tau_{\mathrm{pp}})$ than at the back end, $\sin[\Omega_v(\tau_{\mathrm{pp}} + \Delta u^{-1} L)]$. In CM-THG, each of the three modulation pathways will be affected by group velocity walkoff differently:

- **CSHRS:** Perturbation of $\delta\chi^{(3)}$ involved in generating third harmonic will proceed at the group velocity of the fundamental.

- **Cascaded Amplitude:** Cascaded amplitude modulations involving probe fundamental modulation cascading to third harmonic generation will see no group walkoff effects. However, cascaded amplitude modulations where already-generated third harmonic experiences an amplitude modulation via $\delta k''$ may experience group walkoff sampling effects.

- **Fresnel:** Group velocity mismatch will not smear out sampling of the Fresnel perturbations by the third harmonic generated in the bulk. But if GV mismatch is appreciable, this may introduce an additional phase delay between the CSHRS and Fresnel contributions, so that they might not be perfectly π shifted.

4.6.2 Modeling THG group velocity mismatch

In order to simulate the effects of GVM in an interface scan, we use a model that is based on inserting the GVM directly into the J phase matching integral [38]

Assuming undepleted fundamental. The equation governing generation and propagation of the third harmonic of a probe pulse is, in the traveling frame of the third harmonic pulse is

$$\frac{\partial}{\partial\zeta}E_{3\mathrm{o}}(\zeta,t_3) = -i\frac{\omega_3}{2cn_3}\chi^{(3)}E_{\mathrm{o}}^3(\zeta,t_3+\Delta u^{-1}\zeta)e^{-i\Delta k} \tag{4.128}$$

where the phase mismatch is

$$\Delta k = 3k_1 - k_3, \tag{4.129}$$

and the group velocity mismatch is defined˜[48]

$$\Delta u^{-1} = \Delta u_{3,1}^{-1} = \frac{1}{u_3} - \frac{1}{u_1} = \frac{1}{c}\left(n_3 - n_1 - \lambda_3\frac{\partial n_3}{\partial\lambda_3} - \lambda_1\frac{\partial n_1}{\partial\lambda_1}\right). \tag{4.130}$$

The group velocity walkoff length is defined

$$L_w' = (|\Delta u^{-1}|\Delta\omega_1)^{-1} \tag{4.131}$$

where $\Delta\omega_1$ is the spectral FWHM of the fundamental. For transform-limited pulses,

$$L_w = \frac{\tau_1}{\Delta u^{-1}} \tag{4.132}$$

If $z < L_w$, THG should behave similarly to the CW case. When $z > L_w$, the solutions are more complicated.

We consider a fundamental beam incident on the nonlinear medium beginning at z_0, with a waist located at z_w, written in the spatial frequency domain

$$\hat{E}_{\mathrm{o}}(k_x, k_y, z, t_{\mathrm{o}}) = E_{0,\mathrm{o}}(t_{\mathrm{o}}) \frac{w_{10}^2}{4\pi} \left\{ -(k_x^2 + k_y^2) \left[\frac{w_{10}^2}{4} - i \frac{z_w}{2k_1} \right] \right\}, \tag{4.133}$$

where $E_{0,\mathrm{o}}$ is the slowly varying temporal envelope of the probe field, presumed to be a transform-limited Gaussian here:

$$E_{0,\mathrm{o}}(t_{\mathrm{o}}) = E_{0,\mathrm{o}} e^{-a t_{\mathrm{o}}^2}. \tag{4.134}$$

The equation governing TH generation and propagation now has the transverse Laplacian, and works out to be, in the traveling frame of the third harmonic pulse

$$\begin{aligned} &\frac{\partial}{\partial \zeta} \hat{E}_{3\mathrm{o}}(\zeta, k_x, k_y, t_{3\mathrm{o}}) \\ &\qquad = i \frac{\omega_3 w_{10}^2}{24 c n_3} \chi^{(3)} \frac{E_{0,\mathrm{o}}^3(t_{3\mathrm{o}} + \Delta u^{-1} \zeta)}{(4\pi)^3 A_1^2(\zeta)} \exp\left\{ -(k_x^2 + k_y^2) \frac{w_{10}^2 A_1(\zeta)}{12} \right\} e^{-i \Delta k \zeta} \\ &\qquad\qquad - i \frac{k_x^2 + k_y^2}{2k_3} \hat{E}_{3\mathrm{o}}, \end{aligned} \tag{4.135}$$

where we have defined

$$A_1(\zeta) = 1 + i \frac{2(\zeta - z_w)}{w_{10}^2 k_1} \tag{4.136}$$

We introduce a trial solution for $\hat{E}_{3\mathrm{o}}$ in the form of a Gaussian,

$$\hat{E}_{3\mathrm{o}} = E_{0,3\mathrm{p}}(\zeta) \frac{w_{30}^2}{4\pi} \exp\left\{ -(k_x^2 + k_y^2) \frac{w_{30}^2 A_3(\zeta)}{4} \right\}, \tag{4.137}$$

where $A_3(\zeta)$ is similarly defined to $A_1(\zeta)$ as in Eq. (4.136). We compute the derivative of Eq. (4.137), insert it into Eq. (4.135), and combine terms to arrive at an expression for the third harmonic field's complex deviation from the usual Gaussian, $E_{0,,3\mathrm{p}}$, as a function of propagation

$$\frac{\partial}{\partial \zeta} E_{0,3\mathrm{p}}(\zeta, t_{3\mathrm{o}}) = i \frac{\pi \omega_3 w_{10}^2}{6 c n_3 w_{30}^2} \chi_0^{(3)} \frac{E_{0,\mathrm{o}}^3(t_{3\mathrm{o}} + \Delta u^{-1} \zeta)}{(4\pi)^3 A_1^2(\zeta)} e^{-i \Delta k \zeta}. \tag{4.138}$$

This result should be roughly equivalent to Eq.(2.10.10) in Ref.[39]. Here we have assumed that the fundamental and TH spot sizes are fixed, $w_{10}^2 = 3 w_{30}^2$, the beams are confocal (z_w is the same for both fundamental an TH), and the following ratio is negligible,

$$\frac{1}{3k_1} - \frac{1}{k_3} = \frac{k_3 - 3k_1}{3k_1 k_3} \approx 0. \tag{4.139}$$

To find the TH generated, we must integrate Eq. (4.138)

$$E_{0,3p}(\zeta, t_{3o}) = i\frac{\pi\omega_3 w_{10}^2}{6cn_3 w_{30}^2(4\pi)^3}\chi_0^{(3)}\int \frac{E_{0,o}^3(t_{3o}+\Delta u^{-1}\zeta')}{A_1^2(\zeta')}e^{-i\Delta k\zeta'}\mathrm{d}\zeta'. \tag{4.140}$$

This equation is in agreement with the starting point for the calculations found in Eq. (2a) of Ref. [38], and will form the basis of our model. However, we will deviate slightly from their approach by integrating from $-\infty$ to $+\infty$, including THG in air, not just across the solid material in the focus of the beam. We assume GVM Δu^{-1} and phase mismatch Δk to be negligible in air. At this point, we will also drop the constants in front of the integral, in order to simplify matters. The total far-field third harmonic across a crystal/air boundary is the result of the two integrals, proportional to

$$E_{0,3p}(\zeta, t_{3o}) \propto \chi_{0,xtl}^{(3)}\int \frac{E_{0,o}^3(t_{3o}+\Delta u^{-1}\zeta')}{A_1^2(\zeta')}e^{-i\Delta k\zeta'}\mathrm{d}\zeta' + \chi_{0,air}^{(3)}\int \frac{E_{0,o}^3(t_{3o})}{A_1^2(\zeta')}e^{-i\Delta k\zeta'}\mathrm{d}\zeta', \tag{4.141}$$

where the third-order susceptibilities of air and the crystal are $\chi_{0,air}^{(3)}$ and $\chi_{0,air}^{(3)}$, respectively.

4.6.3 Numerical simulations

Using MATLAB, we set up a pulse with a Gaussian temporal profile, a FWHM of 40 fs, a time axis of 2^7 samples and spacing of 1 fs. We use sapphire as a material, in order to compare our results to Ref. [38]. The third-order susceptibility of sapphire is taken to be $\chi_{0,xtl}^{(3)} = 2.2\times10^{-14}$ esu and that for air is $\chi_{0,air}^{(3)} = 1.2\times10^{-17}$ esu [39]. We assume a focal spot of $w_0 = 4.4$ μm, similar to what was found in the CM-THG measurements.

The integrals for third harmonic generation in the crystal and air, Eq. (4.141), are solved in MATLAB using the adaptive Gauss-Kronrod (GK) quadrature function `quadgk()` which is appropriate for infinite-bounded integrals [97]. In order to ensure convergence in a reasonable amount of time, relative and absolute tolerances are set to 1×10^{-3}.

4.6.4 Interface scan for a thin piece of sapphire

we show the total integrated THG, as would be collected by a PMT, while scanning a thin 330 μm sample of sapphire through the focus, using the $w_1 = 4.4$ μm spot size found in Stoker[38], which translates to a Rayleigh range of $z_R = \pi w_1^2 n(\lambda_1)/\lambda_1 = 134$ μm, where $\lambda_1 = 800$ nm. To calculate accurately the THG that collected in the far field, we must break

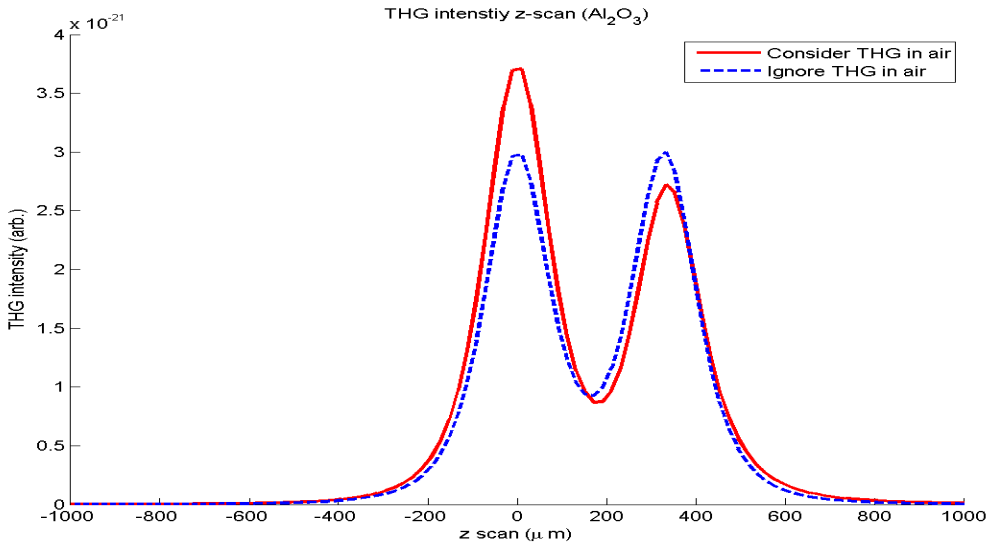

Figure 4.12: Simulated z-scan of a 330 μm sapphire sample, to be compared with Stoker Figs. 1 and 4. Note we reproduce the asymmetry not accounted for by Stoker when THG in air is considered in the model.

the integration apart into three regions: air before the sample, the sample, and air after the sample. We assume phase mismatch in air to be negligible, so that the integration, modified from Eq. (4.140), becomes:

$$E_{0,3p}(\zeta, t_{3o}) = i\frac{\pi\omega_3 w_{10}^2}{6cn_3 w_{30}^2(4\pi)^3}\left\{\chi^{(3)}_{0,\text{air}}\int_{-\infty}^{0}\frac{E^3_{0,o}(t_{3o}+\Delta u^{-1}\zeta)}{A_1^2(\zeta)}\mathrm{d}\zeta\right.$$
$$+\chi^{(3)}_{0,\text{mat}}\int_0^L\frac{E^3_{0,o}(t_{3o}+\Delta u^{-1}\zeta)}{A_1^2(\zeta)}e^{-i\Delta k\zeta}\mathrm{d}\zeta$$
$$\left.+\chi^{(3)}_{0,\text{air}}\int_0^{\infty}\frac{E^3_{0,o}(t_{3o}+\Delta u^{-1}\zeta)}{A_1^2(\zeta)}\mathrm{d}\zeta\right\} \quad (4.142)$$

Integrated pulse intensity for each position of the scan is taken to be

$$I_3(\zeta) = \left|\int_{-\infty}^{\infty} E_{0,3p}(\zeta, t_{3o})\ \mathrm{d}t\right|^2 \quad (4.143)$$

The results for area shown in Fig. 4.12. The z-scan profile is the superposition of two Lorentzians, one centered at each face. Adding in the THG in air leads to a distinct asymmetric profile.

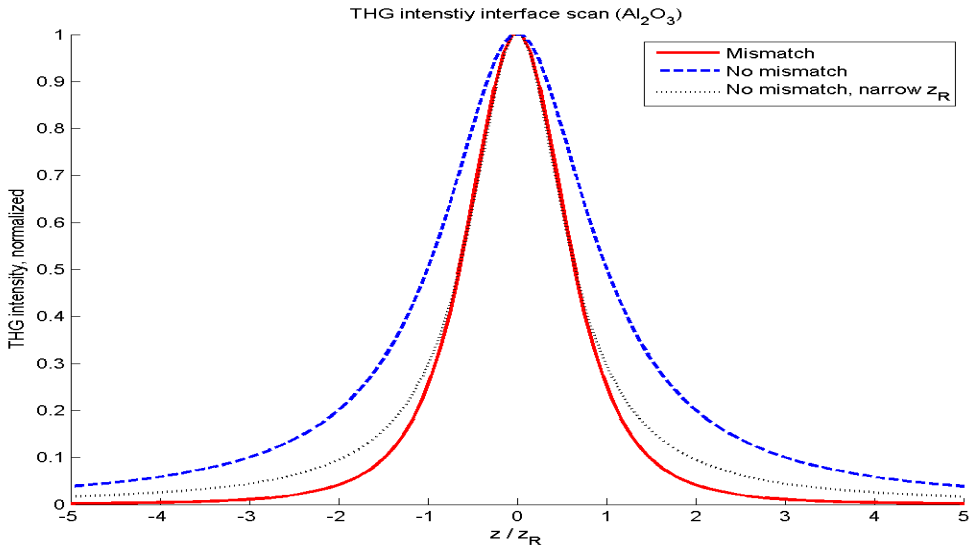

Figure 4.13: Simulated THG z-scan of a thick sapphire sample across the face away from the focusing objective. Scans are shown for the CW case (no mismatch), and the pulse case with group and phase match taken into account. A CW case with narrowed Rayleigh range is also shown for comparison.

4.6.5 Back interface scan profile

Now we examine an interface scan across the back face of a crystal, similar to the CM-THG experiments described later. Instead of three material integrals and two boundaries, we solve the two integrals in Eq. 4.141. The resulting interface scan profile is shown in Fig. 4.13. The simulation reveals the peak intensity of the third harmonic, when the interface lines up with the focal plane, to be 2.5×10^{-5} times less intense than the phase-matched CW case. The shape remains a Lorentzian, with a reduction in FWHM by 64.5%. For comparison, the interface scan profile, neglecting mismatch, with a Rayleigh range narrowed by 64.5% is shown.

4.6.6 Discussion

Even though THG in air is three orders of magnitude weaker than in sapphire, including the air THG makes a noticeable difference in the shape of the z-scan for a thin material. In fact, this asymmetric profile has been observed in experiment but had been left unaccounted for by theory in previous treatments [38]. The authors speculated that the intensity variation across the peaks was due to different amounts of group velocity dispersion (GVD) on the

pulses at the front and back faces. The model shown here does not account for GVD in propagating through the bulk material.

In the interface scan at the back face, within a Rayleigh range z_R of the interface, the general Lorentzian shape predicted by the CW model is preserved when accounting for group velocity mismatch, except for a narrowing of the profile, leading to an apparent reduction in the Rayleigh range. Since this is the case, we anticipate the interface scan behavior for the three contributions of the CM-THG signal will also follow closely the CW case laid out in the theory above. However, there will be slight variations as the interface is translated more than z_R away from the focal plane. Clearly more investigation into finding analytic expressions for THG interface scans with group velocity- and phase-mismatch will need to be conducted. It might be possible to adapt the expressions in Ref. [94] to an interface scan scenario.

4.7 Summary

This is the summary, and walk-through of the theoretical model.

Separation of the contributions to the CM-THG signal requires a model of evolution of the far-field TH as a function of the crystal interface position with respect to the focal plane of the pump and probe fields. We start with the differential equation describing propagation of the probe pulse in the presence of a perturbed linear susceptibility.

4.7.1 Assumptions made

The following list summarizes the assumptions we have made

1. Both fundamental and third harmonic propagate in tightly focused Gaussian spatial modes, sharing the same focal plane.

2. Pulses have a transform-limited Gaussian temporal envelope.

The following effects have been neglected.

1. Variations in the focus due to differing indices of refraction across the interface are negligible.

2. Transverse spatial variations in the pump.

3. Phase and group velocity mismatch. To some degree we may justify this knowing that CARS microscopy has demonstrated the broad spectrum of k wavevectors in a tight focus lead to relaxed phase matching conditions [98, 99].

4. Dispersion and pulse broadening.

4.7.2 Fundamental solutions

The solution for linear propagation of a probe pulse exhibits amplitude and phase modulation of the probe due to the coherence via perturbations of the complex index of refraction.

This solution for the modulated probe fundamental is included as the source term in the equation describing generation and propagation of TH in the presence of a perturbed nonlinear susceptibility. In the tight focusing limit, integration is performed with infinite bounds along the propagation direction to find the far-field TH [39]. We treat this integral as a sum:

$$\int_{-\infty}^{\infty} f(z)\mathrm{d}z = T\int_{-\infty}^{z_L} f_{\mathrm{crystal}}(z)\mathrm{d}z + \int_{z_L}^{\infty} f_{\mathrm{air}}(z)\mathrm{d}z. \tag{4.144}$$

In other words, we integrate over $-\infty < z < z_L$ in the crystal bulk and over $z_L < z < \infty$ in air, where z_L is the interface position. The first integral is multiplied by the perturbed Fresnel transmission coefficient T to account for transmission modulation of bulk-generated third harmonic at the interface.

4.7.3 Total collected far-field signal

We find the far-field TH intensity is a superposition of four components: the unperturbed third harmonic $E_{3,0}$; a coherent second hyper-Raman scattering term $E_{3,\mathrm{cshrs}}$; cascaded amplitude modulations $E_{3,\mathrm{casc}}$; and a Fresnel boundary-modulated term $E_{3,\mathrm{frnl}}$. The detected intensity is

$$\approx |E_{3,0}|^2 + E_{3,0}^* E_{3,\mathrm{cshrs}}(\tau) + E_{3,0}^* E_{3,\mathrm{casc}}(\tau) + E_{3,0}^* E_{3,\mathrm{frnl}}(\tau) + \mathrm{c.c.},$$

where $|E_{3,0}|^2$ is the unperturbed contribution rejected by a lock-in amplifier, and the remaining contributions are the weak VC-modulated TH signal heterodyned with the strong

unmodulated TH, resulting in vibrational signal enhancement. Each of these terms depends on the position of the interface relative to the focal plane ξ and the pump–probe delay τ. We express interface position as $\xi = (z_L - z_0)/z_R$, where $z_L - z_0$ is the distance from the focal plane to the interface referenced to an arbitrary offset, and $z_R = \pi w_0^2/\lambda$ is the Rayleigh range of the focused pulses.

4.7.4 Coherent second hyper-Raman component

The heterodyned CSHRS signal contribution is

$$S_{\text{cshrs}}(\xi,\tau) = E_{3,0}(\xi)^* E_{3,\text{cshrs}}(\xi,\tau) + \text{c.c.} = K_{\text{cshrs}}\; g_{\text{cshrs}}(\xi)\sin(\Omega\tau)\,, \tag{4.145}$$

following the sinusoidal form of $E_{3,\text{cshrs}} \propto \delta\chi^{(3)} \propto \sin(\Omega\tau)$. The coefficient K_{cshrs} indicates the strength of the contribution and $g(\xi)$ describes the dependence on translation of the interface.

4.7.5 Cascaded component

The second contribution is due to cascaded effects from perturbation of the linear susceptibility. The probe energy is modulated by the imaginary part of the index perturbations $\propto \cos(\Omega\tau)$. The modulated probe then generates TH reflecting this prior amplitude modulation. The functional form is:

$$S_{\text{casc}}(\xi,\tau) = E_{3,0}^*(\xi) E_{3,\text{casc}}(\xi,\tau) + \text{c.c.} = K_{\text{casc}}\; g_{\text{casc}}(\xi)\cos(\Omega\tau)\,. \tag{4.146}$$

4.7.6 Fresnel boundary modulation component

The final term is due to modulation of the Fresnel transmission coefficient at the exit face of the crystal:

$$S_{\text{frnl}}(\xi,\tau) = E_{3,0}^*(\xi) E_{3,\text{frnl}}(\xi,\tau) + \text{c.c.} = -K_{\text{frnl}}\; g_{\text{frnl}}(\xi)\sin(\Omega\tau)\,, \tag{4.147}$$

4.7.7 Translation dependence

The translation dependence of these three terms is found by integration of the third harmonic generated in the focal volume, the details of which will be published separately. The resulting

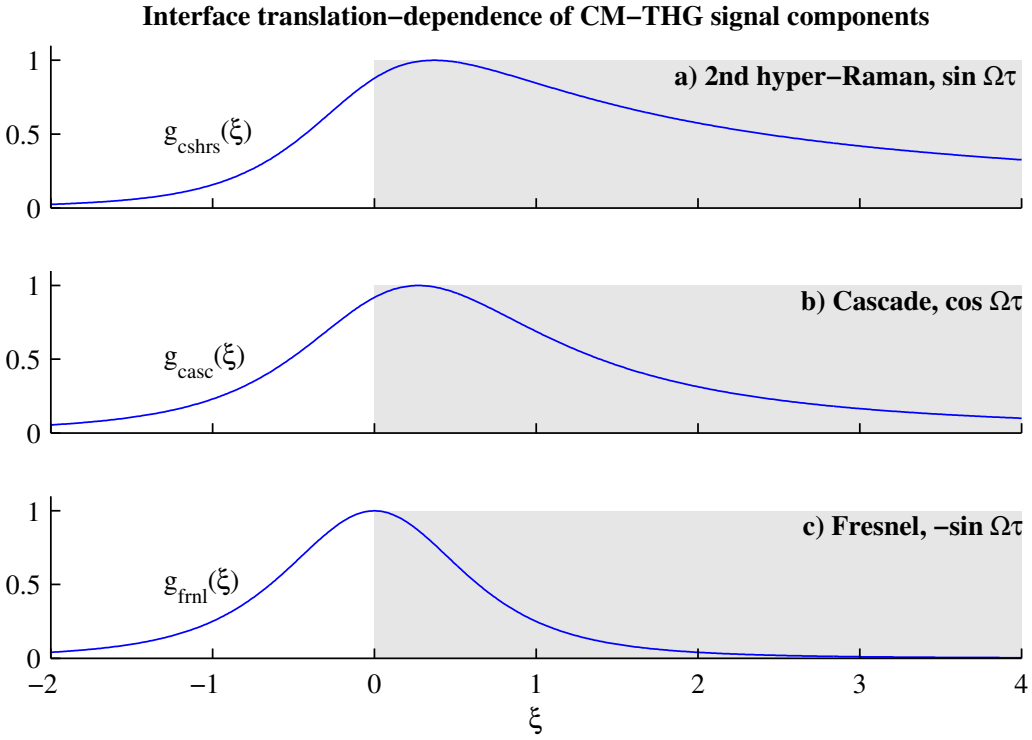

Figure 4.14: Normalized plots of translation dependence of CM-THG contributions. a) Coherent second hyper-Raman, showing a peak when the focus is inside the bulk. b) Cascaded amplitude modulation, exhibiting a peak with the focus in the bulk, but closer to the interface. c) Fresnel modulation, showing a peak when the focus is on the interface. Shaded area shows positions where focus is in the bulk.

translation dependence of each contribution is:

$$g_{\text{cshrs}}(\xi) = \left\{ \frac{\xi\left[\tan^{-1}(\xi) + \pi/2\right]}{4\left(\xi^2+1\right)} + \frac{\xi^2+2}{4\left(\xi^2+1\right)^2} \right\}, \tag{4.148}$$

$$g_{\text{casc}}(\xi) = \frac{\tan^{-1}(\xi) + \pi/2}{\xi^2+1}, \tag{4.149}$$

$$g_{\text{frnl}}(\xi) = \frac{1}{\xi^2+1}. \tag{4.150}$$

Each of these is shown in Fig. 4.14. The CSHRS and cascaded contributions have peaks in the bulk, whereas the Fresnel contribution has its peak when the focus is on the interface.

When combined, these three effects are distinguishable by a shift in the CM-THG vibrational signal with respect to τ.

$$\begin{aligned} S(\xi,\tau) &= [K_{\text{cshrs}}\ g_{\text{cshrs}}(\xi) - K_{\text{frnl}}\ g_{\text{frnl}}(\xi)]\sin(\Omega\tau) \\ &\quad + K_{\text{casc}}\ g_{\text{casc}}(\xi)\cos(\Omega\tau) \\ &= A(\xi)\sin\left[\Omega\tau + \phi(\xi)\right], \end{aligned} \tag{4.151}$$

where $A(\xi)$ is the coherently combined amplitude and the delay shift is

$$\phi(\xi) = \tan^{-1}\left\{\frac{K_{\text{cshrs}}\ g_{\text{cshrs}}(\xi) - K_{\text{frnl}}\ g_{\text{frnl}}(\xi)}{K_{\text{casc}}\ g_{\text{casc}}(\xi)}\right\}. \tag{4.152}$$

Competition between the cascade and the two other contributions in Eq. (4.151) provides a smooth π delay shift transition as the focus is scanned from within the bulk to the interface, as will be shown in Figs. 5.5 and 5.6(b). If we were to neglect CSHRS, we would observe a $\pi/2$ phase shift between surface Fresnel modulations and cascaded amplitude modulations, consistent with previous findings [92].

4.7.8 Conclusion

Capitalizing on the translation dependence and phase shift, we separate the contributions from the CM-THG signal by recording coherent THG vibrational spectra as a function of z_L and fitting the data to the model.

CHAPTER V

CM-THG EXPERIMENTS

Here we present experimental results to confirm the theory presented in the previous section. We observe coherent vibrational modulation of third harmonic generation (CM-THG), and perform an interface scan to confirm the presence of the three sources of CM-THG modulation: coherent second hyper-Raman (CSHRS), cascaded amplitude modulation, and Fresnel boundary modulation.

Here, we report the first observation of CSHRS – with only to our knowledge one prior report of incoherent second hyper-Raman scattering [100]. Despite common use of hyper-Raman spectroscopy [101], weak interaction makes second hyper-Raman measurements elusive [95]. Even though selection rules for second hyper-Raman interactions have been proposed [102], to our knowledge they have never been experimentally verified. As shown in the previous section, heterodyning with the unmodulated TH signal enables measurement of this weak phenomenon.

We probe vibrational coherences (VC), prepared via non-resonant impulsive stimulated Raman scattering (ISRS) [19], both at and near a crystal–air interface. We introduce a method called coherence-modulated third harmonic generation (CM-THG) where the influence of vibrations on probe pulse propagation and TH generation are observed. The measurements are performed with noncentrosymmetric crystals with a nonzero even-order nonlinear response in bulk, making surface-specific even-order measurements difficult to obtain.

5.1 Experimental setup

The setup is shown in Fig. 5.1. The experiment uses pulses from a Ti:sapphire oscillator (KMLabs, Boulder, CO), with 60 nm bandwidth centered at 780 nm. A SF-10 prism pair, with 56 cm tip-to-tip separation compensates for the GDD imparted to the pulses by the

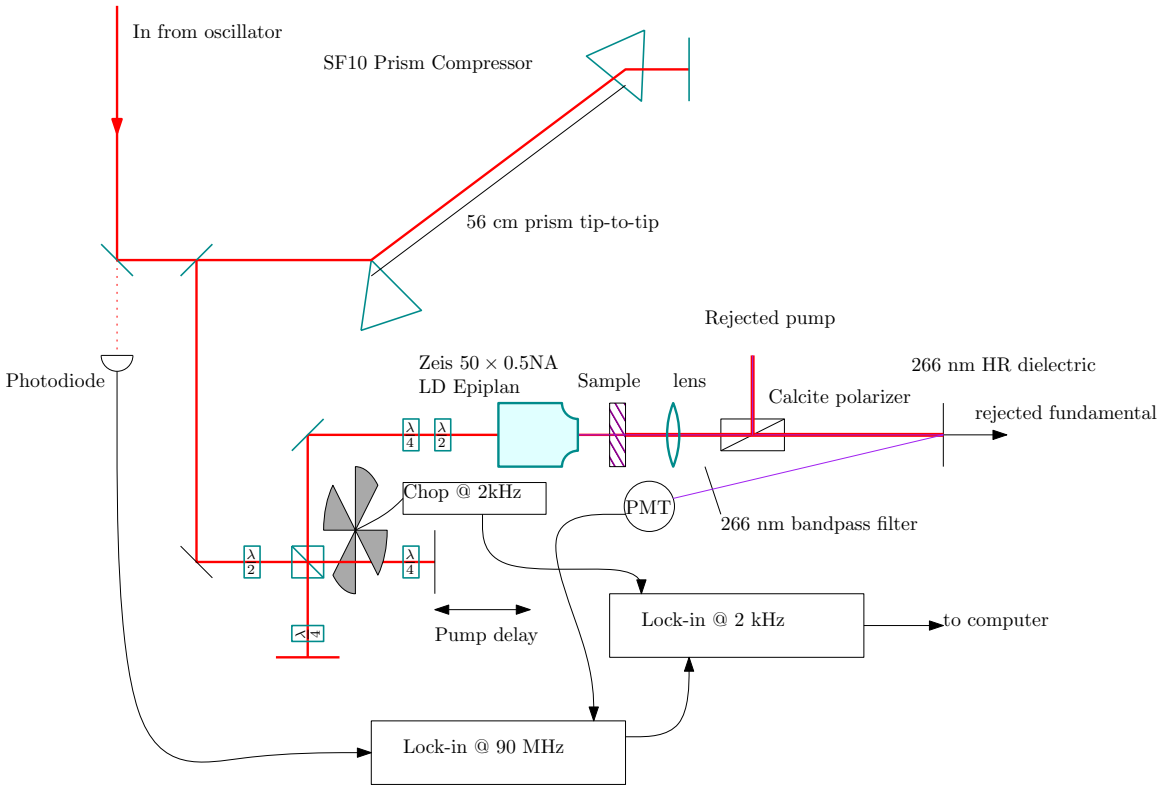

Figure 5.1: CM-THG experimental setup.

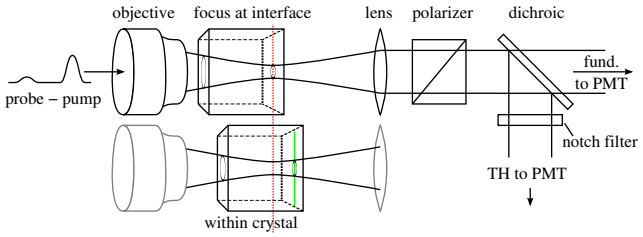

Figure 5.2: CM-THG interface scan experiment. As the crystal is translated through the focus, the CM-THG contributions vary. The CSHRS signal has its peak with the focus in the bulk, as shown. Placing the interface on the focus leads to a peak Fresnel boundary modulation contribution.

optics in the set-up, ensuring short pulses at the sample. A Michelson interferometer using a ThorLabs polarizing cube beamsplitter splits each incident pulse into orthogonally polarized pump and probe pulses. As shown in Fig. 5.2, an objective (Zeiss Epiplan 0.5 NA, 50x long working distance) focuses the pulses onto the back interface of a 100 μm thick, solid crystal sample. Third harmonic in the focal volume, and collected with a 30 mm UV-grade fused silica lens. A calcite polarizer (ThorLabs, 5mm aperture, 20mm thick) is used to reject the pump light after the sample, passing the probe light. Then a dielectric mirror optimized for high reflection at 266 nm (CVI Melles Griot) directs the third harmonic toward an optical interference filter (260BP10, Omega Optical). The filtered probe third harmonic is then measured with a Hamamatsu R928 side-on photomultiplier tube.

We minimize noise by cascading two lock-in detectors. The first operates on the laser oscillator's repetition rate at $\sim$ 90 MHz, the output of which is fed into the second lock-in operating on the pump chop frequency at 2 kHz. Any modulations on the probe pulse due to the pump-induced coherence will occur at the pump chop frequency. Finally A pump–probe delay scan over τ yields a time-resolved trace of the VC.

5.2 Delay scan results

Delay scans for $Bi_4Ge_3O_{12}$ (BGO12), BaF_2 and $LiTaO_3$ (supplied by MTI Corporation, Richmond, CA) are shown in Fig.5.3. We obtain Raman spectra both by windowed fast-Fourier transform (FFT) and linear prediction (LPSVD)[103], as described in Appendix C. In BGO12 we see the expected 92, 203, and 363 cm^{-1} A_1 lattice vibrations [104]. BaF_2 exhibits a single peak, the T_{2g} 240 cm^{-1} mode [105]. $LiTaO_3$ exhibits several peaks; the strongest likely corresponding to the A_1 354 cm^{-1} and/or E 345 cm^{-1} modes [106]

5.2.1 Boiling in liquids

It was found that exposing a liquid such as CCl_4 to the oscillator pulses resulted in enough heating at the focal spot to cause bubbles to form. In our initial delay scans, we thought we had observed a periodic vibrational signal, but the periodicity was simply related to the bubble formation. When the focus is translated to the liquid/glass interface, this phenomenon leads quickly to surface damage on the glass, probably due to lensing from the

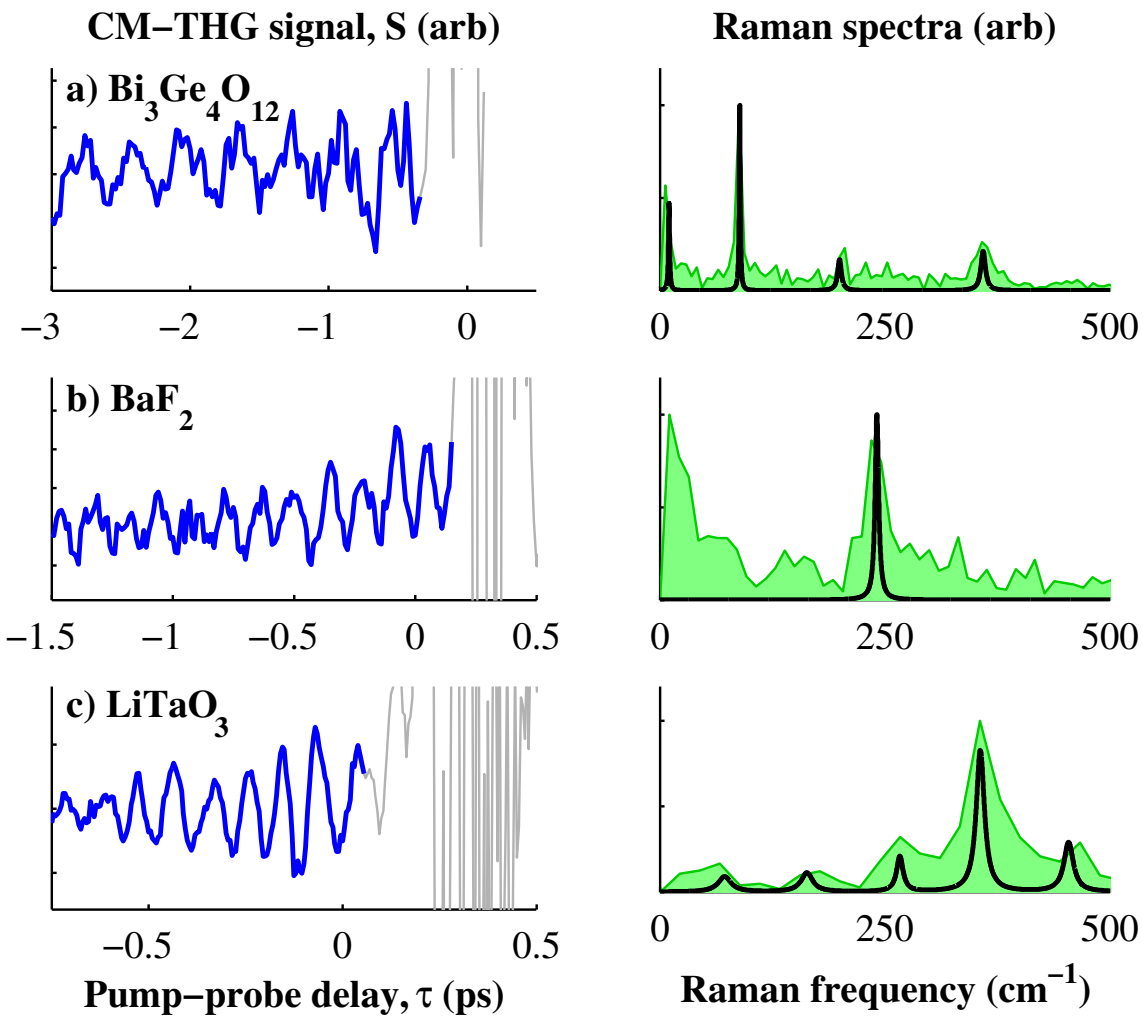

Figure 5.3: CM-THG delay scan results for BGO12, BaF_2, and $LiTaO_3$ (left column). Raman spectra (right column) from windowed FFT (green patch) and LPSVD (black line).

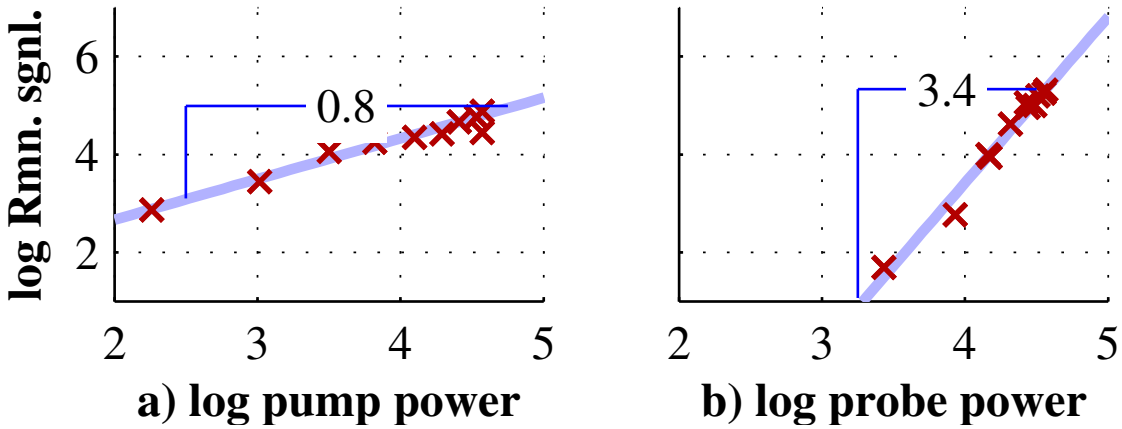

Figure 5.4: Dependence of CMTHG signal on pump and probe power.

bubble, heating and melting of the glass, or surface enhancement of the field due to the formation of a liquid/gas interface. The result is a bright white flash followed by disruption of the beam, evident in an irregular spatial pattern of the fundamental after the sample.

One solution is to use a flow cell. Alternatively, blocking and unblocking the beam periodically allows for the liquid to cool between shots. The periodic attenuation from the lighthouse is enough to make this work.

5.3 Confirm third-order behavior

We confirm the 2nd order behavior of ISRS pumping and 3rd order behavior of TH probing by varying the pump and probe power respectively, while recording the signal strength (area under the curve) of the 92 cm^{-1} mode. A log-log plot (Fig. 5.4) of the signal strength, with respect to pump and probe power respectively, yields linear fit slopes of 0.83 ± 0.10 and 3.39 ± 0.33, for a 95% confidence interval.

5.4 Interface scan, model fit

To examine the translation dependence of the signal contributions, we perform BGO12 interface scans at probe delays long enough to ensure isolation of the long lived 92 cm^{-1} mode. The interface scan is performed with a ThorLabs piezo controller, using the device's internal offset voltage to position the stage. An external control voltage fed into the piezo controller caused fluctuations in the position large enough to cause significant distortions

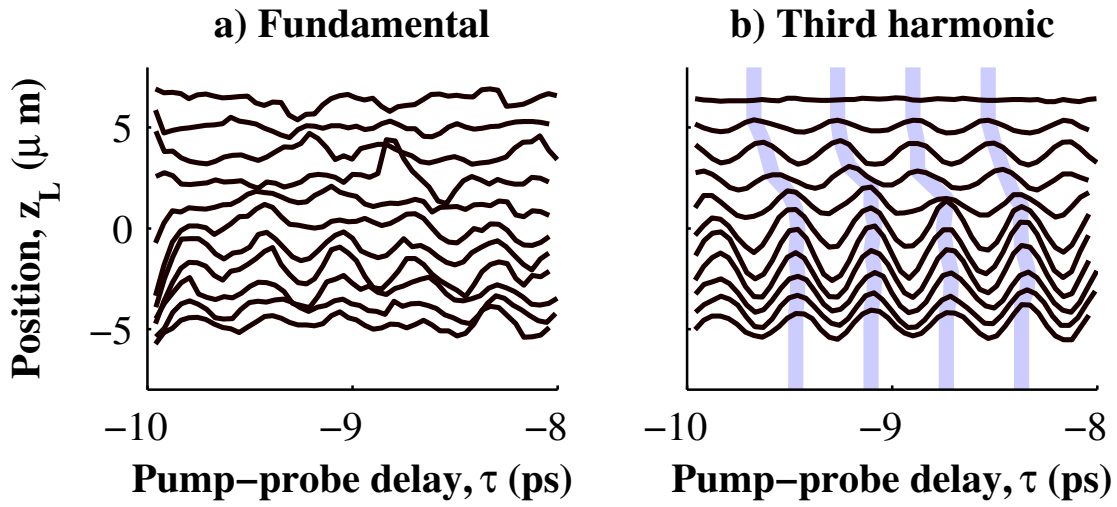

Figure 5.5: Probe fundamental amplitude modulations (a) vs. probe-generated third harmonic modulations (b) through an interface scan. CM-THG consistently exhibits better SNR. Light blue lines connect peaks to highlight phase shift across interface scan.

in the measurement. A better set-up would be to use a feedback-stabilized piezo stage and controller.We simultaneously observe modulations of the probe fundamental intensity and the third harmonic intensity for 11 different interface translation positions, as shown in Fig. 5.5. The delay scans in the figure are scaled and offset by the interface position for visual comparison of signal to noise ratio (SNR) and phase shift across the interface.

To compare the amount of noise in the fundamental and TH scans, we fit each delay scan to a sine function $Y = A\sin(\Omega\tau + \phi)$ using MATLAB's `fminunc()` function. Then we calculate the root mean square error (RMSE) of the fit. Defining SNR $= A/\text{RMSE}$, we find the average SNR for the CM-THG signals is 7.1, while the average for the fundamental amplitude modulations is 1.3. This improvement is due to heterodyne detection of the CM-THG contributions with the unperturbed TH.

Then we repeated the interface scan, this time recording only the TH signal and acquiring delay scans for 37 different interface positions. The results of fitting a sine amplitude and phase to these data are shown in the blue crosses in Fig. 5.6(a), and the blue circles in Fig. 5.6(b), respectively. The predicted π shift in the phase $\phi(\xi)$ observed in Fig. 5.5 is confirmed in Fig. 5.6(b). We extract the separable contributions, CSHRS, cascaded modulation, and Fresnel modulation, through parameter fitting of K_{cshrs}, K_{casc}, K_{frnl}, z_0, and z_R

to expressions for the interface-dependent amplitude and phase,

$$\begin{aligned} S(\xi,\tau) &= \left[K_{\text{cshrs}}\ g_{\text{cshrs}}(\xi) - K_{\text{frnl}}\ g_{\text{frnl}}(\xi)\right]\sin(\Omega\tau) \\ &\quad + K_{\text{casc}}\ g_{\text{casc}}(\xi)\cos(\Omega\tau) \\ &= A(\xi)\sin\left[\Omega\tau + \phi(\xi)\right], \end{aligned} \tag{5.1}$$

where $A(\xi)$ is the coherently combined amplitude and the delay shift is

$$\phi(\xi) = \tan^{-1}\left\{\frac{K_{\text{cshrs}}\ g_{\text{cshrs}}(\xi) - K_{\text{frnl}}\ g_{\text{frnl}}(\xi)}{K_{\text{casc}}\ g_{\text{casc}}(\xi)}\right\}. \tag{5.2}$$

The fit utilized `fminunc()`, repeated with 100 random initial guesses to avoid local minima. The fit shows the same general functional form and a π phase shift as the interface is translated through the focus. The relative strengths of the CSHRS, cascade, and Fresnel contributions are 1.5, 0.12, and 1.1, respectively. This confirms the observation of a strong CSHRS signal and an interface-specific Fresnel-modulated THG signal. Focusing characteristics. The numerical aperture and spot size are related by

$$\text{NA} = n\sin\theta = \frac{2\lambda}{\pi D}$$

where theta is the cone half-angle, Rayleigh range to spot size relation is

$$zR = \frac{\pi w_0^2}{\lambda}.$$

The Rayleigh range of 3.25 μm obtained is in good agreement with the 2.8 μm expected from a 0.5 NA objective underfilled by approximately 60%. Disagreement between the model and the data at the edges of Fig. 5.6 may stem from assuming a perfect Gaussian focus, not correcting the focus for a change in index of refraction across the interface, and neglecting TH absorption in the crystal.

Interface scans with two other objectives have been attempted, but were not successful. The NewFocus asphere 0.55 NA, most likely due to chromatic aberration. We also tried a Meiji 20x 0.4 NA S-plan; it is uncertain why this objective did not reveal such a translation dependence.

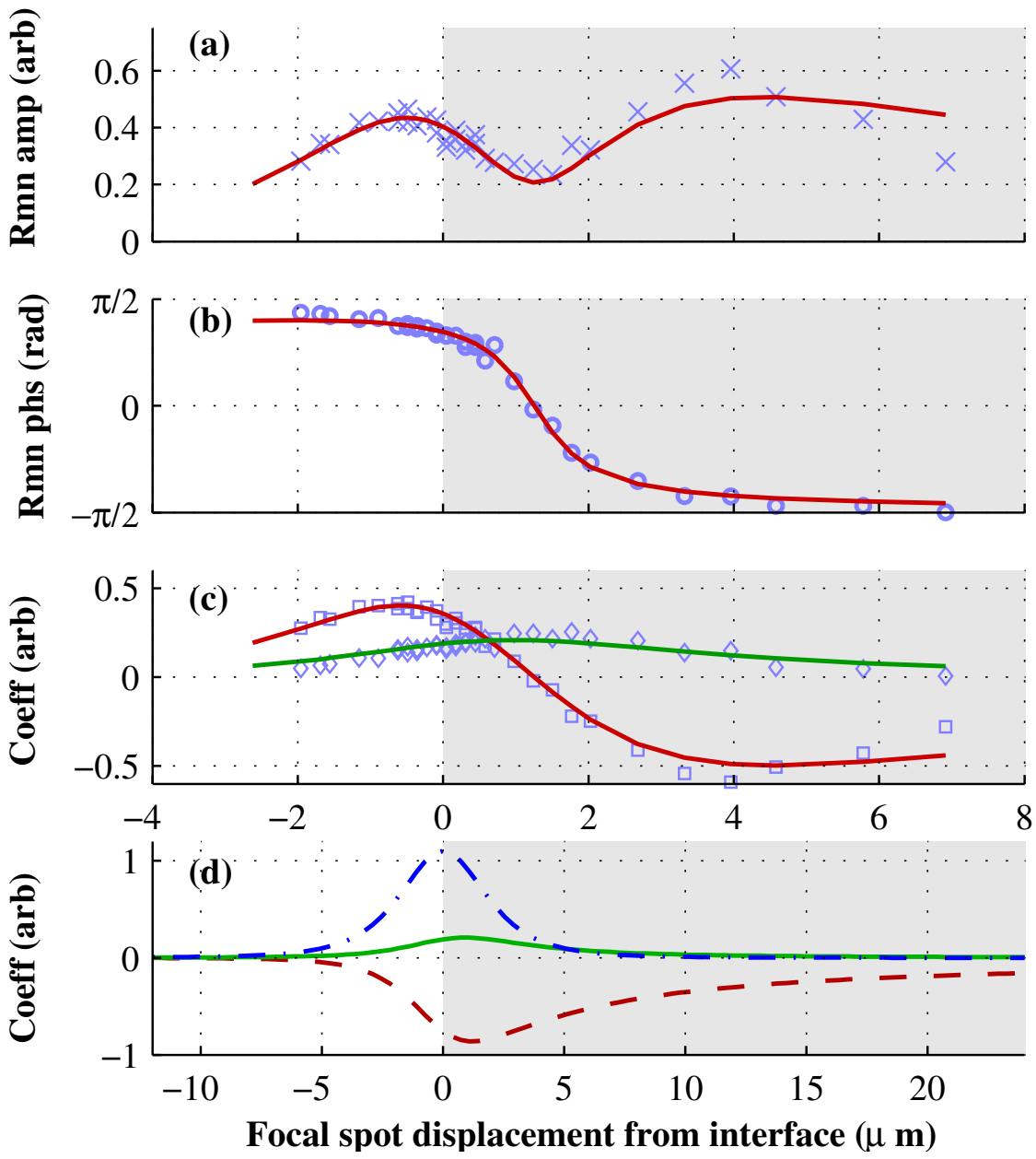

Figure 5.6: Analysis of CM-THG interface scan: (a) Measured amplitude of Raman signal (blue crosses) and model fit (red line). (b) Measured phase of Raman signal (blue circles) and model fit (red line). (c) Decomposition of measured signal into sine (blue squares) and cosine (blue diamonds) components, with model fits (red line and green line, respectively). (e) Model fit, extrapolated beyond interface scan range: CSHRS (red dash line), cascade (green solid line), and Fresnel modulation (blue dash-dot line). Shaded regions on right correspond to focal plane in the bulk, while region on left is focal plane in air.

CHAPTER VI

RAPID BIREFRINGENT DELAY SCANNER

6.1 Signal to noise problems

In a typical pump–probe experiment, an oscillator pulse having 1˜nJ energy and a duration of 50˜fs is split into a pump and probe pulse in a Michelson interferometer. The pump–probe delay is τ. The pump excites a vibrational coherence with amplitude proportional to the intensity of the pump I_{p}. The third harmonic intensity, which would be detected by a square-law detector is $I_{\mathrm{TH}} \propto |\chi^{(3)} E_{\mathrm{o}}^3|$.

The chopping/lock-in amplifier technique can eliminate much of the white noise, but any low-frequency fluctuations that are slower than the lock-in amplifier's time constant still get through. To work around this, we implemented a rapid-scanning alternative. The measurements are taken at such a scan rate that an entire delay scan completes faster than these slow drifts. We introduce a method based on the angle-dependent birefringent delay imparted by a crystal [55]

6.2 Signal averaging

It is commonly reported that signal to noise improves with $\sqrt{n}$ averages. But this does not take into account the spectral character of the noise. Consider a case where we measure a steady illumination of a PMT with a stable light source, neglecting shot noise. Suppose the only source of noise is from PMT gain drifts by 10% over the course of a few minutes. If we were to acquire $n = 1000$ samples over the course of a few hours, we might expect the gain drifts to average out to some degree, and we would obtain a better estimate of the illumination intensity than with a single measurement. But suppose we acquire $n = 1000$ samples over the course of 1 second, at a 1 kHz sampling rate. In this case, the averaged result could easily over- or under-estimate the illumination intensity by 10%, and the acquisition and averaging of many samples has gained us nothing.

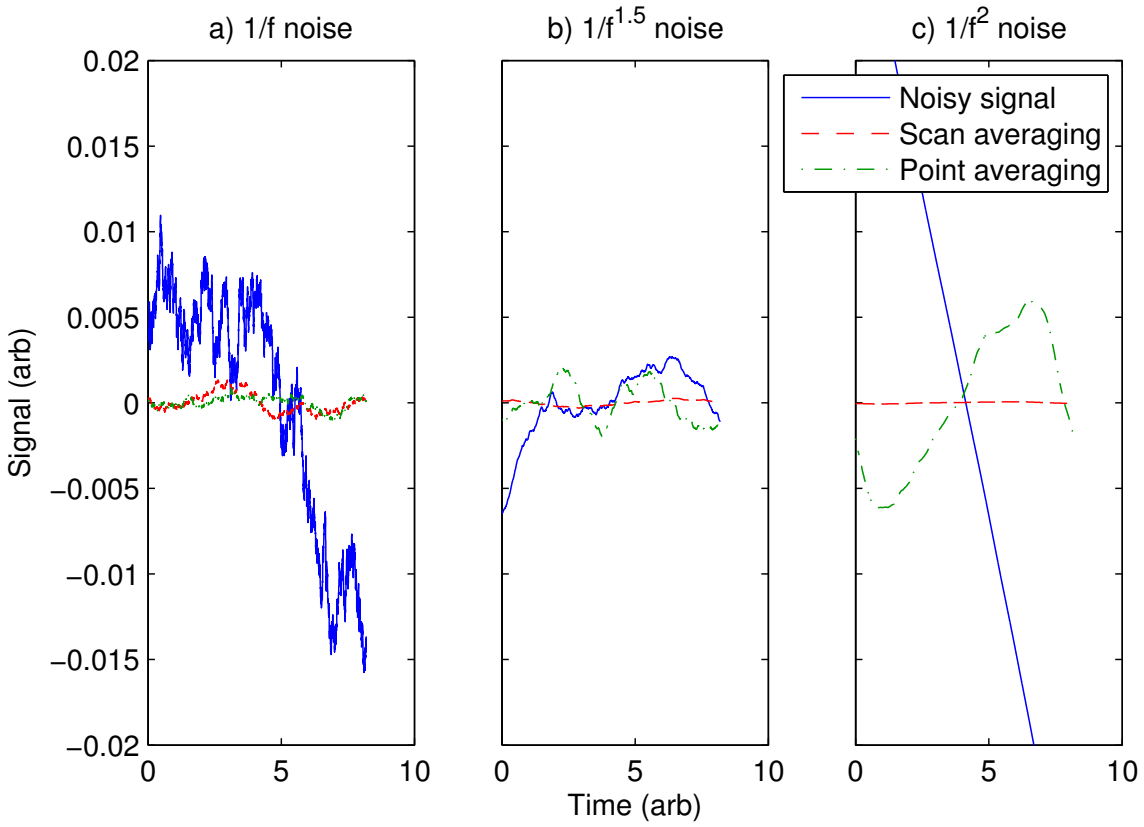

Figure 6.1: Comparison of scan averaging vs. point averaging for increasingly increasingly red noise.

Laser noise and gain drift in the PMT will show up as low-frequency modulations, and will pass through the lock-in's filter, so it seems this is a poor choice. If the fluctuations are slow enough that a few cycles will go through in a delay scan, then the noise may be averaged out by repeating delay scans.

Simulations to show this makes a difference. Whether anything is gained by rapid scan averaging depends on the nature of the noise. If it is $1/f$, that is pink noise, the characteristics of the averaged scans seem about the same. But for $1/f^n$ and $n > 1$ (e.g. red noise), averaging scans seems to produced better results.

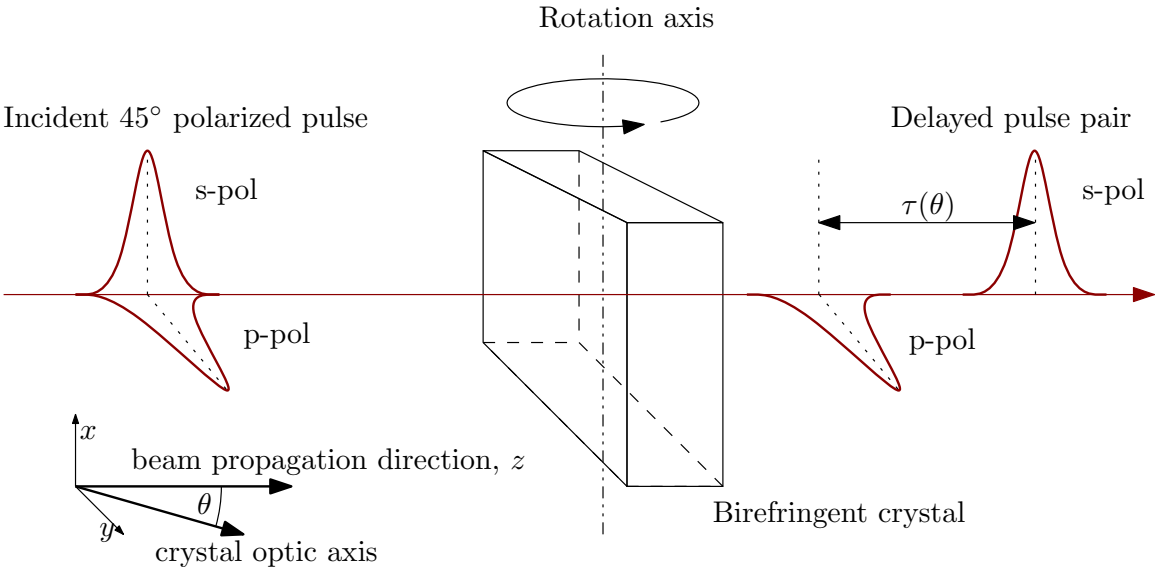

Figure 6.2: A single pass through birefringent delay crystal imparts an angle-dependent delay between the orthogonally polarized incident pulses.

6.3 Set-up and operation principles

The rapid birefringent delay scanner operates on the angle-dependent pulse splitting from a thick birefringent crystal [55]. Figure 6.3 shows the set-up for a single pass through the crystal. We mount the birefringent crystal on a motor shaft, with the optic axis perpendicular to the axis of rotation. A pulse incident at 45° to the eigenaxes of the crystal, the ordinary and extraordinary axes, will be projected onto the eigenaxes, and the pulse propagating along the extraordinary axis experiences a varying group delay as a function of crystal angle, $\tau(\theta)$. Care must be taken to safely block the surface reflection from the crystal (the sweeping surface reflections have earned the device the nickname *lighthouse*).

In practice, we double-pass the rotating delay crystal, as shown in Fig. 6.3. This has the effect of doubling the attainable delay range and compensating for spatial walkoff of the two pulses in the crystal [55]. Since the delay imparted by the crystal can only be positive, a second crystal, with its optic and of rotation axes orthogonal to those of the delay crystal, is placed to pre-compensate the delay. This allows the scanner to sweep a range of delays encompassing time-overlap between the two pulses. We use an uncoated 5 mm thick calcite displacer (Lambda Research Optics, Inc.) for the delay crystal, mounted on a feedback-stabilized brushless DC motor (Faulhaber, supplied by Micro Motion Solutions).

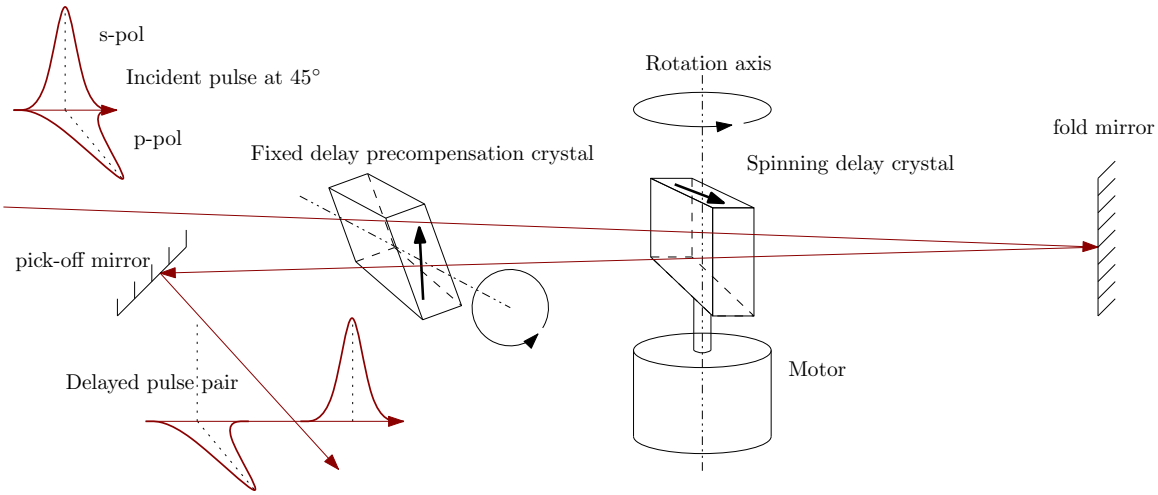

Figure 6.3: Birefringent delay scanner set-up with a double-passed delay crystal and a delay pre-compensation crystal.

We place a 1/2 waveplate before the scanner to control the balance of pump and probe power. For CM-THG measurements, since the signal is proportional to the cube of the probe power and only the square of the pump power, the best signal is obtained with a more intense probe than pump. The output of the pick-off mirror after the scanner is directed through a 1/4 waveplate and a 1/2 waveplate, then focused on to the sample with a Meji $20x$ 0.4 NA objective, and collected as described in the CM-THG section.

In order to produce short enough pulses to excite the high frequency mode in $CdWO_4$, we had to re-build the prism compressor using fused silica prisms (instead of SF10). The less dispersive glass resulted in less residual third order dispersion, allowing us to more effectively compress the pulses at the focus [107]. However, the less dispersive nature of fused silica required us to increase the prism tip-to-tip separation to 215 cm. The compressor is folded to decrease the amount of space it occupies on the table.

We also abandoned the 266 nm bandpass filter (260BP10, Omega Optical), which is only rated for 12% throughput, in favor of spatially separating the fundamental and third harmonic with a pair of Pellin-Broca prisms (ThorLabs) and an iris to block the fundamental. Furthermore, we replaced the calcite polarizer (Thorlabs), which only transmits around 50% of the third harmonic, with a β-BBO Wollaston polarizer with anti-reflection coatings and transmission of 99% (DayOptics, China). These modifications significantly improved the

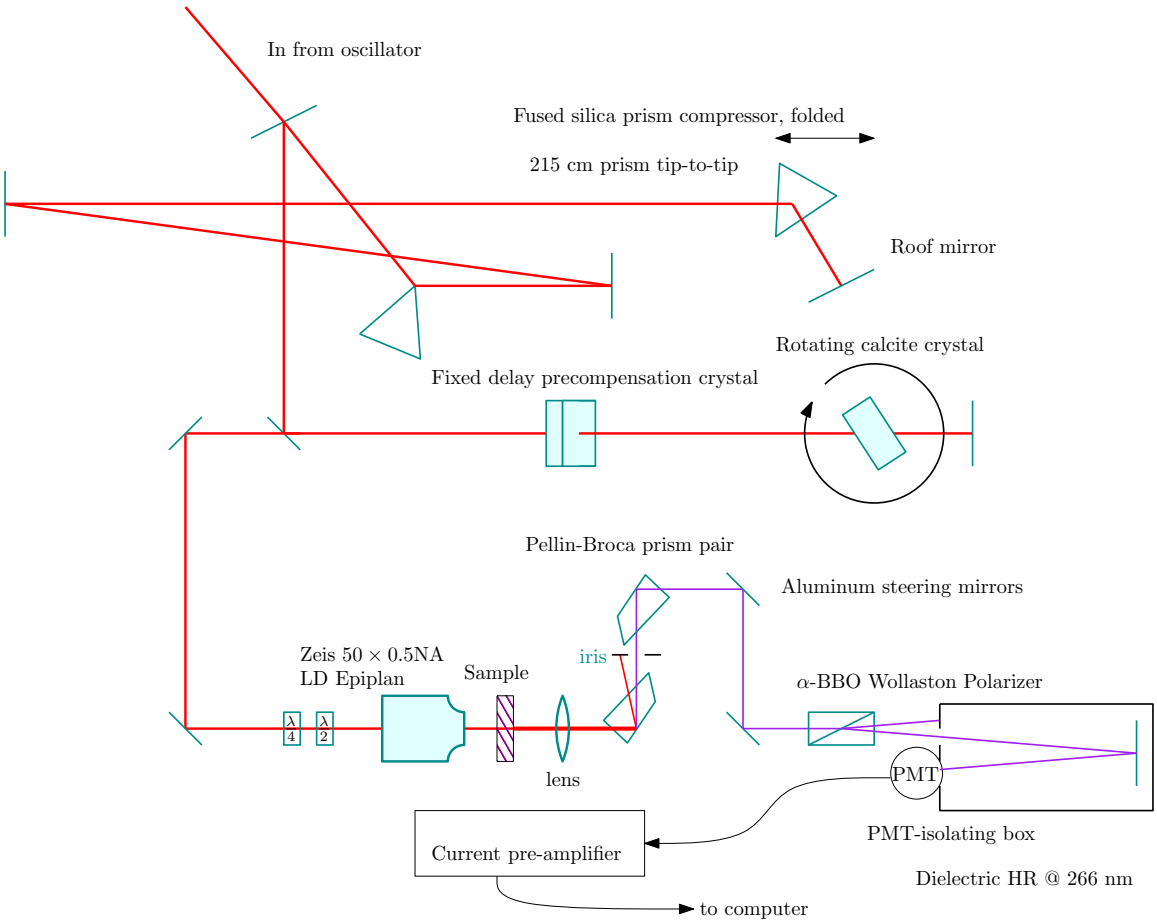

Figure 6.4: Improved CM-THG set-up with birefringent delay scanner.

throughput of third harmonic to the PMT. The final set-up is shown in Fig. 6.3.

6.4 Interferometric delay axis calibration

To be sure of the delay axis calibration, we use two methods. Spectral interferometry while the motor is spinning is not an option, since the delay changes so rapidly on the timescale of the spectrometer integration (3 ms) that the interference fringes blur out. Instead of a delay precompensation crystal, we use a polarizing Michelson interferometer to pre-set the delay to τ_{pre} before the birefringent delay scanner. The output of the Michelson is sampled with a 10% beamsplitter, which directs the pulses through a polarizer and a spectrometer. From the spectral interference fringes, we can measure the pre-compensation delay. Then we measure a cross-correlation after the birefringent scanner. The position of time-overlap corresponds to the crystal angle which compensates for the pre-set delay from the Michelson,

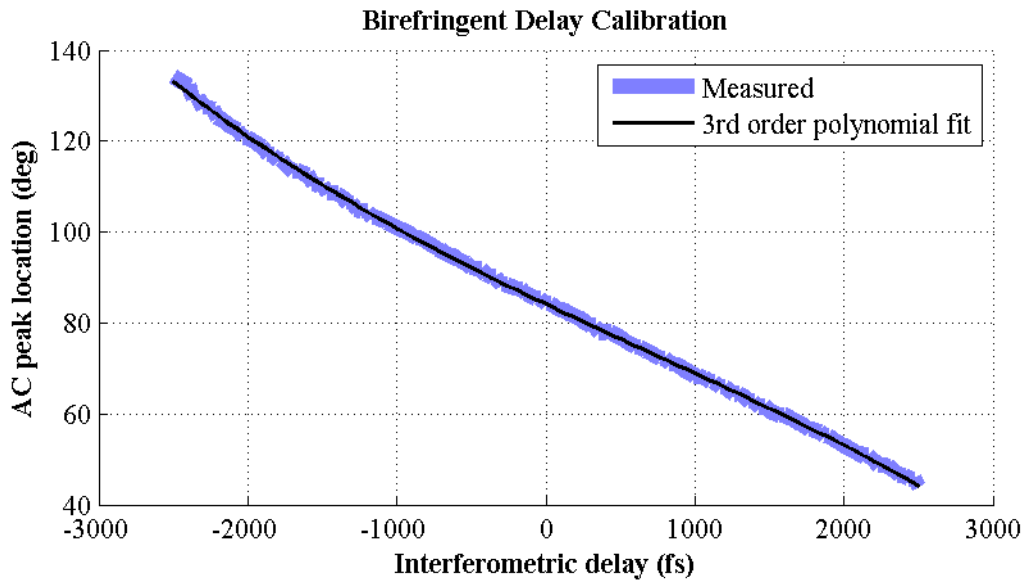

Figure 6.5: Interferometric calibration of birefringent delay scanner. Polynomial fit agrees well with measured data.

that is

$$\tau(\theta) = \tau_{\text{pre}}.$$

We scan one arm of the Michelson through a range of delays to produce the curve shown in Fig. 6.4. The mean of the interferometric delays is subtracted to condition the data, and a 3^{rd}-order polynomial is fit to this curve, and used to map the recorded traces from an function of crystal angle to a function of linear pump–probe delay,

$$f(\theta) \rightarrow f(\tau_{\text{pp}})$$

The calibration curve is actually written in terms of interpolated samples instead of angle. Once acquired, the traces are interpolated to 4096 samples, so that 8192 samples correspond to a full 360° of crystal rotation. The curves shown here are plotted with respect to crystal rotation angle in degrees, not the interpolated sample axis.

The other method will be described after the initial results are presented. It involves acquiring a Raman spectrum, and adapting the delay calibration curve to fit these Raman lines to known reference frequencies.

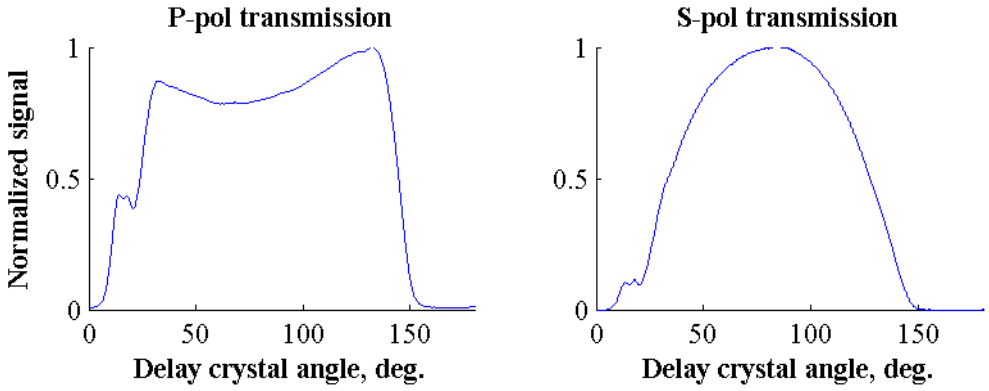

Figure 6.6: Fresnel transmission profiles across rotation angle of birefringent delay crystal.

6.5 Fresnel transmission profile background

Since the pump and probe are orthogonally polarized, incident on the rotating delay crystal, they will each exhibit angle-dependent attenuation that follows the angle-dependent Fresnel reflection from the crystal faces. For the s-polarized probe, the Fresnel transmission peaks at normal incidence, while the Fresnel transmission of the p-polarized pump peaks at the Brewster angle. Figure 6.6 shows the typical Fresnel profiles. Due to the thickness of the crystal there is some roll-off at the edges of the recorded traces, where the crystal is edge-on.

The probe signal has a strong Fresnel background that must be subtracted properly in order to isolate the weak vibrational perturbations. The background can be recorded with the pump blocked, or the time delay set such that the delay trace measures only pre-time-zero, and not the vibrations. But the noise in this signal will add to the noise in the signal of interest. Efforts to subtract using a polynomial fit required constant tuning of the polynomial fit order, depending on the sample. We use a spline fit instead, using MATLAB's spline fitting toolbox, and a smoothing parameter on the order of 10^{-7}. The smoothing parameter is chosen to be small enough to avoid fitting to the low-frequency vibrations, yet large enough to accurately fit the Fresnel profile.

The pump profile will result in a multiplication of the vibrational excitation that should be divided out of the resulting time-resolved scan. If this is not properly done, damping estimates, and algorithms such as LPSVD will not be reliable. In these preliminary experiments, we skip this step, as the signal-to-noise ratio and temporal window will suffice for

FFT (instead of LPSVD) analysis, and we are not for the moment interested in measuring decay constants accurately.

For shorter pulses, this background profile may also be affected by the GDD in the varying length of propagation through the crystal.

6.6 Data acquisition

An NI-DAQmx PCI card DAQ (Data AcQuisition device) is used to capture delay scans from the scanner. A custom program written in C# polls the DAQ for 12000 samples at a 120 kHz sampling rate. The current pre-amplifier, which amplifies the signal from the PMT to the DAQ is set to low-pass filter with a 12 dB slope and cut-off at 100 kHz. With the motor running at 14.771 Hz, or 886.26 RPM (revolutions per minute), 180° of crystal rotation covers approximately 4000 samples. Using the synchronization signal from the motor controller, the DAQ buffer is partitioned into individual 180° scans. We also tried synchronizing to a photodiode placed in such a way as to catch a pass from the surface reflection of the crystal, but found the signal from the motor controller to be much more reliable. The two halves of the 360° crystal rotation (labeled front and back face scans) are kept separate until the final stages of signal averaging, in case there are any deviations between the two of delay calibration or Fresnel transmission profiles. The actual number of samples per scan may vary, depending on motor velocity drift, so all the scans are interpolated to 4096 samples to correct for this drift.

The software records 2000 scans at a time (1000 front and 1000 back face scans), and saves the entire data set in a format that can be read by MATLAB. Averaging and delay linearization are performed in MATLAB after a full data set has been acquired.

It is also important to choose a motor spin direction such that the pump–probe overlap follows the vibrational coherence measurements on the scans. In other words, the scans are to be run backwards. This is to keep ringing and other impulse response artifacts from the PMT and detection electronics from overlapping the vibrational measurements. Otherwise such artifacts are easily mistaken for vibrational modes. This is an important procedure for any rapid scan method which measures small perturbations in a pump–probe configuration.

6.7 Data processing

Once the sets of scans are acquired, a series of MATLAB scripts are employed for analysis. The first loads up each of the scans, interpolates to 4096 points per scan, and averages all the scans together. Optionally, a cross-correlation alignment procedure may be used to keep timing jitter from washing out high-frequency signal components. In practice, we have found this necessary to maintain pump–probe autocorrelation fringes at time-zero, but it did not significantly affect the retrieved Raman spectrum. In addition, the cross-correlation alignment procedure is time-consuming, so we did not implement it for the following analysis.

6.8 Cadmium tungstate reference frequency calibration

Higher frequencies will be more distorted by delay calibration inaccuracies, especially at the extreme ends of the scans. So we select $CdWO_4$ as a calibration crystal, which has a strong Raman line at 912 cm^{-1} [108]. A third-harmonic autocorrelation (THGAC) trace [109] using THG from $CdWO_4$, is acquired with a sampling oscilloscope. The delay axis of the THGAC is calibrated by using an FFT to find the fringe spacing, which corresponds to one optical cycle, or 2.67 fs at our center wavelength of 800 nm. The result in Fig. 6.7 is shown to have a FWHM of about 30 fs, which overestimates the actual duration of the pulses, assuming either a Gaussian or a hyperbolic secant-squared intensity profile. The reciprocal of a pulse duration of 30 fs is $(30\ \text{fs} \times c)^{-1} = 1111\ cm^{-1}$, thus demonstrating we have sufficiently short pulses to excite the target mode in $CdWO_4$.

An adaptive calibration algorithm that starts with a polynomial fit to the interferometric calibration, and adjusts these coefficients based on a specified criteria. We measure a Raman spectrum of the $CdWO_4$ sample with a conventional Raman spectrometer (Central Instrumentation Facility, Colorado State University), and find the peak to be at 896.7 cm^{-1}. Then we acquire and average 8000 scans with CMTHG using the birefringent delay scanner, and run the adaptive calibration algorithm with the criteria of maximizing the peak found between $895 - -900\ cm^{-1}$. When the corrected polynomial delay calibration is applied to the data, a the relevant peak is located at 895.2 cm^{-1}. Considering the temporal window of delay scans limits the spectral resolution in this case to $\Delta\nu = 4.8\ cm^{-1}$, this is in excellent

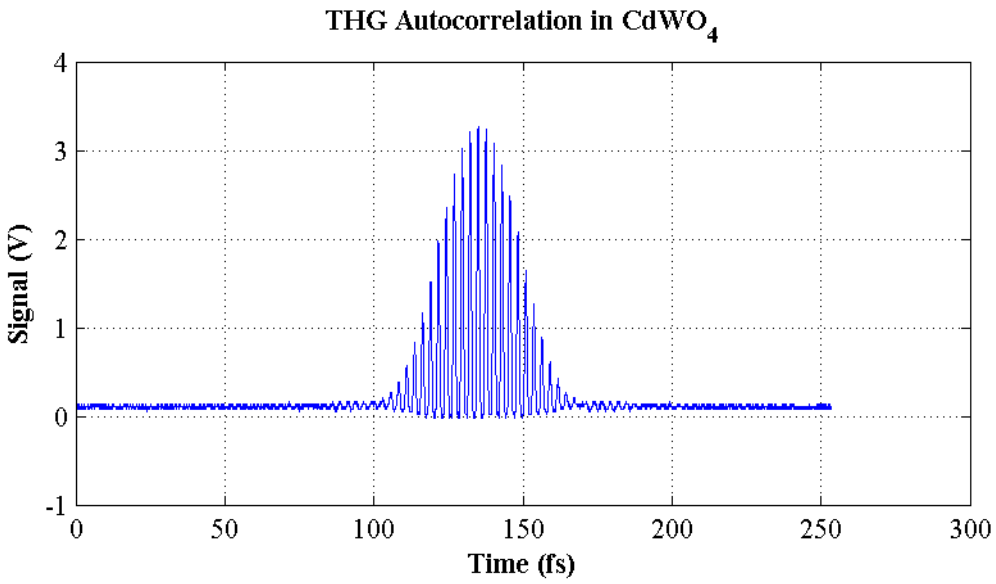

Figure 6.7: THG autocorrelation on interface of $CdWO_4$ confirms a pulse duration of less than 30 fs.

agreement with the conventional Raman measurements.

6.9 Results and discussion

The resulting FFT Raman spectra for 8000 averaged scans for $CdWO_4$, BGO12, BaF_2, and liquid CCl_4 are shown in Fig. 6.8.

The liquid CCl_4 was measured in a UV fused silica cuvette, focusing at the interface between the glass and the liquid. Unlike previous attempts, the of the pulses, indicating the periodic attenuation of the beam sample did not heat to the point of boiling under the influence from the birefringent delay scanner may have allowed heat to dissipate away from the focal volume at a high enough rate to allow us to make the measurements. We also attempted acetone, but found that sample heating and thermal lensing prevented us from making a measurement.

Figure 6.8: Birefringent delay scanner CM-THG measurement results for crystal samples $CdWO_4$, BGO12, BaF_2, and liquid CCl_4.

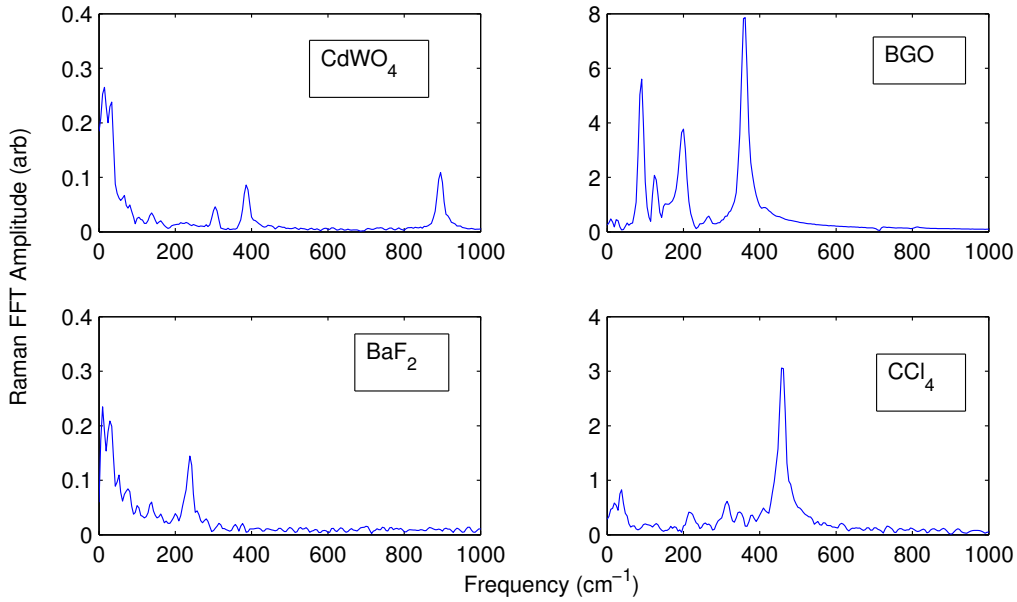

CHAPTER VII

FUTURE WORK

One outstanding question in this work is that of the surface specificity of the modulations of the Fresnel transmission coefficient. Considering the case of reflection from a scattering point of view, the incident light is gradually replaced by light radiated from oscillating dipoles in the medium, the $1/e$ extinction length being [110]

$$L = \frac{\lambda}{2\pi|n-1|} \tag{7.1}$$

So that for the third harmonic $\lambda = 266$ nm and BGO, where $n = 2.6$, the $1/e$ extinction length is $L = 26$ nm. Considering that the lattice length is $a = 1.06$ nm [111], about 24 unit cell lengths are covered by L, bulk vibrational modes will still contribute to the signal. But even methods that don't completely extinguish the bulk vibrational contribution have proved to be useful. For instance, sum frequency studies on the quartz surface, which has a significant contribution to bulk second-order signal (quartz is non-centrosymmetric) has revealed the angle of the Si-O-Si bond at the surface [8].

In spite of the increase in signal-to-noise ratio afforded by the lighthouse method, the CM-THG method will require even more sensitivity before it can be used to measure surface modes such as those on the surface of α-quartz in Ref. [8].

Simultaneous monitoring of fundamental, SH, and TH modulations could reveal information on systems that are not accessible by other means. Considering the fundamental, hyper- and second hyper-Raman interactions have different selection rules and different cross-sections. Simultaneously measuring these three Raman signals might provide additional information. This could be done with a single apparatus, and appropriate dichroic optics on the detection end.

Charge transfer interactions can lead to a measurable change in the Raman cross-section [112]. It is reasonable to assume the hyper- and second hyper-Raman cross sections

are also affected by charge transfer events. In addition, adsorbed molecules show a shift in intensities of Raman bands [10]. In addition to vibrational modulation, the background second harmonic can measure electric field strengths at the surface through field-induced second harmonic generation [35].

In conclusion, the methods presented in this dissertation have the potential to make new measurements of vibrational and electronic dynamics at chemically interesting interfaces.

APPENDIX A

WAVE EQUATIONS

In order to maintain consistency, wave equations for ultrafast pulse propagation are derived here from first principles. More information may be found in any standard textbook on ultrafast and nonlinear optics [39, 48].

A.1 Wave equations for pump and probe

Describe a probe pulse propagating in the presence of a time-varying susceptibility perturbation.

In this section, we derive the equation describing pulse propagation in optical media to ensure that we are using consistent notation and definitions.

We begin with the wave equation for homogeneous, non-magnetic media with no free charges or sources:

$$-\nabla^2\mathcal{E}(z,t)+\mu_0\epsilon_0\frac{\partial^2}{\partial t^2}\mathcal{E}(\mathbf{r},t)+\mu_0\frac{\partial^2}{\partial t^2}\mathcal{P}^L(\mathbf{r},t)=-\mu_0\frac{\partial^2}{\partial t^2}\mathcal{P}^A(\mathbf{r},t), \tag{A.1}$$

where the real field is given by

$$\mathcal{E}(\mathbf{r},t)=\frac{1}{2}\widetilde{\mathcal{E}}(\mathbf{r},t)+\frac{1}{2}\widetilde{\mathcal{E}}^*(\mathbf{r},t), \tag{A.2}$$

the real *linear* polarization is given by

$$\mathcal{P}^L(\mathbf{r},t)=\frac{1}{2}\widetilde{\mathcal{P}}^L(\mathbf{r},t)+\frac{1}{2}\widetilde{\mathcal{P}}^{L*}(\mathbf{r},t), \tag{A.3}$$

and the real *additional* polarization (either linear, nonlinear, or both) is given by

$$\mathcal{P}^A(\mathbf{r},t)=\frac{1}{2}\widetilde{\mathcal{P}}^A(\mathbf{r},t)+\frac{1}{2}\widetilde{\mathcal{P}}^{A*}(\mathbf{r},t). \tag{A.4}$$

Note that the tilde indicates a complex quantity. Upon substitution of the above definitions into the wave equation (A.1), we obtain

$$-\nabla^2\widetilde{\mathcal{E}}(\mathbf{r},t)+\mu_0\epsilon_0\frac{\partial^2}{\partial t^2}\widetilde{\mathcal{E}}(\mathbf{r},t)+\mu_0\frac{\partial^2}{\partial t^2}\widetilde{\mathcal{P}}^L(\mathbf{r},t)=-\mu_0\frac{\partial^2}{\partial t^2}\widetilde{\mathcal{P}}^A(\mathbf{r},t) + \{\text{Similar equation for c.c.}\} \quad \text{(A.5)}$$

The two equations above contain identical information (as required by the real field and polarizations). We are really after the real field, but it is easier to manipulate things with complex notation. We need only to remember to take the real part of $\widetilde{\mathcal{E}}(\mathbf{r},t)$ in the end.

We can write the complex time-domain field and polarizations in term of their inverse Fourier transforms

$$\begin{aligned}\widetilde{\mathcal{E}}(\mathbf{r},t)&=\int \mathrm{d}\omega\widetilde{E}(\mathbf{r},\omega)e^{i\omega t},\\ \widetilde{\mathcal{P}}^L(\mathbf{r},t)&=\int \mathrm{d}\omega\overline{P}^L(\mathbf{r},\omega)e^{i\omega t},\\ \widetilde{\mathcal{P}}^A(\mathbf{r},t)&=\int \mathrm{d}\omega\overline{P}^A(\mathbf{r},\omega)e^{i\omega t}.\end{aligned} \quad \text{(A.6)}$$

Substituting the inverse Fourier transforms for the fields and polarizations into (A.5), yields

$$\int \mathrm{d}\omega\left\{-\nabla^2\widetilde{E}(\mathbf{r},\omega)e^{i\omega t}+\mu_0\epsilon_0\frac{\partial^2}{\partial t^2}\widetilde{E}(\mathbf{r},\omega)e^{i\omega t}+\mu_0\frac{\partial^2}{\partial t^2}\overline{P}^L(\mathbf{r},\omega)e^{i\omega t}\right\} = \int \mathrm{d}\omega\left\{-\mu_0\frac{\partial^2}{\partial t^2}\overline{P}^A(\mathbf{r},\omega)e^{i\omega t}\right\}. \quad \text{(A.7)}$$

Evaluating the temporal derivatives and dropping the $\int \mathrm{d}\omega$ and $e^{i\omega t}$ terms that are common to each term gives us

$$-\nabla^2\widetilde{E}(\mathbf{r},\omega)-\omega^2\mu_0\epsilon_0\widetilde{E}(\mathbf{r},\omega)-\omega^2\mu_0\overline{P}^L(\mathbf{r},\omega)=\omega^2\mu_0\overline{P}^A(\mathbf{r},\omega), \quad \text{(A.8)}$$

which can be rewritten as

$$\nabla^2\widetilde{E}(\mathbf{r},\omega)+\frac{\omega^2}{c^2}\widetilde{E}(\mathbf{r},\omega)+\omega^2\mu_0\overline{P}^L(\mathbf{r},\omega)=-\omega^2\mu_0\overline{P}^A(\mathbf{r},\omega). \quad \text{(A.9)}$$

First, consider the linear polarization term. In the time domain, this term is written as

$$\widetilde{\mathcal{P}}^L(\mathbf{r},t)=\epsilon_0\int_{-\infty}^{\infty}d\tau\chi^{(1)}(t-\tau)\widetilde{\mathcal{E}}(z,\tau), \quad \text{(A.10)}$$

thus the linear polarization (oscillating at the input optical frequency) becomes

$$\overline{P}^L(\mathbf{r},\omega) = \epsilon_0 \int \mathrm{d}t e^{-i\omega t} \widetilde{\mathcal{P}}^L(\mathbf{r},t) = \epsilon_0 \int \mathrm{d}t e^{-i\omega t} \int_{-\infty}^{\infty} d\tau \chi^{(1)}(t-\tau)\widetilde{\mathcal{E}}(\tau). \tag{A.11}$$

Making the substitution $\eta = t - \tau, t = \tau + \eta, dt = d\eta$, we obtain

$$\overline{P}^L(\mathbf{r},\omega) = \epsilon_0 \int_{-\infty}^{\infty} d\eta e^{-i\omega\eta}\chi^{(1)}(\eta) \int_{-\infty}^{\infty} d\tau e^{-i\omega\tau}\widetilde{\mathcal{E}}(\tau) = \epsilon_0 \chi^{(1)}(\omega)\widetilde{E}(\mathbf{r},\omega). \tag{A.12}$$

Plugging (A.12) into (A.9), we arrive at

$$\nabla^2 \widetilde{E}(\mathbf{r},\omega) + \frac{\omega^2}{c^2}\left[1 + \chi^{(1)}(\omega)\right]\widetilde{E}(\mathbf{r},\omega) = -\omega^2 \mu_0 \overline{P}^A(\mathbf{r},\omega). \tag{A.13}$$

Note that $n^2(\omega) \equiv 1 + \chi^{(1)}(\omega)$ and $k^2(\omega) \equiv \frac{\omega^2 n^2(\omega)}{c^2}$. Thus, (A.13) can be written as

$$\nabla^2 \widetilde{E}(\mathbf{r},\omega) + k^2(\omega)\widetilde{E}(\mathbf{r},\omega) = -\omega^2 \mu_0 \overline{P}^A(\mathbf{r},\omega). \tag{A.14}$$

A.2 Slowly Varying Envelope in the Time and Frequency Domain

So far, we have made no assumptions in the derivations beyond those that allowed us to arrive at the typical wave equation that is used in optics, i.e., (A.1). Now we will begin making assumptions. We will assume that the complex electric field contains a complex temporal envelope that varies slowly with respect to t and z. We consider a field propagating in the forward direction only. Thus we write:

$$\widetilde{\mathcal{E}}(\mathbf{r},t) = E(\mathbf{r},t)e^{i(\omega_1 t - k_0 z)}, \tag{A.15}$$

where $E(\mathbf{r},t)$ is a slowly-varying complex envelope with respect to z and t and the temporal and spatial phase that is rapidly varying are only considered at the central frequency of the pulse (ω_1). Furthermore, based on our definition above, we are only considering plane waves.

Note this section closely parallels the derivation in Ch. 13 of Ref [39], except Boyd defines the argument of the exponent $i(k_0 z - \omega_1 t)$ instead of $i(\omega_1 t - k_0 z)$. Both approaches describe fields propagating in the forward direction, and are equally valid.

In the frequency domain, we have:

$$\widetilde{E}(\mathbf{r},\omega) = \int e^{i\omega t}\widetilde{\mathcal{E}}(\mathbf{r},t)dt = \int e^{i(\omega-\omega_1)t}E(\mathbf{r},t)e^{-ik_0 z}dt. \tag{A.16}$$

Defining $\Omega = \omega - \omega_1$, we obtain

$$\widetilde{E}(\mathbf{r},\omega) = e^{-ik_0 z}E(\mathbf{r},\omega). \tag{A.17}$$

Substituting this into (A.14), we obtain

$$\nabla^2\left[e^{-ik_0 z}E(\mathbf{r},\omega)\right] + k^2(\omega)e^{-ik_0 z}E(\mathbf{r},\omega) = -\omega^2\mu_0\overline{P}^A(\mathbf{r},\omega), \tag{A.18}$$

which can be rewritten as

$$e^{ik_0 z}\nabla^2\left[e^{-ik_0 z}E(\mathbf{r},\omega)\right] + k^2(\omega)E(\mathbf{r},\omega) = -\omega^2\mu_0 e^{ik_0 z}\overline{P}^A(\mathbf{r},\omega). \tag{A.19}$$

Next, consider the spatial Laplacian broken down into transverse, $\perp$, and longitudinal, z, components:

$$\begin{aligned}
\nabla^2\left[e^{-ik_0 z}E(\mathbf{r},\omega)\right] &= \nabla_\perp^2\left[e^{-ik_0 z}E(\mathbf{r},\omega)\right] + \frac{\partial^2}{\partial z^2}\left[e^{-ik_0 z}E(\mathbf{r},\omega)\right] \\
&= \nabla_\perp^2\left[e^{-ik_0 z}E(\mathbf{r},\omega)\right] + \frac{\partial}{\partial z}\left[\frac{\partial}{\partial z}E(\mathbf{r},\omega)e^{-ik_0 z} - ik_0 E(\mathbf{r},\omega)e^{-ik_0 z}\right] \\
&= \left\{\nabla_\perp^2 E(\mathbf{r},\omega) + \frac{\partial^2}{\partial z^2}E(\mathbf{r},\omega) - 2ik_0\frac{\partial}{\partial z}E(\mathbf{r},\omega) + (ik_0)^2 E(\mathbf{r},\omega)\right\}e^{-ik_0 z} \\
&= \left\{\nabla_\perp^2 E(\mathbf{r},\omega) + \frac{\partial^2}{\partial z^2}E(\mathbf{r},\omega) - 2ik_0\frac{\partial}{\partial z}E(\mathbf{r},\omega) - k_0^2 E(\mathbf{r},\omega)\right\}e^{-ik_0 z}.
\end{aligned} \tag{A.20}$$

Upon substitution into (A.21), we obtain

$$\begin{aligned}
\nabla_\perp^2 E(\mathbf{r},\omega) + \frac{\partial^2}{\partial z^2}E(\mathbf{r},\omega) - 2ik_0\frac{\partial}{\partial z}E(\mathbf{r},\omega) + \left[k^2(\omega) - k_0^2\right]E(\mathbf{r},\omega) \\
= -\omega^2\mu_0 e^{ik_0 z}\overline{P}^A(\mathbf{r},\omega).
\end{aligned} \tag{A.21}$$

To proceed further, we make a Taylor expansion of $k(\omega)$ about ω_1 written as

$$k(\omega) = k_0 + k_1\Omega + D, \tag{A.22}$$

where

$$D = \sum_{j=2}^{\infty}\frac{k_j}{j!}\Omega^j, \tag{A.23}$$

and

$$k_j = \frac{d^j k(\omega)}{d\omega^j}|_{\omega_1}. \tag{A.24}$$

Squaring $k(\omega)$ yields

$$k^2(\omega) = k_0^2 + 2k_0k_1\Omega + 2k_0D + 2k_1D\Omega + (k_1\Omega)^2 + D^2. \tag{A.25}$$

We can write the difference $k^2(\omega) - k_0^2$ as approximately

$$k^2(\omega) - k_0^2 \approx 2k_0k_1\Omega + 2k_0D + 2k_1D\Omega + (k_1\Omega)^2, \tag{A.26}$$

where we have neglected D^2 because it is very small (if the Taylor expansion is valid). Now the wave equation becomes

$$\left(\nabla_\perp^2 + \frac{\partial^2}{\partial z^2} - 2ik_0\frac{\partial}{\partial z} + 2k_0k_1\Omega + 2k_0D + 2k_1D\Omega + (k_1\Omega)^2\right) E(\mathbf{r},\omega) = -\omega^2\mu_0 e^{ik_0z}\overline{P}^A(\mathbf{r},\omega). \tag{A.27}$$

If we multiply (A.27) by $e^{i\Omega t}$ and integrate with respect to Ω, we obtain the time-domain envelope equation:

$$\left\{\nabla_\perp^2 + \frac{\partial^2}{\partial z^2} - 2ik_0\frac{\partial}{\partial z} + 2k_0k_1\left(-i\frac{\partial}{\partial t}\right) + 2k_0\tilde{D} + 2k_1\tilde{D}\left(-i\frac{\partial}{\partial t}\right) + k_1^2\left(-i\frac{\partial}{\partial t}\right)^2\right\} E(\mathbf{r},t)e^{i\omega_1 t} = -\left(-i\frac{\partial}{\partial t}\right)^2\mu_0 e^{ik_0z}\widetilde{P}^A(\mathbf{r},t), \tag{A.28}$$

where we have used the Fourier transform relations $\left(-i\frac{\partial}{\partial t}\right) \leftrightarrow \omega$ and $\tilde{D} = \sum_{j=2}^{\infty}\frac{k_j}{j!}\left(-i\frac{\partial}{\partial t}\right)^j$.

Rewriting (A.28) gives

$$\left\{\nabla_\perp^2 + \frac{\partial^2}{\partial z^2} - 2ik_0\left(\frac{\partial}{\partial z} + k_1\frac{\partial}{\partial t}\right) + 2k_0\tilde{D} - 2ik_1\tilde{D}\frac{\partial}{\partial t} - k_1^2\frac{\partial^2}{\partial t^2}\right\} E(\mathbf{r},t) = \mu_0 e^{ik_0z}e^{-i\omega_1 t}\frac{\partial^2\widetilde{P}^A(\mathbf{r},t)}{\partial t^2}. \tag{A.29}$$

We will consider a polarization induced in the medium (either non-time-stationary or nonlinear) that oscillates at the central optical frequency of the pulse and propagates with the same phase velocity:

$$\widetilde{P}^A(\mathbf{r},t) = p^A(\mathbf{r},t)e^{i(\omega_1 t - k_0 z)}. \tag{A.30}$$

Taking the first derivative with respect to time of this polarization source term yields

$$\frac{\partial \widetilde{P}^A(\mathbf{r},t)}{\partial t} = e^{-ik_0 z}\left[\frac{\partial p^A(\mathbf{r},t)}{\partial t}e^{i\omega_1 t} + (i\omega_1)p^A(\mathbf{r},t)e^{i\omega_1 t}\right] \tag{A.31}$$

and the second temporal derivative of the polarization density is

$$\frac{\partial^2 \widetilde{P}^A(\mathbf{r},t)}{\partial t^2} = -\omega_1^2 e^{i(\omega_1 t - k_0 z)}\left[1 - \frac{i}{\omega_1}\frac{\partial}{\partial t}\right]^2 p^A(\mathbf{r},t). \tag{A.32}$$

Thus $p^A(\mathbf{r},t)$ is the slowly-varying portion of the rapidly oscillating polarization in the medium. Inserting the resultant temporal derivative back into (A.29) yields

$$\left\{\nabla_\perp^2 + \frac{\partial^2}{\partial z^2} - 2ik_0\left(\frac{\partial}{\partial z} + k_1\frac{\partial}{\partial t}\right) + 2k_0\tilde{D} - 2ik_1\tilde{D}\frac{\partial}{\partial t} - k_1^2\frac{\partial^2}{\partial t^2}\right\}E(\mathbf{r},t) = -\omega_1^2\mu_0\left(1 - \frac{i}{\omega_1}\frac{\partial}{\partial t}\right)^2 p^A(\mathbf{r},t). \tag{A.33}$$

Next, we move to the group rest frame of the pulse with the transformation $\tau = t - u^{-1}z$ and $\zeta = z$. This is followed by making the slowly varying envelope approximation (SVEA), where we neglect $\frac{\partial^2}{\partial \zeta^2}$. Then we also neglect dispersion,

$$\frac{k_1}{k_0} = \frac{u^{-1}}{\frac{n\omega_1}{c}} \equiv \frac{n_g}{n\omega_1} \to\approx \frac{1}{\omega_1} \tag{A.34}$$

And divide both sides by the common $\left(1 - \frac{i}{\omega_1}\frac{\partial}{\partial \tau}\right)$ and the $-2ik_0$ term. We will neglect spatio-temporal coupling indicated on the transverse Laplacian $\nabla_\perp^2$. Furthermore, we will neglect higher order dispersion $\tilde{D}$, leading to

$$\left\{\frac{i}{2k_0}\nabla_\perp^2 + \frac{\partial}{\partial \zeta}\right\}E(x,y,\zeta,\tau) = -i\frac{\mu_0 c\omega_1}{2n_0}\left(1 - \frac{i}{\omega_1}\frac{\partial}{\partial \tau}\right)p^A(x,y,\zeta,\tau). \tag{A.35}$$

Reversing the coordinate transform back to the lab frame, $\tau = t - u^{-1}z$ and $\zeta = z$.

$$\therefore \frac{\partial}{\partial \zeta} \to \frac{\partial}{\partial z} + k_1\frac{\partial}{\partial t} \quad \text{and} \frac{\partial}{\partial \mathrm{t}} \to \frac{\partial}{\partial \tau}$$

and substituting the group velocity $u = 1/k_1$, the wave equation becomes

$$\left\{\frac{i}{2k_0}\nabla_\perp^2 + \frac{\partial}{\partial z} + \frac{1}{u}\frac{\partial}{\partial t}\right\}E(\mathbf{r},t) = -i\frac{\omega_1}{2cn_0\epsilon_0}\left(1 - \frac{i}{\omega_1}\frac{\partial}{\partial t}\right)p^A(\mathbf{r},t). \tag{A.36}$$

This will be the starting point for our calculations. This equation describes the propagation of an ultrafast pulse envelope $E(\mathbf{r},t)$ in the presence of an additional polarization

$p^A(\mathbf{r}, t)$. This equation is versatile, and may be used to describe the propagation of a probe pulse in the presence of a nuclear coherence by making E the fundamental pulse and p^A reflect the time-varying polarization from the coherent oscillations. Or this equation may describe third harmonic generation by choosing a $p^A \propto \chi^{(3)} E^3_{\text{fundamental}}$ that acts as a source term to drive the third harmonic.q

A.2.1 Wave Equation in Spatial Frequency Domain

Using the spatial Fourier transform relation in Eq. (E.2) we can also express Eq. (A.36) in terms of spatial frequencies:

$$\left\{(k_x^2 + k_y^2) + \frac{\partial}{\partial \zeta} + i\tilde{D}\right\} \hat{E}(k_x, k_y; \zeta, \tau) = -i\frac{\mu_0 c \omega_1}{2n_0}\left(1 - \frac{i}{\omega_1}\frac{\partial}{\partial \tau}\right)\hat{p}^A(k_x, k_y; \zeta, \tau). \quad \text{(A.37)}$$

APPENDIX B

RELATING SUSCEPTIBILITIES

In other Raman scattering experiments, it is conventional to refer to the *Raman susceptibility tensor* which is a complex value describing phase and amplitude modulations. To clarify, this is not the same as the Raman effective susceptibility perturbations described in Ch. 2. Here, we relate the effective susceptibility perturbations to other notation found in the literature. Both of these are connected to the Raman differential polarizability $\partial\alpha/\partial q$.

The complex Raman susceptibility found in Ref. [49], and commonly found in CARS experiments is quite distinct from the effective first-order susceptibility perturbation defined. The Raman susceptibility χ_R is a complex value that describes the phase shift and gain (or loss) of a Stokes field propagating along with a laser field in a stimulated Raman scattering experiment. The Raman susceptibility is described in terms of a third-order Raman tensor in the frequency domain is related to the differential polarizability [39],

$$\chi_{\mathrm{R}}(\omega_S) = \frac{(N/6m)(\partial\alpha/\partial q)_0^2}{\omega_v^2 - (\omega_L - \omega_S)^2 + 2i(\omega_L - \omega_S)\gamma}. \tag{B.1}$$

This formulation differs from ours in a number of ways. Equation (B.1) relates the Stokes and laser fields in a stimulated Raman scattering experiment, where the Stokes field will experience gain when $\omega_v \approx \omega_L - \omega_s$. The Stokes polarization is [39]

$$P(\omega_s) = 6\chi_R(\omega_s)|A_L|^2 A_S e^{ik_s z}, \tag{B.2}$$

whereas our susceptibility perturbation relates an additional polarization at an arbitrary frequency to a vibrational *coherence*. The full expression for this perturbation is

$$\delta\chi(t) = -\frac{i}{\hbar}\left(\frac{\partial\alpha}{\partial q}\right)_0^2 \int_0^\infty \mathrm{d}t_2 \langle [q_v(t), q_v(0)]\rho_0\rangle \times |E_{\mathrm{pu}}(t+\tau-t_2)|^2 \tag{B.3}$$

And it depends explicitly on the convolution of the vibrational response with the pump field. These two pictures of the Raman susceptibility share in common the real differential

polarizability,

$$\alpha' = \left(\frac{\partial \alpha}{\partial q}\right)_0 \tag{B.4}$$

In contrast the effective susceptibility perturbation is a real value for non-resonant pump–probe methods. It is a simplification of a 4-wave mixing process, in which 2 fields are from the pump, and the other two are from the probe. But even though $\delta\chi$ is real, it still leads to both phase modulation and amplitude modulation effects through an effective complex perturbation to the wavenumber δk, as shown in Ch. 2.

In an off-resonant ISRS pump–probe experiment, the effective linear polarization, proportional to the probe field is

$$P(t) = E_{\mathrm{pr}}(t+\tau) \int_{-\infty}^{\infty} S(t) \left|E_{\mathrm{pu}}(t)\right|^2 \mathrm{d}t \tag{B.5}$$

Other treatments express the signal field as proportional to this polarization, for a particular optical frequency

$$E_{\mathrm{s}}(t;\omega) = \chi^{\mathrm{R}}(\omega) P(t) \tag{B.6}$$

Inserting the expression for $P(t)$ gives

$$E_{\mathrm{s}}(t;\omega) = \chi^{\mathrm{R}}(\omega) E_{\mathrm{pr}}(t+\tau) \int_{-\infty}^{\infty} S(t) \left|E_{\mathrm{pu}}(t)\right|^2 \mathrm{d}t \tag{B.7}$$

It is possible to have a third-order additional polarization that is complex. This is the case when the probe wavelength is near an electronic resonance. In this case, the vibrational motion, through a complex polarization, modulates the amplitude of the probe pulse directly, not just through the wavenumber k perturbations [53].

APPENDIX C

LP-SVD FOR SPECTRAL ESTIMATION

C.1 Introduction

The Fourier transform decomposes a signal into a sum of sines and cosines. This is the bread and butter of signal analysis. But there are two shortcomings. First, an FFT does not take into account the fact that we expect only damped sinusoids in the time-resolved Raman quantum beats. Second, the spectral resolution of an FFT is limited by the temporal window. Linear prediction methods have improved spectral resolution and better noise rejection than FFT.

We are interested in observing molecular vibrations through time-resolved spectroscopic measurements. The traces produced are proportional directly to the molecular motion, modeled by a sum of exponentially damped sinusoids,

$$q(t) = \sum_{k=1}^{K} c_k e^{-ib_k t} cos(\omega_k t + \phi_k). \tag{C.1}$$

For any given data set $q(t)$, we wish to extract the model parameters c_k, b_k, ω_k, and ϕ_k. The measured signal, with n samples on intervals of Δt is

$$x_n = x(n\Delta t) = \sum_{k=1}^{K} c_k e^{-ib_k n\Delta t} cos(\omega_k n\Delta t + \phi_k) + w(n), \tag{C.2}$$

where $w(n)$ is added white noise. The most obvious method for obtaining frequency information is to perform a `fft` on the measured data. However, there are techniques for extracting the above model parameters that are better with noisy data and short sampling windows. The focus of this paper is on the use of Linear Prediction-Singular Value Decomposition (LP-SVD), developed by Kumaresan and Tufts˜[80] and extended by Barkhuijsen, *et al* to NMR signal processing˜[79]. We will closely follow their discussion, filling in a few details as we go.

C.2 Linear Prediction

C.2.1 Forward Linear Prediction

The fundamental principle behind linear prediction (LP) or autoregression (AR) is modeling each data point as a linear superposition of the previous M data points:

$$x_n = a_1 x_{n-1} + a_2 x_{n-2} + \cdots + a_M x_{n-M}, \tag{C.3}$$

where $a_m (m = 1, \ldots, M)$ are referred to as the LP coefficients or predictor coefficients. Equation˜C.3 is set up for *forward* prediction, that is, modeling each successive sample in terms of the previous samples. Backward prediction will be discussed later in this section.

Now we search for values of a_m that accurately model the signal data. Suppose we have acquired N samples, and that $M < n$. From this we can generate $n - M$ equations based on Eq. C.3 and solve for a_m.

$$\begin{aligned} x_N &= a_1 x_{N-1} + a_2 x_{N-2} + \cdots + a_M x_{N-M} \\ x_{N-1} &= a_1 x_{N-2} + a_2 x_{N-3} + \cdots + a_M x_{N-M-1} \\ &\vdots \\ x_{M+1} &= a_1 x_M + a_2 x_{M-1} + \cdots + a_M x_1 \end{aligned} \tag{C.4}$$

This is, of course, a set of linear equations which can be written in matrix form

$$\begin{pmatrix} x_{N-1} & x_{N-2} & \cdots & x_{N-M} \\ x_{N-2} & & \cdots & x_{N-M-1} \\ \vdots & & \ddots & \vdots \\ x_M & x_{M-1} & \cdots & x_1 \end{pmatrix} \begin{pmatrix} a_1 \\ a_2 \\ \vdots \\ a_M \end{pmatrix} = \begin{pmatrix} x_N \\ x_{N-1} \\ \vdots \\ x_{M+1} \end{pmatrix} \tag{C.5}$$

$$\mathbf{X}\mathbf{a} = \mathbf{h}, \tag{C.6}$$

Where $\mathbf{X}$ is a Hankel matrix constructed from the data, $\mathbf{a}$ is the vector of LP coefficients, and $\mathbf{h}$ is a truncated vector of the last M data points. We solve for $\mathbf{a}$ which minimizes the prediction error. A least squares solution using singular value decomposition (SVD) works well. The SVD of $\mathbf{X}$ is

$$\mathbf{X} = \mathbf{U}\mathbf{\Lambda}\mathbf{V}^*, \tag{C.7}$$

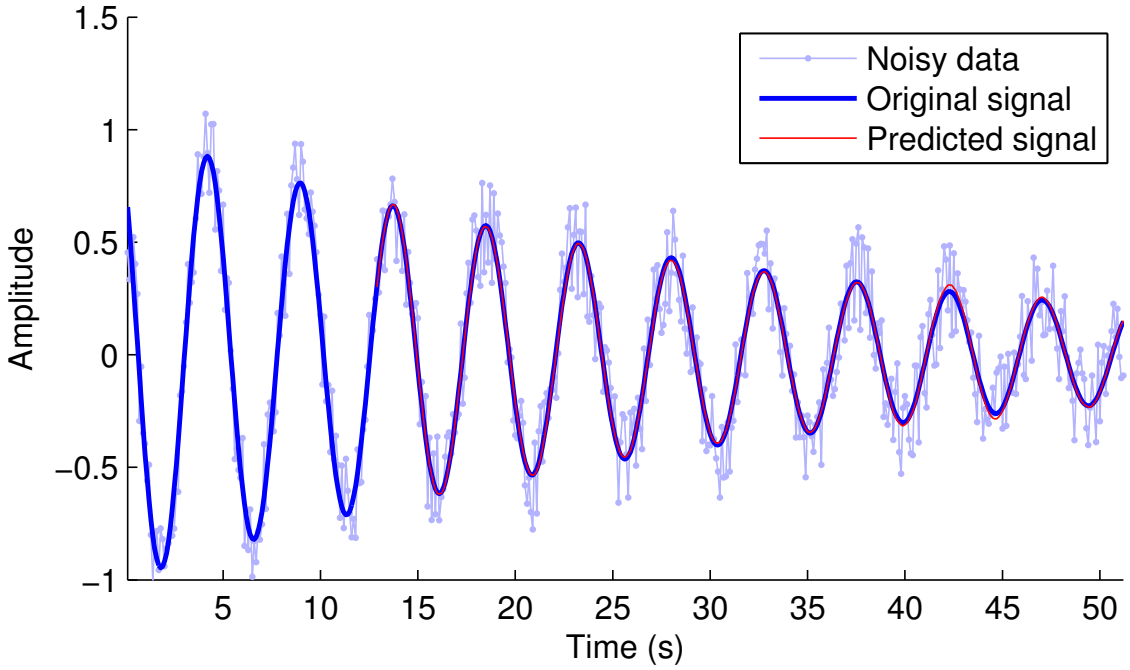

Figure C.1: Forward linear prediction. Simulated noisy signal (line with dot markers), original sinusoid without noise (solid thick line), and LP predicted line (solid thin line)

where $\lambda_i = \Lambda_{ii}$ are the singular values of $\mathbf{X}$, and * denotes the conjugate transpose. It can be shown that for a signal comprised of K frequency components, only $2K$ singular values need to be retained. The rest are noise terms, and are truncated, and we construct

$$\Lambda^{\dagger}_{ij} = \begin{cases} \frac{1}{\lambda_i} & \text{if } i = j \leq 2K, \\ 0 & \text{otherwise.} \end{cases} \tag{C.8}$$

If we don't know K *a priori*, we can instead truncate λ_i values below a threshold.

The least-squares fit for $\mathbf{a}$ is then

$$\mathbf{a} = \mathbf{V}\mathbf{\Lambda}^{\dagger}\mathbf{U}^{*}\mathbf{x}. \tag{C.9}$$

A reconstructed signal is given by

$$\mathbf{y} = \mathbf{X}\mathbf{a}. \tag{C.10}$$

Simulated results for a noisy signal are shown in Fig.˜C.1.

Barkhuijsen, *et al* claim it can be shown that for a signal consisting of a single sinusoidal term [79],

$$x_n = e^{-bn\Delta t}\cos\left(\omega n\Delta t + \phi\right), \tag{C.11}$$

an algebraic solution exists for the first two linear prediction coefficients:

$$a_1 = 2e^{-b\Delta t}\cos(\omega\Delta t) \tag{C.12}$$

$$a_2 = -e^{-2b\Delta t}. \tag{C.13}$$

Working backwards from this, we can solve for b and ω in terms of a_1 and a_2:

$$e^{(-b\pm i\omega)\Delta t} = \left(a_1 \pm \sqrt{a_2^2 + 4a_2}\right)/2. \tag{C.14}$$

Equation˜C.14 is clearly the solution for the complex roots of the polynomial:

$$z^2 - a_1 z - a_2 = 0 \tag{C.15}$$

and also

$$z^2\left(1 - a_1 z^{-1} - a_2 z^{-2}\right) = 0. \tag{C.16}$$

Tufts and Kumaresan relate this to the poles of the transfer function of the so-called prediction-error filter $H(z)$:

$$H(z) = 1 + \sum_{k=1}^{K} a_k z^{-k} \tag{C.17}$$

Working on figure, pole plot for complex roots of error function $H(z)$. Show that backward prediction throws useful data outside unit circle.

C.2.2 Backward Linear Prediction

If instead the linear prediction is performed in a backward manner, the noisy poles are found inside the unit circle and poles corresponding to actual frequency components are outside. The equation for backward LP is

$$\begin{pmatrix} x_2 & x_3 & \cdots & x_{M+2} \\ x_3 & & \cdots & x_{M+3} \\ \vdots & & \ddots & \vdots \\ x_{N-M+1} & x_{N-M+2} & \cdots & x_N \end{pmatrix} \begin{pmatrix} a_1 \\ a_2 \\ \vdots \\ a_M \end{pmatrix} = \begin{pmatrix} x_1 \\ x_2 \\ \vdots \\ x_{N-M} \end{pmatrix} \tag{C.18}$$

Simulation of backward prediction is shown in Fig.˜C.2.

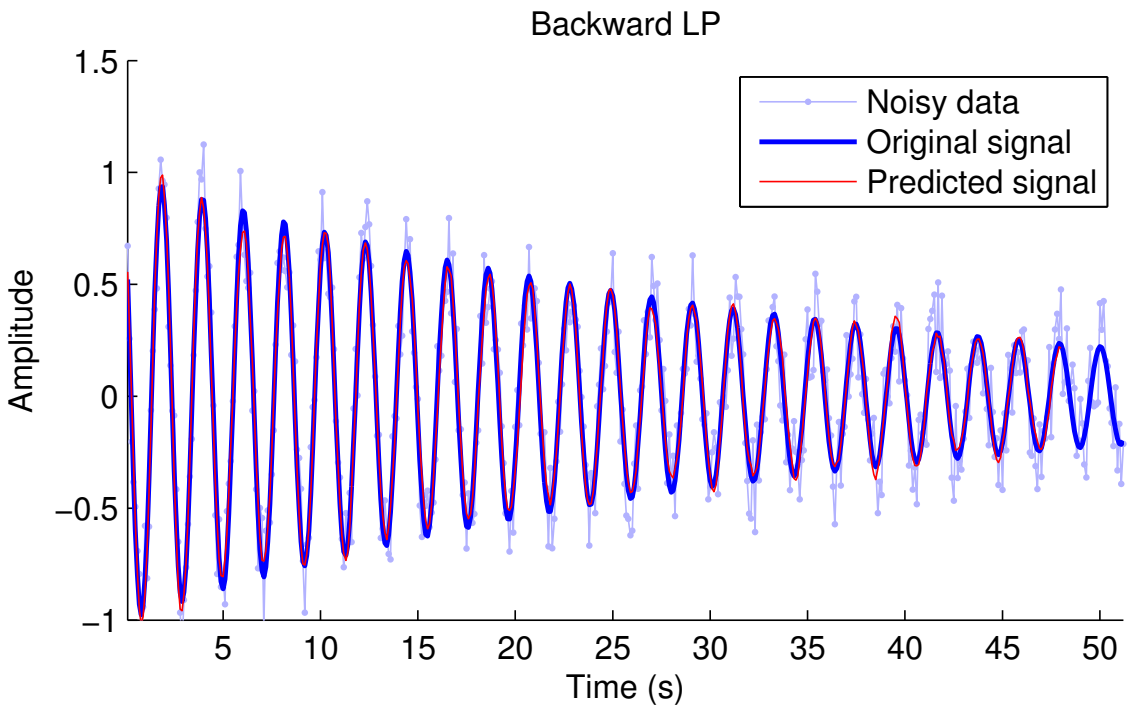

Figure C.2: Backward linear prediction. Simulated noisy signal (line with dot markers), original sinusoid without noise (solid thick line), and LP predicted line (solid thin line)

The roots of the error function $H(z)$ for both forward and backward cases are shown in Fig.˜C.3. The solution to the backwards LP model produces roots of the form

$$s_k = e^{(b_k \pm i\omega_k)\Delta t}, \tag{C.19}$$

where the damping coefficient b_k and frequency ω_k can be found by taking the real and imaginary parts of the log, respectively. The difference between forward and backward LP is illustrated in Fig.˜C.3.

C.3 Amplitude and Phase

Amplitude and phase information is extracted by another least-squares fit. First we examine the case of a single frequency component. Using the previously obtained damping coefficient b_1 and frequency ω_1, we write

$$x_n = x(n\Delta t) = c_1 e^{-b_1 n\Delta t}\cos(\omega_1 n\Delta t + \phi_1) \tag{C.20}$$

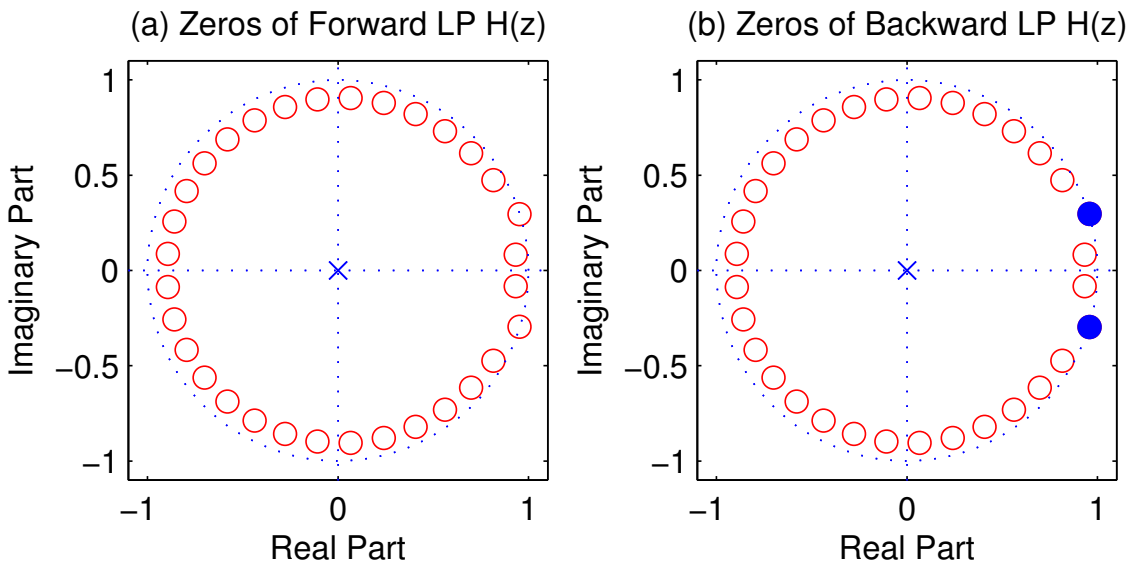

Figure C.3: Zeros of prediction error function $H(z)$ for (a) forward LP and (b) backward LP. In (b), the zeros that lie outside the unit circle are labeled with a solid blue circle.)

which becomes, with a trigonometric expansion

$$x_n = [c_1 \cos\phi_1]\left[e^{-b_1 n\Delta t}\cos(\omega_1 n\Delta t)\right] + [c_1 \sin\phi_1]\left[e^{-b_1 n\Delta t}\sin(\omega_1 n\Delta t)\right]. \tag{C.21}$$

For a single sinusoidal component, we can generate a set of N equations,

$$\begin{pmatrix} e^{-b_1\Delta t}\cos(\omega_1\Delta t) & e^{-b_1\Delta t}\sin(\omega_1\Delta t) \\ e^{-b_1 2\Delta t}\cos(\omega_1 2\Delta t) & e^{-b_1 2\Delta t}\sin(\omega_1 2\Delta t) \\ \vdots & \vdots \\ e^{-b_1 N\Delta t}\cos(\omega_1 N\Delta t) & e^{-b_1 N\Delta t}\sin(\omega_1 N\Delta t) \end{pmatrix} \begin{pmatrix} c_1\cos\phi_1 \\ c_1\sin\phi_1 \end{pmatrix} = \begin{pmatrix} x_1 \\ x_2 \\ \vdots \\ x_N \end{pmatrix}, \tag{C.22}$$

which we use to solve for c_1 and ϕ_1 using another least squares procedure. This is readily extensible to an arbitrary number K of frequency components.

APPENDIX D

CMTHG PLANE-WAVE PUMP MODEL

In this appendix, we carry out the CM-THG model with the simplification of a plane pump. Since the translation dependence of the individual terms does not follow from this model, but does when we incorporate pump longitudinal intensity variations, we conclude this pump intensity profile is important to the CM-THG interface scan behavior.

In an attempt to simplify matters, we first examine the case where we do not consider spatial variation of the pump. It will be shown this is not sufficient to explain the interface scan behavior, and a more detailed model must be constructed.

Perhaps something clever can be done, but the basic problem is that we will have a product of Gaussians in the spatial domain, which may be hard to solve. Neglecting the focusing of the pump, however, simplifies the problem.

We want to verify through this theory a few things observed in the lab. Measurements made under tight focusing conditions show a π phase shift in the measured Raman modulation as the material's face is translated through the focus.

D.1 Effective linear propagation with a Gaussian pulse

We have an equation of the form (Eq. 2.102):

$$\left\{\frac{i}{2k_1}\nabla_\perp^2 + \frac{\partial}{\partial\zeta}\right\} E_{\mathrm{o}}(x,y,\zeta,t_{\mathrm{o}}) = -i\delta k_1(t_{\mathrm{o}})E_{\mathrm{o}}(x,y,\zeta,t_{\mathrm{o}}) \tag{D.1}$$

Let's transform to the spatial frequency domain on x and y. We define the transformation

$$\hat{E}(k_x,k_y,\zeta,t) = \frac{1}{2\pi}\int_{-\infty}^{\infty}\mathrm{d}x\int_{-\infty}^{\infty}\mathrm{d}yE(x,y,\zeta,t)e^{-ik_xx}e^{-ik_yy}. \tag{D.2}$$

and the reverse transform

$$E(x,y,\zeta,t) = \frac{1}{2\pi}\int_{-\infty}^{\infty}\mathrm{dk_x}\int_{-\infty}^{\infty}\mathrm{dk_y}\hat{E}(k_x,k_y,\zeta,t)e^{+ik_xx}e^{+ik_yy} \tag{D.3}$$

The transverse Laplacian transforms according to,

$$\nabla_{\perp}^{2} E(x,y,\zeta,t) \Longleftrightarrow \left(k_x^2 + k_y^2\right) \hat{E}(k_x,k_y,\zeta,t), \tag{D.4}$$

for an input Gaussian beam , so that Eq. (D.1) can be written as

$$\frac{\partial}{\partial\zeta}\hat{E}_{\mathrm{o}}(k_x,k_y,\zeta,t_{\mathrm{o}}) = -i\left[\delta k_1(t_{\mathrm{o}}) + \frac{k_x^2+k_y^2}{2k_1}\right]\hat{E}_{\mathrm{o}}(k_x,k_y,\zeta,t_{\mathrm{o}}) \tag{D.5}$$

This has a solution of the form

$$\hat{E}_{\mathrm{o}}(k_x,k_y,\zeta,t_{\mathrm{o}}) = \hat{E}_{\mathrm{o}}(k_x,k_y,\zeta=0,t_{\mathrm{o}})\exp\left\{-i\left[\delta k_1(t_{\mathrm{o}}) + \frac{k_x^2+k_y^2}{2k_1}\right]\zeta\right\} \tag{D.6}$$

where $\zeta = 0$ is the input to the medium. We have an input beam with a waist at z_w given by

$$\hat{E}_{\mathrm{o}}(k_x,k_y,\zeta=0,t_{\mathrm{o}}) = E_{10}\frac{w_{10}^2}{4\pi}\exp\left\{-(k_x^2+k_y^2)\left[\frac{w_{10}^2}{4} - i\frac{z_w}{2k_1}\right]\right\} \tag{D.7}$$

Inserting this equation into the solution, we obtain

$$\hat{E}_{\mathrm{o}}(k_x,k_y,\zeta,t_{\mathrm{o}}) = E_{10}\frac{w_{10}^2}{4\pi}\exp\left\{-(k_x^2+k_y^2)\left[\frac{w_{10}^2}{4} - i\frac{z_w}{2k_1}\right]\right\} \times \exp\left\{-i\left[\delta k_1(t_{\mathrm{o}}) + \frac{k_x^2+k_y^2}{2k_1}\right]\zeta\right\} \tag{D.8}$$

which simplifies to

$$\hat{E}_{\mathrm{o}}(k_x,k_y,\zeta,t_{\mathrm{o}}) = E_{10}\frac{w_{10}^2}{4\pi}\exp\left\{-(k_x^2+k_y^2)\left[\frac{w_{10}^2}{4} + \frac{i(\zeta-z_w)}{2k_1}\right]\right\} e^{-i\delta k_1(t_{\mathrm{o}})\zeta}, \tag{D.9}$$

and by defining

$$A_1(\zeta) = 1 + \frac{i2(\zeta-z_w)}{w_{10}^2 k_1}, \tag{D.10}$$

we write

$$\hat{E}_{\mathrm{o}}(k_x,k_y,\zeta,t_{\mathrm{o}}) = E_{10}\frac{w_{10}^2}{4\pi}\exp\left\{-(k_x^2+k_y^2)\frac{w_{10}^2}{4}A_1(\zeta)\right\} e^{-i\delta k_1(t_{\mathrm{o}})\zeta}, \tag{D.11}$$

We can transform this into the spatial domain

$$E_{\mathrm{o}}(x,y,\zeta,t_{\mathrm{o}}) = \frac{1}{2\pi}\iint_{-\infty-\infty}^{\infty\infty} E_{10}\frac{w_{10}^2}{4\pi}e^{-(k_x^2+k_y^2)\frac{w_{10}^2}{4}A_1(\zeta)}e^{-i\delta k_1(t_{\mathrm{o}})\zeta}e^{i(k_x x+k_y y)}\mathrm{d}k_x\mathrm{d}k_y \tag{D.12}$$

Pulling out the terms invariant to k_x and k_y,

$$E_{\mathrm{o}}(x,y,\zeta,t_{\mathrm{o}}) = E_{10}\frac{w_{10}^2}{4\pi}e^{-i\delta k_1(t_{\mathrm{o}})\zeta} \times \frac{1}{2\pi}\iint_{-\infty-\infty}^{\infty\infty}\exp\left\{-(k_x^2+k_y^2)\frac{w_{10}^2}{4}A_1(\zeta)\right\}e^{i(k_x x+k_y y)}\mathrm{d}k_x\mathrm{d}k_y \quad \text{(D.13)}$$

In general the inverse Fourier transformation

$$\frac{w^2}{2\pi}\int_{-\infty}^{\infty}\mathrm{d}k_x\int_{-\infty}^{\infty}\mathrm{d}k_y\exp\left\{-(k_x^2+k_y^2)\frac{w^2}{4}\right\}e^{i(k_x x+k_y y)} = \exp\left\{-\frac{(x^2+y^2)}{w^2}\right\} \quad \text{(D.14)}$$

So the solution is given by

$$E_{\mathrm{pr}}(x,y,\zeta,t_{\mathrm{o}}) = \frac{E_{10}}{4\pi A_1(\zeta)}\exp\left\{-\frac{(x^2+y^2)}{w_{10}^2A_1(\zeta)}\right\}e^{-i\delta k_1(t_{\mathrm{o}})\zeta} \quad \text{(D.15)}$$

In summary, we started with the linear propagation equation for a probe pulse, including a time-dependent perturbation to the wavenumber k. We transformed this equation to the spatial frequency domain and found a solution, dependent on the form of the space- and time-dependent probe incident on the medium. Making this initial condition for the probe to be a focusing Gaussian beam, and performing the appropriate simplifications, we arrive at a solution, which turns out to be a focusing Gaussian beam multiplied by a complex modulation term $\exp\{-i\delta k_1(t_{\mathrm{pr}}\zeta\}$. The real and imaginary parts of the wavenumber k perturbation contribute to phase and amplitude modulation of the probe pulse, respectively.

We would like to insert A_1, so first we evaluate its reciprocal.

$$\begin{aligned}\frac{1}{A_1(\zeta)} &= \frac{1}{1+i\frac{2(\zeta-z_w)}{w_{10}^2k_1}}\\ &= \frac{w_{10}^2k_1}{w_{10}^2k_1+i2(\zeta-z_w)}\\ &= \frac{w_{10}^2k_1[w_{10}^2k_1-i2(\zeta-z_w)]}{(w_{10}^2k_1)^2-4(\zeta-z_w)^2}\\ &= \frac{(w_{10}^2k_1)^2-i2w_{10}^2k_1(\zeta-z_w)}{(w_{10}^2k_1)^2-4(\zeta-z_w)^2}\end{aligned} \quad \text{(D.16)}$$

. . . and so on. Proceed to give a solution for E_1 in terms of a magnitude and phase.

D.2 Third harmonic generation and propagation equations

The equation for the TH generation and propagation, assuming no GVM, is given in the frequency domain as

$$\frac{\partial}{\partial\zeta}\hat{E}_{\rm th}(k_x,k_y,\zeta,t_{\rm pr}) = i\frac{\omega_3}{8cn_3}\left(\chi_0^{(3)}+\delta\chi^{(3)}(t_{\rm pr})\right)\hat{E}_{\rm o}^3(k_x,k_y,\zeta,t_{\rm o})e^{-i\Delta k\zeta} - i\left\{\delta k_3(t_{\rm pr})+\frac{k_x^2+k_y^2}{2k_3}\right\}\hat{E}_{\rm th}(k_x,k_y,\zeta,t_{\rm o}) \quad \text{(D.17)}$$

The rhs consists of a source term $\propto \hat{E}_{\rm pr}^3$ plus a propagation term $\propto \hat{E}_{\rm th}$. The driving term time-dependence is

$$\delta\chi^{(3)}(t_{\rm pr}) = \delta\chi_0^{(3)}\sin[\Omega_v(t_{\rm pr}+\tau)] \quad \text{(D.18)}$$

For the source term, we need to return to the spatial domain and take the cube of the fundamental.

$$E_{\rm pr}^3(x,y,\zeta,t_{\rm o}) = \frac{E_{10}^3}{(4\pi)^3A_1^3(\zeta)}\exp\left\{-\frac{3(x^2+y^2)}{w_{10}^2A_1(\zeta)}\right\}e^{-i3\delta k_1(t_{\rm o})\zeta} \quad \text{(D.19)}$$

Given the solution of a Gaussian for the paraxial wave equation presented in the previous section, we can readily compute the source term for an undepleted pump for 3$^{\rm rd}$ harmonic generation. In the spatial domain, the driving term is given by

$$i\frac{\omega_3}{8cn_3}\left(\chi_0^{(3)}+\delta\chi^{(3)}(t_{\rm pr})\right)\frac{E_{10}^3}{(4\pi)^3A_1^3(\zeta)}\exp\left\{-3\frac{(x^2+y^2)}{w_{10}^2A_1(\zeta)}\right\}e^{-i3\delta k_1(t_{\rm o})\zeta} \quad \text{(D.20)}$$

Transforming this driving term to spatial frequency domain, pulling out x- and y-invariant factors,

$$i\frac{\omega_3}{8cn_3}\left(\chi_0^{(3)}+\delta\chi^{(3)}(t_{\rm pr})\right)\frac{E_{10}^3}{(4\pi)^3A_1^3(\zeta)}e^{-i3\delta k_1(t_{\rm o})\zeta} \times\frac{1}{2\pi}\int_{-\infty}^{\infty}{\rm d}x\int_{-\infty}^{\infty}{\rm d}y\exp\left\{-3\frac{(x^2+y^2)}{w_{10}^2A_1(\zeta)}\right\}e^{i(k_xx+k_yy)} \quad \text{(D.21)}$$

The double integral evaluates according to the Fourier relationship

$$\frac{1}{2\pi}\int_{-\infty}^{\infty}{\rm d}x\int_{-\infty}^{\infty}{\rm d}y\exp\left\{-\frac{(x^2+y^2)}{w^2}\right\}e^{i(k_xx+k_yy)} = w^2\exp\left\{-\left(k_x^2+k_y^2\right)\frac{w^2}{4}\right\} \quad \text{(D.22)}$$

So that

$$i\frac{\omega_3}{8cn_3}\left(\chi_0^{(3)}+\delta\chi^{(3)}(t_{\rm pr})\right)\frac{E_{10}^3}{(4\pi)^3A_1^3(\zeta)}e^{-i3\delta k_1(t_{\rm o})\zeta} \times\left(\frac{w_{10}^2A_1(\zeta)}{3}\right)\exp\left\{-(k_x^2+k_y^2)\frac{w_{10}^2A_1(\zeta)}{12}\right\} \quad \text{(D.23)}$$

and the source term is finally

$$i\frac{\omega_3 w_{10}^2}{24cn_3}\left(\chi_0^{(3)}+\delta\chi^{(3)}(t_{\rm pr})\right)\frac{E_{10}^3}{(4\pi)^3A_1^2(\zeta)}e^{-i3\delta k_1(t_{\rm o})\zeta}\exp\left\{-(k_x^2+k_y^2)\frac{w_{10}^2A_1(\zeta)}{12}\right\} \tag{D.24}$$

D.3 Full solution

Finally, we have the equation that we wish to solve

$$\begin{aligned}\frac{\partial\hat{E}_{\rm th}}{\partial\zeta}=i\frac{\omega_3 w_{10}^2}{24cn_3}\left(\chi_0^{(3)}+\delta\chi^{(3)}(t_{\rm pr})\right)\frac{E_{10}^3}{(4\pi)^3A_1^2(\zeta)}\\ \times e^{-i3\delta k_1(t_{\rm o})\zeta}\exp\left\{-(k_x^2+k_y^2)\frac{w_{10}^2A_1(\zeta)}{12}\right\}e^{-i\Delta k\zeta}\\ -i\left\{\delta k_3(t_{\rm pr})+\frac{k_x^2+k_y^2}{2k_3}\right\}\hat{E}_{\rm th}\end{aligned} \tag{D.25}$$

Let us rewrite the equation by defining

$$\Gamma=i\left\{\delta k_3(t_{\rm pr})+\frac{k_x^2+k_y^2}{2k_3}\right\} \tag{D.26}$$

and

$$\begin{aligned}f(\zeta)=i\frac{\omega_3 w_{10}^2}{24cn_3}\left(\chi_0^{(3)}+\delta\chi^{(3)}(t_{\rm pr})\right)\frac{E_{10}^3}{(4\pi)^3A_1^2(\zeta)}e^{-i3\delta k_1(t_{\rm o})\zeta}\\ \times\exp\left\{-(k_x^2+k_y^2)\frac{w_{10}^2A_1(\zeta)}{12}\right\}e^{-i\Delta k\zeta}\end{aligned} \tag{D.27}$$

Now the differential equation becomes

$$\frac{{\rm d}\hat{E}_{\rm th}(\zeta)}{{\rm d}\zeta}+\Gamma\hat{E}_{\rm th}(\zeta)=f(\zeta), \tag{D.28}$$

which has the solution

$$\hat{E}_{\rm th}(\zeta,t)=e^{\Gamma\zeta}\int_0^\zeta f(\zeta')e^{\Gamma\zeta'}{\rm d}\zeta'+\mathcal{C}'e^{-\Gamma\zeta}. \tag{D.29}$$

Which lets us arrive at a general solution

$$\begin{aligned}\hat{E}_{\rm th}(k_x,k_y;\zeta)=e^{-i\left[\delta k_3(t_{\rm pr})+\frac{k_x^2+k_y^2}{2k_3}\right]\zeta}\int_0^\zeta f(\zeta')e^{i\left[\delta k_3(t_{\rm th})+\frac{k_x^2+k_y^2}{2k_3}\right]\zeta'}{\rm d}\zeta'\\ +\hat{E}_{\rm th}(k_x,k_y;\zeta=0)e^{-i\left[\delta k_3(t_{\rm th})+\frac{k_x^2+k_y^2}{2k_3}\right]\zeta}\end{aligned} \tag{D.30}$$

D.4 Gaussian Solutions with zero input TH

Let us assume that the we have no injected control 3$^{\text{rd}}$ harmonic field and that the solution of the field takes the form of a Gaussian

$$\hat{E}_{\text{th}}(k_x, k_y; \zeta) = E_{30}(\zeta)\frac{w_{30}^2}{4\pi}\exp\left\{-(k_x^2+k_y^2)\frac{w_{30}^2 A_3(\zeta)}{4}\right\}e^{-i\delta k_3(t_o)\zeta} \tag{D.31}$$

where

$$A_3 = 1 + \frac{2i(\zeta-\zeta_{w3})}{w_{30}^2 k_3} \tag{D.32}$$

and E_{30} is function of ζ, w_{30} is the focusing waist of the third harmonic beam, and ζ_{w3} is the position of the focus. Note here that $E_{30}(\zeta)e^{-i\delta k_3(t_{\text{pr}})\zeta}$ describes the complex deviation from the unperturbed Gaussian that would be generate in absence of a coherence.

Now there are three factors that are functions of ζ, whose derivatives we lay out in preparation of finding the derivative of the entire expression by the product rule

$$\begin{aligned}\frac{\partial}{\partial\zeta}\hat{E}_{\text{th}} = \frac{w_{30}^2}{4\pi}\Bigg\{&\frac{\partial E_{30}(\zeta)}{\partial\zeta}\exp\left[-(k_x^2+k_y^2)\frac{w_{30}^2A_3(\zeta)}{4}\right]e^{-i\delta k_3(t_o)\zeta}\\ &+E_{30}(\zeta)\frac{\partial\exp\left[-(k_x^2+k_y^2)\frac{w_{30}^2A_3(\zeta)}{4}\right]}{\partial\zeta}e^{-i\delta k_3(t_o)\zeta}\\ &+E_{30}(\zeta)\exp\left[-(k_x^2+k_y^2)\frac{w_{30}^2A_3(\zeta)}{4}\right]\frac{\partial e^{-i\delta k_3(t_o)\zeta}}{\partial\zeta}\Bigg\}\end{aligned} \tag{D.33}$$

The first cannot be reduced a priori:

$$\frac{\partial E_{30}(\zeta)}{\partial\zeta}. \tag{D.34}$$

The second is an exponential with a function of ζ in the argument:

$$\begin{aligned}&\frac{\partial}{\partial\zeta}\exp\left\{-(k_x^2+k_y^2)\frac{w_{30}^2A_3(\zeta)}{4}\right\}\\ &\qquad=\left\{-(k_x^2+k_y^2)\frac{w_{30}^2}{4}\right\}\exp\left\{-(k_x^2+k_y^2)\frac{w_{30}^2A_3(\zeta)}{4}\right\}\frac{\partial A_3(\zeta)}{\partial\zeta}\end{aligned} \tag{D.35}$$

and the derivative of $A_3(\zeta)$ is

$$\frac{\partial A_3}{\partial\zeta} = \frac{2i}{w_{30}^2k_3} \tag{D.36}$$

so that

$$\frac{\partial}{\partial\zeta}\exp\left\{-(k_x^2+k_y^2)\frac{w_{30}^2A_3(\zeta)}{4}\right\} = -i\frac{k_x^2+k_y^2}{2k_3}\exp\left\{-(k_x^2+k_y^2)\frac{w_{30}^2A_3(\zeta)}{4}\right\}. \tag{D.37}$$

And the third factor's derivative is

$$\frac{\partial}{\partial\zeta}e^{-i\delta k_3(t_\mathrm{o})\zeta} = -i\delta k_3(t_\mathrm{o})e^{-i\delta k_3(t_\mathrm{o})\zeta} \tag{D.38}$$

The derivative of the two exponentials together is

$$\begin{aligned}\frac{\partial}{\partial\zeta}\exp\left[-(k_x^2+k_y^2)\frac{w_{30}^2A_3(\zeta)}{4} - i\delta k_3(t_\mathrm{o})\zeta\right]& \\ = -i\left[\frac{k_x^2+k_y^2}{2k_3}+\delta k_3(t_\mathrm{o})\right]\exp\left[-(k_x^2+k_y^2)\frac{w_{30}^2A_3(\zeta)}{4}\right]e^{-i\delta k_3(t_\mathrm{o})\zeta}&\end{aligned} \tag{D.39}$$

Finally the full derivative is

$$\begin{aligned}\frac{\partial}{\partial\zeta}\hat{E}_\mathrm{th} = \frac{\partial E_{30}(\zeta)}{\partial\zeta}\frac{w_{30}^2}{4\pi}\exp\left\{-(k_x^2+k_y^2)\frac{w_{30}^2A_3(\zeta)}{4}\right\}e^{-i\delta k_3(t_\mathrm{o})\zeta}& \\ - iE_{30}(\zeta)\frac{w_{30}^2}{4\pi}\left[\frac{k_x^2+k_y^2}{2k_3}+\delta k_3(t_\mathrm{o})\right]\exp\left[-(k_x^2+k_y^2)\frac{w_{30}^2A_3(\zeta)}{4}\right]e^{-i\delta k_3(t_\mathrm{o})\zeta}&\end{aligned} \tag{D.40}$$

Which condenses to

$$\begin{aligned}\frac{\partial}{\partial\zeta}\hat{E}_\mathrm{th} = \frac{w_{30}^2}{4\pi}\left\{\frac{\partial E_{30}(\zeta)}{\partial\zeta} - iE_{30}(\zeta)\left[\frac{k_x^2+k_y^2}{2k_3}+\delta k_3(t_\mathrm{o})\right]\right\}& \\ \times\exp\left[-(k_x^2+k_y^2)\frac{w_{30}^2A_3(\zeta)}{4}\right]e^{-i\delta k_3(t_\mathrm{o})\zeta}&\end{aligned} \tag{D.41}$$

Or alternative putting the derivative in terms of $\hat{E}_\mathrm{th}$,

$$\begin{aligned}\frac{\partial\hat{E}_\mathrm{th}(k_x,k_y;\zeta)}{\partial\zeta} = -i\left\{\delta k_3(t)+\frac{k_x^2+k_y^2}{2k_3}\right\}\hat{E}_\mathrm{th}& \\ + \frac{w_{30}^2}{4\pi}\exp\left\{-(k_x^2+k_y^2)\frac{w_{30}^2A_3(\zeta)}{4}\right\}e^{-i\delta k_3(t_\mathrm{o})\zeta}\frac{\partial E_{30}(\zeta)}{\partial\zeta}&\end{aligned} \tag{D.42}$$

Substituting this into the lhs Eq. (D.44) gives

$$\begin{aligned}-i\left\{\delta k_3(t)+\frac{k_x^2+k_y^2}{2k_3}\right\}\hat{E}_\mathrm{th} + \frac{w_{30}^2}{4\pi}\exp\left\{-(k_x^2+k_y^2)\frac{w_{30}^2A_3}{4}\right\}e^{-i\delta k_3(t_\mathrm{o})\zeta}\frac{\partial E_{30}(\zeta)}{\partial\zeta}& \\ = i\frac{\omega_3w_{10}^2}{24cn_3}\left(\chi_0^{(3)}+\delta\chi^{(3)}(t)\right)\frac{E_{10}^3}{(4\pi)^3A_1^2(\zeta)}e^{-i3\delta k_1(t_\mathrm{o})\zeta}\exp\left\{-(k_x^2+k_y^2)\frac{w_{10}^2A_1}{12}\right\}e^{-i\Delta k\zeta}& \\ - i\left\{\delta k_3(t)+\frac{k_x^2+k_y^2}{2k_3}\right\}\hat{E}_3&\end{aligned} \tag{D.43}$$

which simplifies, after two $\hat{E}_{\rm th}$ terms cancel,

$$\frac{w_{30}^2}{4\pi}\exp\left\{-(k_x^2+k_y^2)\frac{w_{30}^2 A_3}{4}\right\}e^{-i\delta k_3(t_{\rm o})\zeta}\frac{\partial E_{30}(\zeta)}{\partial\zeta}$$
$$= i\frac{\omega_3 w_{10}^2}{24cn_3}\left(\chi_0^{(3)}+\delta\chi^{(3)}(t_{\rm pr})\right)\frac{E_{10}^3}{(4\pi)^3 A_1^2(\zeta)}e^{-i3\delta k_1(t_{\rm o})\zeta}\exp\left\{-(k_x^2+k_y^2)\frac{w_{10}^2 A_1}{12}\right\}e^{-i\Delta k\zeta} \tag{D.44}$$

Rearranging to isolate the derivative of E_{30},

$$\frac{\partial E_{30}(\zeta)}{\partial\zeta} = i\frac{\pi\omega_3 w_{10}^2}{6cn_3 w_{30}^2}\left[\chi_0^{(3)}+\delta\chi^{(3)}(t_{\rm pr})\right]\frac{E_{10}^3}{(4\pi)^3 A_1^2(\zeta)}e^{-i[3\delta k_1(t_{\rm o})-\delta k_3(t_{\rm o})]\zeta}e^{-i\Delta k\zeta}$$
$$\exp\left[-\left(k_x^2+k_y^2\right)\left(\frac{w_{10}^2 A_1(\zeta)}{12}-\frac{w_{30}^2 A_3(\zeta)}{4}\right)\right]. \tag{D.45}$$

Next we insert the definitions of $A_1(\zeta)$ and $A_3(\zeta)$:

$$\frac{\partial E_{30}(\zeta)}{\partial\zeta} = i\frac{\pi\omega_3 w_{10}^2}{6cn_3 w_{30}^2}\left[\chi_0^{(3)}+\delta\chi^{(3)}(t_{\rm pr})\right]\frac{E_{10}^3}{(4\pi)^3 A_1^2(\zeta)}e^{-i[3\delta k_1(t_{\rm o})-\delta k_3(t_{\rm o})]\zeta}e^{-i\Delta k\zeta}$$
$$\times\exp\left[-\left(k_x^2+k_y^2\right)\left(\frac{w_{10}^2}{12}+i\frac{\zeta-z_w}{6k_1}-\frac{w_{30}^2}{4}-i\frac{\zeta-\zeta_{w3}}{2k_3}\right)\right]. \tag{D.46}$$

D.5 Four critical approximations

To recover a solution similar to that given in Boyd, we must assume that

$$\left[\frac{w_{10}^2}{12}+i\frac{\zeta-z_w}{6k_1}\right]=\left[\frac{w_{30}^2}{4}+i\frac{\zeta-\zeta_{w3}}{2k_3}\right] \tag{D.47}$$

Or, equivalently that the spot size of the beams is fixed by the relationship,

$$w_{10}^2 = 3w_{30}^2, \tag{D.48}$$

the foci are located at the same point,

$$z_w = \zeta_{w3}, \tag{D.49}$$

and the ratio

$$\frac{1}{3k_1}-\frac{1}{k_3}=\frac{k_3-3k_1}{3k_1k_3}\approx 0. \tag{D.50}$$

Since $\Delta k/k$ is small, this is entirely reasonable. Note this is not equivalent to neglecting phase mismatch. This reduces the equation to

$$\frac{\partial E_{30}(\zeta)}{\partial\zeta} = i\frac{\pi\omega_3 w_{10}^2}{6cn_3 w_{30}^2}\left[\chi_0^{(3)}+\delta\chi^{(3)}(t_{\rm pr})\right]\frac{E_{10}^3}{(4\pi)^3 A_1^2(\zeta)}e^{-i[3\delta k_1(t_{\rm o})-\delta k_3(t_{\rm o})]\zeta}e^{-i\Delta k\zeta}. \tag{D.51}$$

At this point, we examine the exponential argument, breaking it apart into real and imaginary components,

$$\begin{aligned} -i[3\delta k_1(t_{\mathrm{o}}) - \delta k_3(t_{\mathrm{o}})]\zeta &= \left[-i3\delta k_1'(t_{\mathrm{pr}}) + 3\delta k_1''(t_{\mathrm{pr}}) + i\delta k_3'(t_{\mathrm{pr}}) - \delta k_3''(t_{\mathrm{pr}})\right]\zeta \\ &= \left[3\delta k_1''(t_{\mathrm{pr}}) - \delta k_3''(t_{\mathrm{pr}})\right]\zeta - i\left[3\delta k_1'(t_{\mathrm{pr}}) - \delta k_3'(t_{\mathrm{pr}})\right]\zeta \end{aligned} \tag{D.52}$$

So the exponent at the end is

$$e^{\left[3\delta k_1''(t_{\mathrm{pr}}) - \delta k_3''(t_{\mathrm{pr}})\right]\zeta} e^{-i\left[3\delta k_1'(t_{\mathrm{pr}}) - \delta k_3'(t_{\mathrm{pr}})\right]\zeta} e^{-i\Delta k\zeta}. \tag{D.53}$$

We may be able to make a simplification if we can demonstrate

$$3\delta k_1'(t_{\mathrm{pr}}) - \delta k_3'(t_{\mathrm{pr}}) \ll \Delta k \tag{D.54}$$

It seems that this is effectively a perturbation to the phase mismatch. To prove the inequality more rigorously, we start with

$$\delta k_1'(t_{\mathrm{pr}}) \propto \frac{\omega_1}{2cn_1}\delta\chi_0^{(1)}(\omega_1)\left|U_s\right|^2 \tag{D.55}$$

and

$$\delta k_3'(t_{\mathrm{pr}}) \propto \frac{\omega_3}{2cn_3}\delta\chi_0^{(1)}(\omega_3)\left|U_s\right|^2 \tag{D.56}$$

Remember we have not clearly defined $\delta\chi_0^{(1)}$, but it may depend on the probe frequency. so that the difference

$$3\delta k_1'(t_{\mathrm{pr}}) - \delta k_3'(t_{\mathrm{pr}}) = \frac{\omega_3\left|U_s\right|^2}{2c}\left(\frac{\delta\chi_0^{(1)}(\omega_3)}{n_3} - \frac{\delta\chi_0^{(1)}(\omega_1)}{n_1}\right) \tag{D.57}$$

It's not immediately obvious this is less than the phase mismatch term. Regardless, if we can make this approximation, the phase modulation due to the real part of the wavenumber k perturbations to the fundamental and the third harmonic is negligible, and the equation for $E_{30}(\zeta)$ becomes

$$\frac{\partial E_{30}(\zeta)}{\partial\zeta} = i\frac{\pi\omega_3 w_{10}^2}{6cn_3 w_{30}^2}\left[\chi_0^{(3)} + \delta\chi^{(3)}(t_{\mathrm{pr}})\right]\frac{E_{10}^3}{(4\pi)^3 A_1^2(\zeta)} e^{\left[3\delta k_1''(t_{\mathrm{pr}}) - \delta k_3''(t_{\mathrm{pr}})\right]\zeta} e^{-i\Delta k\zeta} \tag{D.58}$$

If we grant that the attenuation exponential term is small, we approximate

$$e^{[3\delta k_1''(t_{\mathrm{pr}}) - \delta k_3''(t_{\mathrm{pr}})]\zeta} \approx 1 + [3\delta k_1''(t_{\mathrm{pr}}) - \delta k_3''(t_{\mathrm{pr}})]\zeta, \tag{D.59}$$

and the product

$$\left[\chi_0^{(3)} + \delta\chi^{(3)}(t_{\rm pr})\right]\left\{1 + [3\delta k_1''(t_{\rm pr}) - \delta k_3''(t_{\rm pr})]\zeta\right\}$$
$$\approx \chi_0^{(3)} + \delta\chi^{(3)}(t_{\rm pr}) + \chi_0^{(3)}[3\delta k_1''(t_{\rm pr}) - \delta k_3''(t_{\rm pr})]\zeta. \quad \text{(D.60)}$$

The equation for $E_{30}(\zeta)$ is

$$\frac{\partial E_{30}(\zeta)}{\partial\zeta} = i\frac{\pi\omega_3 w_{10}^2}{6cn_3 w_{30}^2}\left\{\chi_0^{(3)} + \delta\chi^{(3)}(t_{\rm pr}) + \chi_0^{(3)}[3\delta k_1''(t_{\rm pr}) - \delta k_3''(t_{\rm pr})]\zeta\right\}$$
$$\times \frac{E_{10}^3}{(4\pi)^3 A_1^2(\zeta)} e^{-i\Delta k\zeta} \quad \text{(D.61)}$$

factoring out $\chi_0^{(3)}$,

$$\frac{\partial E_{30}(\zeta)}{\partial\zeta} = i\frac{\pi\omega_3 w_{10}^2}{6cn_3 w_{30}^2}\chi_0^{(3)}\left\{1 + \delta\chi^{(3)}(t_{\rm pr})/\chi_0^{(3)} + [3\delta k_1''(t_{\rm pr}) - \delta k_3''(t_{\rm pr})]\zeta\right\}$$
$$\times \frac{E_{10}^3}{(4\pi)^3 A_1^2(\zeta)} e^{-i\Delta k\zeta} \quad \text{(D.62)}$$

We will integrate both sides to reveal the solution

$$E_{30}(\zeta) = i\frac{\pi\omega_3 w_{10}^2}{6cn_3 w_{30}^2}\chi_0^{(3)}\frac{E_{10}^3}{(4\pi)^3}\left\{\left[1 + \delta\chi^{(3)}(t_{\rm pr})/\chi_0^{(3)}\right]\int_0^\zeta \frac{e^{-i\Delta k\zeta'}}{A_1^2(\zeta')}{\rm d}\zeta'\right.$$
$$\left. + [3\delta k_1''(t_{\rm pr}) - \delta k_3''(t_{\rm pr}))\int_0^\zeta \frac{e^{-i\Delta k\zeta'}}{A_1^2(\zeta')}\zeta'{\rm d}\zeta'\right\} \quad \text{(D.63)}$$

These two integrals describe the effects of to distinct phenomena. The first corresponds to the coherent second hyper-Raman process expressed in $\delta\chi^{(3)}(t_{\rm pr})$. The second describes attenuation effects on the probe fundamental $\delta k_1''(t_{\rm pr})$ and the third harmonic $\delta k_3''(t_{\rm pr})$.

Note that if we were considering group velocity walkoff, we would not be able to pull the time-dependent terms outside of the ζ-dependent integration. Also E_{10} would not be independent of ζ, and would be found inside the integrals as well.

D.6 Tight focusing

Tight focusing turns out to be easier to solve. In a tight focus, we make the assumption that $\Delta k\zeta \ll 1$ so that we have the integrals

$$E_{30}(\zeta) = i\frac{\pi\omega_3 w_{10}^2}{6cn_3 w_{30}^2}\chi_0^{(3)}\frac{E_{10}^3}{(4\pi)^3}\left\{\left[1 + \delta\chi^{(3)}(t_{\rm pr})/\chi_0^{(3)}\right]\int_0^\zeta \frac{1}{A_1^2(\zeta')}{\rm d}\zeta'\right.$$
$$\left. + [3\delta k_1''(t_{\rm pr}) - \delta k_3''(t_{\rm pr})]\int_0^\zeta \frac{\zeta'}{A_1^2(\zeta')}{\rm d}\zeta'\right\} \quad \text{(D.64)}$$

We'll examine the integrals separately. The first is

$$\begin{aligned}\int_0^\zeta \frac{1}{A_1^2(\zeta')}\mathrm{d}\zeta' &= \int_0^\zeta \frac{1}{\left[1+\frac{i2(\zeta'-z_w)}{w_{10}^2 k_1}\right]^2}\mathrm{d}\zeta' \\ &= \int_0^\zeta \frac{1}{(C+D\zeta')^2}\mathrm{d}\zeta'\end{aligned} \tag{D.65}$$

where for convenience we have defined the complex constants

$$C = 1 - i\frac{2z_w}{w_{10}^2 k_1} \tag{D.66}$$

and

$$D = i\frac{2}{w_{10}^2 k_1}. \tag{D.67}$$

such that

$$A_1(\zeta) = C + D\zeta. \tag{D.68}$$

There are no real values of ζ' which can force the denominator to zero, so the integral is straightforward:

$$\int_0^\zeta \frac{1}{(C+D\zeta')^2}\mathrm{d}\zeta' = \frac{1}{D(C+D\zeta')}\bigg|_0^\zeta = \frac{1}{D(C+D\zeta)} - \frac{1}{DC} = \frac{1}{D}\left[\frac{1}{C+D\zeta} - \frac{1}{C}\right] \tag{D.69}$$

Recognizing that $A_1(\zeta = 0) = C$, and plugging in definitions, the integral evaluates as follows

$$\int_0^\zeta \frac{1}{A_1^2(\zeta')}\mathrm{d}\zeta' = -i\frac{w_{10}^2 k_1}{2}\left[\frac{1}{A_1(\zeta)} - \frac{1}{A_1(0)}\right] \tag{D.70}$$

The other integral is more complicated. Using MAXIMA, we find

$$\begin{aligned}\int_0^\zeta \frac{\zeta'}{(C+D\zeta')^2}\mathrm{d}\zeta' &= \frac{\ln(C+D\zeta')}{D^2} + \frac{C}{CD^2+D^3\zeta'}\bigg|_0^\zeta \\ &= \frac{1}{D^2}\left[\ln(C+D\zeta') + \frac{C}{C+D\zeta'}\right]_0^\zeta \\ &= \frac{1}{D^2}\left[\ln(C+D\zeta) + \frac{C}{C+D\zeta} - \ln(C) - 1\right]\end{aligned} \tag{D.71}$$

Re-inserting the definitions of D and C,

$$\int_0^\zeta \frac{\zeta'}{A_1^2(\zeta')}\mathrm{d}\zeta' = -\frac{\left(w_{10}^2 k_1\right)^2}{4}\left\{\ln\left[A_1(\zeta)\right] + \frac{A_1(0)}{A_1(\zeta)} - \ln\left[A_1(0)\right] - 1\right\} \tag{D.72}$$

Inserting these results into the expression for $E_3(\zeta)$,

$$E_{30}(\zeta) = i\frac{\pi\omega_3 w_{10}^2}{6cn_3 w_{30}^2}\chi_0^{(3)}\frac{E_{10}^3}{(4\pi)^3}\left\{\left[1+\delta\chi^{(3)}(t_{\rm pr})/\chi_0^{(3)}\right]\left(-i\frac{w_{10}^2 k_1}{2}\right)\left[\frac{1}{A_1(\zeta)}-\frac{1}{A_1(0)}\right]\right.$$
$$\left.+[3\delta k_1''(t_{\rm pr})-\delta k_3''(t_{\rm pr})]\left[-\frac{\left(w_{10}^2 k_1\right)^2}{4}\right]\left\{\ln\left[A_1(\zeta)\right]+\frac{A_1(0)}{A_1(\zeta)}-\ln\left[A_1(0)\right]-1\right\}\right\} \quad \text{(D.73)}$$

Factoring out a few constants,

$$E_{30}(\zeta) = i\frac{\pi\omega_3 w_{10}^2}{6cn_3 w_{30}^2}\chi_0^{(3)}\frac{E_{10}^3}{(4\pi)^3}\left(-i\frac{w_{10}^2 k_1}{2}\right)\left\{\left[1+\delta\chi^{(3)}(t_{\rm pr})/\chi_0^{(3)}\right]\left[\frac{1}{A_1(\zeta)}-\frac{1}{A_1(0)}\right]\right.$$
$$\left.+[3\delta k_1''(t_{\rm pr})-\delta k_3''(t_{\rm pr})]\left(-i\frac{w_{10}^2 k_1}{2}\right)\left[\ln\left[A_1(\zeta)\right]+\frac{A_1(0)}{A_1(\zeta)}-\ln\left[A_1(0)\right]-1\right]\right\} \quad \text{(D.74)}$$

To clear things up, we separate $E_{30}(\zeta)$ into a function of ζ plus a constant

$$E_{30}(\zeta) = i\frac{\pi\omega_3 w_{10}^2}{6cn_3 w_{30}^2}\chi_0^{(3)}\frac{E_{10}^3}{(4\pi)^3}\left(-i\frac{w_{10}^2 k_1}{2}\right)\left\{\left[1+\delta\chi^{(3)}(t_{\rm pr})/\chi_0^{(3)}\right]\frac{1}{A_1(\zeta)}\right.$$
$$\left.+[3\delta k_1''(t_{\rm pr})-\delta k_3''(t_{\rm pr})]\left(-i\frac{w_{10}^2 k_1}{2}\right)\left[\ln\left[A_1(\zeta)\right]+\frac{A_1(0)}{A_1(\zeta)}\right]\right\}+Q \quad \text{(D.75)}$$

where

$$Q = i\frac{\pi\omega_3 w_{10}^2}{6cn_3 w_{30}^2}\chi_0^{(3)}\frac{E_{10}^3}{(4\pi)^3}\left(-i\frac{w_{10}^2 k_1}{2}\right)\left\{-\left[1+\delta\chi^{(3)}(t_{\rm pr})/\chi_0^{(3)}\right]\frac{1}{A_1(0)}\right.$$
$$\left.+[3\delta k_1''(t_{\rm pr})-\delta k_3''(t_{\rm pr})]\left(-i\frac{w_{10}^2 k_1}{2}\right)\left[\ln\left[A_1(0)\right]+1\right]\right\}. \quad \text{(D.76)}$$

The final solution for the third harmonic field, repeated here for convenience is

$$\hat{E}_{\rm th}(k_x,k_y;\zeta) = E_{30}(\zeta)\frac{w_{30}^2}{4\pi}\exp\left\{-(k_x^2+k_y^2)\frac{w_{30}^2 A_3(\zeta)}{4}\right\}e^{-i\delta k_3(t_o)\zeta} \quad \text{(D.77)}$$

D.7 Detected signal

The mod-squared detected signal, such as would be recorded by a PMT, is written

$$E_{\rm th} = E_{\rm th}E_{\rm th}^* \propto \left[E_{30}e^{-i\delta k_3\zeta}\right]\left[E_{30}e^{-i\delta k_3\zeta}\right]^* = E_{30}E_{30}^*. \quad \text{(D.78)}$$

Note how the complex conjugation removes the effect of the modulation by $-i\delta k_3$ in the full trial solution. Thus, we only need to consider $E_{30}(\zeta)$ instead of $E_{\rm th}(\zeta)$ when calculating the detected signal.

D.8 Translating focus about the back interface

Here we attempt to relate the model to experimental measurements where we have observed that translating the focus around the back interface leads to a π phase shift in the measured modulations.

At the back interface, there is a sharp discontinuity in the optical properties in addition to a sudden change in the forward propagating fundamental and third harmonic due to modulation of the Fresnel transmission coefficients. So if we desire to recover the field incident on a detector placed some distance away from the interface, the integral breaks apart. Let's consider the total third harmonic generated by a focusing Gaussian beam originating in the sample, focusing at z_w, and exiting through an interface to air at ζ_i. Material response is designated by an 'm' subscript, air response is designated by an 'a' subscript.

$$\begin{aligned} E_{30} = i\frac{\pi\omega_3 w_{10}^2}{6cn_3 w_{30}^2}\frac{E_{10}^3}{(4\pi)^3}\Bigg\{ & T_3(\delta n)\chi^{(3)}_{0,\mathrm{m}}\int_{-\infty}^{\zeta_i}\frac{1}{A_1^2(\zeta')}\mathrm{d}\zeta' + T_3(\delta n)\delta\chi^{(3)}(t_{\mathrm{pr}})\int_{-\infty}^{\zeta_i}\frac{1}{A_1^2(\zeta')}\mathrm{d}\zeta' \\ & + T_3(\delta n)\chi^{(3)}_{0,\mathrm{m}}[3\delta k_1''(t_{\mathrm{pr}}) - \delta k_3''(t_{\mathrm{pr}})]\int_{-\infty}^{\zeta_i}\frac{\zeta'}{A_1^2(\zeta')}\mathrm{d}\zeta' \\ & + T_1^3(\delta n)\chi^{(3)}_{0,\mathrm{a}}\int_{\zeta_i}^{\infty}\frac{1}{A_1^2(\zeta')}\mathrm{d}\zeta'\Bigg\} \end{aligned} \tag{D.79}$$

where T_1 is the fundamental modulated transmission coefficient, and T_3 is the modulated transmission coefficient at the third harmonic. The transmission coefficient t is the initial coefficient plus a small perturbation, so its cube is approximated

$$T_1^3(\delta n) = [T_{0,1} + \delta T_1(t_{pr})]^3 \approx T_{0,1} + 3\delta T_1(t_{\mathrm{o}}) \tag{D.80}$$

Also the third harmonic transmission perturbation multiplied by small terms is neglected,

$$T_3(\delta n) = T_{0,3} + \delta T_3(t_{\mathrm{o}}) \tag{D.81}$$

so that

$$T_3(\delta n)\delta\chi^{(3)} \approx T_{0,3}\delta\chi^{(3)} \tag{D.82}$$

and

$$T_3(\delta n)(3\delta k_1'' - \delta k_3'') \approx T_{0,3}(3\delta k_1'' - \delta k_3'') \tag{D.83}$$

If we were considering group velocity mismatch, T_1^3 would have a dependence on ζ and so would remain inside the integral. The dependence would have to account for the fact that the TH pulse arrival time at the back interface is slowed down by its group velocity and the sample thickness.

We should be careful that ζ_w and ζ_i are sufficiently far from $\zeta = 0$, as it was assumed in arriving at this solution that $E_{30}(\zeta = 0) = 0$. To shorten up the notation, we define

$$V(z_1, z_2) = \int_{z_1}^{z_2} \frac{1}{A_1^2(\zeta')} \mathrm{d}\zeta', \tag{D.84}$$

$$W(z_1, z_2) = \int_{z_1}^{z_2} \frac{\zeta'}{A_1^2(\zeta')} \mathrm{d}\zeta', \tag{D.85}$$

and

$$Z = i \frac{\pi \omega_3 w_{10}^2}{6 c n_3 w_{30}^2} \frac{E_{10}^3}{(4\pi)^3}, \tag{D.86}$$

and then we have

$$\begin{aligned} E_{30} = Z \Big[& (T_{0,3} + \delta T_3)\, \chi_{0,\mathrm{m}}^{(3)} V(-\infty, \zeta_i) + T_{0,3} \delta\chi^{(3)}(t) V(-\infty, \zeta_i) \\ & + T_{0,3} \chi_{0,\mathrm{m}}^{(3)} (3\delta k_1'' - \delta k_3'') W(-\infty, \zeta_i) + T_{0,1} \chi_{0,\mathrm{a}}^{(3)} V(\zeta_i, \infty) + 3\Delta t_1 \chi_{0,\mathrm{a}}^{(3)} V(\zeta_i, \infty) \Big] \end{aligned} \tag{D.87}$$

When we examine the square magnitude of this expression, we will see the square of each term plus cross-terms. We will neglect squares and cross-terms containing small quantities multiplied by small quantities, namely $\delta\chi^{(3)}$, $(3\delta k_1'' - \delta k_3'')$, and δT. We group terms according to whether they are time-varying (and small) or not.

$$\begin{aligned} E_{30} = Z \Big\{ & \Big[T_{0,3} \chi_{0,\mathrm{m}}^{(3)} V(-\infty, \zeta_i) + T_{0,1} \chi_{0,\mathrm{a}}^{(3)} V(\zeta_i, \infty) \Big] + \Big[\delta T_3 \chi_{0,\mathrm{m}}^{(3)} V(-\infty, \zeta_i) \\ & + T_{0,3} \delta\chi^{(3)} V(-\infty, \zeta_i) + T_{0,3} \chi_{0,\mathrm{m}}^{(3)} (3\delta k_1'' - \delta k_3'') W(-\infty, \zeta_i) + 3\delta T \chi_{0,\mathrm{a}}^{(3)} V(\zeta_i, \infty) \Big] \Big\} \end{aligned} \tag{D.88}$$

All the time-varying terms in the second set of square brackets are relatively weak, so that

the square magnitude is approximately

$$|E_{30}|^2 = Z^2 \Big\{ \Big| \chi^{(3)}_{0,\mathrm{m}} V(-\infty,\zeta_i) + T_0 \chi^{(3)}_{0,\mathrm{a}} V(\zeta_i,\infty) \Big|^2 + \Big[T_{0,3} \chi^{(3)}_{0,\mathrm{m}} V(-\infty,\zeta_i) + T_{0,1} \chi^{(3)}_{0,\mathrm{a}} V(\zeta_i,\infty) \Big] \times \Big[\delta T_3 \chi^{(3)}_{0,\mathrm{m}} V^*(-\infty,\zeta_i) + T_{0,3} \delta\chi^{(3)} V^*(-\infty,\zeta_i) + T_{0,3} \chi^{(3)}_{0,\mathrm{m}} (3\delta k_1'' - \delta k_3'') W^*(-\infty,\zeta_i) + 3\delta T_1 \chi^{(3)}_{0,\mathrm{a}} V^*(\zeta_i,\infty) \Big] + \mathrm{c.c.} \Big\} \quad \text{(D.89)}$$

where c.c. is the complex conjugate of the second term in the curly braces. We would like to compare the relative strengths of the CsHRS term, $\delta\chi^{(3)}$, the cascaded amplitude modulations, $(3\delta k_1'' - \delta k_3'')$, and the effects of the modulated transmission coefficient of the fundamental and third harmonic ΔT_1, δT_3. On top of this we may have to consider modulated transmission of the third harmonic as well, but it shall be left out for the moment. The terms proportional to the CsHRS response are

$$\delta\chi^{(3)} \Big\{ V^*(-\infty,\zeta_i) \Big[T_{0,3} \chi^{(3)}_{0,\mathrm{m}} V(-\infty,\zeta_i) + T_{0,1} \chi^{(3)}_{0,\mathrm{a}} V(\zeta_i,\infty) \Big] + V(-\infty,\zeta_i) \Big[T_{0,3} \chi^{(3)}_{0,\mathrm{m}} V^*(-\infty,\zeta_i) + T_{0,1} \chi^{(3)}_{0,\mathrm{a}} V^*(\zeta_i,\infty) \Big] \Big\} \quad \text{(D.90)}$$

As any quantity plus its conjugate is the twice the real part, we find the CsHRS response is proportional to

$$\delta\chi^{(3)} \times \Re \Big\{ V^*(-\infty,\zeta_i) \Big[T_{0,3} \chi^{(3)}_{0,\mathrm{m}} V(-\infty,\zeta_i) + T_{0,1} \chi^{(3)}_{0,\mathrm{a}} V(\zeta_i,\infty) \Big] \Big\} \quad \text{(D.91)}$$

Likewise the cascaded amplitude modulations work out to

$$\chi^{(3)}_{0,\mathrm{m}} (3\delta k_1'' - \delta k_3'') \times \Re \Big\{ W^*(-\infty,\zeta_i) \Big[T_{0,3} \chi^{(3)}_{0,\mathrm{m}} V(-\infty,\zeta_i) + T_{0,1} \chi^{(3)}_{0,\mathrm{a}} V(\zeta_i,\infty) \Big] \Big\} \quad \text{(D.92)}$$

The effect of transmission modulation of the fundamental is proportional to

$$3\delta T \chi^{(3)}_{0,\mathrm{a}} \times \Re \Big\{ V^*(\zeta_i,\infty) \Big[T_{0,3} \chi^{(3)}_{0,\mathrm{m}} V(-\infty,\zeta_i) + T_{0,1} \chi^{(3)}_{0,\mathrm{a}} V(\zeta_i,\infty) \Big] \Big\} \quad \text{(D.93)}$$

and finally the effect of the modulation of the third harmonic transmission is proportional to

$$\delta T_3 \chi^{(3)}_{0,\mathrm{m}} \times \Re \Big\{ V^*(-\infty,\zeta_i) \Big[T_{0,3} \chi^{(3)}_{0,\mathrm{m}} V(-\infty,\zeta_i) + T_{0,1} \chi^{(3)}_{0,\mathrm{a}} V(\zeta_i,\infty) \Big] \Big\} \quad \text{(D.94)}$$

We review the general behavior of each of these terms, discerning the sinusoidal dependence

$$\delta\chi^{(3)} \propto \sin(\Omega_v \tau) \tag{D.95}$$

$$(3\delta k_1'' - \delta k_3'') \propto \cos(\Omega_v \tau) \tag{D.96}$$

$$\delta T \propto \sin(\Omega_v \tau) \tag{D.97}$$

We now turn our attention to the integrals in V and W, using the shorthand in the previous section expanding A_1 in terms of C and D

$$\begin{aligned} V(-\infty, \zeta_i) = \int_{-\infty}^{\zeta_i} \frac{1}{A_1^2(\zeta')} \mathrm{d}\zeta', &= \int_{-\infty}^{\zeta_i} \frac{1}{(C + D\zeta')^2} \mathrm{d}\zeta' \\ &= \frac{1}{D(C + D\zeta')}\Big|_{-\infty}^{\zeta_i} = \frac{1}{D(C + D\zeta_i)} = -i\frac{w_{10}^2 k_1}{2} \frac{1}{A_1(\zeta_i)} \end{aligned} \tag{D.98}$$

$$V(\zeta_i, \infty) = \int_{\zeta_i}^{\infty} \frac{1}{A_1^2(\zeta')} \mathrm{d}\zeta' = \frac{1}{D(C + D\zeta')}\Big|_{\zeta_i}^{\infty} = -\frac{1}{D(C + D\zeta_i)} = i\frac{w_{10}^2 k_1}{2} \frac{1}{A_1(\zeta_i)} \tag{D.99}$$

$$\begin{aligned} W(-\infty, \zeta_i) = \int_{-\infty}^{\zeta_i} \frac{\zeta'}{A_1^2(\zeta')} \mathrm{d}\zeta' &= \int_{-\infty}^{\zeta_i} \frac{\zeta'}{(C + D\zeta')^2} \mathrm{d}\zeta' \\ &= \frac{1}{D^2} \left[\ln(C + D\zeta') + \frac{C}{C + D\zeta'} \right]_{-\infty}^{\zeta_i} \\ &= \frac{1}{D^2} \left\{ \ln A_1(\zeta_i) + \frac{C}{A_1(\zeta_i)} - \lim_{\zeta' \to -\infty} \left[\ln A_1(\zeta') + \frac{C}{A_1(\zeta')} \right] \right\} \end{aligned} \tag{D.100}$$

The limit presents us with a problem rooted in the presence of a ζ' in the numerator of the integrand. This ζ' comes from the attenuation of the pulse caused by perturbations in $\chi^{(1)}$. This is linear attenuation, and accumulates linearly as a function of propagation distance. We have not accounted for finite sample thickness and Gaussian focusing pump beams, which would cause this attenuation to fade off outside the Rayleigh range. In light

of this, we would rather integrate from 0 to ζ_i, where we define $\zeta = 0$ to be the beginning of the interaction region. Then the integral becomes

$$W(-\infty, \zeta_i) \approx \frac{1}{D^2}\left[\ln A_1(\zeta_i) + \frac{C}{A_1(\zeta_i)} - \ln A_1(0) - \frac{C}{A_1(0)}\right] \tag{D.101}$$

The quantity common to each of the three effects then becomes

$$\begin{aligned}\left[T_{0,3}\chi^{(3)}_{0,\mathrm{m}}V(-\infty,\zeta_i) + T_{0,1}\chi^{(3)}_{0,\mathrm{a}}V(\zeta_i,\infty)\right] \\ = T_{0,3}\chi^{(3)}_{0,\mathrm{m}}\int_{-\infty}^{\zeta_i}\frac{1}{A_1^2(\zeta')}\mathrm{d}\zeta' + T_{0,1}\chi^{(3)}_{0,\mathrm{a}}\int_{\zeta_i}^{\infty}\frac{1}{A_1^2(\zeta')}\mathrm{d}\zeta' \\ = -i\frac{w_{10}^2 k_1}{2A_1(\zeta_i)}\left[T_{0,3}\chi^{(3)}_{0,\mathrm{m}} - T_{0,1}\chi^{(3)}_{0,\mathrm{a}}\right],\end{aligned} \tag{D.102}$$

thus making it clear that the unperturbed THG depends on a difference between the susceptibilities and the transmission coefficients. Note that we expect the quantity in brackets to be positive, given that the transmission coefficient is less than 1 and the material response is equal to or less than the response of air.

The CsHRS term is proportional to (be careful to double-check the sign!)

$$\left(\frac{w_{10}^2 k_1}{2}\right)^2 \frac{1}{|A_1(\zeta_i)|^2}\left[T_{0,3}\chi^{(3)}_{0,\mathrm{m}} - T_{0,1}\chi^{(3)}_{0,\mathrm{a}}\right]\delta\chi^{(3)} \tag{D.103}$$

The third harmonic transmission-modulated term is like it,

$$\left(\frac{w_{10}^2 k_1}{2}\right)^2 \frac{1}{|A_1(\zeta_i)|^2}\left[T_{0,3}\chi^{(3)}_{0,\mathrm{m}} - T_{0,1}\chi^{(3)}_{0,\mathrm{a}}\right]\delta T_{0,3}\chi^{(3)}_{0,\mathrm{m}} \tag{D.104}$$

And the fundamental transmission-modulated term is opposite

$$-\left(\frac{w_{10}^2 k_1}{2}\right)^2 \frac{1}{|A_1(\zeta_i)|^2}\left[T_{0,3}\chi^{(3)}_{0,\mathrm{m}} - T_{0,1}\chi^{(3)}_{0,\mathrm{a}}\right]3\delta T_{0,1}\chi^{(3)}_{0,\mathrm{a}} \tag{D.105}$$

D.9 Conclusion

These terms are identical in the way they depend on the placement of the boundary ζ_i. In order to account for the fact that these terms each have a unique dependence on the interface placement, we will need to account for axial intensity variations of the pump in a Gaussian focus. It will be shown in the next chapter this is sufficient to describe the experimental results, without introducing the added complexity of the transverse variations in the pump pulse.

APPENDIX E

NOTATION AND COORDINATE SYSTEMS

E.1 Abbreviations

The following is a list of commonly used abbreviations and their expansions:

CW Continuous Wave (not pulsed)

FWHM Full Width at Half Maximum

THG Third Harmonic Generation.

VC Vibrational Coherence

E.2 Symbols

Symbols and their units.

$*$ Complex conjugate

Δk Phase mismatch in THG.

$\epsilon_0 \approx 8.854 \times 10^{-12}\mathrm{F/m}$ Vacuum electric permittivity.

τ_p Resonant pulse train chirped pump pulse separation.

τ_{pp} Pump–probe pulse time delay [ps].

τ_{pr} Probe–reference pulse time delay [ps].

τ_{p} Pump pulse FWHM duration.

$\chi^{(3)}$ Third order nonlinear optical susceptibility.

Ω_v Vibrational frequency.

ω_1 Fundamental optical frequency

ω_3 Third harmonic optical frequency.

b Confocal parameter of a Gaussian beam.

A Gaussian focusing denominator term.

$\mathcal{E}$ Real-valued electric field

$\widetilde{\mathcal{E}}$ Complex electric field.

$E(\mathbf{r}, t)$ Complex pulse envelope.

$E_{\mathrm{o},1}$ Probe fundamental electric field, drives harmonic generation.

$E_{\mathrm{o},3}$ Probe third harmonic field

E_{p} Pump electric field.

$k_0, k_1, k_2, \ldots$ Taylor expansion coefficients of propagation wavenumber

$k_{0,1}$ Propagation wavenumber of the fundamental.

$k_{0,3}$ Propagation wavenumber of the third harmonic.

k_x, k_y Transverse spatial frequencies [m^{-1}]

T Fresnel field transmission coefficient.

t Time [s]

u_{p} Pump pulse group velocity.

U_t Complex temporal pulse envelope.

U_s Complex spatial pulse envelope.

x, y Spatial transverse coordinates [m].

z Longitudinal coordinate.

z_R Rayleigh range of a Gaussian beam.

E.3 Notation

Some of the expressions in these notes are long and cover several lines. In an effort to improve readability and keep things compact, we drop explicit time- and space-dependence from functions. To remind the reader that the vibrational perturbations are still functions of pump–probe delay and interface placement, we will write all such terms with a lowercase delta prefix and a tilde over the symbol, e.g. $\delta\chi^{(3)}(\tau, z) \equiv \widetilde{\delta\chi}^{(3)}$.

While vibrational perturbations are prefixed with a lowercase δ, the uppercase Δ is reserved for phase mismatch, Δk.

Also, in order to prevent confusion of time t and Fresnel field transmission coefficient, we will denote the Fresnel field transmission coefficient with a capital T, even though in the standard notation it is a lowercase t and the power transmission coefficient is $T = t^2$.

Some complex quantities may be broken down into real and imaginary parts,

$$\widetilde{\delta\Delta k} = \widetilde{\delta\Delta k}' + i\widetilde{\delta\Delta k}'',$$

where the real part is denoted by a single quote ($'$) and the imaginary part a double quote ($''$).

Terms related to the fundamental or third harmonic are designated with subscripts $_1$ and $_3$, respectively. Pump and probe pulses are marked with subscripts $_\mathrm{p}$ and $_\mathrm{o}$ (note the probe subscript is *o* not 0). For example, third harmonic field generated by the probe pulse is $E_{\mathrm{o},3}$. The FWHM duration of the pump pulse is τ_p. In cases where a reference pulse is involved, it is denoted by a $_\mathrm{r}$ subscript.

E.4 Fourier transforms and domains

Functions that have been transformed into the spatial frequency domain via Fourier transform are denoted with a hat,

$$E(x, y, z) \to \hat{E}(k_x, k_y, z).$$

The convention for spatial Fourier transform, relating the coordinates x and y to the spatial frequencies k_x and k_y respectively are the inverse Fourier transform,

$$E(x,y,z) = \iint_{-\infty-\infty}^{\infty,\infty} \hat{E}(k_x,k_y,z)e^{i(k_x x+k_y y)}\ \mathrm{d}k_x\ \mathrm{d}k_y, \tag{E.1}$$

and the Fourier transform,

$$\hat{E}(kx,ky,z) = \frac{1}{4\pi^2}\iint_{-\infty-\infty}^{\infty,\infty} E(x,y,z)e^{-i(k_x x+k_y y)}\ \mathrm{d}x\ \mathrm{d}y. \tag{E.2}$$

The spatial frequencies may be thought of as indication of direction, or angle of propagation.

Assuming Gaussian beams, the transverse Laplacian transforms in the spatial frequency domain to

$$\nabla_\perp^2 \to (k_x^2 + k_y^2)$$

E.5 Coordinate frames

Coordinate transforms are common in this document to make equations more compact and to facilitate integration. We begin with fields as a function of (x,y,z,t), in the laboratory frame, and referenced with $t=0$ at the center (peak) of the probe pulse. That is, the pump pulse has a peak at $t=-\tau$, where τ is the pump–probe delay.

The first transformation in Section 2.2 is to the traveling group frame of the probe $(x,y,z,t) \to (x,y,\zeta,t_\mathrm{o})$. The transformations are $t_\mathrm{o} = t - u_\mathrm{o}^{-1}z$ and $\zeta = z$, where u_o is the group velocity of the probe pulse. The reason for a new variable in the direction of propagation, $z \to \zeta$ is that the derivatives will transform,

$$\frac{\partial}{\partial z} + \frac{1}{u_\mathrm{o}}\frac{\partial}{\partial t} = \frac{\partial}{\partial \zeta}, \tag{E.3}$$

thus reducing the PDE to having a derivative of ζ instead of both z and t.

When focusing Gaussian beams are considered, including the axial intensity variating of the pump, we transform the coordinate along the propagation axis to ξ, which is normalized by the Rayleigh length, $(x,y,\zeta,t_\mathrm{o}) \to (x,y,u,t_\mathrm{pr})$. The normalized coordinate is $u = \zeta/z_R$ where z_R is the Rayleigh length.

Finally, when we perform the integrals for focusing Gaussian beams, we make one further transformation of the axial coordinate to one that is both normalized by the Rayleigh length and referenced to the focal plane, that is the position of the waist u_w: $(x, y, u, t_{\rm pr}) \rightarrow (x, y, x, t_{\rm o})$. In the process, the interface position is now u_L.

Afterward, in the section in detected signals, we shift to z_L instead of x_L. I think z_L is the displacement of the interface from the focal plane, in regular, non-normalized coordinates.

E.6 Miller indices, and optical properties of a crystal

Miller indices are used to describe directions, e.g. $[abc]$, and planes, e.g. (abc) in a crystal. The following is a brief relation of the Miller index notation to the optic axis of a uniaxial crystal. For more detail, see Refs. [113, 114].

E.6.1 Optic axis

For instance, the optical axis of a uniaxial crystal is specified by [001]. When specifying a direction, the last coordinate c corresponds to the axis of highest symmetry. The optic axis is the direction of propagation such that any incident polarization sees the same index. That is, a beam propagating along the optic axis will experience no birefringent effects. This is usually along the axis of highest symmetry. If the crystal is symmetric upon rotation about this axis, there is no reason for the optic properties to vary. A crystal with hexagonal structure often has a fourth, redundant coordinate specified, so that the optic axis is denoted by [0001]

If we were to specify the surface of a crystal cut so that it is normal to the optic axis, the face would be (001). A face cut at (100) or (010) would be cut along, or parallel to the optic axis, while a face cut at (011) would have a surface normal at 45° to the optic axis.

It is also common to see a curly brace notation to specify crystal faces. These specify the entire family of planes that are, by the symmetry of the crystal lattice, equivalent. For a centrosymmetric, cubic crystal, the three planes $(001), (010), (100)$ are equivalent, and can be represented by 001.

E.6.2 Raman selection rules

A full listing of selection rules for Raman-active vibrational modes is found in Ref. [115], and selection rules for hyper- and second hyper-Raman interactions may be found in Ref. [102]. The x, y, z coordinates in these articles are related to the Miller indices by $[x, y, z]$. For example, the Raman tensor for the A mode of a cubic class T crystal is [115]

$$\begin{pmatrix} a & 0 & 0 \\ 0 & a & 0 \\ 0 & 0 & a \end{pmatrix} \tag{E.4}$$

which may be excited with pump light polarized along any axis x, y, or z, and probed along any axis x, y, or z without the same measured intensity of the Raman interaction. To be specific, if we have a crystal cut to the (001) face, we may pump with light propagating along the [001] direction with pump polarization along [010], and the probe, propagating in the same direction may be polarized either [010] or [100]. The depth of modulation imparted to the probe will be the same in either polarization.

However, the $F(z)$ mode in the same symmetry class crystal has the Raman tensor [115]

$$\begin{pmatrix} 0 & b & 0 \\ b & 0 & 0 \\ 0 & 0 & 0 \end{pmatrix} \tag{E.5}$$

Thus a pump incident on the (001) face with polarization [010] will not excite the $F(z)$ mode. The polarization must be rotated 45° so that it is polarized along [110], to excite the mode, and the probe must also be polarized similarly. With plane-wave pulses, it would be impossible to excite the $F(z)$ mode with pulses incident normal to the (100) or (010) faces.

REFERENCES

[1] D. Brune, R. Hellborg, H. J. Whitlow, and O. Hunderi, eds., *Surface characterization.* Scandinavian Science Publisher, 1997.

[2] N. Esser and W. Richter, "Raman scattering from surface phonons," in *Light Scattering in Solids VIII*, pp. 96–168, Springer Berlin / Heidelberg, 2000.

[3] L. M. Peter, "Characterization and modeling of Dye-Sensitized solar cells," *The Journal of Physical Chemistry C*, vol. 111, pp. 6601–6612, May 2007.

[4] H. Greijer, J. Lindgren, and A. Hagfeldt, "Resonance raman scattering of a Dye-Sensitized solar cell: Mechanism of thiocyanato ligand exchange," *The Journal of Physical Chemistry B*, vol. 105, pp. 6314–6320, July 2001.

[5] J. A. Carter, Z. Wang, and D. D. Dlott, "Spatially resolved vibrational energy transfer in molecular monolayers," *The Journal of Physical Chemistry A*, vol. 112, pp. 3523–3529, Apr. 2008.

[6] R. Fuchs and K. L. Kliewer, "Optical modes of vibration in an ionic crystal slab," *Physical Review*, vol. 140, p. A2076, Dec. 1965.

[7] G. Benedek and J. P. Toennies, "Helium atom scattering spectroscopy of surface phonons: genesis and achievements," *Surf. Sci.*, vol. 299, pp. 587–611, 1994.

[8] "Surface vibrational modes of α-quartz(0001) probed by sum-frequency spectroscopy," *Physical Review Letters*, vol. 101, p. 016101, 2008.

[9] M. L. Howe, K. L. Watters, and R. G. Greenler, "Investigation of thin surface films and adsorbed molecules using raman spectroscopy," *J. Phys. Chem.*, vol. 80, no. 4, pp. 382–385, 1976.

[10] H. Jeziorowski and H. Knözinger, "Laser raman spectra of molecules adsorbed on silica surfaces," *Chem. Phys. Lett*, vol. 43, no. 1, pp. 37–40, 1976.

[11] A. Campion, "Raman spectroscopy of molecules adsorbed on solid surfaces," *Annual Review of Physical Chemistry*, vol. 36, no. 1, pp. 549–572, 1985.

[12] V. E. Henrich and P. A. Cox, *The surface science of metal oxides.* Cambridge University Press, 1996.

[13] H. Ibach, "Low-Energy Electron Spectroscopy – a Tool for Studies of Surface Vibrations," *J. Vac. Sci. Tech.*, vol. 9, no. 2, pp. 713–719, 1972.

[14] H. Ibach, "Recent advances in electron energy loss spectroscopy of surface vibrations," *J. Chem. Soc. Faraday T.*, vol. 92, pp. 4771–4774, 1996.

[15] W. Moritz, J. Landskron, and M. Deschaur, "Perpsectives for surface structure analysis with low energy electron diffraction," *Surf. Sci.*, vol. 603, pp. 1306–1314, 2009.

[16] Y. J. Chabal, "Surface infrared-spectroscopy," *Surf. Sci. Rep.*, vol. 8, no. 5–7, pp. 211–357, 1988.

[17] M. Sovago, R. K. Campen, G. W. H. Wurpel, M. Müller, H. J. Bakker, and M. Bonn, "Vibrational response of hydrogen-bonded interfacial water is dominated by intramolecular coupling," *Phys. Rev. Lett.*, vol. 100, p. 173901, 2008.

[18] T. Nomoto and H. Onishi, "Fourth-order coherent raman spectroscopy in a time domain: applications to buried interfaces," *Phys. Chem. Chem. Phys.*, vol. 9, pp. 5515–5521, 2007.

[19] Y. Yan, J. Gamble, and K. A. Nelson, "Impulsive stimulated scattering: General importance in femtosecond laser pulse interactions with matter, and spectroscopic applications," *The Journal of Chemical Physics*, vol. 83, pp. 5391–5399, Dec. 1985.

[20] J. F. McGilp, "Epioptics: linear and non-linear optical spectroscopy of surfaces and interfaces," *Journal of Physics: Condensed Matter*, vol. 2, no. 40, pp. 7985–8006, 1990.

[21] D. S. Roseburgh and R. J. Cole, "A comparison of surface sensitive reflection spectroscopies," *Journal of Physics: Condensed Matter*, vol. 16, no. 39, pp. S4279–S4288, 2004.

[22] B. F. Levine, C. V. Shank, and J. P. Heritage, "Surface Vibrational Spectroscopy Using Stimulated Raman-Scattering," *IEEE J. Quantum Electron.*, vol. 15, no. 12, pp. 1418–1432, 1979.

[23] G. Eesley, "Surface raman ellipsometry," *IEEE J. Quantum Elect.*, vol. QE-17, no. 7, pp. 1285–1292, 1981.

[24] Y. R. Shen, "Surface-properties probed by 2nd-harmonic and sum-frequency generation," *Nature*, vol. 337, no. 6207, pp. 519–525, 1989.

[25] Y. M. Chang, L. Xu, and H. W. K. Tom, "Observation of coherent surface optical phonon oscillations by time-resolved surface second-harmonic generation," *Phys. Rev. Lett.*, vol. 78, pp. 4649–4652, 1997.

[26] K. B. Eisenthal, "Liquid interfaces probed by second-harmonic and sum-frequency spectroscopy," *Chem. Rev.*, vol. 96, pp. 1343–1360, 1996.

[27] P. B. Miranda and Y. R. Shen, "Liquid interfaces: A study by sum-frequency vibrational spectroscopy," *J. Phys. Chem. B*, vol. 103, pp. 3292–3307, 1999.

[28] Y. Shen, "Surface contribution versus bulk contribution in surface nonlinear optical spectroscopy," *Applied Physics B: Lasers and Optics*, vol. 68, pp. 295–300, Mar. 1999.

[29] S. Cattaneo and M. Kauranen, "Bulk versus surface contributions in nonlinear optics of isotropic centrosymmetric media," *physica status solidi (b)*, vol. 242, no. 15, pp. 3007–3011, 2005.

[30] H. Held, A. Lvovsky, X. Wei, and Y. Shen, "Bulk contribution from isotropic media in surface sum-frequency generation," *Phys. Rev. B*, vol. 66, no. 20, p. 205110, 2002.

[31] J. E. Sipe, D. J. Moss, and H. M. van Driel, "Phenomenological theory of optical second- and third-harmonic generation from cubic centrosymmetric crystals," *Physical Review B*, vol. 35, no. 3, p. 1129, 1987.

[32] T. Stehlin, M. Feller, P. Guyot-Sionnest, and Y. R. Shen, "Optical second-harmonic generation as a surface probe for noncentrosymmetric media," *Optics Letters*, vol. 13, p. 389, May 1988.

[33] D. J. Bottomley, G. Lüpke, C. Meyer, and Y. Makita, "Exact separation of surface and bulk contributions to anisotropic second-harmonic generation from cubic centrosymmetric media," *Optics Letters*, vol. 20, pp. 453–455, Mar. 1995.

[34] X. Wei, S. C. Hong, A. I. Lvosky, H. Held, and Y. R. Shen, "Evaluation of surface vs bulk contributions in sum-frequency vibrational spectroscopy using reflection and transmission geometries," *J. Phys. Chem. B*, vol. 104, no. 14, pp. 3349–3354, 2000.

[35] R. Hellwarth, "Third-order optical susceptibilities of liquids and solids," *Progress in Quantum Electronics*, vol. 5, pp. 1–68, 1979.

[36] T. Tsang, "Optical third-harmonic generation at interfaces," *Phys. Rev. A*, vol. 52, no. 5, pp. 4116–4125, 1995.

[37] Y. Barad, H. Eisenberg, M. Horowitz, and Y. Silberberg, "Nonlinear scanning laser microscopy by third harmonic generation," *Appl. Phys. Lett.*, vol. 70, no. 8, pp. 922–924, 1997.

[38] D. Stoker, M. C. Downer, M. F. Becker, and J. W. Keto, "Optical third-harmonic surface microscopy using ultra-short laser pulses," *physica status solidi (c)*, vol. 2, no. 12, pp. 3978–3982, 2005.

[39] R. W. Boyd, *Nonlinear optics*. Academic press, 2 ed., 2002.

[40] E. J. Suoninen, "Selection of method," in *Surface characterization* (D. Brune, R. Hellborg, H. J. Whitlow, and O. Hunderi, eds.), Scandinavian Science Publisher, 1997.

[41] S. D. Silvestri, J. G. Fujimoto, E. P. Ippen, E. B. Gamble, L. R. Williams, and K. A. Nelson, "Femtosecond time-resolved measurements of optic phonon dephasing by impulsive stimulated raman scattering in [alpha]-perylene crystal from 20 to 300 k," *Chemical Physics Letters*, vol. 116, pp. 146–152, May 1985.

[42] M. Cho, M. Du, N. F. Scherer, G. R. Fleming, and S. Mukamel, "Off-resonant transient birefringence in liquids," *The Journal of Chemical Physics*, vol. 99, no. 4, pp. 2410–2428, 1993.

[43] P. Vohringer and N. F. Scherer, "Transient grating optical heterodyne detected impulsive stimulated raman-scattering in simple liquids," *J. Phys. Chem.*, vol. 99, no. 9, p. 2684, 1995.

[44] J. K. Wahlstrand, R. Merlin, X. Li, S. T. Cundiff, and O. E. Martinez, "Impulsive stimulated raman scattering: comparison between phase-sensitive and spectrally filtered techniques," *Optics Letters*, vol. 30, pp. 926–928, Apr. 2005.

[45] A. Nazarkin, G. Korn, M. Wittmann, and T. Elsaesser, "Generation of multiple Phase-Locked stokes and Anti-Stokes components in an impulsively excited raman medium," *Physical Review Letters*, vol. 83, no. 13, p. 2560, 1999.

[46] R. A. Bartels, T. C. Weinacht, S. R. Leone, H. C. Kapteyn, and M. M. Murnane, "Nonresonant control of multimode molecular wave packets at room temperature," *Physical Review Letters*, vol. 88, p. 033001, Jan. 2002.

[47] J. W. Wilson, P. Schlup, and R. A. Bartels, "Synthetic temporal aperture coherent molecualr phase spectroscopy," *Chem. Phys. Lett.*, vol. 463, pp. 300–304, 2008.

[48] S. A. Akhmanov, V. A. Vysloukh, and A. S. Chirkin, *Optics of femtosecond laser pulses*. American Institute of Physics, 1992.

[49] Y. R. Shen and N. Bloembergen, "Theory of stimulated brillouin and raman scattering," *Physical Review*, vol. 137, p. A1787, Mar. 1965.

[50] S. Ruhman, A. G. Joly, and K. A. Nelson, "Time-resolved observations of coherent molecular vibrational motion and the general occurrence of impulsive stimulated scattering," *Journal of Chemical Physics*, vol. 86, no. 11, pp. 6563–6565, 1987.

[51] P. N. Butcher and D. Cotter, *The elements of nonlinear optics*. Cambridge University Press, July 1991.

[52] S. Mukamel, *Principles of Nonlinear Optical Spectroscopy*. Oxford University Press, New York, 1995.

[53] J. Chesnoy and A. Mokhtari, "Resonant impulsive-stimulated raman scattering on malachite green," *Phys. Rev. A*, vol. 38, no. 7, pp. 3566–3576, 1988.

[54] M. Takeda, H. Ina, and S. Kobayashi, "Fourier-transform method of fringe-pattern analysis for computer-based topography and interferometry," *Journal of the Optical Society of America A*, vol. 72, no. 1, pp. 156–160, 1982.

[55] P. Schlup, J. Wilson, K. Hartinger, and R. A. Bartels, "Dispersion-balancing of variable-delay monolithic pulse splitters," *Applied Optics*, vol. 46, no. 23, pp. 5967–5973, 2007.

[56] V. Boudon, J. L. Domenech, D. Bermejo, and H. Willnerc, "High-resolution raman spectroscopy of the nu(1) region and raman-raman double resonance spectroscopy of the 2 nu(1)-nu(1) band of (sf6)-s-32 and (sf6)-s-34. determination of the equilibrium bond length of sulfur hexafluoride," *Journal of Molecular Spectroscopy*, vol. 228, no. 2, pp. 392–400, 2004.

[57] J. R. Ferraro, K. Nakamoto, and C. W. Brown, *Introductory Raman Spectroscoyp*. Academic Press, London, 2 ed., 2003.

[58] M. D. Levinson and S. S. Kano, *Introduction to Nonlinear Laser Spectroscopy*. Academic Press, Inc., revised ed., 1988.

[59] T. C. Weinacht, R. Bartels, S. Backus, P. H. Bucksbaum, B. Pearson, J. M. Geremia, H. Rabitz, H. C. Kapteyn, and M. M. Murnane, "Coherent learning control of vibrational motion in room temperature molecular gases," *Chemical Physics Letters*, vol. 344, no. 3-4, pp. 333–338, 2001.

[60] R. A. Bartels, T. C. Weinacht, S. R. Leone, H. C. Kapteyn, and M. M. Murnane, "Nonresonant control of multimode molecular wave packets at room temperature," *Physical Review Letters*, vol. 88, no. 3, p. 033001, 2002.

[61] E. Gershgoren, R. A. Bartels, J. T. Fourkas, R. Tobey, M. M. Murnane, and H. C. Kapteyn, "Simplified setup for high-resolution spectroscopy that uses ultrashort pulses," *Optics Letters*, vol. 28, no. 5, pp. 361–363, 2003.

[62] A. M. Weiner, D. E. Leaird, J. S. Patel, and J. R. Wullert, "Programmable femtosecond pulse shaping by use of a multielement liquid-crystal phase modulator," *Optics Letters*, vol. 15, no. 6, pp. 326–328, 1990.

[63] A. Nazarkin, G. Korn, M. Wittmann, and T. Elsaesser, "Generation of multiple phase-locked stokes and anti-stokes components in an impulsively excited raman medium," *Physical Review Letters*, vol. 83, no. 13, pp. 2560–2563, 1999.

[64] R. A. Bartels, T. C. Weinacht, S. R. Leone, H. C. Kapteyn, and M. M. Murnane, "Nonresonant control of multimode molecular wave packets at room temperature," *Physical Review Letters*, vol. 88, no. 3, 2002.

[65] N. Dudovich, D. Oron, and Y. Silberberg, "Single-pulse coherently controlled nonlinear raman spectroscopy and microscopy," *Nature*, vol. 418, no. 6897, p. 512, 2002.

[66] D. Oron, N. Dudovich, and Y. Silberberg, "Femtosecond phase-and-polarization control for background-free coherent anti-stokes raman spectroscopy," *Physical Review Letters*, vol. 90, no. 21, p. 213902, 2003.

[67] S. H. Lim, A. G. Caster, and S. R. Leone, "Single-pulse phase-control interferometric coherent anti-stokes raman scattering spectroscopy," *Physical Review A*, vol. 72, no. 4, p. 041803, 2005.

[68] A. Zumbusch, G. R. Holtom, and X. S. Xie, "Three-dimensional vibrational imaging by coherent anti-stokes raman scattering," *Physical Review Letters*, vol. 82, no. 20, pp. 4142–4145, 1999.

[69] Y. J. Lee and M. T. Cicerone, "Vibrational dephasing time imaging by time-resolved broadband coherent anti-stokes raman scattering microscopy," *Applied Physics Letters*, vol. 92, no. 4, 2008.

[70] K. Hartinger and R. A. Bartels, "Single-shot measurement of ultrafast time-varying phase modulation induced by femtosecond laser pulses with arbitrary polarization," *Applied Physics Letters*, vol. 92, no. 2, p. 021126, 2008.

[71] A. Shalit, Y. Paskover, and Y. Prior, "In situ heterodyne detection in femtosecond time resolved four wave mixing," *Chemical Physics Letters*, vol. 450, no. 4-6, pp. 408–416, 2008.

[72] R. W. Hellwarth, "3rd-order optical susceptibilities of liquids and solids," *Progress in Quantum Electronics*, vol. 5, pp. 1–68, 1977.

[73] N. H. Matlis, S. Reed, S. S. Bulanov, V. Chvykov, G. Kalintchenko, T. Matsuoka, P. Rousseau, V. Yanovsky, A. Maksimchuk, S. Kalmykov, G. Shvets, and M. C.

Downer, "Snapshots of laser wakefields," *Nature Physics*, vol. 2, no. 11, pp. 749–753, 2006.

[74] E. N. Leith and Upatniek.J, "Reconstructed wavefronts and communication theory," *Journal of the Optical Society of America*, vol. 52, no. 10, p. 1123, 1962.

[75] J. A. Valdmanis, "Real time picosecond optical oscilloscope," *Ultrafast Phenomena V*, p. 82, 1986.

[76] A. Brun, P. Georges, G. Lesaux, and F. Salin, "Single-shot characterization of ultrashort light-pulses," *Journal of Physics D-Applied Physics*, vol. 24, no. 8, pp. 1225–1233, 1991.

[77] I. Wilke, A. M. MacLeod, W. A. Gillespie, G. Berden, G. M. H. Knippels, and A. F. G. van der Meer, "Single-shot electron-beam bunch length measurements," *Physical Review Letters*, vol. 88, no. 12, 2002.

[78] K. Hartinger and R. A. Bartels, "Pulse polarization splitting in a transient wave plate," *Optics Letters*, vol. 31, no. 23, pp. 3526–3528, 2006.

[79] H. Barkhuijsen, R. de Beer, W. Bovee, and D. van Ormondt, "Retrieval of frequencies, amplitudes, damping factors, and phases from time-domain signals using a linear least-squares procedure," *Journal of Magnetic Resonance*, vol. 61, pp. 465–481, 1985.

[80] D. W. Tufts and R. Kumaresan, "Estimation of frequencies of multiple sinusoids: Making linear prediction perform like maximum likelihood," *Proceedings of the IEEE*, vol. 70, no. 9, pp. 975–989, 1982.

[81] P. Schlup, J. Wilson, and R. Bartels, "Sensitive and selective detection of Low-Frequency vibrational modes through a Phase-Shifting fourier transform spectroscopy," *Quantum Electronics, IEEE Journal of*, vol. 45, no. 7, pp. 777–782, 2009.

[82] A. Assion, T. Baumert, M. Bergt, T. Brixner, B. Kiefer, V. Seyfried, M. Strehle, and G. Gerber, "Control of chemical reactions by feedback-optimized phase-shaped femtosecond laser pulses," *Science*, vol. 282, no. 5390, pp. 919–922, 1998.

[83] R. Bartels, S. Backus, E. Zeek, L. Misoguti, G. Vdovin, I. P. Christov, M. M. Murnane, and H. C. Kapteyn, "Shaped-pulse optimization of coherent emission of high-harmonic soft x-rays," *Nature*, vol. 406, no. 6792, pp. 164–166, 2000.

[84] J. Piasecki, B. Colombeau, M. Vampouille, C. Froehly, and J. A. Arnaud, "New method of measuring the impulse response of optical fibers," *Applied Optics*, vol. 19, pp. 3749–3755, Nov. 1980.

[85] L. Yang and S. Mukamel, "Dissecting quantum pathways in two-dimensional correlation spectroscopy of semiconductors," *Journal of Physics: Condensed Matter*, vol. 20, no. 39, p. 395202, 2008.

[86] I. Noda, "Recent advancement in the field of two-dimensional correlation spectroscopy," *Journal of Molecular Structure*, vol. 883-884, pp. 2–26, July 2008.

[87] Y. L. Li, L. Huang, R. J. D. Miller, T. Hasegawa, and Y. Tanimura, "Two-dimensional fifth-order raman spectroscopy of liquid formamide: Experiment and theory," *The Journal of Chemical Physics*, vol. 128, no. 23, p. 234507, 2008.

[88] F. Ding and M. T. Zanni, "Heterodyned 3D IR spectroscopy," *Chemical Physics*, vol. 341, pp. 95–105, Nov. 2007.

[89] K. Hartinger and R. A. Bartels, "Single-shot measurement of ultrafast time-varying phase modulation induced by femtosecond laser pulses with arbitrary polarization," *Applied Physics Letters*, vol. 92, no. 2, p. 021126, 2008.

[90] R. Trebino and D. J. Kane, "Using phase retrieval to measure the intensity and phase of ultrashort pulses: frequency-resolved optical gating," *Journal of the Optical Society of America A*, vol. 10, pp. 1101–1111, May 1993.

[91] D. Kane, "Real-time measurement of ultrashort laser pulses using principal component generalized projections," *Selected Topics in Quantum Electronics, IEEE Journal of*, vol. 4, no. 2, pp. 278–284, 1998.

[92] Y. Liu, A. Frenkel, G. A. Garrett, J. F. Whitaker, S. Fahy, C. Uher, and R. Merlin, "Impulsive light scattering by coherent phonons in laalo$_3$: Disorder and boundary effects," *Phys. Rev. Lett.*, vol. 75, no. 2, pp. 334–337, 1995.

[93] E. W. V. Stryland and M. Sheik-Bahae, "Z-scan measurements of optical nonlinearities," in *Characterization Techniques and Tabulations for Organic Nonlinear Materials*, pp. 655–692, Marcel Dekker, Inc., 1998.

[94] R. S. Tasgal and Y. B.Band, "Third-harmonic generation in isotropic media by focused pulses," *Phys. Rev. A*, vol. 70, p. 053810, 2004.

[95] S. Shin, Y. Tezuka, A. Sugawara, and M. Ishigame, "Silent central modes of the superionic conductor likso$_4$ studied by means of hyper-raman scattering: Evidence of coupling between lithium-ion conduction and sulfate-ion rotation," *Phys. Rev. B*, vol. 44, no. 21, pp. 11724–11733, 1991.

[96] P. A. Williams, A. H. Rose, K. S. Lee, D. C. Conrad, G. W. Day, and P. D. Hale, "Optical, thermo-optic, electro-optic, and photoelastic properties of bismuth germanate (Bi4Ge3O12)," *Applied Optics*, vol. 35, pp. 3562–3569, July 1996.

[97] L. Shampine, "Vectorized adaptive quadrature in MATLAB," *Journal of Computational and Applied Mathematics*, vol. 211, pp. 131–140, Feb. 2008.

[98] A. Zumbusch, G. R. Holtom, and X. S. Xie, "Three-Dimensional vibrational imaging by coherent Anti-Stokes raman scattering," *Physical Review Letters*, vol. 82, p. 4142, May 1999.

[99] J. Cheng, A. Volkmer, and X. S. Xie, "Theoretical and experimental characterization of coherent anti-Stokes raman scattering microscopy," *Journal of the Optical Society of America B*, vol. 19, pp. 1363–1375, June 2002.

[100] W. Yu and R. R. Alfano, "Multiple-photon light scattering," *Phys. Rev. A*, vol. 11, no. 1, pp. 188–190, 1975.

[101] V. N. Denisov, B. N. Mavrin, and V. B. Podobedov, "Hyper-raman scattering by vibrational excitations in crystals, glasses and liquids," *Phys. Rep.*, vol. 151, no. 1, pp. 1–92, 1987.

[102] J. H. Christie and D. J. Lockwood, "Selection rules for three- and four-photon raman interactions," *J. Chem. Phys.*, vol. 54, no. 3, pp. 1141–1154, 1971.

[103] H. Barkhuijsen, R. de Beer, W. M. M. J. Bovée, and D. van Ormondt, "Retrieval of frequencies, amplitudes, damping factors, and phases from time-domain signals using a linear least-squares procedure," *Journal of Magnetic Resonance (1969)*, vol. 61, pp. 465–481, Feb. 1985.

[104] M. Couzi, J. R. Vignalou, and G. Boulon, "Infrared and raman study of the optical phonons in $bi_4ge_3o_{12}$ single crystal," *Solid State Commun.*, vol. 20, pp. 461–465, 1976.

[105] D. van der Marel and H. W. den Hartog, "Raman spectroscopy of baf2:r3+ and srf2:r3+ solid solutions between 300 and 1400 k," *Phys. Rev. B*, vol. 25, no. 11, pp. 6602–6608, 1982.

[106] A. F. Penna, A. Chaves, P. d. R. Andrade, and S. P. S. Porto, "Light scattering by lithium tantalate at room temperature," *Phys. Rev. B*, vol. 13, no. 11, pp. 4907–4917, 1976.

[107] Müller, Squier, Wolleschensky, Simon, and Brakenhoff, "Dispersion pre-compensation of 15 femtosecond optical pulses for high-numerical-aperture objectives," *Journal of Microscopy*, vol. 191, pp. 141–150, Aug. 1998.

[108] V. V. Fomichev and O. I. Kondratov, "Vibrational spectra of compounds with the wolframite structure," *Spectrochimica Acta Part A: Molecular Spectroscopy*, vol. 50, pp. 1113–1120, June 1994.

[109] D. Meshulach, Y. Barad, and Y. Silberberg, "Measurement of ultrashort optical pulses by third-harmonic generation," *Journal of the Optical Society of America B*, vol. 14, no. 8, pp. 2122–2125, 1997.

[110] V. C. Ballenegger and T. A. Weber, "The Ewald–Oseen extinction theorem and extinction lengths," *American Journal of Physics*, vol. 67, pp. 599–605, July 1999.

[111] A. F. Lima, S. O. Souza, and M. V. Lalic, "Electronic structure and optical absorption of the bi4ge3o12 and the bi4si3o12 scintillators in ultraviolet region: An ab initio study," *Journal of Applied Physics*, vol. 106, no. 1, p. 013715, 2009.

[112] F. R. Aussenegg and M. E. Lippitsch, "On raman scattering in molecular complexes involving charge transfer," *Chemical Physics Letters*, vol. 59, pp. 214–216, Nov. 1978.

[113] J. F. Nye, *Physical properties of crystals: their representation by tensors and matrices.* Oxford University Press, 1985.

[114] D. R. Lovett, *Tensor properties of crystals.* CRC Press, Jan. 1999.

[115] R. Loudon, "The raman effect in crystals," *Advances in Physics*, vol. 13, no. 52, p. 423, 1964.